Development of novel laser processes for ophthalmology and dentistry

Wojciech Stanisław Góra

Submitted for the degree of Doctor of Philosophy

Heriot-Watt University

School of Engineering and Physical Sciences

May 2016

Abstract

This thesis is focused on the development of novel laser processes for ophthalmology and dentistry. Firstly an in-depth investigation into the possibility of using 10.6 μm CO_2 laser radiation for removal of hard dental tissue is presented. Different processing regimes are investigated to find optimal processing parameters that allow precise tissue removal without introducing any unwanted damage. Moreover the temperature increase during laser processing is measured to ensure process safety at the early stage research. When using a water spray the maximum recorded temperature increase in the pulpal chamber was ~3 ^{o}C (for a repetition rate of 250 Hz) which is below the critical level of 5.5 ^{o}C which would cause tissue necrosis.

The application of picosecond plasma mediated ablation of porcine sclera to create cavities which could form portals of entry to enhance drug delivery to the posterior eye is also investigated. To ensure that the process would not present a risk of unwanted damage to the eye both the temperature rise in the tissue and power transmission through the tissue is investigated during laser processing. The feasibility of this tissue modification as a means to improve drug permeation through the sclera is investigated with a Franz cell setup. It was found that if a drug (fluorescein dextran was used to simulate drug diffusion) is placed in a 5 mm by 5 mm by 100 μm cavity its permeation through the tissue increases by 11 – 12 times in first 5 hours compared to unmodified tissue.

To support experimental work and provide insight to the physical mechanism of the tissue removal process two theoretical computational models are developed. First an ALE moving boundary model is applied to investigate single pulse removal of hard dental tissue. For single line plasma mediated scanning ablation of porcine sclera a 2D finite element blow-off model is which confirms the presence of a heat accumulation phenomenon that can influence the depth of the cavity formed.

Consequently in this thesis the viability of two laser processes for application to modification of hard dental and soft scleral tissue has been demonstrated which opens up the possibility for developing novel procedures for surgery and dieses treatment.

Acknowledgements

Foremost, I would like to thank Dr Jonathan Shephard and Prof. Duncan Hand for the continuous support and guidance during the duration of the PhD study. Moreover I would like thanks everyone that have shown their support, i.e. Dr Richard Carter, Dr Rainer Beck, Dr Robert Maier, Dr Artur Urich, Dr Lisa McIntosh, Prof. Clive Wilson, Prof. Baljean Dhillon and anyone that I might have forgotten. Further I would like to thank technical and support staff, my colleagues from the Heriot-Wat University, especially members of the Applied Optics and Photonics research group for the times spent together.

The biggest thanks go to my parents Grażyna and Artur for their motivation and support throughout the duration of studies.

ACADEMIC REGISTRY

Research Thesis Submission

Name*:*	Wojciech Stanisław Góra		
School/PGI:	School of Engineering and Physical Sciences		
Version: *(i.e. First, Resubmission, Final)*	Final	Degree Sought (Award and Subject area)	Doctor of Philosophy

Declaration

In accordance with the appropriate regulations I hereby submit my thesis and I declare that:

1) the thesis embodies the results of my own work and has been composed by myself
2) where appropriate, I have made acknowledgement of the work of others and have made reference to work carried out in collaboration with other persons
3) the thesis is the correct version of the thesis for submission and is the same version as any electronic versions submitted*.
4) my thesis for the award referred to, deposited in the Heriot-Watt University Library, should be made available for loan or photocopying and be available via the Institutional Repository, subject to such conditions as the Librarian may require
5) I understand that as a student of the University I am required to abide by the Regulations of the University and to conform to its discipline.

* *Please note that it is the responsibility of the candidate to ensure that the correct version of the thesis is submitted.*

Signature of Candidate*:*		Date:	10/05/2016

Submission

Submitted By *(name in capitals):*	WOJCIECH GORA
Signature of Individual Submitting:	
Date Submitted:	10/05/2016

For Completion in the Student Service Centre (SSC)

Received in the SSC by *(name in capitals):*			
Method of Submission *(Handed in to SSC; posted through internal/external mail):*			
E-thesis Submitted (mandatory for final theses)			
Signature:		Date:	

Contents

List of publications

Conference publications

W. S. Góra, A. McDonald, D. P. Hand, J. D. Shephard, "Microsecond enamel ablation with 10.6μm CO_2 laser radiation", accepted to SPIE Photonics West BiOS Conference 2016.

R. J. Beck, W. S. Góra, N. MacIntyre, S. Gunadi, D. Jayne, D. P. Hand, J. D. Shephard," Precision resection of intestine using ultrashort laser pulses ", accepted to SPIE Photonics West BiOS Conference 2016,

W. S. Góra, R. M. Carter, B. Dhillon, D. P. Hand, J. D. Shephard, " Ultrafast laser machining of porcine sclera", SPIE European Conferences on Biomedical Optics Proceedings 9542, Medical Laser Applications and Laser-Tissue Interactions VII, 95420T (15 July 2015); doi:10.1117/12.2183627.

R. J. Beck, W. S. Góra, R. M. Carter, S. Gundadi, D. Jayne, D. P. Hand, J. D. Shephard, "Precision machining of pig intestine using ultrafast laser pulses", SPIE European Conferences on Biomedical Optics Proceedings 9542, Medical Laser Applications and Laser-Tissue Interactions VII, 95421B (15 July 2015); doi:10.1117/12.2197930.

W. S. Góra, A. Urich, L. McIntosh; R. M. Carter, C, G. Wilson, B. Dhillon, D. P. Hand, J. D. Shephard, "High precision laser sclerostomy", SPIE Photonics West BiOS Conference Proceedings 9307, Ophthalmic Technologies XXV, 93071Y (12 March 2015); doi: 10.1117/12.2079146.

W. S. Góra, E. M. Harvey, B. Dhillon, S. Parson, R. R. J. Maier, D. P. Hand, J. D. Shephard, "Picosecond laser ablation of porcine sclera", SPIE Photonics West BiOS Conference Proceedings 8567, Ophthalmic Technologies XXIII, 856726 (26 March 2013); doi: 10.1117/12.2004828.

Conference presentations

R. J. Beck, W. S. Góra, R. M. Carter, N. MacIntyre, S. Gundadi, D. Jayne, D. P. Hand, J. D. Shephard, "Ultrafast laser machining of pig intestine",4th *International Conference* on *Oncological Engineering 2015, Leeds, UK.*

W. S. Góra, A. Urich, L. McIntosh, R. M. Carter, B. Dhillon, C. G. Wilson, D. P. Hand, J. D. Shephard, "Ultrashort pulse laser machining of porcine sclera", Photon 14 Conference, London, UK, 2014

W. S. Góra, E. M. Harvey, H. J. Baker, A. McDonald, S. H. Parson, B. Dhillon, D. P. Hand, J. D. Shephard, " Optimal processing parameters for laser machining of hard and soft biological tissue", Innovative Manufacturing Research Conference- Laser Based Processes, Edinburgh, UK, 2012.

Chapter 1. Introduction

Since the construction of the first working laser in 1960 [1], laser development has driven towards new wavelength bands, a wider range of radiation parameters as well as the miniaturization of laser devices to incorporate them seamlessly into many branches of life. The properties of laser radiation, such as coherency, monochromaticity and the capability to reach high powers enabled laser applications in many different areas such as: medicine, industry, telecommunications, science and the military.

There are already procedures where lasers are used as a surgical tool, e.g. corrective eye surgery or as a replacement for dental bur in dental practices. However uptake is not widespread and there is scope for many other applications where lasers may offer a significant advantage by offering new possibilities, such as: quicker processing times, minimize the loss of the healthy tissue as well as allow new performing new procedures. In this project novel laser based medical techniques are developed targeting two potential areas: dentistry and ophthalmology.

1.1. Lasers in medical application

Due to the diversity of medical treatments and surgeries, no single laser is versatile enough for applications targeting all forms of biological tissue and processing regimes. The optical characteristics of tissue can be defined by: reflectivity, scattering coefficient, absorption coefficients and particle size [2]. The results of laser interaction with tissue are also dependent on the laser parameters, such as: wavelength, average/peak energy, pulse duration, repetition rate, working mode (continuous wave (CW), pulse) and output spatial profile [3]. As a result of these different requirements and parameters there are various type of medical lasers in use [3]:

- Gas lasers (e.g. CO_2 laser, argon ion laser, HeCd (Helium-Cadmium) laser, HeNe (Helium-Neon) laser, excimer laser). Example of applications: spine surgery and disk herniation [4].
- Solid state lasers (e.g. ruby laser, Nd:YAG (Neodymium doped Yttrium Aluminium Garnet): laser, Er:YAG (Erbium doped Yttrium Aluminium Garnet) laser, Er:YSGG (Erbium doped Yttrium Scandium Galium Garnet) laser, Ho:YAG (Holmium doped Yttrium Aluminium Garnet) laser, Ti:sapphire (Titanium-Sapphire) laser, Alexandrite laser, dye laser). Example of applications: photocoagulation of retina, LASIK (refractive surgery) and cutting of cancerous tissue [5].

- Diode lasers. Example of applications: hair removal, treatment of vascular lesion and tattoo removal [5].
- Free electron lasers. Example application: ocular surgery [6].

Most of the medical lasers can operate either in pulse mode or in CW mode. Figure 1.1 shows the spectrum of the most common medical lasers.

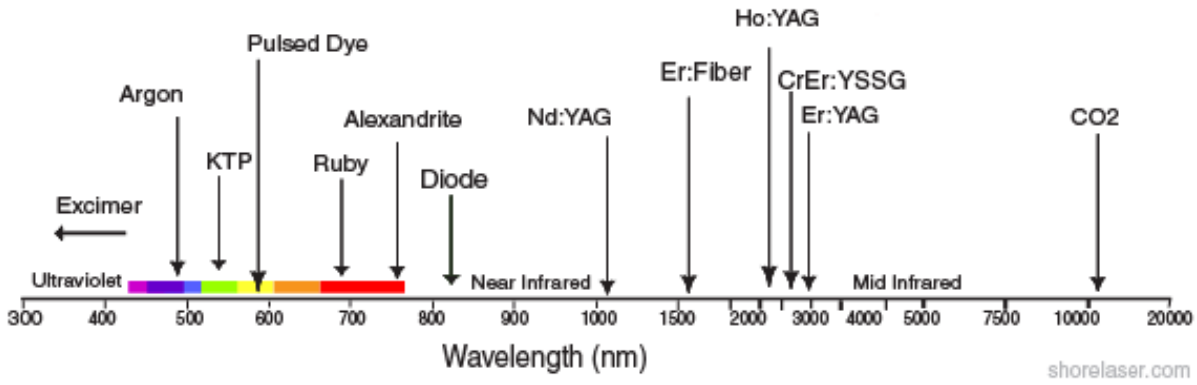

Figure 1.1 Spectrum of popular medical lasers. Graph taken from [7].

When considering most of the laser based processes a characteristic parameter that can describe a laser's usefulness in a specific treatment is penetration depth. The value of the penetration depth is an inverse of the absorption coefficient for a selected radiation wavelength and is defined as the depth where the intensity reaches 37% (drops to 1/e) of the intensity on the surface of the tissue [8]. Moreover the type of interaction between the laser and tissue can be divided into a few different regimes that can be separated by different pulse durations, total energy or the irradiance. Figure 1.2 shows different processing regimes as a function of pulse duration, irradiance and total energy.

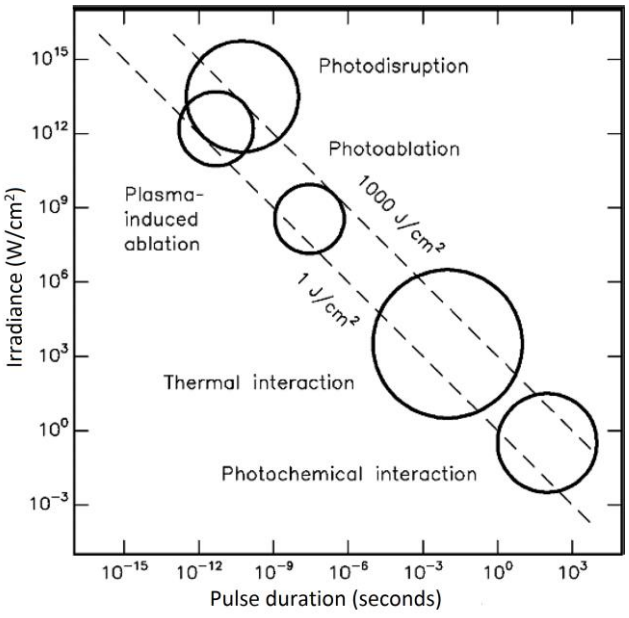

Figure 1.2 Various types of tissue laser interactions as a function of total exposure time, irradiance and pulse duration. Graph taken from [9].

1.2. Motivation – CO_2 laser removal of enamel

Through the concept of minimally invasive treatments, lasers are rising in popularity in dentistry. Currently used dental drills can create tunnels around 1 mm wide and the application of laser devices allows drilling of tunnels of width ~0.2 mm [10]. The increased precision of the focused laser beam allows removal of decayed tissue with minimal loss of healthy tissue. Moreover, the walls around a cavity prepared by laser radiation are more acid resistant and have higher resistance to future infections [10]. This is the result of high temperature, (>440 ^{o}C), where minerals decompose and form a new phases with higher acid resistance [10]. Additionally surgical procedures carried out by lasers are a lot quieter and less painful (no vibrations), which benefits patients. As a consequence lasers have found application in many different dental surgeries such as:

- hard tissue procedures (Er:YAG – 2.94 μm and Er:YSGG – 2.79 μm lasers [11]),
- soft tissue procedures (argon – 514 nm, KTP (potassium-titanyl-phosphate crystal) – 532 nm, Nd:YAG – 1064 nm, Er:YAG– 2.94 μm, Er:YSGG– 2.79 and CO_2 – 9.3 – 10.6 μm lasers [12]) ,
- aesthetic procedures (diode – 700 – 2000 nm, argon – 514 nm, KTP – 532 nm and CO_2 – 9.3 – 10.6 μm lasers[13]).

Currently in the United States of America, in dental practices Er:YAG lasers are used for removal of hard dental tissue after being approved by the Food and Drug Administration. In this thesis an alternative, to Er:YAG lasers, for the removal of hard dental tissue, is investigated – CO_2 laser radiating at the wavelength of 10.6 μm. The emitting band of CO_2 laser overlaps with the absorption of the phosphate band of hard dental tissue, which provides the basis for efficient tissue removal. Moreover, according to theoretical research presented by Villa Verde [14-16], CO_2 laser pulses with duration in the range of ~10 μs, would be capable of removing dental tissue without introducing any unwanted thermal damage and at the same time minimizing cracking.

Compared to Er:YAG, CO_2 laser production costs are smaller, as they are not heavily constrained by the cost of the laser medium [35], which directly influences the cost of the whole system. Moreover Er:YAG laser repetition rates are constrained by the laser medium and limited to 30 Hz [35], whereas CO_2 lasers are easily capable of reaching much higher repetition rates (e.g. 400 Hz [17, 18]). Additionally CO_2 laser are currently used, and approved, in dental practices for aesthetic procedures, but not for hard dental tissue removal. As a result the potential of using CO_2 for both aesthetic procedures and

hard dental tissue removal is very attractive as it significantly limits cost and amount of different devices required in a dental practice.

1.3. Motivation – picosecond laser ablation of sclera

Similarly to the dentistry, in ophthalmology the application of lasers managed to improve or even allow some of the ophthalmic procedures. The main difference between lasers used for dentistry and ophthalmology is pulse duration, as in ophthalmology any kind of heat deposition can be catastrophic as human eye is much less susceptible to heat than hard dental tissue. As a result most of the lasers used in clinical practise are ultrafast pico- and femtosecond lasers.

The use of ultrashort pulses has two main advantages over longer pulse durations. Firstly, absorption of ultrashort pulses is based on nonlinear interactions, which allows the laser to be absorbed in otherwise transparent tissue. Secondly, the removal mechanism is based on laser induced breakdown, where plasma is created when a specific, tissue dependant, threshold is reached. As a result heat deposition into the tissue is minimal which allows for "cold" ablation process, minimizing heat deposition into the tissue. One of the, currently popular, procedure that has been enabled by ultrafast femtosecond lasers is the LASIK procedure, which is an eye sight corrective surgery. The laser used in this thesis is a picosecond laser instead of previously mentioned femtosecond lasers as it more cost effective, more reliable and offers higher processing rates (amount of the material removed/time).

This work is focused on finding optimal parameters for creating cavities within scleral tissue without introducing unwanted damage. The main applications that these processes are targeting are improved drug delivery to the posterior part of the eye as such a cavity can be used as a portal of entry for implants that release drugs over time. This approach is much less invasive than the currently used method which requires an injection into the central part of the eye, which can only be achievable by puncturing an eye with a needle. The second procedure that could be improved by a controlled removal of scleral is surgery targeting glaucoma. When treating glaucoma the goal is to decrease the pressure inside the eyeball, hence the controlled thinning of sclera, would allow higher local deformation, slightly increasing the volume of an eye leading to a decreased pressure.

1.4. Thesis outline

Thesis outline is presented below:

- **Chapter 2** provides all of the important information regarding both hard dental tissue as well as ophthalmic tissue. Information regarding tissue structures, its thermomechanical and optical properties. Additionally current clinical application and key research finding in both areas are presented.
- **Chapter 3** presents an in-depth investigation into CO_2 laser removal is presented. Many different irradiation parameters are tested (pulse energy, pulse duration, repetition rate, converging/diverging beam), the influence of the water spray and temperature increase during laser processing is measured.
- **Chapter 4** describes a complete investigation into the ultrafast laser ablation of porcine sclera. The influence of different processing parameters (pulse energy, repetition rate, scanning speed, cavity shape and scanning strategy) onto the final shape of cavity is tested. Consequently the safety of the process is investigated by testing temperature increase and possibility of radiation being transmitted through the tissue during the process. Moreover the change in the permeability due to the cavity creation is tested.
- **Chapter 5** provides two theoretical models to support experimental results from two preceding chapters. Firstly an ALE (Arbitrary Lagrangian–Eulerian) moving boundary model of CO_2 laser removal of enamel is presented. In the second part of the chapter a 2D finite element blow-off model for picosecond removal of soft ophthalmic tissue is conferred.
- **Chapter 6** provides a summarization of the key findings of the thesis.

Chapter 2. Literature review of lasers in dentistry and ophthalmology

Chapter 2 presents background information for the experimental thesis. It describes the structures of dental and ophthalmic tissues and their optical and thermomechanical parameters. Previous results achieved with different lasers are presented and potential drawbacks are discussed. Additionally different modelling approaches are presented alongside with modelling results applied in investigation of laser-material interaction. Consequently currently used laser based devices in medical practices and their application in the fields of dentistry and ophthalmology are shown.

2.1. Introduction

One of the areas where lasers have been exceptionally successful in medicine is where they can offer more precise and less invasive therapies; many of which can be carried out relatively quickly in comparison to traditional invasive surgical procedures. Moreover applications of lasers can enable novel procedures that are not possible using traditional medical equipment. In as little as a few years from constructing the first laser device, lasers were taken from a laboratory prototype to the first laser based treatment in 1962 [19]. Since then lasers have become part of various medical treatments and surgeries in dentistry, ophthalmology, otolaryngology, urology, dermatology, gastroenterology, gynaecology, cardiology, orthopaedics and neurosurgery [20].

2.2. Lasers in dentistry

In order to introduce new lasers into dental applications, and evaluate the effectiveness, fundamental knowledge about the interaction between the laser radiation and the human tooth is necessary. In order to understand the influence of laser radiation on human dental tissue, knowledge of the tooth structure, as well as optical (absorption coefficient, scattering, reflectance) and thermal (thermal diffusivity, thermal conductivity, specific heat, density) properties are essential [21].

2.2.1. Tooth structure

Teeth have two main parts: roots, which are the part within the jaw, covered with tissue. The visible part of the tooth is the crown and is covered with enamel. The human tooth is composed of four tissue layers:

- *enamel*, which covers crown of the tooth and is the hardest substance ii the human body [22],
- *dentine*, which is the main part of the tooth (by volume) [22],
- *pulp*, soft tissue, which is responsible for vital functions [22],
- *cementum*, a bone like tissue, that protects the root[22].

Figure 2.1 shows a tooth in cross section with the main parts annotated.

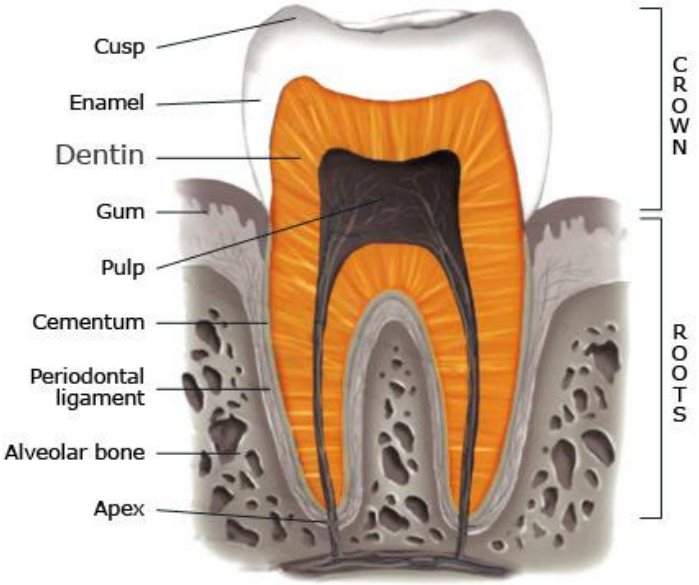

Figure 2.1 Human tooth cross section with all major parts marked. Image taken from[23].

2.2.1.1. Enamel

Enamel is the hardest of all tissues in the human body and its function is to protect exposed parts of tooth. The majority of the enamel tissue structure (85% by volume) is composed of enamel rods, which are made of tightly packed hydroxyapatite crystal rods. These crystal rods have diameters from 4 to 8 μm and are aligned in rows along the tooth, generally perpendicular position to the underlying dentine [24]. In addition to the hydroxyapatite, enamel consists of water (12%) and protein/lipids (3%) [24]. Enamel is thickest at the top of the tooth where it reaches up to 2.5 mm. Figure 2.2 shows enamel cross section with keyhole shaped rods.

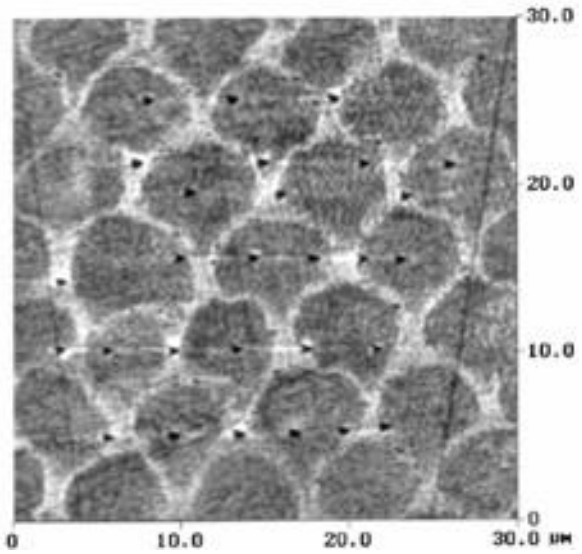

Figure 2.2 Enamel section obtained with atomic force microscopy with clearly visible hydroxyapatite crystal rods. Image taken from [25].

2.2.1.2. Dentine

Dentine is the tissue that sits below enamel and it is a dominating mass in a tooth structure. It is responsible for supporting the enamel and for absorbing the pressure that is applied to the tooth during mastication. Dentine is an organic matrix of collagenous proteins which is made of dentine tubules [26]. Human dentine consists of hydroxyapatite (47% by volume), water (20%) and proteins/lipids (33%) [21]. Figure 2.3 shows the structure of dentine with visible dentine tubules.

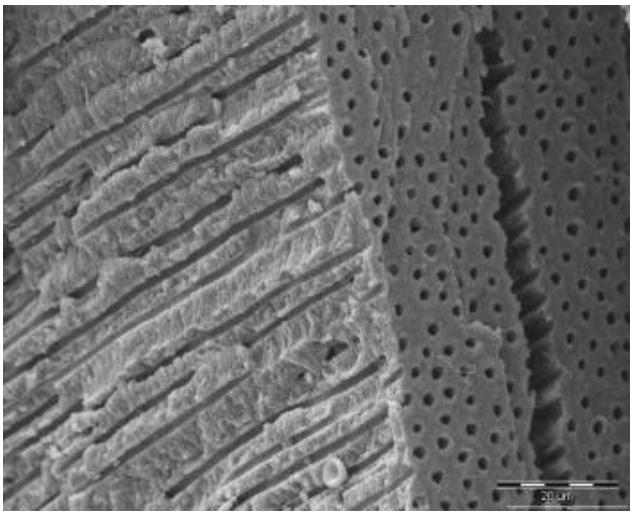

Figure 2.3 SEM micrograph of the structure of human dentine with clearly visible dentine tubules. Image taken from [27].

2.2.1.3. Pulp

Pulp is a soft tissue, formed in the centre part of the tooth and filled with blood vessels, nerves and connective tissue and it is mainly responsible for the creating dentin through odontoblasts [28]. Excessive energy deposition would destroy the living tissue of the tooth pulp is the tissue most likely to be damaged by a process which is not optimised; hence care must be taken in characterizing or improving laser parameters not to damage the pulp. Extreme heat accumulation introduced by laser radiation can damage or even destroy dental pulp. Temperature rises in excess of 5.5^{o}C can lead to permanent damage to the tissue [21, 29]. To prevent tissue destruction accurate temperature measurement and subsequent control of the temperature is necessary.

2.2.2. Optical properties of human tooth

Knowledge of the optical properties of the tissue targeted in a laser process is essential to select the best suited laser and processing parameters. Choosing a laser that is not suited for the targeted application can lead to either having no effect on the tissue at all or having a catastrophic, destructive, results.

Absorption defines the ability of the tissue to absorb radiation of a particular wavelength. A low value of absorption means that almost no light would be absorbed. The level of absorption is often presented by the absorption coefficient (μ_a [cm^{-1}]). Absorption is highly dependent on the chemical structure of dental hard tissues. There are a few absorption bands localized around ion absorptions (OH^-, CO_2^{2-}, PO_3^{-4}) and compounds (H_20) [30]. Figure 2.4 shows an infrared transmission spectrum of dental enamel with marked areas of the main absorbers.

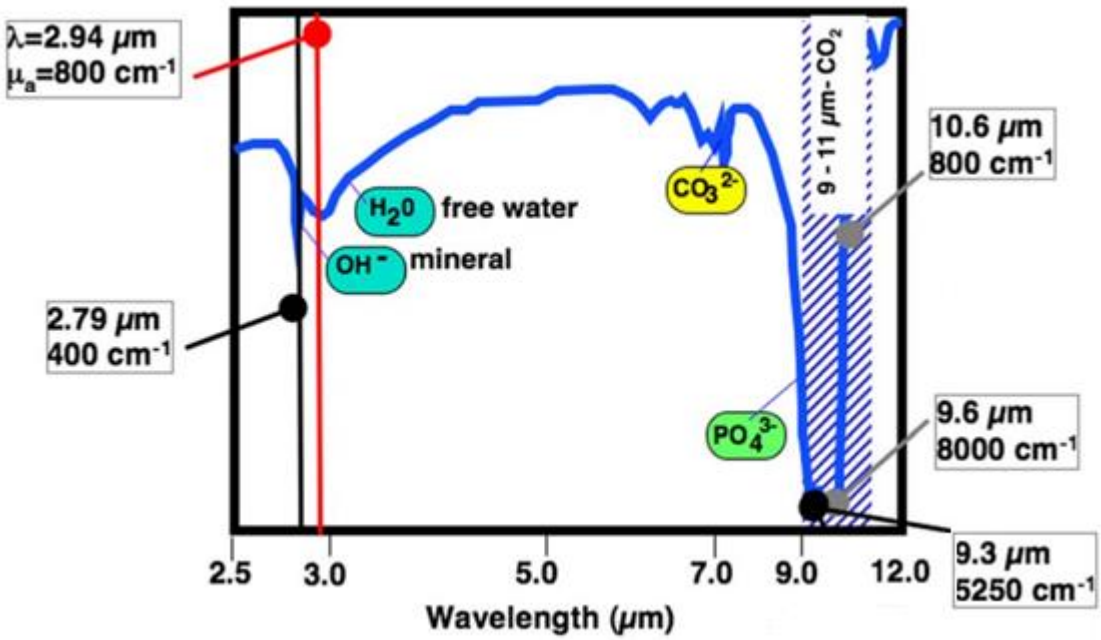

Figure 2.4 Infrared transmission spectrum of dental enamel powder with all of the important absorption bands (namely OH^-, H_2O, CO_c^{2-} and $PO_3^{4=}$) annotated. The highlighted area (9-11μm) shows wavelength band of CO_2 lasers which overlaps with the band of high absorption of enamel. Graph adapted from [31].

Solid state erbium lasers (2.79 and 2.94 μm) and CO_2 lasers (9.3, 9.6, 10.3 and 10.6 μm) are the best suited lasers for dental hard tissue removal because they fit into two wavelength bands from 2.7μm to 3.0μm and from 9.0μm to 12μm, where tissue absorption is considerably higher. Absorption coefficients for visible light are low (Table 2.1). High transmission is also observed for longer wavelengths in the near IR (Near-infrared radiation 0.75 μm – 1.4 μm) around 1053nm. The situation is different in the mid IR, where the structural elements of dental tissue (water and phosphorus) have their bands of absorption. Laser radiation of 2.79 μm (Er:YSGG) is suitable for the narrow absorption band of OH^- ions and radiation of 2.94 μm (Er:YAG) overlap with the water absorption band. The highest values of absorption are for the wavelengths from the phosphate band (PO_3^{-4} in Figure 2.4), therefore CO_2 lasing wavelengths are very well suited for hard

dental tissue surgery. Table 2.1 shows values of absorption coefficients, scattering coefficients and reflectance of hard dental tissue for selected wavelengths from visible light, near IR and mid IR.

Table 2.1 Optical properties of dental hard tissue [21, 29, 30, 32, 33].

Wavelength	Absorption coefficient μ_a cm^{-1}		Scattering coefficient μ_s cm^{-1}		Reflectance
	Enamel	Dentine	Enamel	Dentine	Hard dental tissue
543 nm (green)	<1	3-4	105	280	No data
632 nm (red)	<1	3-4	60	280	No data
1053 nm	<1	3-4	15	260	No data
2.79 µm Er:YSGG	480	No data	~0	~0	5%
2.94 µm Er:YAG	800	No data	~0	~0	5%
9.3 µm CO_2	5500	5000	~0	~0	38%
9.6 µm CO_2	8000	6500	~0	~0	49%
10.3 µm CO_2	1125	1200	~0	~0	16%
10.6 µm CO_2	825	800	~0	~0	13%

The scattering coefficient describes the rate at which radiation is deflected by in many directions by medium in which it propagates. As a result high values of scattering will ensure energy deposition in layers close to the surface layer of tissue. For green light (543 nm) the scattering coefficient is rather high, but longer wavelengths (red light and near IR) the scattering significantly decreases. High transmission and low scattering values in the near IR region are very beneficial for caries (dental tissue broken down as a result of bacteria growth) detection, because caries lesion scatter light significantly more than healthy enamel tissue [34]. On the other hand this is not ideal for tissue removal as the radiation is absorbed deeper leading to increased heat accumulation as well as decreasing the amount of tissue removed. In the highly absorbent wavelength bands (2.7 – 3.0 µm and 9.0 – 11.0 µm) the value of the scattering coefficient is small and hence not easily measurable due to the high absorption.

Another optical parameter that needs to be taken into account is reflectance. In the wavelength band around 3.0 μm reflectance is negligible, but in the 9.0 – 11.0 μm range reflectance is considerably higher, therefore it has to be taken into consideration when optimising laser parameters for enamel removal.

2.2.3. Thermophysical properties of human tooth

Many dental procedures are carried out using laser devices delivering high energy intensities, which can lead to a local temperature rise in the tooth. Localized heat deposition, as well as its propagation through tissue, can result in thermally induced damage of hard or soft dental tissue. Knowledge of the thermophysical parameters of the human tooth and the heat transfer process is essential for further development of lasers in clinical applications [35].

The thermophysical parameters connected with heat transfer in a human tooth are: thermal conductivity TC (κ [W/(m·K)]), thermal diffusivity TD (α [m^2/s]), specific heat (c_p [J/(kg·K)]) and the tooth structure (e.g. density (ρ [kg/m^3]). Thermal conductivity determines the ability of a specific material to conduct heat and is given by: $\kappa = \left(\frac{\Delta Q}{\Delta t}\right) \times \left(\frac{L}{A} \times \Delta T\right)$, where ΔQ [J] is the heat transmitted through a thickness L[m], during time t[s], in the direction to the surface A [m^2], due to the temperature difference ΔT[^oC]. Specific heat describes the amount of energy, which is required to increase 1 kg of material by 1 °C. Thermal diffusivity is a ratio of thermal conductivity to volumetric heat capacity and is given by: $\alpha = \frac{\kappa}{c_p \rho}$ [36].

In order to measure heat transfer parameters several methods were developed: monotonic heating regime with IR thermography [37], thermocouple method [38], infrared camera method [39], flash laser method [40], differential scanning calorimeter method [35] and traditional calorimeter cup [38]. Results acquired by these methods are highly discrepant, because of a number of problems such as: heterogeneous teeth structure, imperfect contact between probes and tooth structure and the thermal, spatial and temporal resolution of an IR camera [35]. Table 2.2 shows the range of values of the thermophysical properties of human dental hard tissue obtained by these methods.

Table 2.2 Differences in thermophysical properties of a human tooth measured using different methods [24].

Property \ Tooth component	Enamel	Dentine	Pulp
Thermal conductivity κ [W/(m·K)]	0.92 - 0.93	0.36 – 0.96	0.63
Thermal diffusivity α [m^2/s]	2.27 – 4.69	1.83 – 2.60	1.5
Specific heat c_p [J/(kg·K)]	0.71 – 0.75	0.87 – 1.59	4.2
Density ρ [kg/m^3]	2.80 – 2.97	1.96 – 2.18	1.00

Extreme temperature changes in human teeth can damage dental hard tissue (enamel and dentine), soft tissue (pulp) or restorative materials, e.g. cement. The difference in the thermophysical properties of enamel and dentine may result in cracking, carbonisation and melting when extreme localised heating and high temperature gradients occur. Additionally heat can irreversibly destroy soft pulp tissue if the intrapulpal temperature rise (IPTR) exceeds ~5.5ºC (in addition to its normal temperature) [24]. In order to safely remove enamel in a manner that would allow for the process to be approved for clinical practice, further the understanding of temperature and stress behaviour during laser removal is necessary [14-16, 41].

Unfortunately discrepancies between mathematical simulation and experimental measurements are considerable. This is a result of the differences in measurements of the thermophysical parameters and simplifications used in the mathematical models, i.e. whether the model is homogenous, isotropic, linear or a layered tooth structure and whether dental fluid flow (DFF) and pulpal blood flow (PBF) is consider negligible. Therefore, numerical modelling that would rule out all of these simplifications and be applicable to a wide range of dental applications would be of great benefit. In Chapter 5.2 an ALE (Arbitrary Lagrangian–Eulerian) moving boundary model is presented using COMSOL software package. The model attempts to simulate single pulse CO_2 laser ablation of enamel.

2.2.4. Dental tissue removal

Two main removal mechanisms occur for hard dental tissue: water mediated explosive ablation and, a plasma mediated ablation [42]. Plasma mediated ablation requires a specific irradiance threshold to be reached so that plasma can be created. Usually the irradiance needed for laser induced breakdown of enamel is higher than 0.1 GW/cm^2 hence this is the main removal mechanism for ultrashort pico- and femtosecond laser pulses [42]. Whenever this threshold is exceeded plasma is created which absorbs most

of the incoming laser radiation; decreasing ablation efficiency by shielding the underlying structure. This type of ablation is discussed in more detail in section 2.3.5.

The other main removal mechanism for dental tissue, explosive ablation, is based on a rapid heating of the water confined within the tissue. Increased heat leads to increased subsurface pressure which exceeds the strength of the tissue and leads to the explosion [43]. The explosive ablation can be achieved below the melting temperature regimes for dental enamel which is between 900 ^{o}C and 1200 ^{o}C [42]. As a result of the explosion an ablation plume is created in front of the target which interacts with the incoming laser radiation [42]. The plume usually consists of water, hard tissue components and organic materials. As a result the plume will absorb some of the incoming radiation shielding the underlying structure [42]. The plume decrease efficiency of the removal process but they can be used as a diagnostic tool if thermal emission of the plume or composition of the plume were recorded [42]. The influence of an ablation plume on the process is similar to the influence of plasma (plasma shielding) in ultrafast laser processing (see Section 2.4.5).

Hard dental tissue has high absorption regions in the infrared wavelength regime which allows for lasers operating in that range to precisely remove the tissue. Since the first feasibility tests of modifying the tooth structure [32], only Er:YAG, Er:YSGG and Nd:YAG lasers have been approved for modification of dental tissue and caries removal. Recent studies [33] showed that CO_2 lasers operating at highly absorbed wavelengths (9.6 μm, 10.6 μm), should be capable of efficient removal of hard dental tissue without introducing any unwanted thermal damage.

Current studies of pulsed TEA (transversely excited atmospheric pressure) CO_2 lasers and RF (radio frequency discharged) CO_2 slab lasers showed that they are capable of ablating dental hard tissue without introducing thermal and mechanical damage [34]. Early feasibility tests carried out using a continuous wave CO_2 laser were not promising because of extensive thermal and mechanical damage. However, further studies of the dental application of CO_2 lasers showed that devices operating in pulsed mode are able to ablate dental hard tissue without introducing extensive damages [33].

The first systematic investigation of CO_2 laser ablation tests performed by Fried [33] showed the potential of enamel and dentine ablation using a 9.6 μm TEA CO_2 laser. Pulses of 8 μs duration were used to penetrate 200 μm thick sections. Tests carried out on a prepared flat section do provide information about the interaction between laser radiation and hard dental tissue, but further tests on unmodified tooth surfaces are necessary to fully investigate the potential of this process. All of the work presented in

Chapter 3 was carried out on unmodified dental tissue, as it was not ground or smoothed to provide a flat surface.

In Firied's work [30] the spot size was 280 μm, the repetition rate was 2 Hz and no water spray was used. Enamel and dentine ablation rates and efficiencies are shown in Figure 2.5. The value of ablation efficiency describes how much of the tissue (Volume) was removed per unit of energy – mm^3/J. The value of removal rate describes the depth achieved per single pulse - μm/number of pulses.

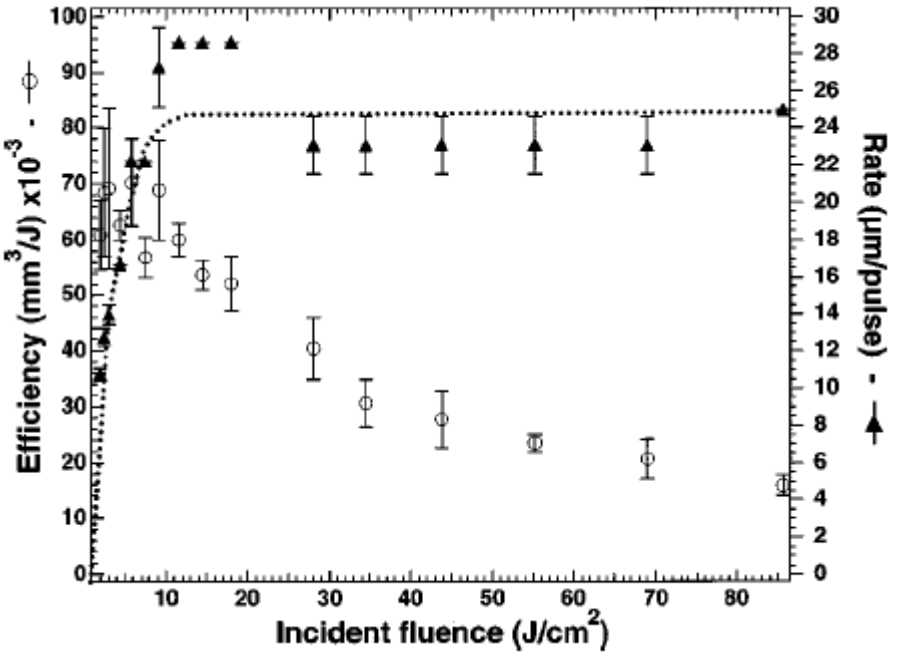

Figure 2.5 Circles describe ablation efficiency of 200 μm thick sections of enamel. Triangles describe ablation rate for ablation of 200 μm thick sections of enamel. Graph taken from [30].

When looking at the depth achieved with a single laser pulse (Triangles on Figure 2.5) it can be seen that for fluences above ~25 J/cm^2 the removal rate stabilizes and does not increase. Even when the fluence is increased to 80 J/cm^2, the ablation rate does not increase due to the influence of the ablation plume that absorbs incoming radiation (This process is described in more detailed in Section 2.2.4). As a result the value of ablation efficiency decreases as the increase value of energy/fluence does not remove more material. Ablation results of the perforation of a 200 μm thick section are shown in Figure 2.6. It is shows that 8 μs pulses (9.6 μm wavelength) are capable of hard dental tissue removal without introducing any cracking. Similar experiments were undertaken in Chapter 3, where different pulse parameters were tested to investigate the feasibility of a 10.6 μm CO_2 laser to remove hard dental tissue without introducing cracking to either the ablation site or the adjacent tissue.

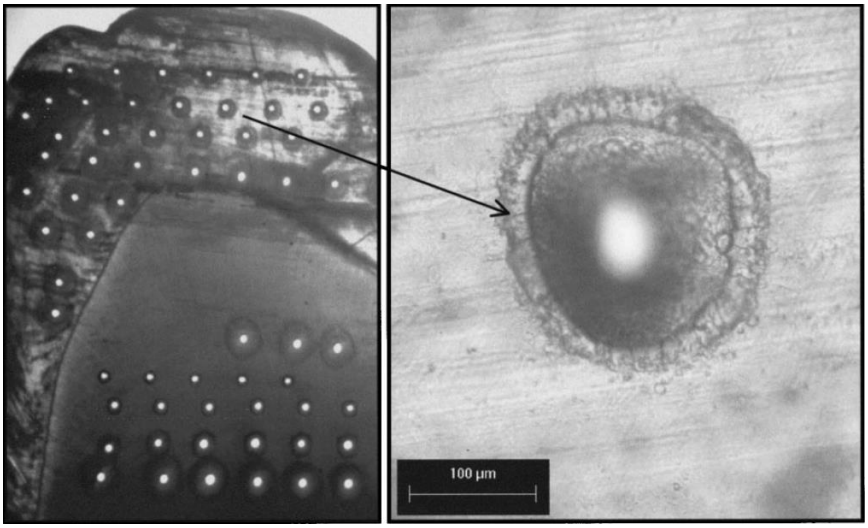

Figure 2.6 Results of laser ablation in 200 µm thick sections of enamel and dentine with 8 µs pulses (λ = 9.6 µm). Images taken from [30].

Another laser type investigated for the ablation of hard dental tissue were ultrafast pico- and femtosecond lasers. In the research presented by Rode [44, 45] two different lasers were used. Both femtosecond (wavelength of 780 nm, pulse duration of 150 fs, Clark-MXR CPA-2001) and picosecond (wavelength of 1064 nm, pulse duration of 60 ps) systems were used to investigate possibility of using laser to remove dental tissue. Moreover during laser processing the intrapulpal temperature rise was recorded by placing a thermocouple in the pulpal chamber.

Figure 2.7 shows an optical microscope image and SEM micrograph of a cavity created with the femtosecond laser. During laser processing with femtosecond pulses, for approximately two minutes, a temperature rise of around 3 ^{o}C was recorded, which is below the critical limit that would cause necrosis of living tissue inside the pulpal chamber [30]. The created cavity did not show any thermal damage nor did adjacent tissue. Moreover there was no visible cracking introduced to the area during laser processing.

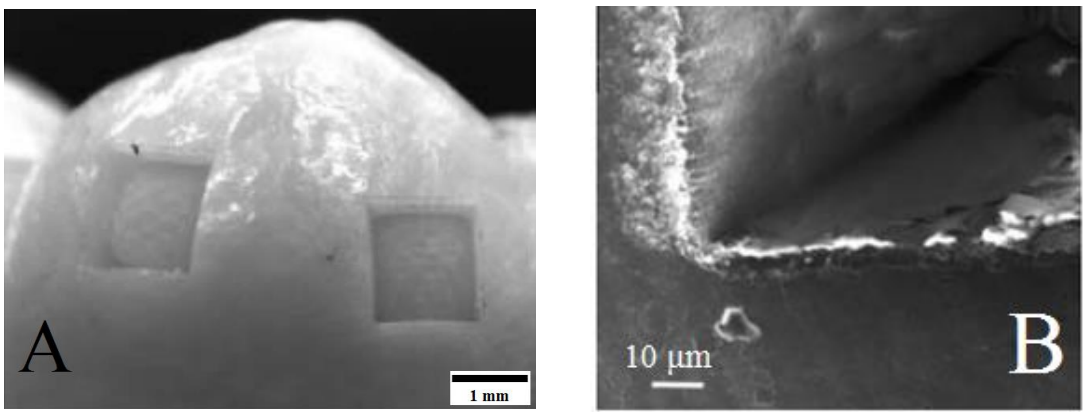

Figure 2.7 (A) Optical microscope picture of the 2 mm^2 by 0.25 mm square cavity created with 150 fs pulses, 1 kHz laser repetition rate, and average power 1W. (Right) SEM image of the corner of the created cavity. Images taken from [44].

On the other hand processing with the picosecond laser did led cracking (see Figure 2.8). Figure 2.8 B shows an SEM micrograph of a cavity created with the use of picosecond pulses. Here, processing with 60 ps has led to thermal damage observed as cracking (visible in the corner of the cavity). Additionally, compared to the cavity created with femtosecond pulses, this cavity has a much less regular shape and more uneven bottom surface.

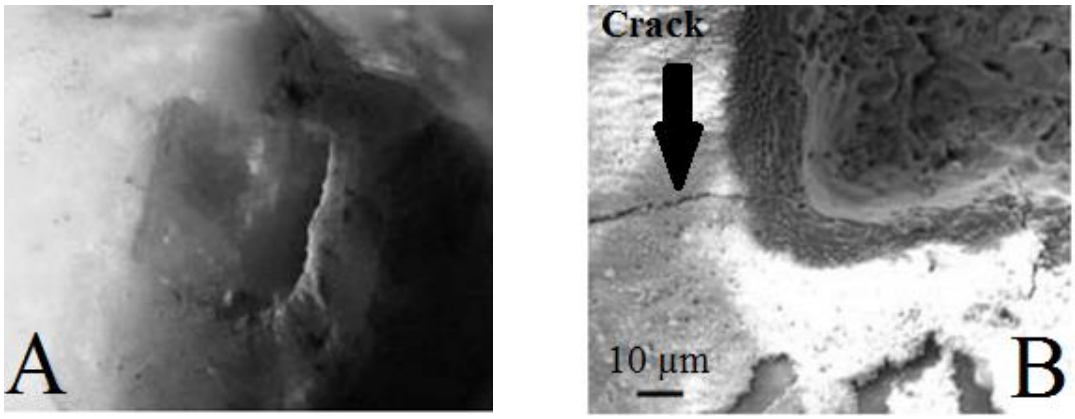

Figure 2.8 (A) Optical microscope picture of the 2 mm^2 by 0.25mm deep square cavity created with 60 ps pulses, 1 kHz laser repetition rate, and average power 1W. (B) SEM image of the corner of the created cavity. Images taken from [44].

Fried et al. [17, 18] demonstrated that integration of a scanner with a CO_2 laser enables is capable of area removal of tissue without introducing cracking or thermal damage to the hard dental tissue. They have used a 9.3 µm CO_2 laser system with pulse energies up to 5 mJ, repetition rate of 400 Hz with 50, 60 and 75 µs pulses. To ensure that the temperature in the pulpal chamber does not increase by more than 5.5 ^oC thermocouples were placed in the pulpal chamber. Incisions created during those experiments can be seen on Figure 2.9. A work focused on removing larger areas using 10.6 µm CO_2 laser is presented in Section 3.6.

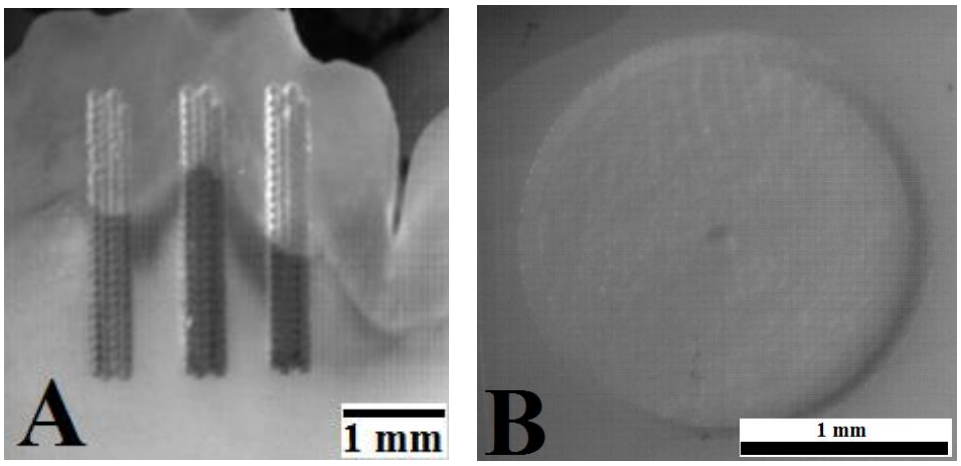

Figure 2.9 (A) Incision in the tooth created using a 9.3 µm, 400 Hz repetition rate, 60 µs pulse duration Inlight laser. (B) A 200 µm deep and 2 mm wide circular cavity created in enamel using a 9.3 µm, 400 Hz repetition rate, 75 µs pulses. Images taken from [17].

This system was capable of creating both square and circular cavities when using and X-Y integrated scanner. To keep the temperature rise within acceptable limits a water spray was used and a maximum temperature increase of 3.5 ^{o}C was recorded when creating a circular cavity [17]. This research showed that CO_2 lasers are capable of creating not only single shot craters but if a galvanometer scan head is introduced to the system they can be successfully applied to removal bigger areas of the tissue.

The work by Fried not only focused on using CO_2 lasers but also investigated Er:YAG lasers operating at 2.94 µm and Er:YSCC operating at 2.79 µm [33, 46]. Sets of 3 mm long linear lesions were created in 5 mm by 5 mm bovine enamel blocks. Figure 2.10 shows cross section of the lesion created with Er:YAG laser with and without assistance from a water spray.

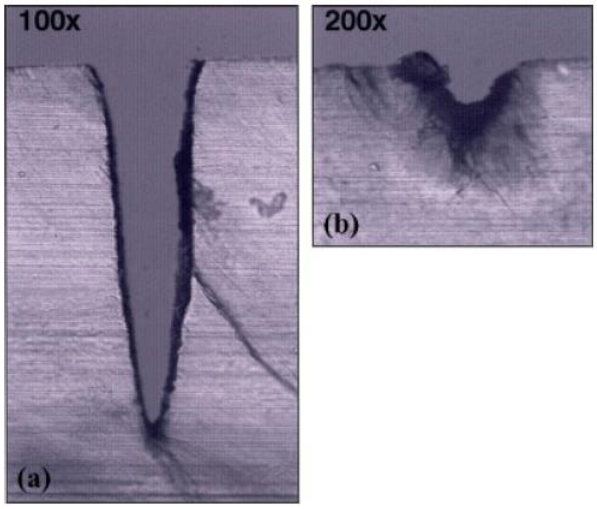

Figure 2.10 Image of the 100 µm thick bovine enamel cross section with a lesions created with a Q switched Er:YAG laser with the application of water spray (a) and without water spray (b). The depth of the crater on left is 490 µm and the crater on the right is 52 µm. Images taken from [46].

The addition of the water spray has increased ablation efficiency as well as producing a better surface quality compared to the surface obtained without the use of water spray. This is mainly due to the fact that waster has a high absorption of 2.94 μm laser radiation. When there was no water spray present significant thermal damage on the sides of the created lesion are observed. No samples had visible cracks as a result of laser processing even though the creation of cracks in enamel irradiated with Er:YAG radiation has been reported elsewhere [47].

Additionally Fried investigated the influence of the water spray on CO_2 laser ablation (see Figure 2.11) [46]. For CO_2 laser removal of enamel the application of water decreases the efficiency of the ablation leading to shallower lesions. However, the application of a water spray is advisable as it prevents deposition of unwanted, re-melted, material on the sides of the lesions [46]. Moreover it helps to keep the temperature increase below the critical level preventing necrosis inside the pulpal chamber.

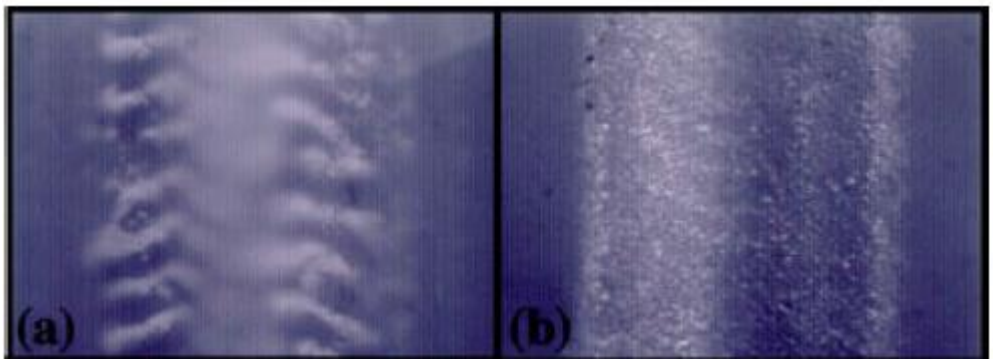

Figure 2.11 View from above of the linear lesions created with 9.6 μm CO_2 TEA laser radiation with 70 J/cm^2 fluence without addition of water (a) and with the addition of water (b). Images taken from [46].

In other studies, performed by Della Rosa [38], a different dental tissue was targeted, and the study investigated the possibility for laser based removal of dentine, which is the tissue directly underlying the enamel (Figure 1.3). Lateral incisions were made on 3 mm by 3 mm block of human dentine with a use of three different lasers with different pulse duration and fluence: 5 μs, 100 μs (fluence of 20 J/cm^2, wavelength of 9.6 μm); 200 μs (fluence of 20 and 40 J/cm^2, wavelength of 2.79 μm) and 5 ns (fluence of 10 J/cm^2, wavelength of 355 nm). Table 2.3Table 2.1 shows polarized images of the incisions.

Table 2.3 Comparison of cross-sections of incisions created in dentine by using 9.6 µm CO2 laser, 2.79 µm Er:YSSG laser and Nd:YAG 355 nm. Data and images taken from [48].

Pulse duration, Fluence, laser wavelength and scale bars	Polarised images of and cross-sections of incisions made with different lasers (without water spray).	
5 µs 20 J/cm^2 CO_2 laser λ 9.6 µm	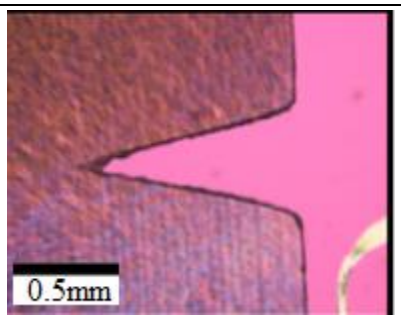	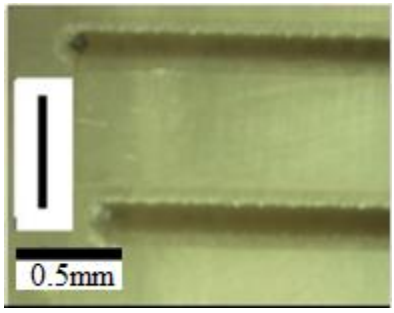
100 µs 20 J/cm^2 CO_2 laser λ 9.6 µm	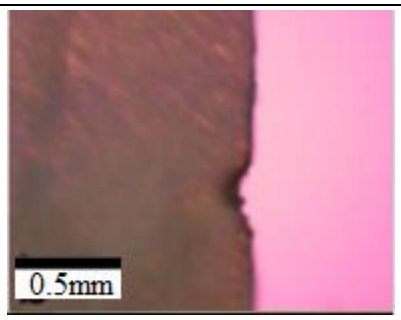	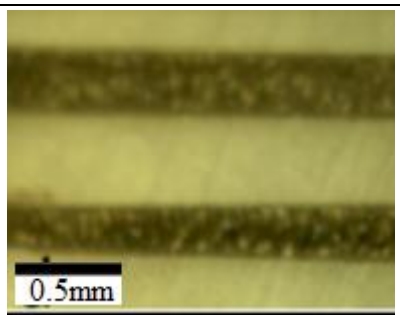
200 µs 20 J/cm^2 Er:YSGG laser λ 2.79 µm	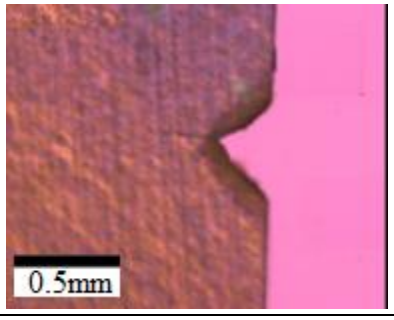	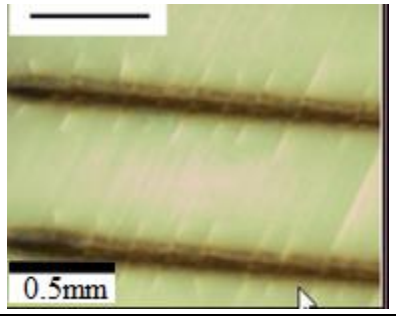
200 µs 40 J/cm^2 Er:YSGG laser λ 2.79 µm	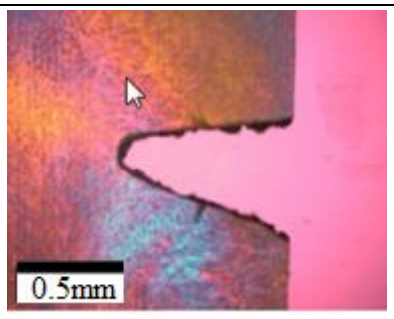	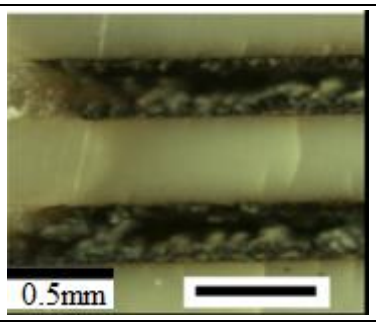
5 ns 10 J/cm^2 UV laser λ 355 nm	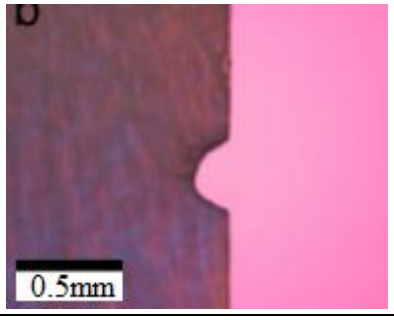	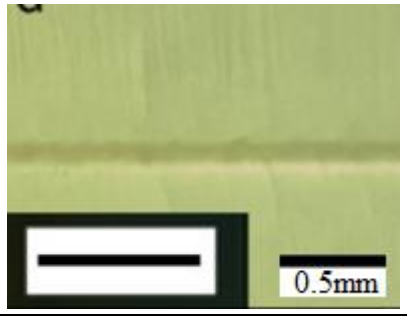

Laser machining of dentine with pulses of 5 ns pulse duration, fluency 10 J/cm^2 and wavelength 355nm showed small cracks on the surface with higher fluences did resulting in larger cracks, which makes the process unsuitable for clinical applications [48]. Thermal damage is indicated either by a black oxidized layer on the surface or as cracks due to increased stres during laser processing. The CO_2 laser (9.6 μm) produced visible thermal damage with a thickness of ~10 μm around the ablation periphery. The thermally damaged zone introduced by an Er:YSGG laser is smaller, but at a high incident fluence introduced cracking [38].

Early CO_2 lasers (before year ~2000), not capable of emitting short pulses in the range of 10 μs, were tested and they caused excessive heating to the tissue and have been disregarded as a viable option for hard dental tissue removal since [29, 30]. With the evolution of laser devices, leading to shortening of the pulse duration in CO_2 lasers, Er:YAG lasers, 9.6 μm or 10.6 μm CO_2 lasers are capable of removing hard dental tissue. Er:YAG laser removal rate is limited by the laser medium and is limited to values between 10 to 30 Hz by the gain media, whereas CO_2 lasers are capable of obtaining ablation rates (volume of the material removed/time) achieved by high speed dental drills 0.1 – 1 mm^3/s [35]. Furthermore Erbium based lasers are more expensive compared to CO_2 lasers and commercially available CO_2 lasers use a 10.6 μm wavelength [30].

2.2.5. Medical systems used for tissue removal

Currently there are Er:YAG and CO_2 lasers in use in dental practices where they have been approved to remove hard dental tissue. There are two main routes for delivery of laser radiation from the laser source to the ablations site. Either using large mode area fibres or an articulated arm system [49]. An example of the device incorporating fibre for delivery of laser radiation is Laterna OPUS DUO system which combines both CO_2 and Er:YAG lasers [50](Figure 2.12 on the left). The second approach is to use an articulated arm that is based on sets of mirrors that are mounted in joints and are connected by tubes. Whenever the arm is moved the mirrors start to adapt their position accordingly to continue guiding the beam in the correct way [49]. Even though it is possible to move the arm around this approach is restrictive. An example of the articulated arm application is a Fotona AT Fidelis Er line (Figure 2.12 on the right) that uses Er:YAG laser to removal dental hard tissue.

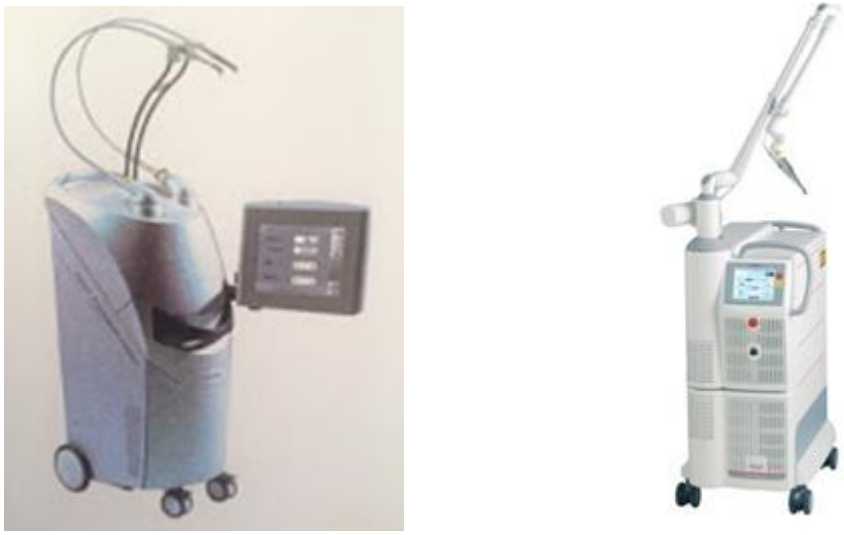

Figure 2.12 (Left) Laterna OPUS DUO fibre delivery system [50] and (Right) articulated arm delivery system Fotona AT Fidelis [51].

Currently Er:YAG lasers have been approved for use in dental practices in the United States of America there for the removal of hard dental tissue. CO_2 lasers operating at 10.6 µm are approved as well, but only for soft tissue procedures. In this thesis (Chapter 3) we investigate a possibility of using a 10.6 µm CO_2 laser to remove enamel tissue without introducing any unwanted damage. Different pulse energies, pulse durations and irradiation patterns are tested. Moreover the increase of temperature during laser processing is investigated by placing the thermocouples into the pulpal chamber. The second theme that was investigated is the application of the ultrafast picosecond laser in ophthalmology.

2.3. Lasers in ophthalmology

2.3.1. Introduction

The first example of laser based surgery in ophthalmology was carried out in 1961 by Zaret [52] who used a ruby laser for retinal coagulation. Due to the unique optical properties of the components of the eye and the capabilities from varying laser parameters (e.g. wavelength, spot size, intensity, and pulse duration), lasers can be applied in diagnostic medicine or surgery for specific tissue. Lasers are used in variety of ophthalmological non-invasive treatments targeting anterior eye segments (cornea, lens. iris) and posterior segments (retina, choroidea, sclera) [53]. A wide spectrum of ophthalmic applications resulted in many different types of lasers currently used in clinical procedures, such as: Nd:YAG lasers, argon lasers, excimer lasers, Er:YAG lasers and CO2 lasers.

2.3.2. The structure of the human eye

The outer part of the eye is made of the sclera and cornea. The central layer of the human eye is choroid, ciliary body and iris. The inner layer of the eye within the posterior segment is the retina. The bulk of the eye that fills the inside of the eye is the vitreous body. Figure 2.13 shows the structure of a human eye.

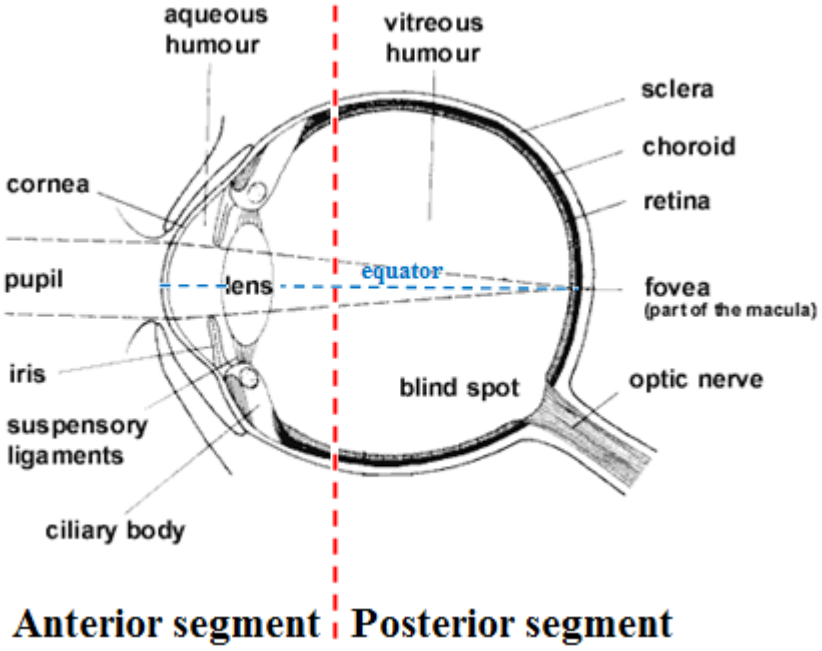

Figure 2.13 Structure of human eye. Image adapted from [54].

2.3.3. Structure and properties of sclera

The sclera forms the outer layer of the eye, which fulfils functions essential for the integrity of the eye. Its main function is providing protection for the inner eye. Moreover, the sclera is responsible for allowing rotation of the eye without any major distortions. The sclera is made of protein fibrils, collagen, elastin, interfibrillar proteoglycans and glycoproteins [54]. The major part (up to 75% by weight) of the scleral tissue is composed of collagen fibres [55]. Elastin is composed of hydrophobic amino acids and its role is to supplement collagen structure (up to 5% by weight) [54]. Space between the fibres is filled with proteoglycans, which are composed of protein core with glycoproteins chains attached to it [56]. Figure 2.14 shows structure of human sclera on the micron scale.

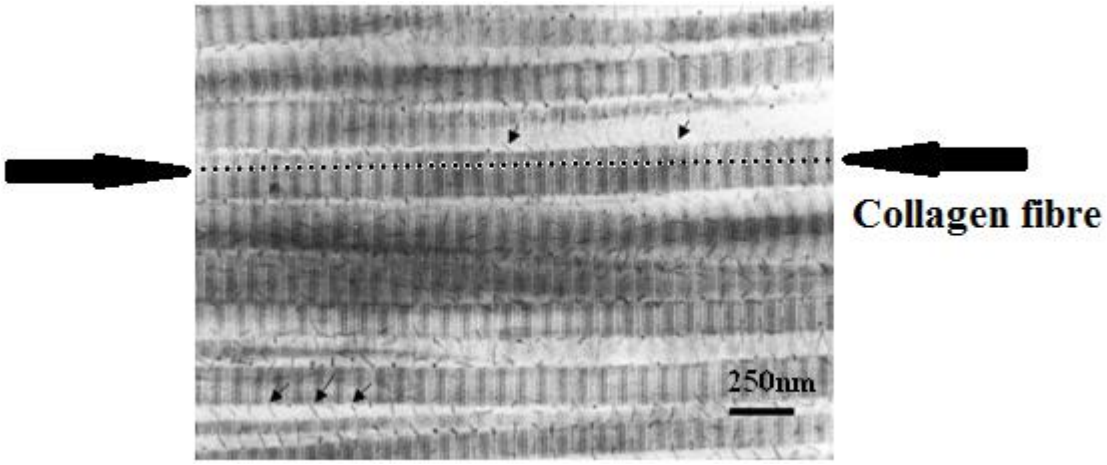

Figure 2.14 Structure of human sclera showing the well-defined fibrous matrix structure with fibres stretching horizontally. Image taken from [55].

Knowledge of the dimensions of the sclera is essential for preparing new surgical procedures or designing a new way of distributing drugs into the eye as any drastic modification in scleral structure can undermine the stability and mechanical resilience of the eye. The average thickness of human sclera is 670 ± 80 µm [57]. The thickest part of the sclera is positioned in the posterior eye where the thickness averages 996 ± 181 µm [57]. In the area of the equator the sclera is thinnest with an average thickness of 491±91µm [57]. In the proximity of the border between sclera and cornea the average thickness of the sclera is 588 ± 63 µm [57].

A - Reflection, transmission and absorption of human sclera

B - Scattering of human sclera

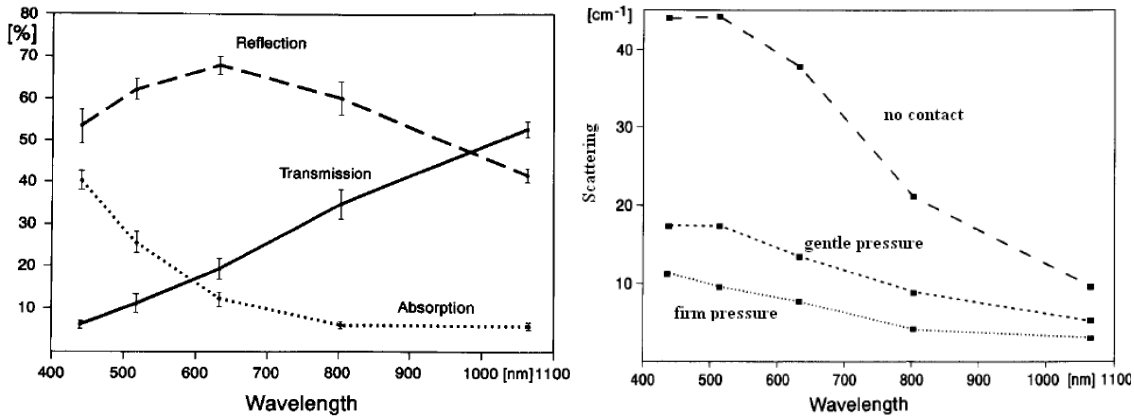

Figure 2.15 (A) Absorption, reflection, transmission and (B) scattering of human sclera. Graphs taken from [58].

Figure 2.15 shows the optical properties of human sclera as a function of wavelength. Electromagnetic radiation in the visible range is reflected off the surface of sclera in 50 - 70%, but for longer wavelengths reflectance decreases down to 40% at 1064 nm [58]. Transmission is highly wavelength dependent and increases towards longer wavelengths. For 450 nm the transmission is only around 10%, whereas for 1064 nm it is 53% [58]. At short wavelengths (below 600nm) more light is absorbed than is transmitted through the sclera. For longer wavelengths absorption decreases to around 6% for 1064nm [58]. Scattering is highly wavelength dependent and decreases at longer wavelength and if the sclera is subjected to increased pressure the value of scattering also decreases [51].

2.3.4. Drug delivery to posterior eye

There is an increasing need for the development of a less invasive, yet highly successful route for drug delivery to the posterior segment of the eye. It is a result of many diseases: age related macular degeneration (AMD), macular oedema, uveitis, diabetic retinopathy, cytomegalovirus (CMV), retinitis and retinitis pigmentosa [59], all of which can cause partial or full visual impairment. Drug delivery to the posterior part of the eye can be done using four different routes: topical, systemic, intravitreal and periocular [60].

In a topical delivery route, medication is applied on the surface of the eye. Unfortunately this route of drug delivery is generally insufficient because of the rapid outflow through nasolacrimal ducts and systemic absorption [60]. Systemically distributed drugs are spread by blood flow. However this delivery route is disturbed by the blood-retinal barrier (BRB) and can aggravate drug related toxicities by nonspecific absorption [55]. As a result drugs delivery to the posterior eye segment is only practical by intravitreal and the periocular route [60].

The intravitreal route of drug delivery involves direct injection of the medicament into the vitreous humour where the drug would diffuse and reach the posterior of the eye. Drugs can be applied in the form of a solution (Figure 2.16 A), particles (Figure 2.16 A), suspension (Figure 2.16 A) or implants (Figure 2.16 B and C). Implant can be either surgically placed directly into the vitreous body (Figure 2.16 B), or placed within the sclera (Figure 2.16 C) and would release the drug over time. The majority of medicaments treating posterior eye disease are distributed this way. Nevertheless, too frequent drug delivery using this solution can lead to retinal detachment and increase intraocular pressure [61, 62]. Figure 2.16 shows the intravitreal route of drug delivery.

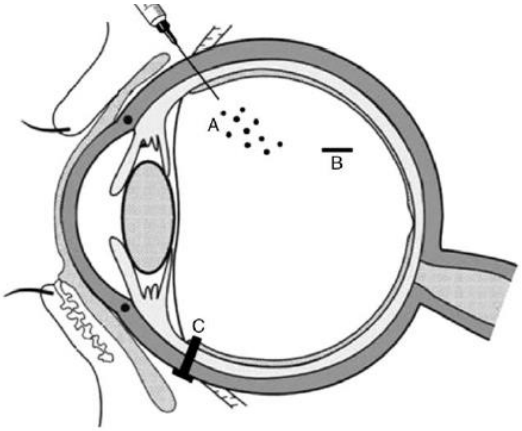

Figure 2.16 Intravitreal route of drug delivery to the posterior eye (A- particles, B – implants, C- scleral plugs (implants). Image taken from [59].

The periocular technique for distributing drugs is based on deposition of molecules on the external surface of the sclera. This method of delivering medicine minimizes the risk of retinal damage which occurs readily with the intravitreal route [63].The periocular route is acknowledged as the least invasive and most efficient way to transport medicaments to posterior segment of the eye [60]. Figure 2.17 highlights periocular pathways responsible for drug transport within the eye and identifies possible areas where drugs could be placed and diffuse over time. Drugs are usually delivered to specific locations using injections and would reach the posterior part of the eye using a transcleral route [60].

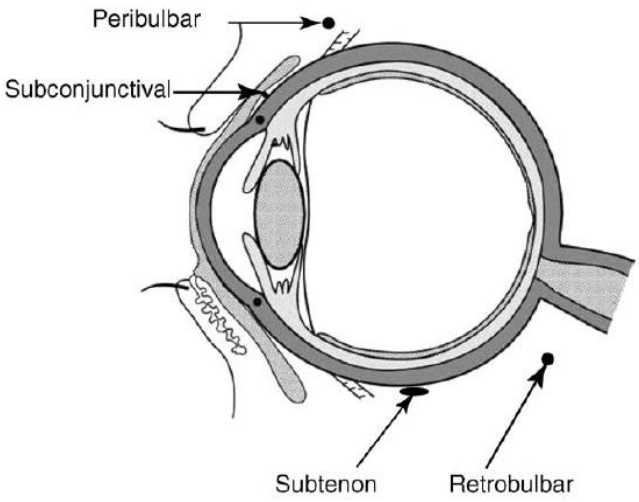

Figure 2.17 Schematic of the human eye with annotated spots responsible for periocular drug delivery to the posterior part of the eye. Image taken from [60].

To take advantage of different drug delivering routes, many delivery systems have been developed. One of the methods is based on injection of biodegradable or non-biodegradable implants through an intravitreal route of drug delivery. These implants

continually release molecules over months or even years. Non-biodegradable implants require post treatment surgical removal, but they do allow more controlled and lasting drug distribution [60]. Currently (as of 2011) in clinical application two different non-biodegradable implants are used Vitrasert® [64] and Retisert® [65]. The Retisert® implant releases fluocinolone acetonide in daily dosage of 0.3 – 0.6 μg per day over the span of 30 months [65]

The microparticle (between 1 and 1000 μm) and nanoparticle (between 1 and 1000 nm) method is very similar to the previous, but the particles release drugs in a shorter duration, over weeks to months. Many preclinical studies showed that micro- and nanoparticles are an efficient way of delivering drugs through the intravitreal route [63], nevertheless this method still has to be clinically tested and approved [60].

Light activated drugs (photodynamic therapy) and light activated drug delivery systems create a group of light inducted systems. This drug delivery system is based on localizing a photosensitive element in the targeted tissue followed by activation with laser radiation [60].

Iontophoresis is a non-invasive method for transscleral drug delivery, which uses a small electric current to amplify the absorption of an ionized drug into the tissue. It enhances the efficiency of many drugs such as: fluorescein, steroids, antibiotics, antivirals and macromolecules [60]. Transscleral iontophoresis is capable of delivering high concentration drugs to retina and choroid with a small probability of side effects [66]. Recently there iontophoresis devices were developed, such as OcuPhor® [67], but these require further investigation before being fully introduced to clinical practise.

The last method of drug delivery is based on the application of solid or hollow microneedles to deliver drugs to the posterior of the eye. Needles are capable of delivering encapsulated or free drugs through the sclera [60]. Hollow microneedles are used for delivery of insulin or vaccines and solid microneedles are used for delivering drugs which are coated onto the needles [68]. This approach is connected with previously mentioned periocular technique for drug delivery, where microneedles are used to deliver drug to targeted regions (Figure 2.17).

There are several techniques to deliver drug to the posterior part of the eye, presented here. Work presented in Chapter 4 is focused on finding optimal parameters for creating a cavity within the scleral tissue that could be potentially used to place an implant that would release the drug over time.

2.3.5. Ultrafast laser removal mechanism

The use of high peak power ultrafast picosecond laser sources focused into small areas where the irradiance exceeds 10^{10} W/cm^2 [69] allows for removal of biological tissue with minimal amounts of collateral damage. When a tissue specific, threshold is exceeded plasma is created that absorbs most of the incoming laser radiation [70]. As a result it is possible to remove tissues that are otherwise transparent as the removal process is based on the non-linear absorption not absorption coefficient.

Since the 1970s, when first the laser goniopuncture was applied as a treatment for glaucoma [71] was introduced, there has been an interest in exploiting the possibilities offered by laser devices in the field of ophthalmology. Part of this research has focussed on using the laser to target different parts of the eye e.g. lens and cornea [72-75]. Unfortunately these processes were accompanied by strong photodisruption effects, such as cavitation bubble formation, shockwave generation and bubble jetting, due to the use of nanosecond lasers [70, 76]. However, there now exist commercially available pico- and femtoseconds lasers that are capable of creating plasma while keeping the photodisruptive side effects to a minimum.

To fully exploit the possibilities of laser induced breakdown it was necessary to investigate the whole process in great depth. Vogel [60, 67-74] investigated many different properties for a range of lasers to gain a better understanding of this process. These experiments were focused on investigating conditions for plasma creation in distilled water as a substitute for ophthalmic tissue to simplify the conditions of the experiment. This simplification was valid due to the fact that a vast amount of biological tissue consists of water. For example, porcine sclera, that is often used as a substitute for human sclera in early stage research, contains 70% water [77].

To create plasma there is a need for multiphoton ionization to provide seed electrons for a multiphoton avalanche [70]. In materials with high linear absorption seed electrons can be provided by thermionic emission [70]. To achieve that condition in materials which are transparent a tissue specific irradiance threshold needs to be exceeded. This requires the laser beam to be focused to a relatively small spot size.

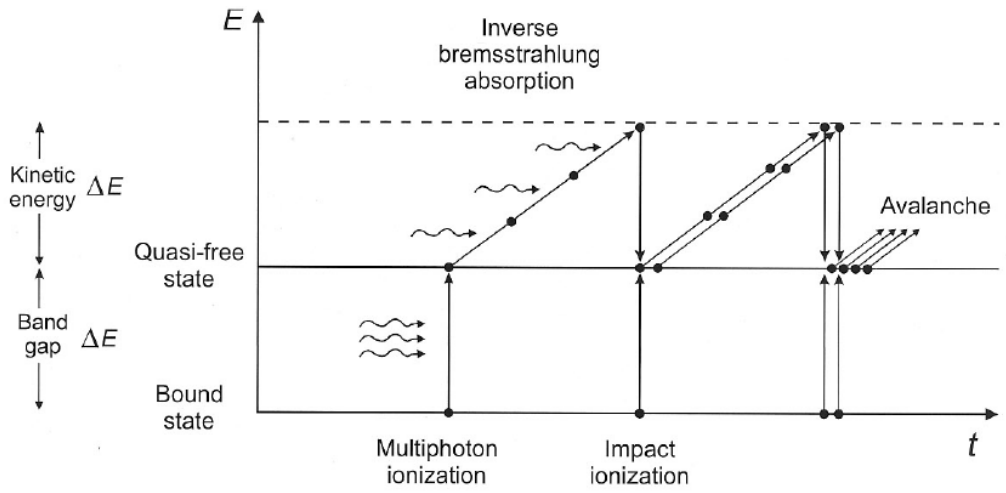

Figure 2.18 Schematic describing different energy levels during plasma formation. Image taken from [70, 78]

Figure 2.18 describes the plasma formation procedure. When the value of irradiance is high enough electrons are promoted from a ground state to the valence band so it can absorb energy in the form of photons [70]. The process is called Inverse Bremsstrahlung Absorption (IBA). As a result the electron has a kinetic energy that exceeds the band gap energy and it can produce another free electron [70]. Consequently these two electrons can gain more energy through IBA. This process can be repeated over and over again and create a multiphoton avalanche [70]. The timescale of a single multiphoton ionisation cycle is in the range of 5 femtoseconds [70]. Figure 2.19 explains plasma formation phenomenon at different times during the duration of an ultrashort pulse.

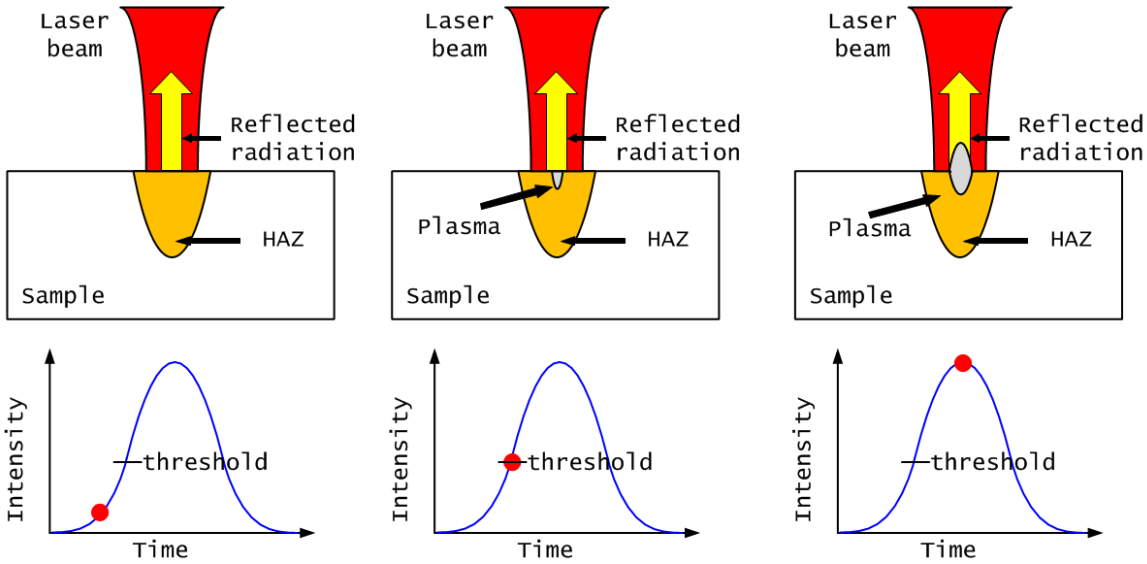

Figure 2.19 Temporal evolution of the plasma during an ultrashort pulse. HAZ – Heat affected zone.

Figure 2.19 shows the temporal evolution of the plasma during an ultrashort pulse. When a tissue specific, threshold is exceeded plasma is created in the focal region of the beam. When plasma is created it absorbs the incoming laser radiation and it grows towards the direction of this incoming laser radiation. Since the plasma absorbs the majority of the incoming radiation the region directly beneath the plasma is shielded [79-82]. As a result it is possible to have a highly localized deposition of energy in material or tissues that are otherwise relatively poorly absorbing at a specific wavelength [83].

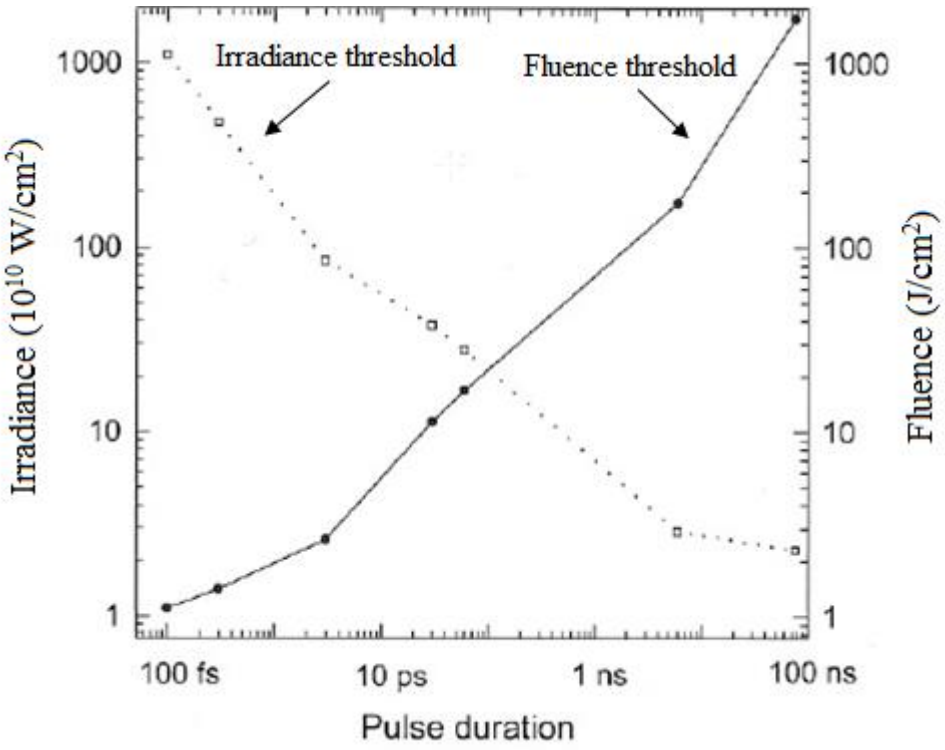

Figure 2.20 Laser induced breakdown threshold as a function of pulse duration for laser fluence and irradiance for distilled water. It shows how does the relation change over the span of different regimes of pulse duration. Figure adapted from [83].

Figure 2.20 shows how the laser induced breakdown threshold changes over the span of the laser pulse duration. A decrease in pulse duration requires an increase in irradiance to induce breakdown and create plasma. This is due to the fact that for shorter pulse durations the time to create plasma decreases hence increased irradiance is required to compensate [83]. For longer pulses there is more time for multiple multiphoton ionisation cycles to take place as one cycle takes ~5 femtoseconds. As a result lower irradiance is required as the there is plenty of time for the cycle to repeat. Thus the irradiance required for plasma creation with a 100 femtosecond pulses is 10^{13} W/cm^2 and for 10 picosecond is $6 \cdot 10^{11}$ W/cm^2 and for 1 nanosecond pulse is $2 \cdot 10^{10}$ W/cm^2.[70, 83]

The magnitude of the previously described plasma shielding effect relies on the high absorption coefficient of plasma, which leads to major part of the incoming radiation being absorbed by the plasma. Therefore it is crucial to investigate the transmission properties of plasma. An experiment to measure this was carried out by Vogel [82] which investigated properties of a plasma created in water with a 30 ps pulsed Nd:YAG laser. Figure 2.21 shows transmission calculated using the moving breakdown distribution model with fitted values of the absorption coefficient (Figure 2.21A) as well as the temporal shape of the pulse transmitted through the plasma (Figure 2.21B). Results are shown for different values of β which is the ratio of the incident irradiance to the threshold irradiance. Figure 2.21A shows transmission through the plasma and it is clear that for higher irradiance (higher ratio of irradiance/threshold) transmission through the plasma is lower, as the plasma itself is larger and absorbs more radiation. Figure 2.21B shows a shape of the pulse transmitted through the plasma for different values of the ratio between irradiance and plasma creation threshold. For irradiance lower than the threshold ($\beta < 1$) the whole pulse is transmitted. When the value of irradiance exceed the plasma threshold ($\beta > 1$), plasma shielding is clearly visible, as the pulse shape does change significantly. The reflectivity of the plasma itself is minimal and it was found to be in the range few percent [81, 82].

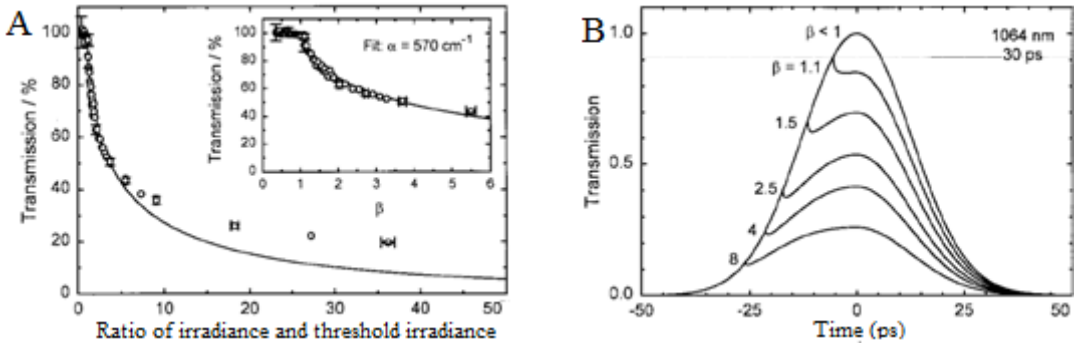

Figure 2.21 (A) Transmission calculated using the moving breakdown distributed shielding model as a function of different ratios of irradiance to threshold irradiance (β). (B) The shape of the pulse transmitted through the plasma for ratios of irradiance to threshold irradiance (β). The pulse duration used was 30 picoseconds. Graph taken from [82].

2.3.6. Overview of the laser applications in ophthalmology

As mentioned previously applications of laser induced breakdown processes in ophthalmology have been investigated since the 1970s [71-75]. This has been facilitated by more recent developments in ultrafast laser technology due to the associated minimized photodisruptive effects [76]. Research carried out by Nuzzo [84, 85] was

focused on evaluating the possibility of using femtosecond lasers for corneal transplantation. The laser used was an Intralase FS60 system delivering 200 fs, 3 µJ pulses, at a rate of 60 kHz at 1.05 µm. It was shown that corneal transplantation is viable using femtosecond pulses as there were no signs of disruption to the collagen fibrous structure following the procedure. Figure 2.22 shows a cross-section of corneal tissue with a completed incision.

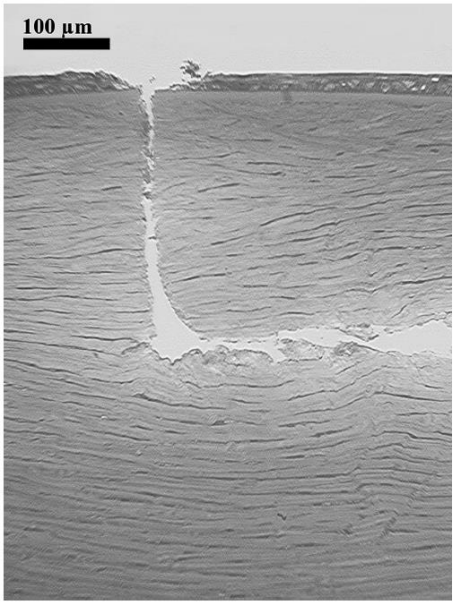

Figure 2.22 TEM micrographs of the corneal cross-section with a completed incision (in a dissected sample) created using a 200 fs pulsed laser [84].

Other research [86, 87] focused on the possibility of creating micro incisions in a crystalline lens with a femtosecond laser. Such a procedure targets presbyopia which is a condition that is associated with difficulty in reading small text [88]. With age the lens becomes less flexible [88] and this procedure is focused on creating gliding planes to increase the ability of a lens to deform. This is known as a lentotomy [86]. A femtosecond laser with a minimum pulse width of 125 fs operating at the wavelength of 780 nm, with an average power between 2.5 and 10 mW and a repetition rate of 5 kHz was used. Figure 2.23 shows a "steering wheel" laser scanning pattern and a pattern that was cut in the crystalline lens of a porcine eyeball.

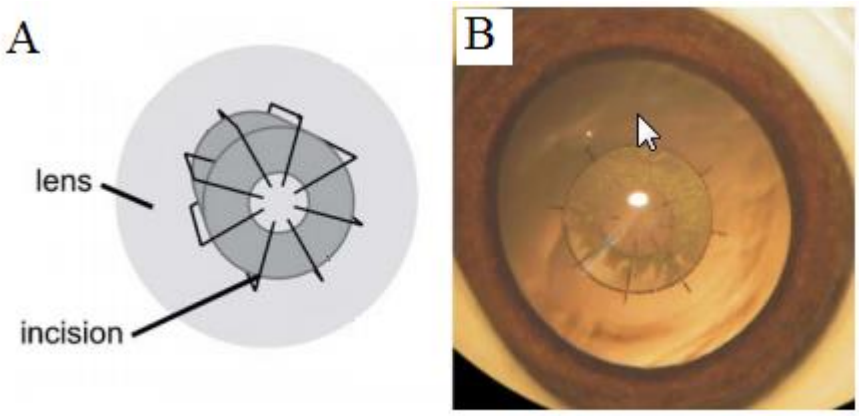

Figure 2.23 (A) Laser scanning pattern that was used for the incision in a lentotomy procedure (B) and a crystalline lens with the laser pattern cut into it [86].

Jiang [89] investigated the minimally invasive femtosecond laser photodisruption of rabbit sclera. To evaluate its feasibility the experiment was carried out on hydrated sclera in order to closely represent living tissue. A femtosecond laser (50 fs pulses at 800 nm with pulse energies up to 125 µJ) was used to investigate different scanning approaches and the influence on hydrated rabbit sclera. Figure 2.24 shows results of a single line scanning ablation (A), rectangular cavity (B) and a circular cavity (C).

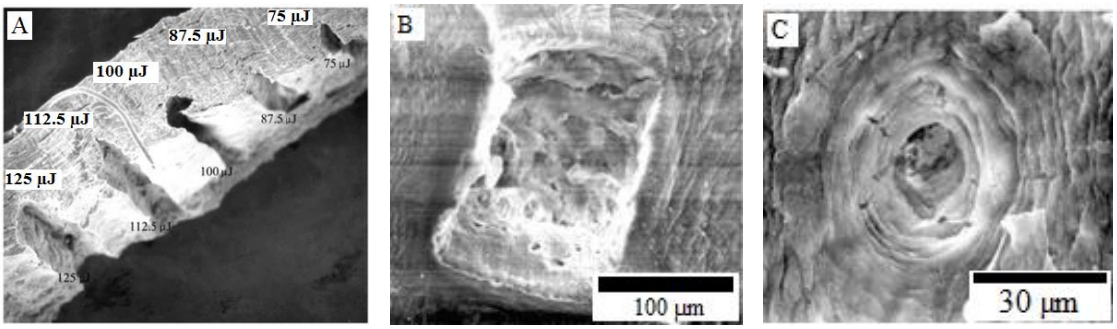

Figure 2.24 SEM micrographs of the (A) cross-section of linear lesions, (B) rectangle cavity and (C) a circular cavity for fs ablation of hydrated rabbit sclera [89].

Improved results of femtosecond laser photodisruption in hydrated rabbit sclera were obtained using a mode-locked Ti:sapphire oscillator pumped by Nd:YVO_4 laser [90]. With the use of an amplifier the laser produced 800 nm wavelength pulses of duration 50 femtoseconds and with energies of up to 125 µJ (NB laser capable of 2 mJ) and a repetition rate of 1 kHz. Studies showed that the femtosecond laser can ablate scleral tissue without introducing unwanted collateral damage. The ablation threshold for the hydrated rabbit sclera was 31.25 µJ with a power density 4.06 x 10^{14} W/cm^{-2} [90]. Figure 2.25 shows SEM micrographs of the cross section through linear lesions created in rabbit

sclera when focusing the beam 100 µm below the tissue surface. The laser spot radius used for that experiment was 7 µm. Figure 2.26 shows SEM micrographs of a circular cavity created by focusing 200 µm below the surface without any scanning. Figure 1.28 also shows a square cavity that was created with a "snake like" scanning pattern again with the beam focus 200 µm beneath the surface.

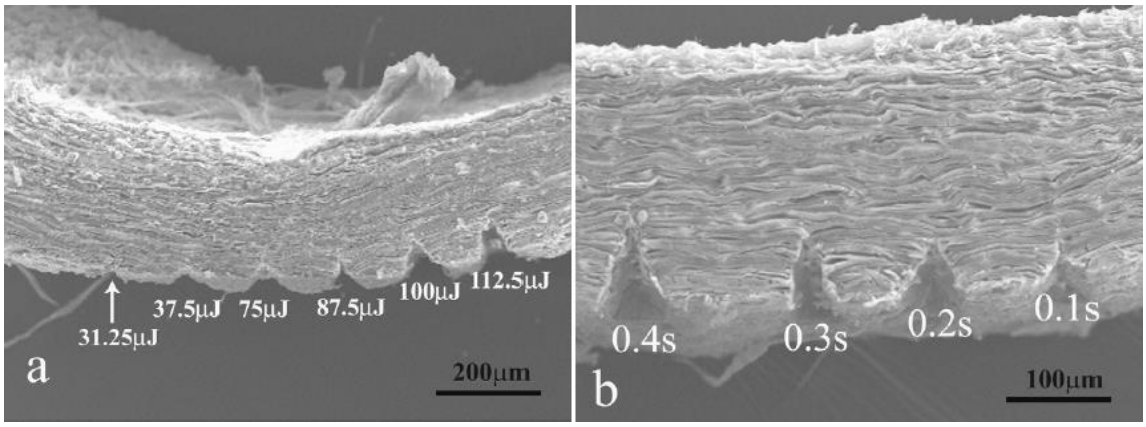

Figure 2.25 Cross sections of rabbit sclera after laser ablation with 50 fs pulses at a wavelength of 800 nm with and repetition rate of 1 kHz, (Left) different pulse energies and a constant exposure time of 0.1s and (Right) a constant energy 37.50 µJ and different exposure times [90].

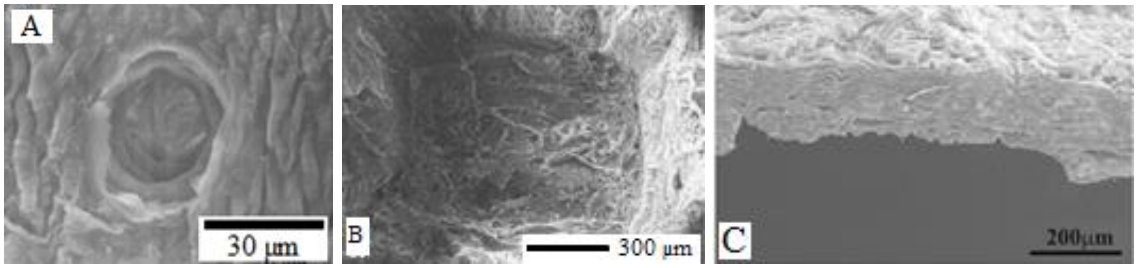

Figure 2.26 SEM micrographs of laser ablated cavities using 50 fs pulses at a wavelength of 800 nm with and repetition rate of 1 kHz (A) circular, (B) square and (C) cross section of the square cavity. Images taken from [90].

The femtosecond laser was successful in creating differently shaped cavities (see Figure 2.25-26) without introducing any wanted damage to the ablated region or the surrounding tissue. In Chapter 4 results of investigations to generate similar shapes with a picosecond laser, are presented. Picosecond lasers are more cost effective, more reliable and offer better processing rates than femtosecond lasers.

Some groups have investigated the use of wavelengths slightly deeper into the IR to decrease the influence of scattering on the photodisruption process in order to create a lesion within the tissue without destroying tissue on the surface. Sacks [91-94] suggested that using a longer wavelength e.g. 1700 nm can be beneficial due to lower scattering.

Here a femtosecond laser at 1700 nm (8 µJ, 130 fs, 1 kHz, FWHM 3µm) was used to create subsurface photodisruption in hydrated human sclera. The beam was focused below the tissue surface and created a cavity using a simple raster snake like scanning pattern. The laser was capable of creating a sub-10µm width incision without introducing unwanted damage [91-94]. Figure 2.27 shows a lesion created and the scanning pattern that was used in the process.

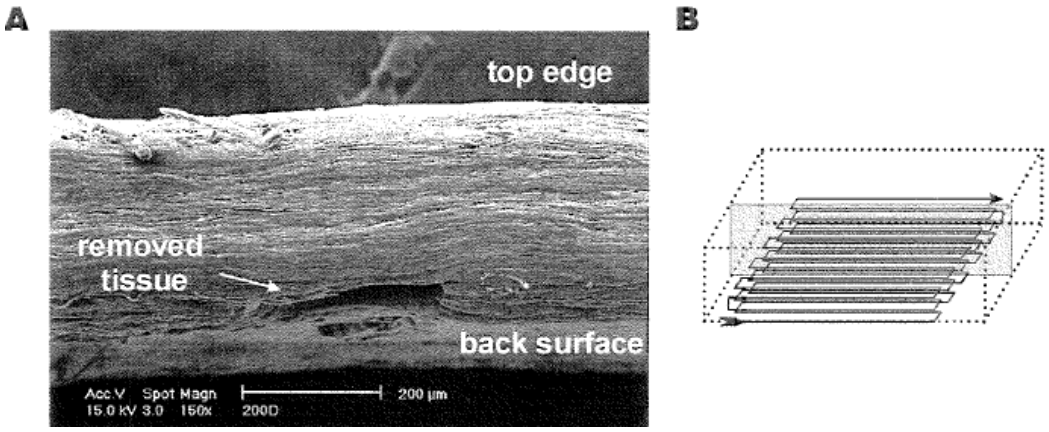

Figure 2.27 SEM micrograph of (A) the lesions in hydrated human sclera created using a 1700 nm fs laser and (B) the scanning pattern that was used. Images taken from [94].

Further work was presented by Chai [95, 96] and was focused on creating vertical subsurface cavities *in vivo* using a femtosecond laser emitting at 1700 nm. *S*ubsurface drainage channels were created that were located closer to the surface compared to preceding results with the same laser. Such a channel can be used to decrease intraocular pressure in the treatment of glaucoma. Figure 2.28 shows the OCT images of the created subsurface channels.

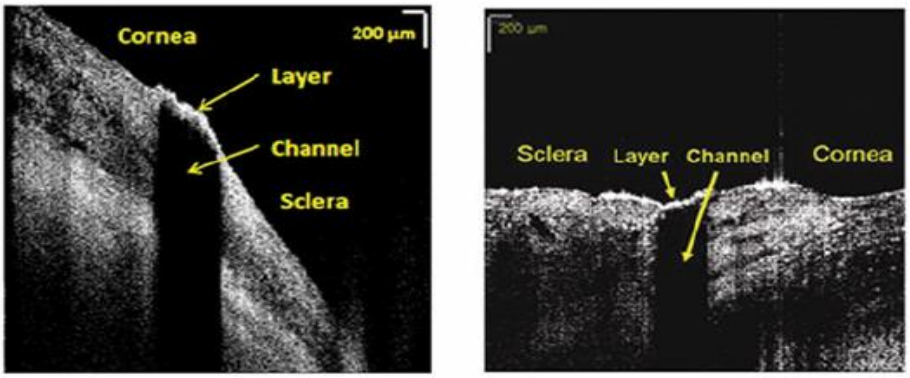

Figure 2.28 OCT images of created subsurface channels. Images taken from [95].

Currently the use of lasers for an eye sight corrective surgery known as laser-assisted *in situ* keratomileusis, or LASIK (laser-assisted *in situ* keratomileusis), is very popular. In this procedure a femtosecond laser creates a flap which, when lifted back, allows access to the cornea which is subsequently reshaped with an excimer laser [69, 97]. Figure 2.29

shows the IntraLase FS system which is clinically approved for the LASIK procedure [98]. This system is capable of performing both a refractive surgery (lamellar keratomy) [99] and a corneal transplant (keratoplasty) [100, 101].

Figure 2.29 Clinically approved IntraLase FS system used for the Lasik procedures. Image taken from [98].

The most popular surgery targeting glaucoma is laser trabeculoplasty [102]. The procedure is based on creating a fluid flow through the eye drainage system. Another procedure for glaucoma is laser viscocanalostomy that removes part of the sclera to enable access to the eye to filter out fluid to the body or to decrease the intraocular pressure. The procedure is similar to research reported by Sacks and Chai [91-96] where the creation of subsurface channels was investigated. Figure 2.30 shows an Aura PT system used in glaucoma surgery. This system uses an Nd:YAG laser (pulse duration of 4 nanoseconds) operating at a wavelength of 1064 nm with the beam focused down to an 8 µm diameter spot [103].

Figure 2.30 Image of an Aura PT system used in glaucoma surgery. Image taken from [104].

2.4. Theoretical models for laser tissue interactions

Theoretical modelling is a powerful tool when coupled with experimental results which can result in increased understanding of the physical mechanisms of a process. Modelling can also be used as a guide to selecting parameters which are best suited for a process, decreasing the amount of time required to determine optimised processing parameters. However, to obtain results that closely represent the physical reality it is necessary to have precise values for the thermomechanical properties and, if possible, know how these values change with temperature. Two key modelling approaches that have been employed for modelling of laser processes are heuristic modelling and mechanistic modelling. Heuristic models can be divided into blow-off models and steady state models and mechanistic models can be divided into steady state vaporization models and thermomechanical models. [70, 105].

2.4.1. Blow-off model

For a model to be described as a blow-off model it has to fulfil four conditions [70, 105]:

- The absorbed laser energy has to be described by Beer-Lambert law.
- The ablation has to be described by a specific threshold, below which energy is only stored into the material as thermal energy.
- The removal of the material can only begin after the laser pulse has finished.
- Thermal confinement conditions are fulfilled.

This model was used to estimate the depth of the etching in polymers caused by a nanosecond UV laser [106, 107].

2.4.2. Steady state model

Compared to the blow-off model, where material removal starts after the laser pulse terminates, in a steady state model material removal takes effect during the period of the laser pulse. Material removal will commence whenever the material specific threshold is exceeded which is similar to the previously mentioned blow-off model. The steady state model can only be used when modelling laser processes where material removal happens during the laser pulse, which is usually for pulses not shorter than tens of microseconds [70, 105].

2.4.3. Steady state vaporization model

Steady state vaporization models, for laser removal of tissue, were based on models developed for ablation of metals [108]. In this case the removal of material is based on a moving boundary during a rapid vaporization. Moreover the surface should have a constant vaporization temperature during the process. This approach has been successfully used in modelling of a photoablation process [109, 110].

2.4.4. Thermomechanical model

A thermomechanical model is a steady state model which incorporates mechanical effects and allows for the tissue to undergo state changes between solid, liquid and vapour states. They were initially applied to the ablation of metals [111, 112] but have been used to simulate ablation of biological tissue. When applied to the simulation of biological tissue the model allows the tissue to undergo a transition from a solid state through a liquid state and to a vapour [70, 105, 113].

2.4.5. Molecular dynamics models

With the constant evolution of theoretical modelling and increases in computational power a new type of model is under continued development, known as molecular dynamics. This type of theoretical modelling is vastly more complicated compared to all of those mentioned previously as it simulates ablation, or any other physical process, as a natural progression of molecular interactions within the system [70]. This particular modelling approach has been used to examine single pulse picosecond laser ablation of silicon [114] or to investigate shock wave creation and dispersions during interaction with picosecond laser [115].

2.5. Model application

There is a range of software modelling packages available where the most popular finite element simulation software being used in theoretical modelling are COMSOL Multiphysics® Modelling Software [116], Dassault Systèmes Abaqus [117], MathWorks - MATLAB [118] or Autodesk Simulation ALGOR [119]. The COMSOL package has been used by Brueye [120] to investigate keyhole digging during spot laser welding using the ALE (Arbitrary Lagrangian Eulerian) method. The ALE method is a moving mesh method that at each time step solves a hyper-elastic problem to obtain a stable mesh deformation. The velocity of the change is dependent on the heat transfer direction and magnitude. It was found that ALE method gives promising results but only for simple topographies and the surrounding gas is only represented by the boundary conditions on the sample surface. Hence this approach is not the best when considering laser ablation in ultrashort pulse regime where interaction is much more abrupt and happens on a much shorter time scale.

Villa Verde [14-16] used an Autodesk Simulation package to create a thermomechanical model focused on investigation of dental enamel response to mid-infrared radiation. She presented a mesoscopic finite element simulation of Er:YAG (2.94 μm) and CO_2 (10.6 μm) laser ablation of enamel tissue. More specifically that research was focused on stress and temperature increases within the enamel rod during laser ablation. It was found that CO_2 laser pulses with lengths around 10 μs should be best suited for removal of hard dental tissue as they do not introduce high transient stresses [14-16]. It was predicted that shorter pulses limit the amount of heat deposited into the tissue as more energy is absorbed into the ablation plume [42]. This minimises the chance of increasing the temperature in pulpal chamber over the critical level as well as minimising melting and cracking of the boundaries of the crater. Finally, according to the simulation results, shorter pulses in the range of 1 – 2 μs could lead to intense tissue cracking due to the higher transient stresses present [14-16].

Research by Cvetkovic [121], who used the steady state modelling approach, was focused on a larger scale; not just limited to the ablation region. Modelling of the heat distribution within the whole eye during high intensity laser surgery was carried out. The simulation used a 193 nm ArF excimer laser irradiating a train of 10 consecutive 14 nanosecond pulses with a fluence of 2 J/cm^2. The simulated temperature for the excimer laser was around 200 ^{o}C in the anterior part of the eye. The same calculations were made for a 1064 nm Nd:YAG laser radiation and the temperature increase was around 90 ^{o}C [121] and for a 694 nm Ruby laser where the temperature increase was found to be around

58 ºC [121]. It was concluded that the pupil opening largely affects the maximum temperature reached in the eye as the absorption of the pupil is highly wavelength dependant [121].

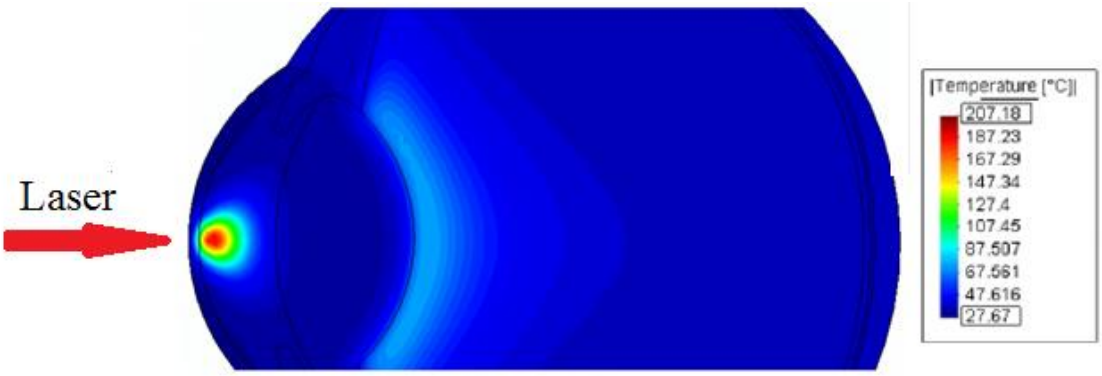

Figure 2.31 Temperature distribution in the eye after being irradiated with 10 pulse of 193 nm ArF excimer laser. Image adapted from [121].

A different type of simulation, demonstrating the plasma shielding effect, was created for laser removal of titanium carbide [122]. This steady state blow-off model is a 1D finite element simulation where the substrate is created from nanometre scale layers and the heat dissipates accordingly to the heat conduction equation. Figure 2.32 shows a schematic of the simulation and the way plasma grows towards the source of the laser radiation.

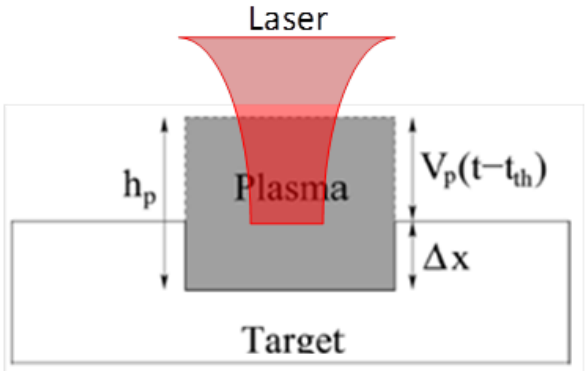

h_p – height of plasma
V_p – volume of plasmat
t – time
t_{th}- time necessary to reach plasma threshold

Figure 2.32 Simulation schematic with plasma growing towards the source of laser radiation. Graph taken from [122].

Analysing the results of the simulation it is clear that plasma shielding can have a major effect on the results of laser machining, especially when the value of irradiance is increased. Whenever irradiance is below 6 J/cm^2 only around 5% of the incoming energy is absorbed by the plasma. When the value of energy is increased up to 10 J/cm^2 25% of the energy is absorbed and when energy used is 25 J/cm^2 around 50% of the incoming energy is absorbed. It can be concluded that plasma has a major influence when selecting optimal processing parameters to efficiently ablate titanium carbide [122].

A more complex approach to investigate ultrafast laser ablation of biological tissue and water was proposed by Jiao [123]. This used rate equations and radiative ultrafast equations to investigate how plasma is created during ultrashort pulse processing of biological tissue. It was shown that plasma is created in the beam focus by picosecond pulses and grows toward the source of laser radiation. Moreover the plasma shielding effect is demonstrated showing the plasma absorbing incoming laser radiation and its consecutive growth. Figure 2.33 shows results of the simulation for 30 picosecond laser pulses creating plasma in water and it decay over time. Simulation result does provide the information about the lifetime of the plasma created in distilled water that enhances the knowledge of the process itself.

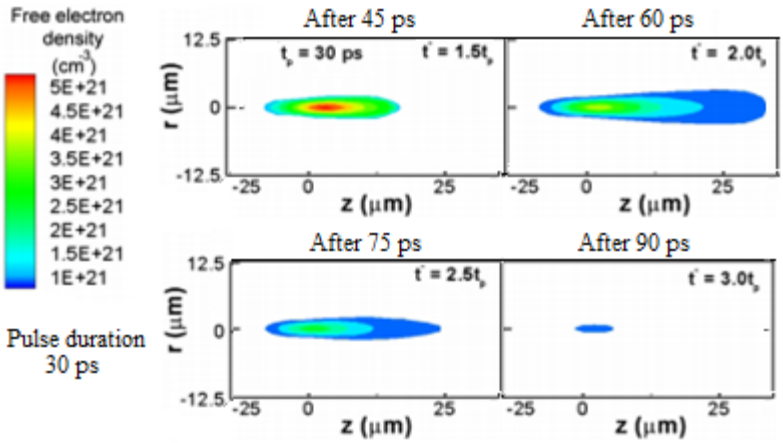

Figure 2.33 Shape and size of the plasma as a function of time after 30 ps pulse irradiation, Image adapted from [123].

It is very hard to create a theoretical model that can recreate the results obtained through the experiments due to the simplification that are introduced into the model. Especially when trying to model extreme processes which occur in very short timescales. In this case certain simplifications and assumption are necessary. Nevertheless even a simple theoretical model can provide some valuable information and enhance understanding of the process.

In Chapter 5 two different models are presented. For CO_2 laser removal of hard dental tissue (Chapter 3) an ALE (Arbitrary Lagrangian–Eulerian) moving boundary model is presented. For ultrafast laser removal of porcine sclera (Chapter 4) a 2D finite element blow-off model is described.

2.6. Conclusions

In the first part of the chapter thermomechanical and optical parameters of hard dental tissue were presented. Consequently the mechanism of removal of tissue was presented

followed by a presentation of research regarding hard dental tissue removal with a variety of lasers, such as: Er:YAG (2.94 μm), CO_2 (9.3 μm, 9.6 μm and 10.6 μm) as well as ultrafast pico- and femtosecond lasers (1064 nm and 780 nm respectively). Currently CO_2 lasers are used in medical practices are operating at 10.6 μm and it was proposed by Villa Verde [14] that 10.6 μm CO_2 laser radiation with pulses in the range of 10 μs (possibly with the assist of water spray [42]) is capable of repeatable removal of enamel with minimal amount of melting and no thermal damage to the pulp in the pulpal chamber [124]. Shortening of the pulse duration from 200-300 μs to ~10 μs has enabled minimization of thermal damage to the tissue but this trend does not continue into shorter pulse duration, as shorter pulse durations 0.1–1 μs can induce high stress and lead to undesirable cracking [14]. On the other hand Fried's research suggests that due to the thermal relaxation time of 70 – 80 μs there will not be any benefit of using pulses of duration ~10 μs as they will not offer any benefit over longer pulse durations of 50 - 100 μs. A successful created crater could be potentially used as an entry portal to administrate a photo-activated antibacterial drug [125] into the carious tissue therefore minimizing the diameter of necessary craters.

In the second part, regarding ophthalmology, optical and structural parameters of sclera were presented as well as different routes of drug delivery to the posterior part of an eye. Consequently different approaches using a variety of lasers were presented as possible laser sources to modify scleral tissue. The types of laser used in the presented research were ultrafast femtosecond lasers operating at different wavelengths: 780 nm, 800 nm and 1700 nm. Unfortunately there is no in-depth research investigating which laser parameters, scanning strategies are best suited to offer a precise control of the cavity. Moreover picosecond lasers should be capable of removing scleral tissue without any unwanted thermal damage and offer increased ablation rate compared to femtosecond lasers.

To conclude the literature review different types of theoretical models were presented as well as a few examples of models used to simulate laser material interactions. A steady state vaporization ALE moving boundary approach, similar to one chosen by Bruyere [120] to simulate keyhole welding, was selected to simulate CO_2 laser removal of hard dental tissue. On the other hand single line scanning picosecond ablation of scleral tissue will be simulated using steady state model similar to one that was used by Marla [122] to simulate nanosecond laser removal of titanium carbide.

Chapter 3. CO_2 laser removal of hard dental tissue

This chapter describes an in-depth investigation into the possibility of using 10.6 μm CO_2 pulsed laser radiation to modify and remove dental hard tissue. There were two main driving factors behind choosing a laser that operates at this particular wavelength: (i) a wavelength of 10.6 μm overlaps with a phosphate band in enamel, which provides a high value of absorption; (ii) currently CO_2 lasers used in dental practice, targeting different soft tissue procedures, operate at 10.6 μm. The development of a laser based removal process that allows the creation of craters, narrower that currently achievable by traditional dental bur, without introducing detrimental cracking to the bulk tissue could enable more precise dental procedures. An optimised process would reduce removal of healthy tissue during drilling and could also provide a potential way to distribute antibacterial fluid to underlying carious tissue. Different pulse durations, pulse energies and out-of-focus single pulse removal is investigated. The influence of water spray on single pulse laser ablation is explored and the temperature increase in the pulpal chamber, during different laser irradiation strategies, is measured. Moreover the increase of temperature in the pulpal chamber is tested by placing thermocouples through the root canals.

3.1. Introduction

The wavelength of 10.6 µm overlaps with a phosphate band (PO_3^{-4}) absorption in dental hard tissue hence CO_2 laser radiation has been selected as a potential source for modification of the tissue. At the beginning of the chapter experimental setup and its capabilities are described. Consequently an in-depth analysis of single pulse ablation of hard dental tissue is presented. To select suitable parameters to allow for the minimally invasive removal of hard dental tissue parameters that are investigated are:

- Different pulse length,
- Different fluences,
- Different focusing planes,
- Machining with converging and diverging beam,
- Multiple pulse ablation in the same spot,
- Trepanned laser drilling.

Furthermore to ensure that the maximum temperature increase during laser machining process does not exceed the critical safety limit of maximum temperature increase of 5.5 ^{o}C in pulpal chamber [30] thermocouples were placed inside pulpal chamber to record temperature increase. Finally, different experimental scenarios were carried out to replicate, a real clinical procedure.

3.2. Experimental setup

3.2.1. Laser

Experimental setup is built around a radio frequency excited Rofin UK SC x20 CO_2 laser. This laser is capable of emitting wavelengths from 10.4 μm to 11.2 μm and was setup to operate at the wavelength of 10.6 μm. The Rofin laser emits a slightly elliptical beam (7.5 mm x 9 mm) and has a M^2 factor of 1.2 [126] Laser was set up to generate 200 μs pulses with a repetition rate of 250 Hz (Duty Cycle = 5%) with an average output power of 36 W. This system was previously used by Dr Krystian Wlodarczyk [127], but it was modfied and rebuild for the purpuse of this experimental work. Figure 3.1 shows laser, beam relay system and motorized stages used to control the position of the sample.

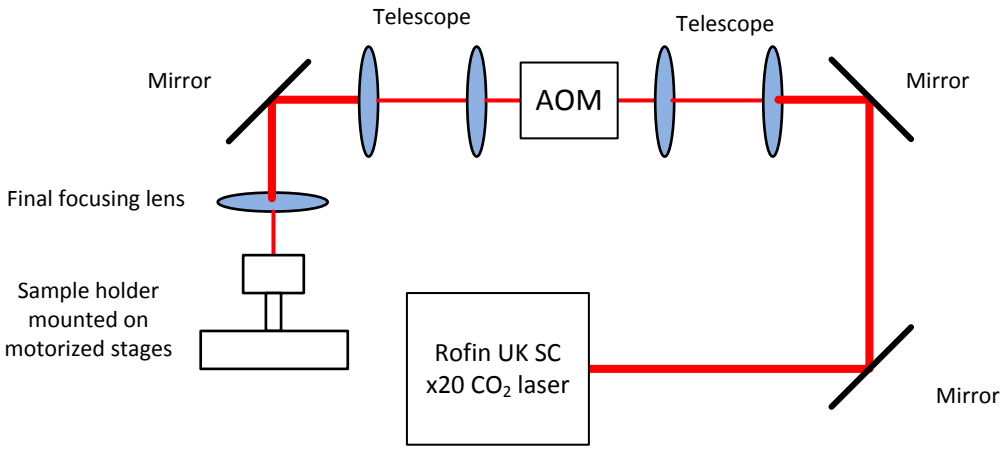

Figure 3.1 Schematic of the experimental setup.

The setup includes an acousto-optic modulator (AOM) (NEOS Technologies) which is placed on shelf above laser and translation stages. To pass through the AOM the beam is raised by set of mirrors and subsequently resized to fit entry aperture of the modulator as the diameter of the beam was 7.40 mm by 8.42 mm (measured at $1/e^2$ intensity) [59, 60] and the aperture diameter of the modulator is only 5 mm. The beam was demagnified by composing a telescope out of two 6.35 cm (2.5 ”) and 3.81 cm (1.5 ”) focal length ZnSe coated meniscus plano-convex lenses which resulted in beam diameter of 4.55 mm x 4.96 mm.

After the AOM the beam is magnified by a telescope composed of two ZnSe coated meniscus lenses of focal lengths 3.81 cm (1.5 ”) and 12.7 cm (5 ”), which gives a magnification of 3.33 times which results in the beam diameter, measured at $1/e^2$ of 15.2 mm x 17.5 mm. Consequently beam is reflected off of the 45° mirror to reach final working lens which is a 3.81 cm (1.5 ”) focal length ZnSe meniscus lens.

3.2.2. Acousto-optic modulator

A significant part of the setup is a germanium crystal based AOM (NEOS Technologies) that allows selecting pulse duration as well as the shape of the pulse by selecting a specific part of the overall laser pulse. Moreover it is used for fine control over power transmitted through the output of the system and allows having a precise control over multiple pulse trains. The output power is selected by changing the amplitude of the signal that is applied to the crystal and the pulse duration is selected by the pulse duration and signal frequency of the applied signal. The modulator is controlled by a pulse generator that is working in a delayed pulse mode which is explained in Section 3.2.2.2

To allow for the laser to heat up and stabilise the modulator was aligned so that the 0^{th} diffraction order would go to a heat sink, and the 1^{st} diffraction order would be transmitted through the optical system. Figure 3.2 shows measured AOM transmission as a function of voltage applied to the germanium crystal.

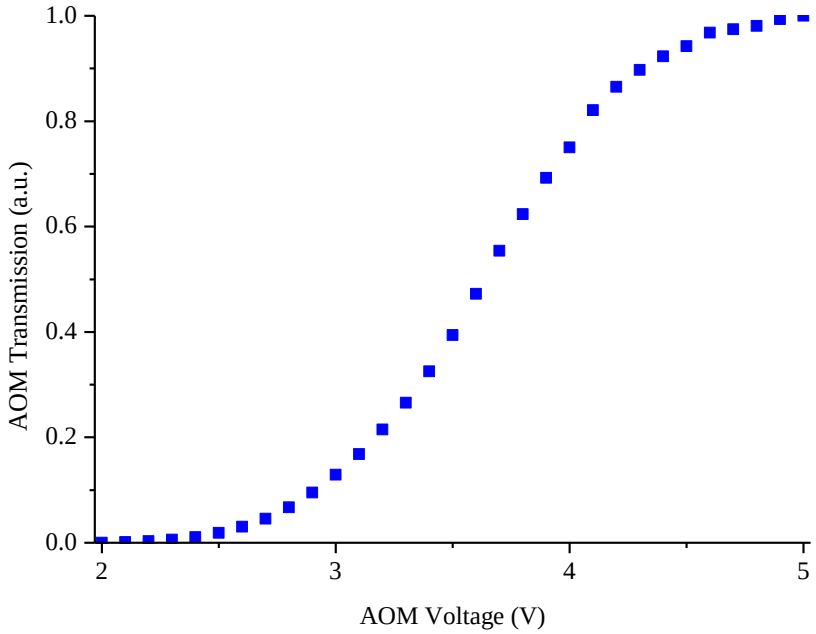

Figure 3.2 AOM Transmission as a function of applied driving voltage.

If possible it is recommended for the beam passing through AOM to be as small as possible, because larger beams are distorted becoming more elliptical due to non-symmetric distribution of the refractive index throughout the crystal. Unfortunately the AOM performance is limited by the maximum allowed optical power density, which in this case was 5 W/mm^2 [128]. With the laser beam resized (4.55 mm x 4.96 mm at 1/e^2) to fit the aperture this limits the total power available for the process in order to not exceed the power handling capabilities of the modulator. Having that power restriction has a

significant consequence when investigating shorter pulse durations in the range of 10 µs (as discussed in Chapter 3.4).

3.2.2.1. Pulse duration

One of the most important objectives in this project was to find the optimal parameters of ablation of the hard dental tissue that allow for an efficient ablation of the tissue without introducing any unwanted thermal damage or cracking to the tissue or cause necrosis in the pulpal chamber by increasing the temperature by more than 5.5 ^{o}C [29]. To do this a range of pulse durations from 10 to 200 µs and fluences up to 200 J/cm^2 were trialled. The application of the AOM allowed selection of specific pulse durations and pulse energies while investigating their influence on laser processing of human enamel.

Measurement of different pulse durations (1/e^2) selected by the AOM modulator was done with a fast pyroelectric sensor with a response time of ~100 ns, which is 100 times shorter that shortest pulse duration that is investigated. Figure 3.3 shows different pulse durations measured with the pyroelectric sensor. For longer pulses, such as 100 and 200 µs, there is a visible slope at the beginning, but for shorter pulses this slope disappears and the energy distribution over the whole pulse is less varied.

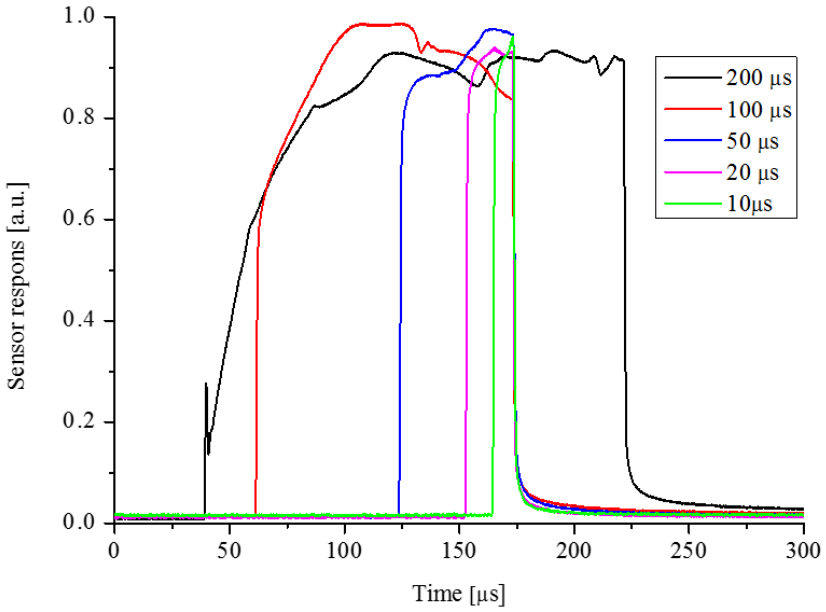

Figure 3.3 Shape of pulses with different durations measured with a thermopile with a response time of ~100ns.

3.2.2.2. Control of pulse amount and shape

The use of an AOM allows not only control of pulse duration and pulse energy, but it also allows control of pulse trains in terms of duration and frequency. Unfortunately the previous pulse generator setup used to control the AOM did not offer this possibility

hence the system was modified by adding another pulse generator to act as a gate. The modified AOM and laser controlling arrangement is shown on the Figure 3.4.

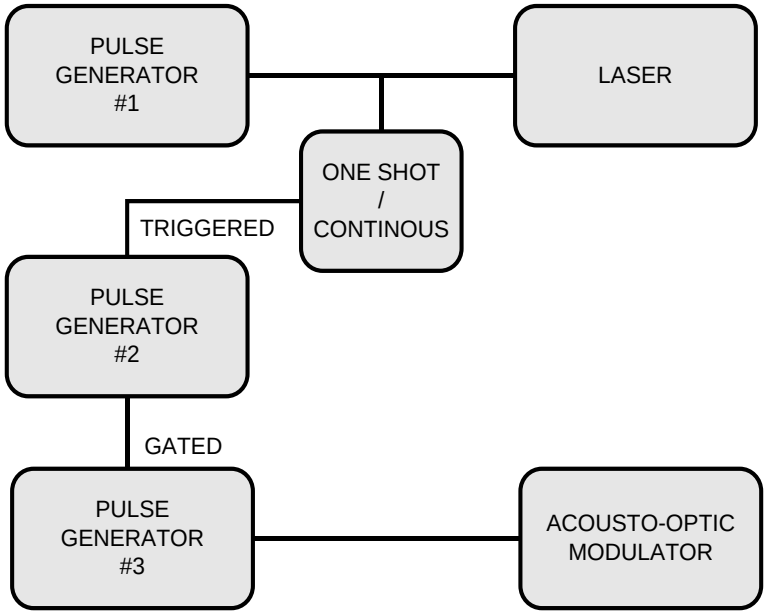

Figure 3.4 System of pulse generators controlling the laser and AOM.

Pulse generator #1 is used to set the excitation parameters for the laser and sets the global process repetition rate. Pulse generator #2 is working in a delayed pulse mode to ensure that it covers a whole laser pulse (in the next period) and is triggered by a single shot button or it is working in continuous mode. This sets the number of pulses in a particular pulse train. Pulse generator #3 is controlling the pulse duration of the acousto-optic modulator and is gated by the signal from Pulse Generator #2. This sets the pulse duration for the process. Figure 3.5 shows operating mode of this setup for three pulses.

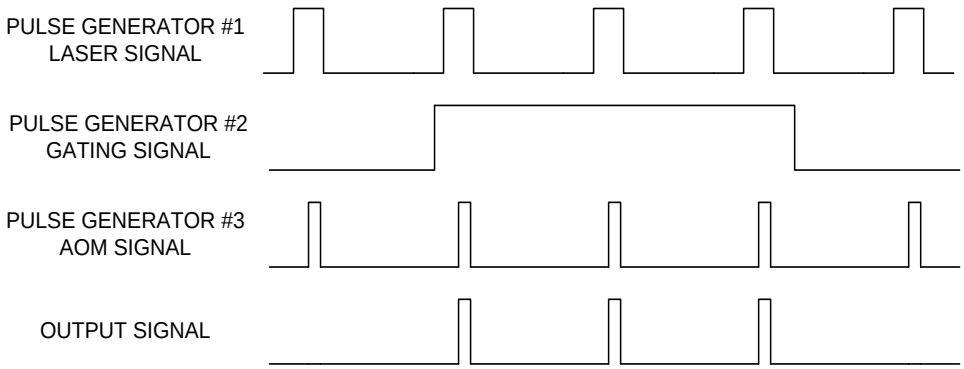

Figure 3.5 Principle of operation of the pulse generator configuration. Pulse generator #1 is responsible for generating the laser operating signal. Pulse generator #2 is a gating signal that selects which pulses are going to be transmitted. Pulse generator #3 selects which part of the pulse is going to be transmitted.

3.2.3. Focused spot size

During experiments two different focused spot diameters were used. A smaller focused spot size was used when investigating high fluences up to 200 J/cm^2 whereas a larger spot was used when investigating the possibility of removing more tissue and for drilling deeper cavities. Beam diameters were measured using a 10%-90% knife edge method and consequently they were multiplied by 1.561 [129] to obtain the beam diameter at 1/e^2 intensity. It should be highlighted that the spot at focus showed a slightly elliptical geometry. The smaller focussed spot (focussed with the 1.5" focal length lens) had diameters of 27 µm by 22 µm from the knife edge measurement giving 42 µm by 35 µm at 1/e^2 intensity. The larger focussed spot (focussed with the 1.5" focal length lens) had diameters of 58 µm by 47 µm from the knife edge measurement giving 91 µm by 74 µm at 1/e^2 intensity. Figure 3.6 and Figure 3.7 show results of the 10%-90% knife edge measurement for both the smaller and larger beam.

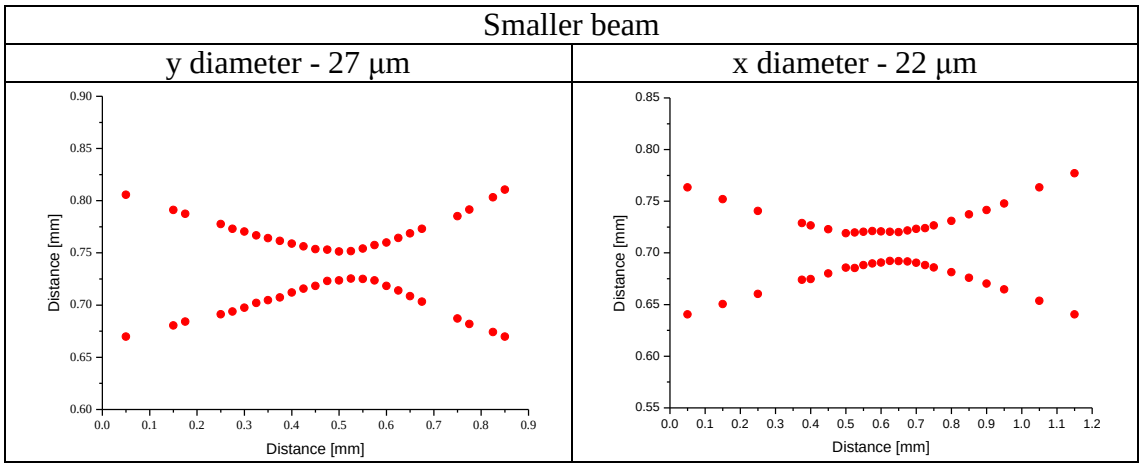

Figure 3.6 Smaller laser beam diameters through focus measured using a 10%-90% knife edge method. Two spot sizes were used during the experiments. As is shown the beams had different diameters in the x and y directions.

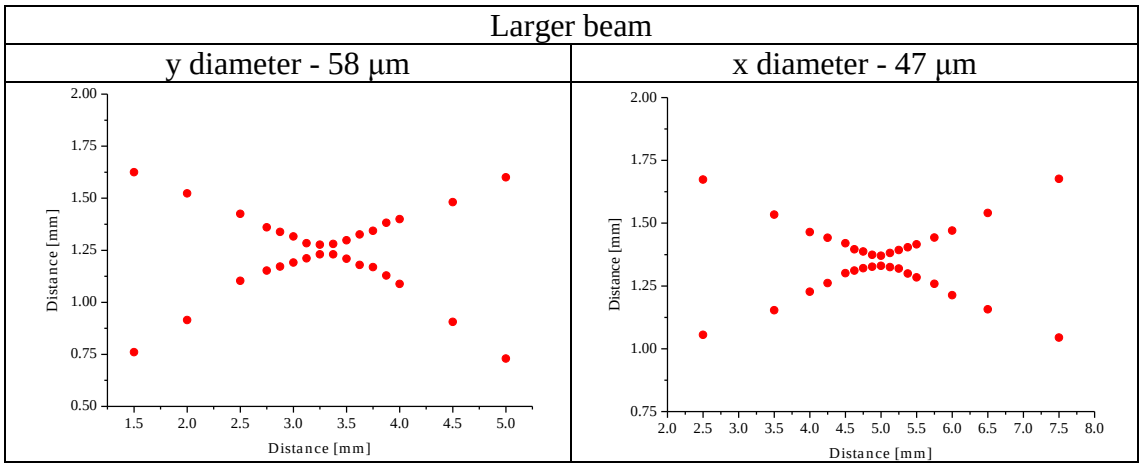

Figure 3.7 Larger laser beam diameters through focus measured using a 10%-90% knife edge method. Two spot sizes were used during experiments. As is shown the beams had different diameters in the x and y directions.

3.2.4. Sample positioning

Sample position is controlled by precision X-Y Aerotech motorized stages. For focus control (Z axis) the final, working lens is mounted on a separate Z dimension motorized stage. The final lens has its focus aligned with the focus of a CCD camera. The camera has a mounted microscope objective of 20x magnification, which allows the sample to be positioned with an accuracy +/-15 μm from its focus. As discussed two spot sizes were used in the experiments. For the smallest beam waist the Rayleigh range has been calculated, using Equation (3.1), as 76 μm

$$z_R = \frac{\pi {w_0}^2}{\lambda} \tag{3.1}$$

where z_R is Rayleigh range, w_0 is beam waist radius and λ is the radiation wavelength. As this is approximately five times the positioning accuracy achievable using the camera the alignment system was deemed acceptable.

3.3. Dental samples

Human teeth samples used in these experiments were provided by Dr Ailbhe McDonald from the UCL Eastman Dental Institute. Experiments were carried *in vitro* on molar teeth that have been selected to have a reasonably wide and approximately flat areas of sound enamel (i.e. no signs of caries). To recreate conditions in dental practice as closely as possible we have carried out our experiments without any modification to the enamel surface such as grinding or polishing. To keep the samples in good condition they were stored in a 96% ethanol solution. Figure 3.8 shows a non-irradiated surface of a human tooth where the characteristic pattern of tightly packed hydroxyapatite rods can be seen (the structure of the tooth is discussed in detail in 2.32.

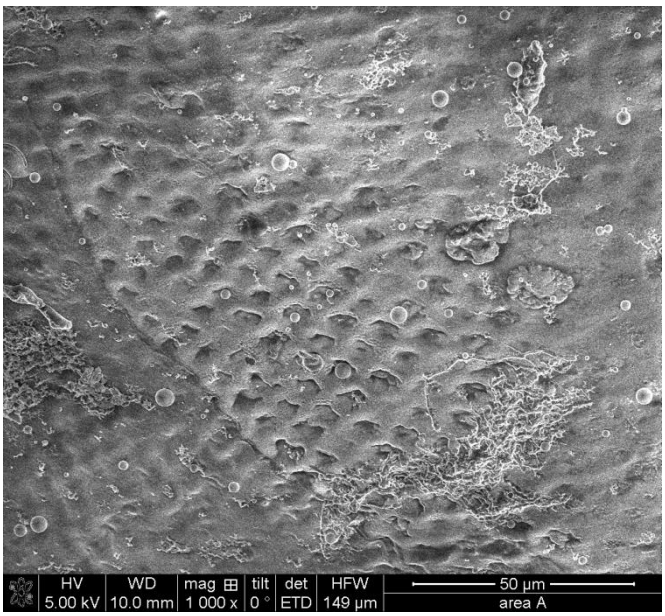

Figure 3.8 Scanning Electron Microscope micrograph of non-irradiated surface of human dental enamel.

The surface morphology micrographs of the non-irradiated and irradiated enamel surfaces have been obtained with scanning electron microscopy (FEI Quanta 3D FEG) without introducing any coating to the surface beforehand. Surface profiles and crater depth have been measured with white light interferometry using both Zygo NewView 5000 and Alicona 4G surface profilometers. One of the issues of using these devices for determining the depth and the shape of cavities is that for narrow and deep craters they struggle to get a good signal return from the walls and especially from the bottom surface as there is not enough of light reflected

3.4. Single pulse ablation

3.4.1. Enamel removal

The most important step was to find a suitable pulse regime in which there is efficient ablation without introducing any unwanted thermomechanical damage to the surrounding tissue as well as minimising cracking introduced to the ablation site or the surrounding tissue. The mechanism of hard dental tissue removal, water mediated explosive ablation, is described in Section 2.3.5. In this experiment unpolished molar samples underwent single pulse laser machining with pulse durations ranging from 10 μs to 200 μs with fluences ranging from 10 J/cm^2 to 100 J/cm^2. Focussed spot size diameter used in this experiment was 42 μm by 35 μm measured at 1/e^2. Figure 3.9 shows maximum crater depth as a function of fluence for different pulse durations. Figure 3.10– 3.15 show SEM

micrographs of cavities created with single pulse CO_2 laser ablation with different values of fluence (10, 20, 40, 60, 80 and 100 J/cm^2) with different pulse durations: 10, 20, 50, 100 and 200 µs.

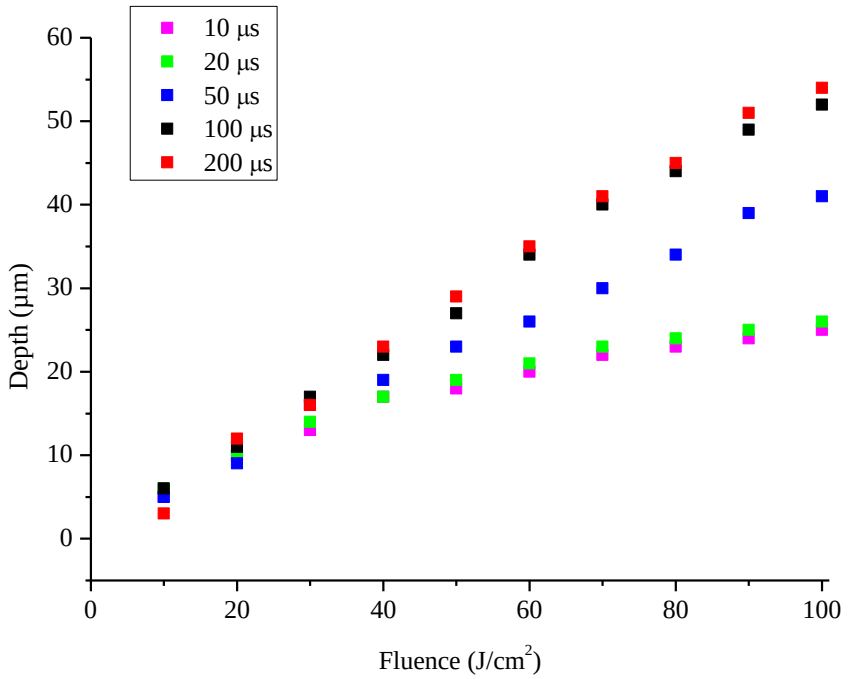

Figure 3.9 Maximum crater depth as a function of fluence for different pulse durations ranging from 10 µs to 200 µs.

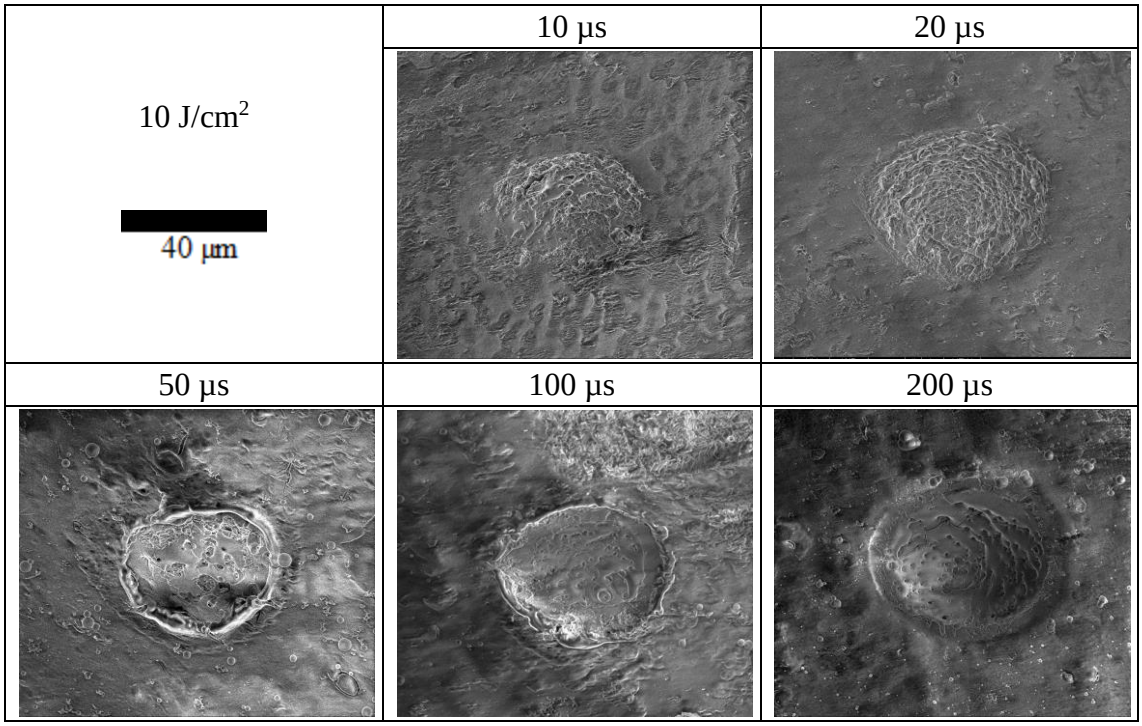

Figure 3.10 SEM micrographs of cavities created with single pulse CO_2 laser ablation with a fluence of 10 J/cm^2 with different pulse durations: 10, 20, 50, 100 and 200 µs.

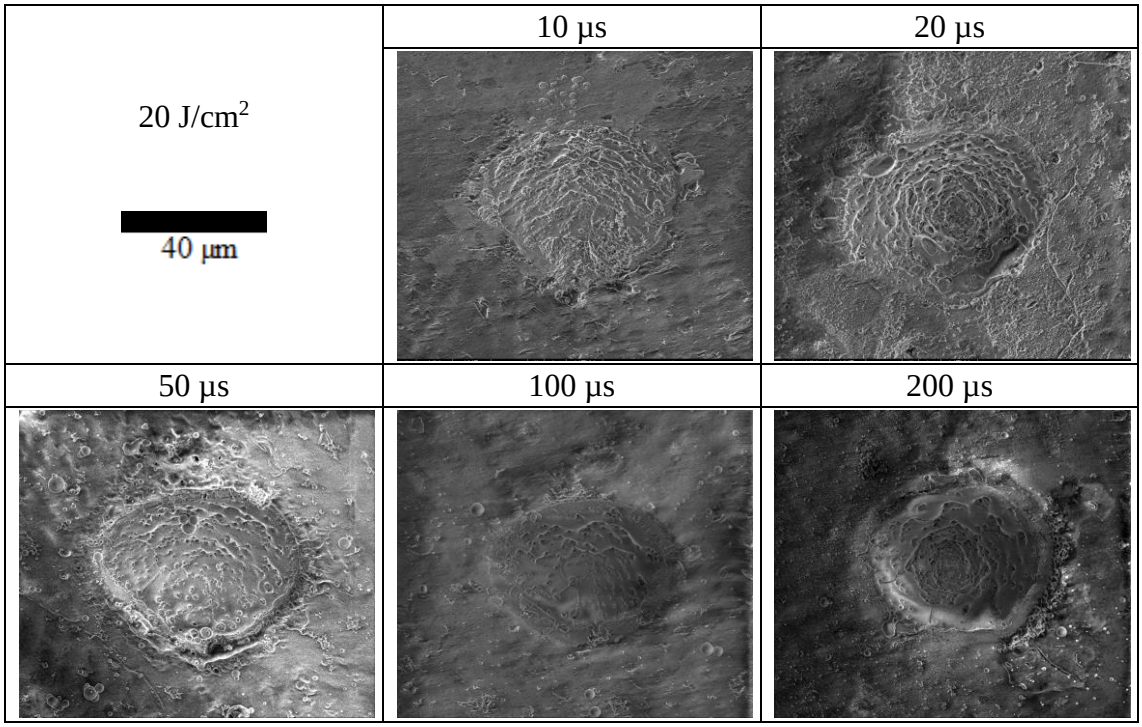

Figure 3.11 SEM micrographs of cavities created with single pulse CO_2 laser ablation with a fluence of 20 J/cm^2 with different pulse durations: 10, 20, 50, 100 and 200 µs.

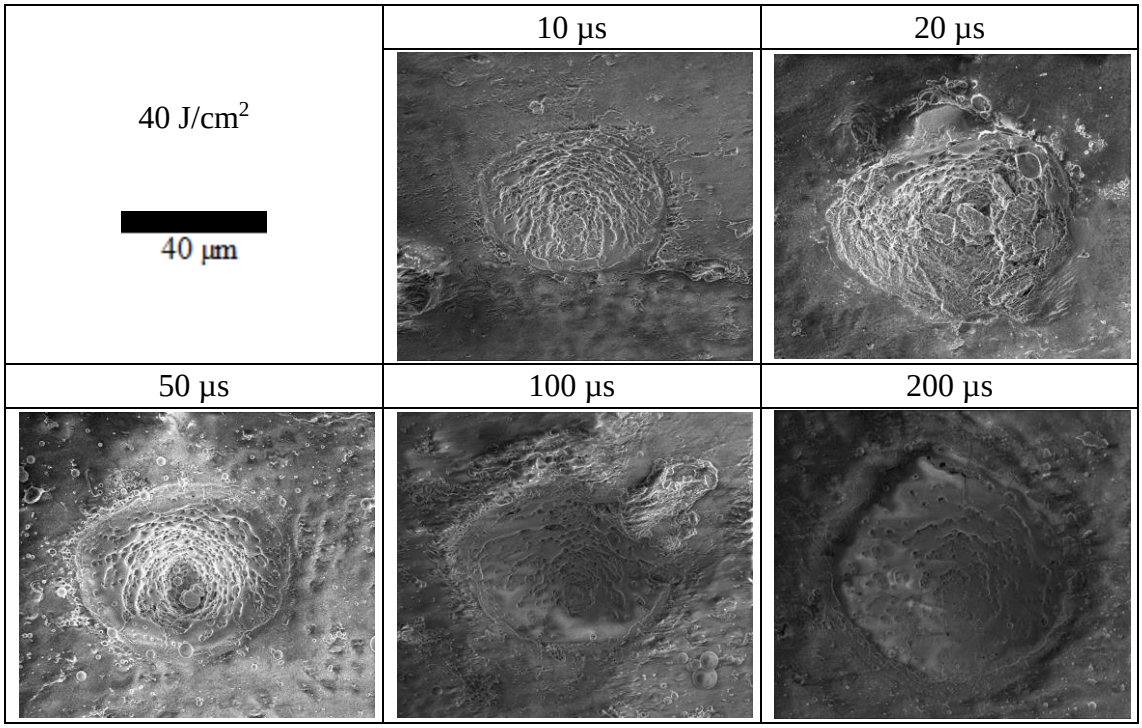

Figure 3.12 SEM micrographs of cavities created with single pulse CO_2 laser ablation with a fluence of 40 J/cm^2 with different pulse durations: 10, 20, 50, 100 and 200 µs.

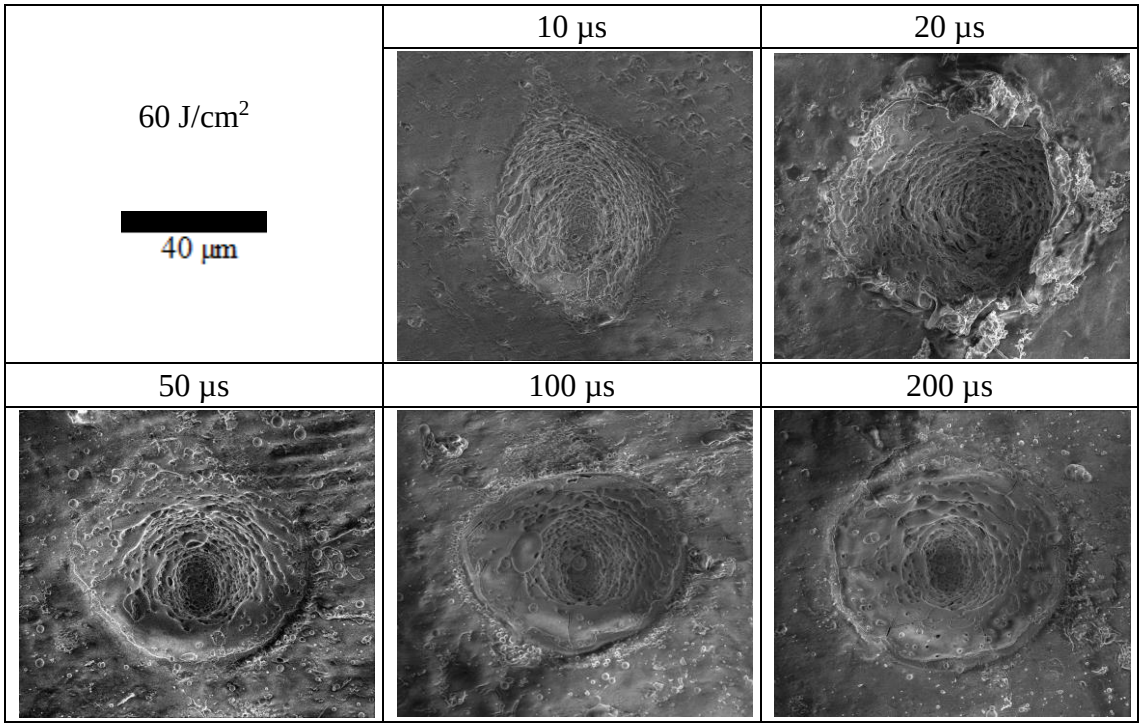

Figure 3.13 SEM micrographs of cavities created with single pulse CO_2 laser ablation with a fluence of 60 J/cm^2 with different pulse durations: 10, 20, 50, 100 and 200 µs.

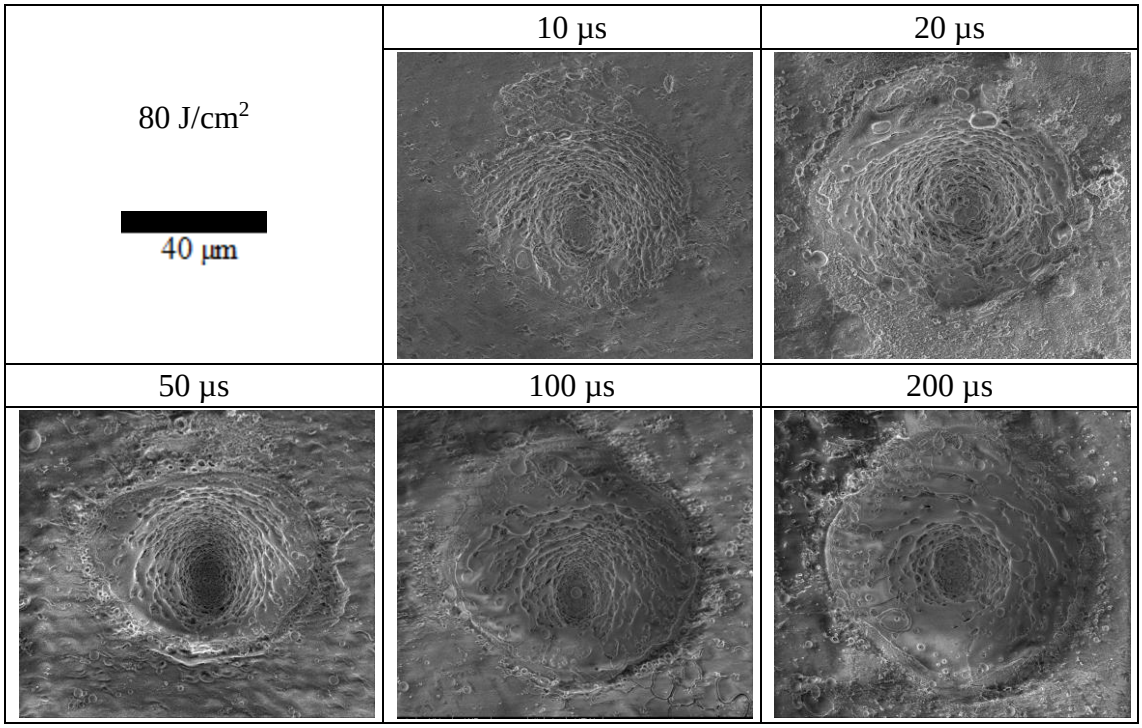

Figure 3.14 SEM micrographs of cavities created with single pulse CO_2 laser ablation with a fluence of 80 J/cm^2 with different pulse durations: 10, 20, 50, 100 and 200 µs.

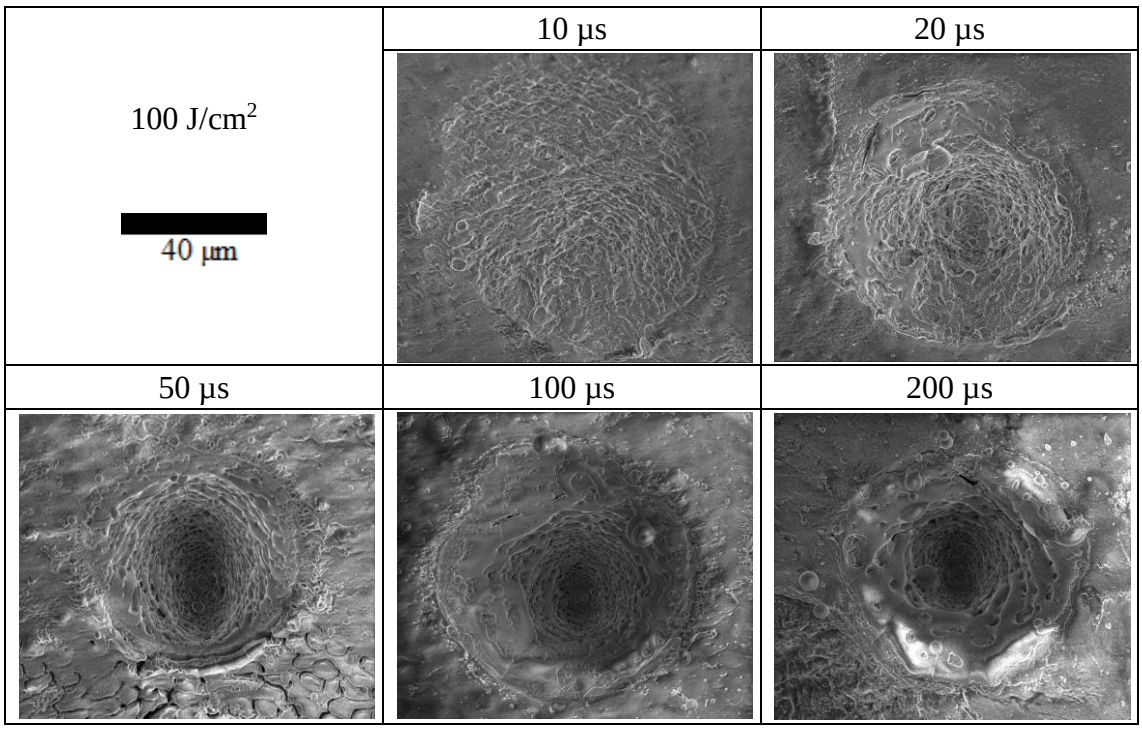

Figure 3.15 SEM micrographs of cavities created with single pulse CO_2 laser ablation with a fluence of 100 J/cm^2 with different pulse durations: 10, 20, 50, 100 and 200 µs.

Initial results suggest that a CO_2 laser operating at the wavelength of 10.6 µm is capable of precise dental hard tissue removal. Furthermore, by selecting specific values of pulse energy you can select desired values of the cavity depth. Similar results were achieve by Fried [30] where he presented cavities created with a CO_2 laser, but in his research cavities were created in a controlled environment as grinded and polished block of hard dental tissue were used as oppose to untreated surface of enamel. The difference in the crater depth for different pulse durations, especially at higher fluences, is a result of the creation of an ablation plume that consists of water, hard tissue components and organic materials [42]. The ablation plume absorbs incoming laser radiation minimizing the amount of radiation that reaches the enamel surface which leads to a decreased amount of material removed. Shorter pulse durations results in higher values of irradiance, for a fluence of 40 J/cm^2 for 200 µs the irradiance is $2 \cdot 10^5$ W/cm^2 and for 10 µs the peak irradiance is $4 \cdot 10^6$ W/cm^2. As a result, for shorter pulses, the ablation plume is created much quicker and has a higher influence on the incoming laser radiation [42]. The influence of the ablation plume is clearly visible when comparing how the crater depth changes with increased fluence for 10 µs to 200 µs. For 10 µs an increase in fluence by 150% (from 40 J/cm^2 to 100 J/cm^2) changes the irradiance from $4 \cdot 10^6$ W/cm^2 to $1 \cdot 10^7$ W/cm^2 which produces an increase in crater depth by approximately 80% (from 18 µm to 25 µm). For longer pulse durations of 200 µs the same increase of fluence of 150%

(from 40 J/cm^2 to 100 J/cm^2) changes the irradiance changes from 2·10^5 W/cm^2 to 5·10^5 W/cm^2 which increases the crater depth from 22 µm to approximately 55 µm (150% increase). This is noticeable when looking at a relationship between ablation efficiency and fluence for different pulse durations (10, 20, 50, 100 and 200 µs).

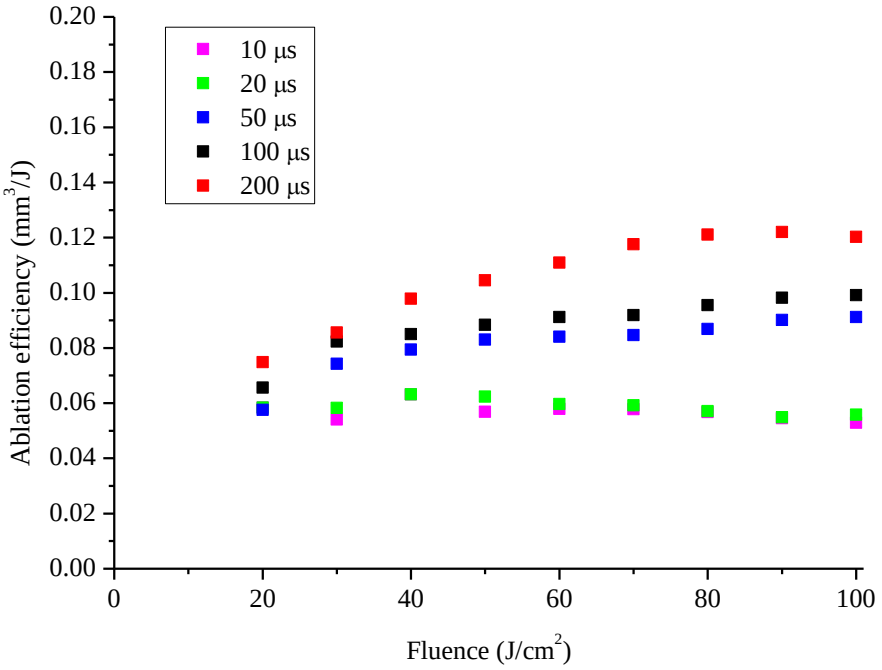

Figure 3.16 Ablation efficiency (mm^3 of material removed per J) as a function of fluence.

Figure 3.16 shows the dependence of the ablation efficiency on the laser fluence incident on the sample surface. Ablation efficiency has been calculated only for fluences above 20 J/cm^2 as for lower fluences the crater is not very well defined and it is hard to accurately measure the dimensions. In order to estimate the amount of the removed enamel the volume of the crater has been calculated by using an approximated formula (Equation (3.2) for the volume under a 2D Gaussian function with an elliptical base. Figure 3.17 shows a schematic for the calculations.

$$V = 2\pi \cdot depth \cdot \frac{1}{3} radius_x \cdot \frac{1}{3} radius_y \qquad (3.2)$$

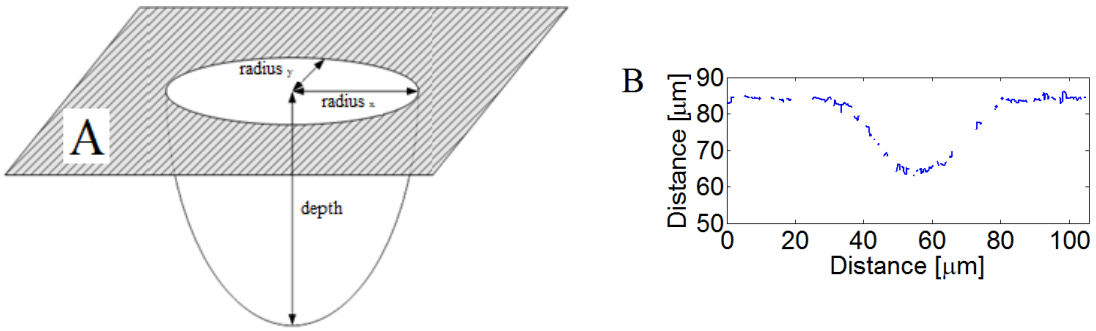

Figure 3.17 (A) Schematic used to calculate the volume of the tissue removed. (B) An exemplary cross section profile of the cavity showing Gaussian like shape.

The dimensions of the craters were measured with a white light interferometer. For the longest pulse duration of 200 µs the ablation efficiency is increasing up to a fluence of to 90 J/cm^2 (Irradiance of 4.5·10^5 W/cm^2). For slightly shorter pulses (50 µs, 100 µs) the ablation efficiency is increasing but not as markedly. Up to approximately 30 J/cm^2 (where the irradiance for 50 µs is 6·10^5 W/cm^2 and for 100 µs pulse is 3·10^5 W/cm^2) the ablation efficiency dependence on fluence follows the same trend as for a 200 µs pulse. However, above 30 J/cm^2 the ablation efficiency is significantly lower. Shorter pulse durations, therefore a proportionally higher irradiance, leads to quicker development of an ablation plume and hence a decreased ablation efficiency as the ablation plume interacts with incoming radiation [42].

For shorter pulse lengths 10 and 20 µs the ablation efficiency is independent of fluence. Compared to the longer pulse duration of 200 µs the irradiance is higher (by a factor of 20 for a 10 µs pulse and 10 for a 20 µs pulse) which allows for the plasma creation threshold to be reached much sooner compared to the longer pulse durations. Assuming a fluence of 40 J/cm^2 the irradiance for a 10 µs is 4·10^6 W/cm^2 and for 20 µs is 2·10^6 W/cm^2 compared to 2·10^4 W/cm^2 for a 200 µs pulse. As a result there is no benefit (in terms of ablation efficiency) of increasing pulse energies as all of the results in is depositing more thermal energy into the plume which subsequently would be deposited into the substrate. This could have catastrophic results for the tissue leading to increased stresses, cracking, carbonization and dehydration.

For the shortest (10 µs) and the longest (200 µs) pulse durations additional experiments have been carried out to investigate the relation between crater depth, ablation efficiency and fluence for higher values of fluence up to 200 J/cm^2 (irradiances

up to $2 \cdot 10^7$ W/cm^2 for 10 µs and $1 \cdot 10^6$ W/cm^2 for 200 µs). Results of this experiment are shown in Figure 3.18.

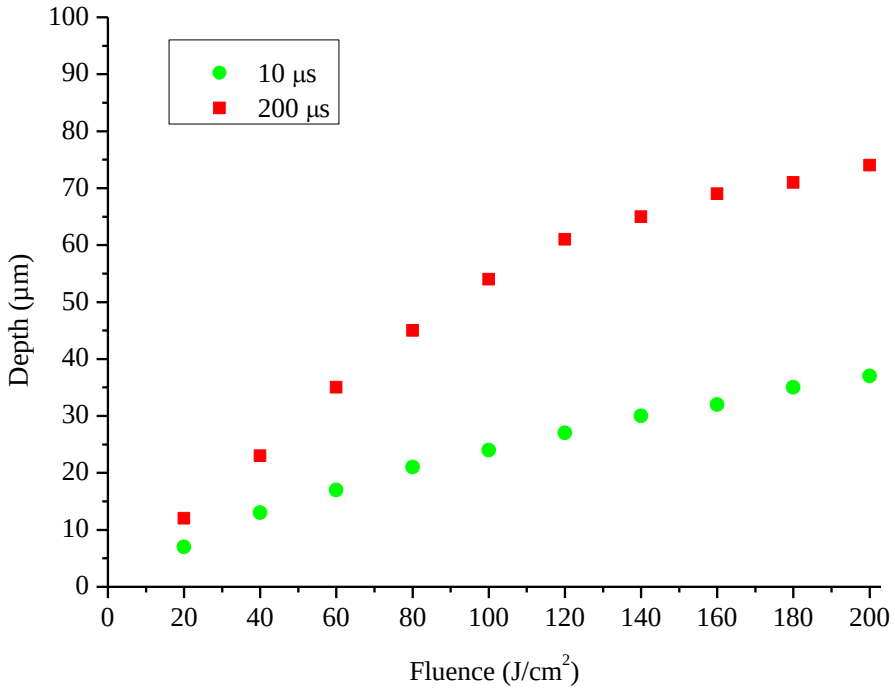

Figure 3.18 Maximum crater depth for 10 µs and 200 µs pulses as a function of fluence. For fluences below 100 J/cm^2 results are same as on the Figure 3.7.

The focussed spot size diameter used in this experiment was the same as in the previous experiment, 42 µm by 35 µm measured at $1/e^2$. The crater depth for a 10 µs pulse duration follows the same trend line up to 200 J/cm^2, whereas for a longer pulse duration of 200 µs the trend flattens at around a fluence of 100 J/cm^2 (an irradiance of $5 \cdot 10^5$ W/cm^2). This is due to the fact of an increased influence of the ablation plume on the processing parameters. These changes in trend are more clearly visible on a graph presenting value of fluence rather than crater depth (see Figure 3.19).

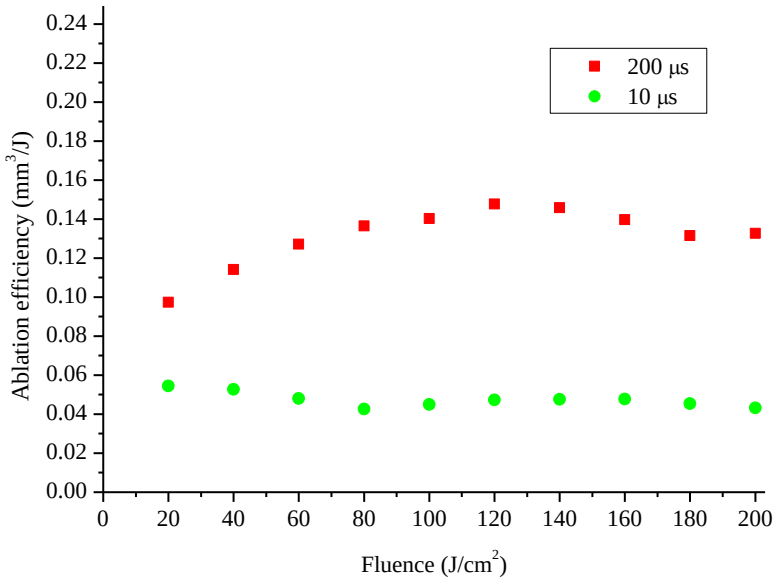

Figure 3.19 Ablation efficiency (mm^3/J) as a function of fluence for craters created with 10 and 200 µs single pulse ablation. For fluences below 100 J/cm^2 results are same as on Figure 3.16.

Figure 3.19 shows ablation efficiency as a function of fluence for two different pulse durations. For a shorter pulse duration (10 µs) the ablation efficiency is constant across the whole fluence range investigated in this experiment. For longer pulse durations (200 µs) the change of the regime of laser machining with and without an ablation plume is much more noticeable (compared to Figure 3.18). For fluences up to ~100 J/cm^2 (~$5 \cdot 10^5$ W/cm^2) the ablation efficiency increases in a linear fashion, whereas for higher fluences (over 100 J/cm^2) ablation efficiency has a rather flat, or slightly decreasing trend, which is a result of an increased effect of the ablation plume, consisting of water, hard tissue components and organic materials, on the incoming laser radiation [42].

It was shown that increasing the laser fluence doesn't result in increased efficiency. For both tested pulse durations (10 and 200 µs) the increment of both crater depth and ablation efficiency is not proportional to increment of the fluence. When a higher value of fluence is used a bigger ablation plume is created which absorbs incoming radiation and shields underlying tissue. As a result fluence that is capable of creating a well-defined cavity and minimizes the amount of the energy deposited in the tissue is within the range of 40 – 60 J/cm^2.

3.4.2. Cracking of dental enamel during laser processing

While investigating optimum parameters for the ablation of human enamel one of the crucial elements is to minimize, or ideally eliminate, cracking and crazing (a net combined of shallow, surface micro-cracks) to the ablated crater as well as to the adjacent tissue. Any cracking undermines the structural integrity of the tissue and is not acceptable

but the crazing observed on the re-melted surface are smaller than cracks that can be caused by commonly used dental burs [130] and therefore would not considered to be an issue. To investigate this five different pulse durations have been compared 10, 20, 50, 100 and 200 µs. Figure 3.20 shows SEM micrographs and horizontal cross section profiles for craters created with a single pulse, a fluence of 30 J/cm^2 and a spot size of 42 µm by 35 µm (see Figure 3.6).

Pulse duration	SEM micrograph	Horizontal cross-section
10 µs	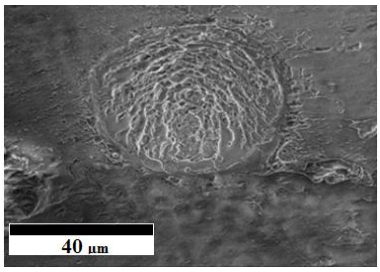	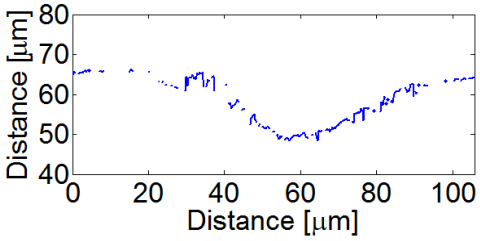
20 µs	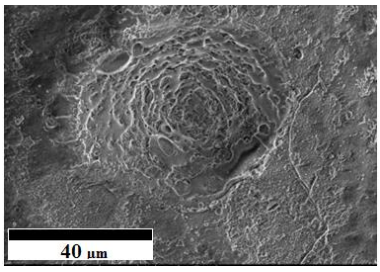	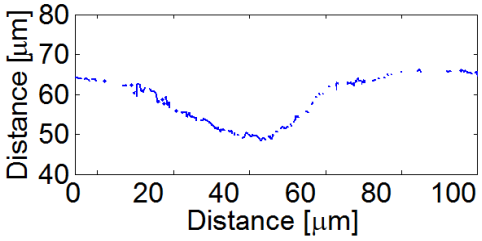
50 µs	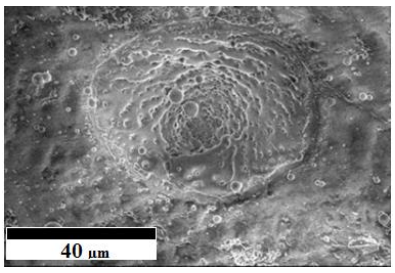	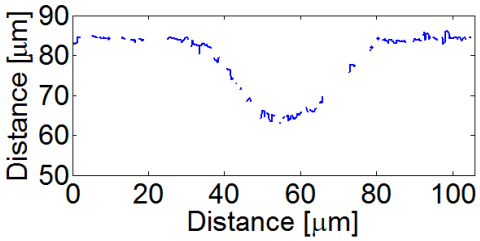
100 µs	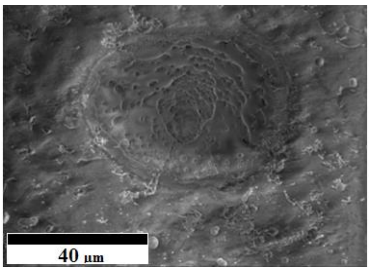	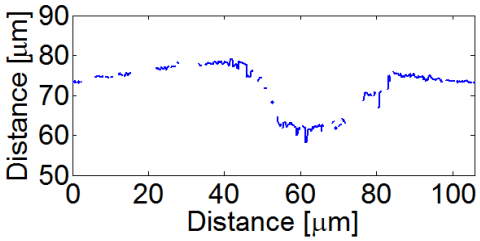
200 µs	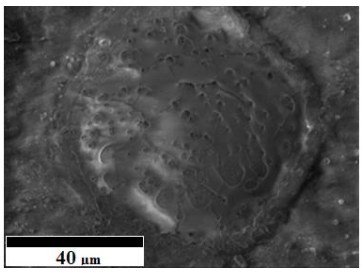	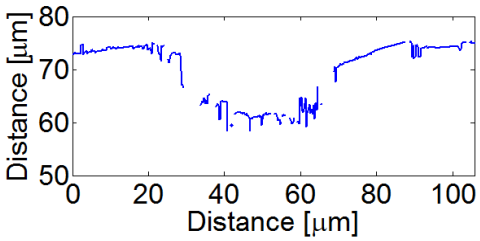

Figure 3.20 SEM micrographs and horizontal cross-sections of craters created with a single pulse ablation with fluence of 30 J/cm^2 for different pulse durations.

The difference in the processes between shorter (~10 μs) and longer (~200 μs) pulse lengths discussed previously (3.4.1) is clearly visible. Assuming a constant value of fluence for a shorter pulse duration (10 μs) irradiance is 20 times higher compared to longer pulses (200 μs). Hard dental tissue removal is based on an explosive water removal process which is a result of increased subsurface pressure that leads to an explosion and associated removal of material [42]. Moving to longer pulse durations decreases value of irradiance, and longer processing times lead to increased melting on the surface (Figure 3.20) which results in small cracks and crazing on the remelted surface. Moreover due to the longer pulse duration and longer processing times the area influenced by a single laser pulse is larger as opposed to shorter pulse durations (Figure 3.21) whilst maintaining the same spot size.

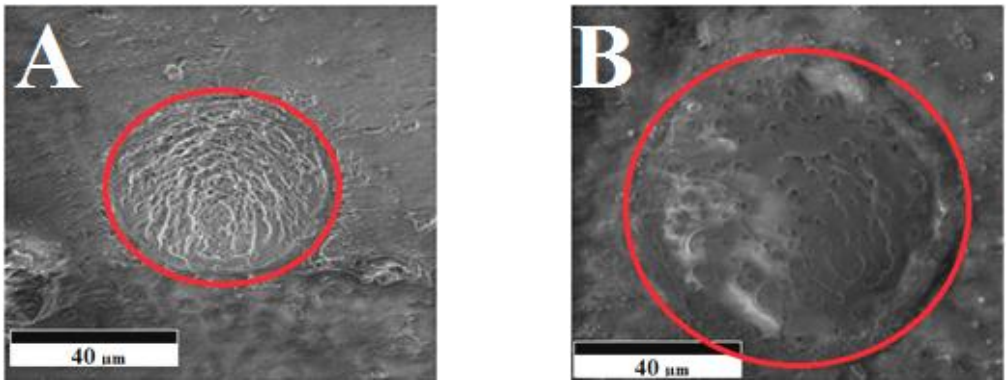

Figure 3.21 SEM micrographs of craters created with a single pulse ablation with fluence of 40 J/cm^2 with (A) 10 μs and (B) 200 μs with an area highlighted that was observed to be affected by the laser pulse. For 200 μs pulse duration the whole area within the red circle has a distinguished look of "glazed" melted area.

For craters created with pulses of duration between 10 and 20 μs there is almost no visible cracking introduced. There is some small surface crazing visible on the crater walls (not larger than 2-3 μm) that are a result of stresses from thermal shock established during rapid cooling and solidification of the tissue. For longer pulse durations (from 50 to 200 μs) more significant cracks are visible compared to those for shorter pulse durations. Figure 3.22 shows the bottom of the crater using a 200 μs single pulse irradiation with a fluence of 40 J/cm^2. Moreover for 200 μs pulse durations the affected area is covered with a melted layer of enamel (it's hard to notice on the figure, but a "glazed" melted area covers the whole processed area), which is not the case for shorter pulse duration (~10 μs) where is almost no melting present due to the difference in pulse duration. As a result cracks and crazing (a net of surface micro-cracks) is present in a remelted layer of the enamel over the whole area (annotated by red circle – 200 μs pulse duration). However,

no cracks were introduced to the tissue adjacent to the ablation site as, again, it is expected that the cracking is created by rapid solidification of the melted enamel. The small craters, visible on Figure 3.22, are created as the melted layer of enamel did not cover the whole processed area and it is possible to see the underlying layer of enamel.

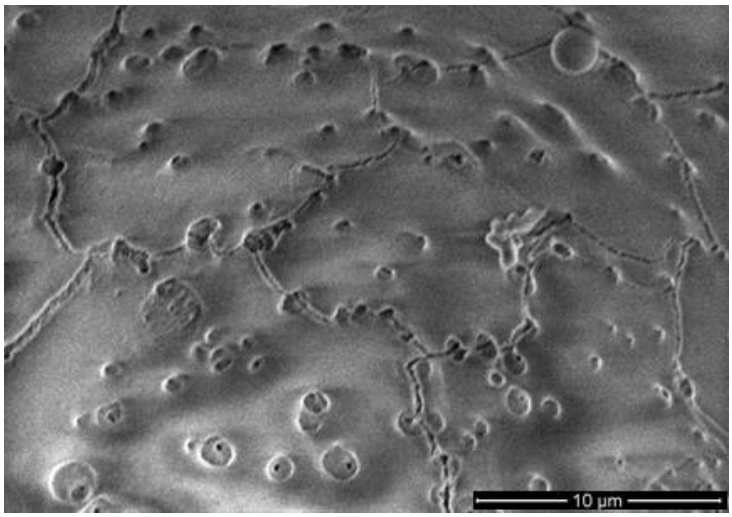

Figure 3.22 SEM micrograph of the crater bottom created with a single 200 µs pulses with a fluence of 40 J/cm^2. Cracks are clearly visible over the whole area.

These results confirm predictions from the model of Vila Verde [14-16] which, through mesoscopic scale simulation of the stresses introduced by CO_2 laser radiation to hard dental tissue, highlighted that pulse durations of ~10 µs should be best suited for removal of hard dental tissue as longer pulses ~100 µs could increase the temperature rise inside the pulpal chamber due to longer pulse durations and increased thermal diffusion. It is therefore possible to conclude that shorter pulses in the range of 10's of µs seem to be well suited for removal of the hard dental tissue. A 10 µs pulse leads to a shorter process duration, minimizes the amount of melted tissue and minimizes the heat affected zone.

Shorter pulse durations were not tested due to the limitations of the AOM. It would not be possible to reach required fluences (30-40 J/cm^2) for pulse durations in the range of 1 to 2 µs without exceeding the damage threshold for the AOM. Nevertheless, according to the simulation results presented by Vila Verde, pulses in the order of 0.5 to 1 µs will lead to cracking of the enamel [14-16]. The reason behind it is the increased value of increased transient stresses within the tissue itself, which is a direct effect of the higher peak irradiance. When a constant fluence is maintained, the peak irradiance is inversely proportional to the pulse duration – decreasing pulse duration by a factor of 10, increases value of peak irradiance by a factor of 10. Hence pulses in the order of 5 to 10 µs have optimal duration as they do not cause a lot of melting on the surface and do not introduce high values of transient stresses.

3.5. Ablation of dental tissue using out-of-focus pulses

When investigating a potential application in dentistry it is crucial to understand that the conditions in the surgery are far different and less easily controlled compared to those in a laboratory environment. This following experiment was focused on investigating the influence of beam defocussing on the ablation process. The effects of the beam not being ideally focused on the surface were studied in two cases where the beam is in focus beneath surface (i.e. a converging beam is incident on the surface) and where the focus is above the surface (i.e. a diverging beam is incident on the surface). These experiments were carried out with and without compensation for changes in fluence due to the change in spot size on the sample surface. Figure 3.23 shows diagram of the principle of focusing below, above and on the surface.

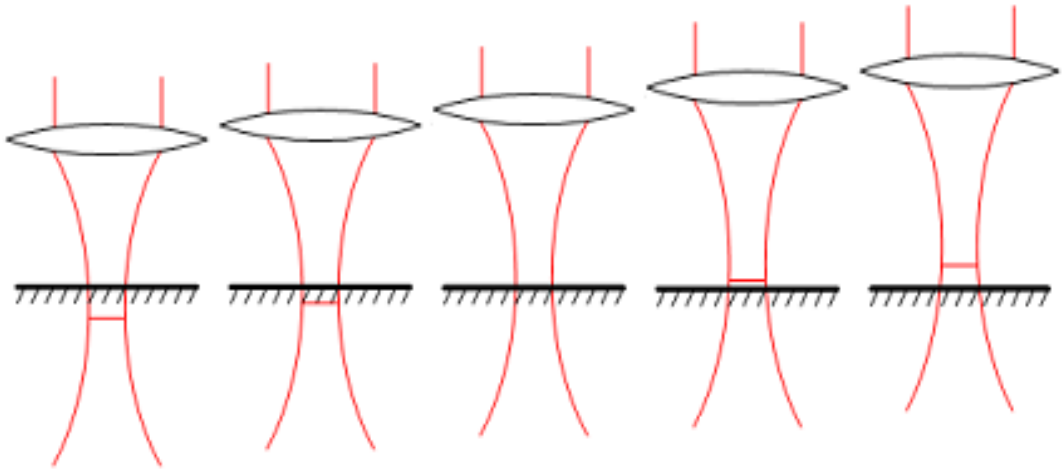

Focused below the surface | Focused on the surface | Focused above the surface

Figure 3.23 Schematic diagram of the principle of focusing below, above and on the surface.

3.5.1. Change in spot size whilst maintaining constant fluence at the surface

When considering a real life application of the process it is important to maintain a constant value of fluence on the surface to maintain similar processing parameters. Unfortunately that scenario might not be possible in clinical applications, e.g. when a dentist is in a control of the end face of the delivery system. Whenever the focus plane is below or above the surface an increased energy is required hence a device that would change the energy depending on the focal position would be necessary.

This experiment investigated machining with a divergent and convergent beam whilst maintaining a constant fluence on the surface. The laser beam has been focused 200 µm and 100 µm above the surface, focussed directly on the surface and focussed 200 µm and 100 µm below the surface. The difference in irradiated area on the sample surface

has been accounted for by increasing the pulse energy so that a consistent level of fluence at the surface (40 J/cm^2) is sustained for all of the experiments. Table 3.1 shows the change in the fluence at beam focus and beam diameters for the defocused beam positions, Figure 3.24 shows the dependence of the cavity depth as a function of the focus position and Figure 3.25 shows SEM micrographs of the resultant ablated craters.

Table 3.1 Fluence and beam diameter for out of focus positions

Focus Position	Fluence at beam focus required to maintain 40 J/cm^2 at surface [J/cm^2]	Pulse energy required to maintain 40 J/cm^2 at surface [mJ]	Spot diameter on surface	
			x [µm]	y [µm]
Focus on surface	40	0.46	35	42
Focus 100 µm from surface	100	1.08	53	65
Focus 200 µm from surface	233	2.99	89	107

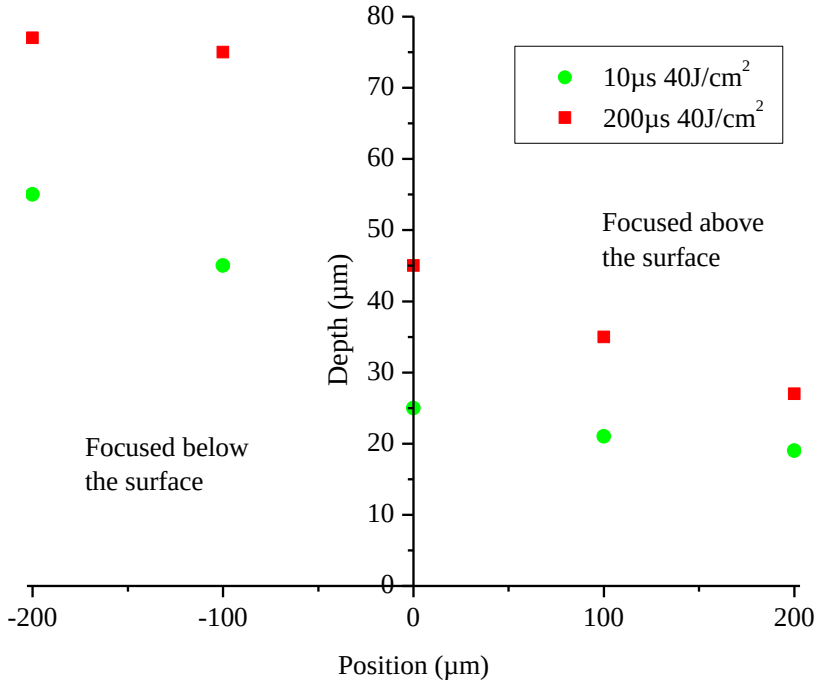

Figure 3.24 Cavity depth as a function of focus position whilst maintaining a constant fluence on the surface of 40 J/cm^2.

Pulse duration	Focus position	Pulse duration
10 µs		200 µs
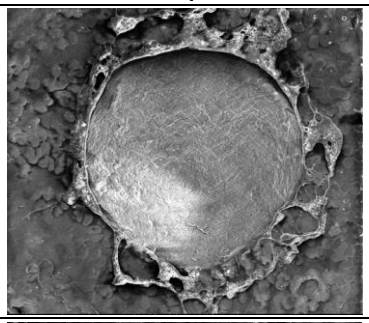	Focused 200 µm above the surface 100 µm	
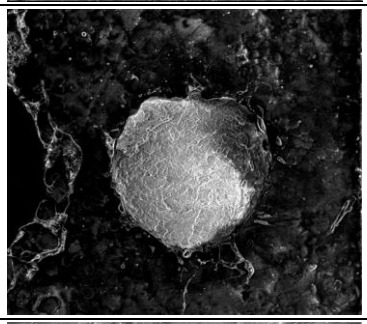	Focused 100 µm above the surface 100 µm	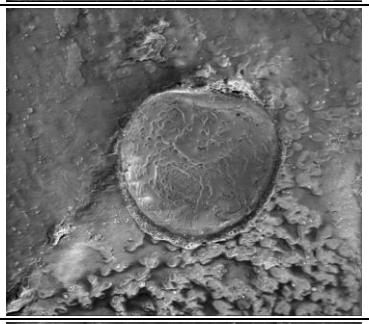
	Focused on the surface 100 µm	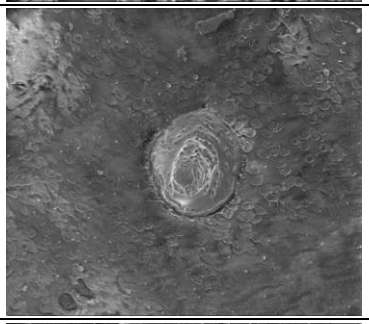
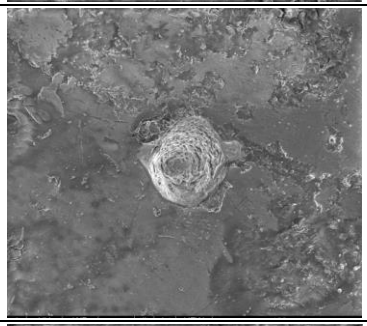	Focused 100 µm below the surface 100 µm	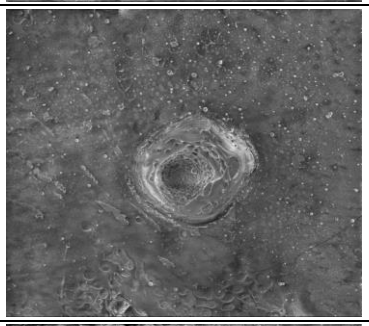
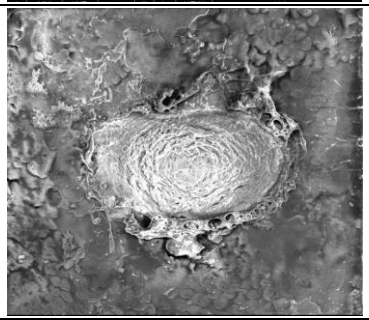	Focused 200 µm below the surface 100 µm	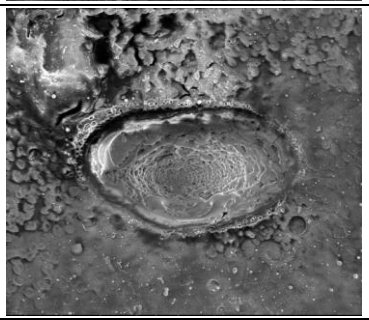

Figure 3.25 Craters created with single pulse ablation for 10 µs and 200 µs, with a fluence 40 J/cm^2 with the beam focus 200 µm above and below the surface, 100 µm above and below the surface and focused on the surface.

Laser machining with a converging beam into the bulk produced narrower and deeper cavities and machining with a diverging beam into the bulk produced wider and shallower cavities irrespective of the value of fluence that is on the surface. With a converging beam, i.e. a beam focus below the surface the maximum value of fluence/irradiance is reached below the surface and focused spot size is smaller than the beam radius on the surface (Figure 3.23). When beam is focussed 100 µm below the surface with a value of fluence on the surface of 40 J/cm^2 value of fluence 100 µm below the surface is ~94 J/cm^2. On the other hand when machining with a diverging beam the value of the fluence/ irradiance will have it maximum value on the surface and as the beam diverges into the sample the value of fluence or irradiance decreases but the area of interaction increases (Figure 3.23). When beam is focussed 100 µm above the surface with a value of fluence on the surface of 40 J/cm^2 the value of the fluence 100 µm below the surface is ~15 J/cm^2. As a result cavities created with diverging beam (focus above the surface) are wider and shallower compared to those created with the converging beam (focus below the surface).

Figure 3.26 shows the ablation efficiency as a function of beam focus position. The volume of the removed tissue was calculated as an approximation of a Gaussian cone with an elliptical base as discussed in Section 3.4.1. Laser machining with a converging beam leads to a deeper cavity due to the nature of the converging beam having its highest value of fluence. On the other hand machining with a diverging beam creates a shallower, but significantly wider.

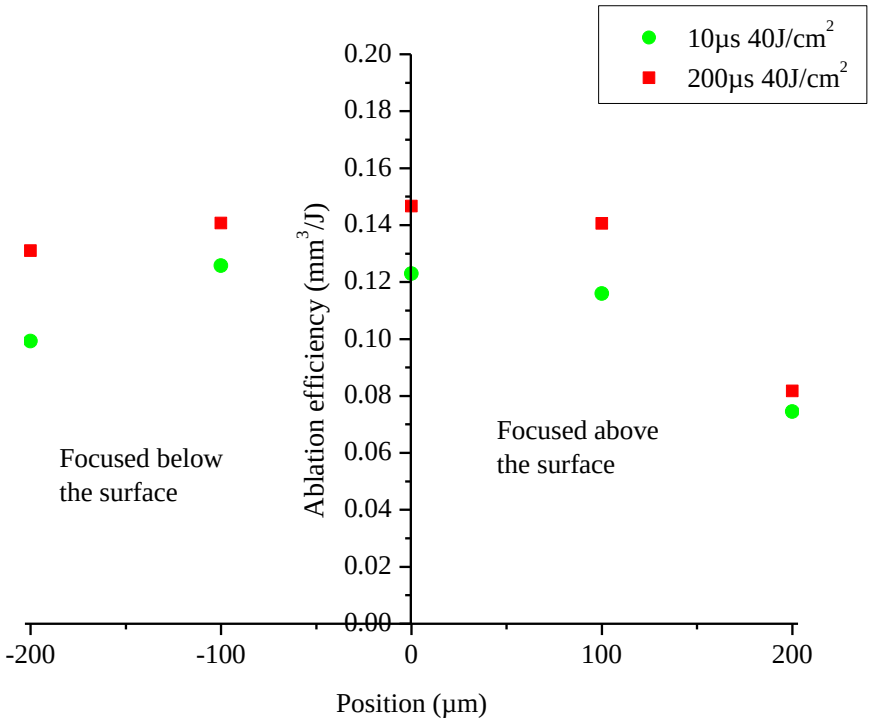

Figure 3.26 Ablation efficiency as a function of focus position whilst maintaining a constant fluence on the surface of 40 J/cm^2.

Machining with a divergent and convergent beam is less efficient, than with a focussed beam. The created cavities have a larger volume but it is necessary to use a higher value of fluence at beam focus (hence a higher overall pulse energy) to compensate for the larger size of the beam on the surface. Whenever the beam is focused ~200 μm below the surface the ablation efficiency is lower, up to ~23% for 10 μs and 11% for 200 μs pulse duration. When the beam is focused ~100 μm below the surface the decrease in ablation efficiency is ~2% for 10 μs and 4% for 200 μs pulse duration. On the other when the beam is focused ~200 μm above the surface the ablation efficiency is lower, up to ~42% for 10 μs and 55% for 200 μs pulse duration and when the beam is focused ~100 μm above the surface the loses are ~5% for 10 μs and 4% for 200 μs pulse duration.

The likely consequence for a real life procedure (i.e that the laser beam will not be ideally focused on the surface at all times) is that process efficiency is going to vary. If the laser can be focused within ±100 μm the efficiency drop is relatively low, up to 5%. The different shape (shallower-wider and deeper-narrower) of the cavities when machining out of focus won't have too much of the influence when removing larger areas as multiple laser pulses will be used. One of the ways to decrease influence if the tapering on to the process is to use longer focal length, which would provide longer Rayleigh range. Moreover a device that would control the distance of the end face of the device to the surface based on a constant feedback loop and quickly changing focus can be created. Additional such a feedback loop could be used to measure, in real time, the distance from the target and adjust the power of the laser accordingly. Alternatively having a device that fixed the position of the beam focus (to within 100 μs) would be beneficial.

3.5.2. Change in spot size without maintaining constant fluence

A similar experiment was carried out for machining with a converging and diverging beam but without having any compensation for the reduction in fluence due to the changing beam diameter. Every crater in this experiment has been created with a single pulse ablation and an energy of 0.46 mJ (equivalent to a fluence of 40 J/cm^2 for the focussed spot). This results in a lower fluences at the surface for the defocussed beams as specified in Table 3.2. Figure 3.27 shows the crater depth depending on the offset from focal position. Figure 3.28 shows SEM micrographs of craters created in the experiment. All of the cavities were created with fluence of 40 J/cm^2.

Table 3.2 Actual fluence on the surface for different beam size at different focus positions.

Focus position	Fluence in beam focus	Actual fluence on the surface
In focus	40 J/cm^2	40 J/cm^2
Focus 100 µm from the surface		17 J/cm^2
Focus 200 µm from the surface		6 J/cm^2

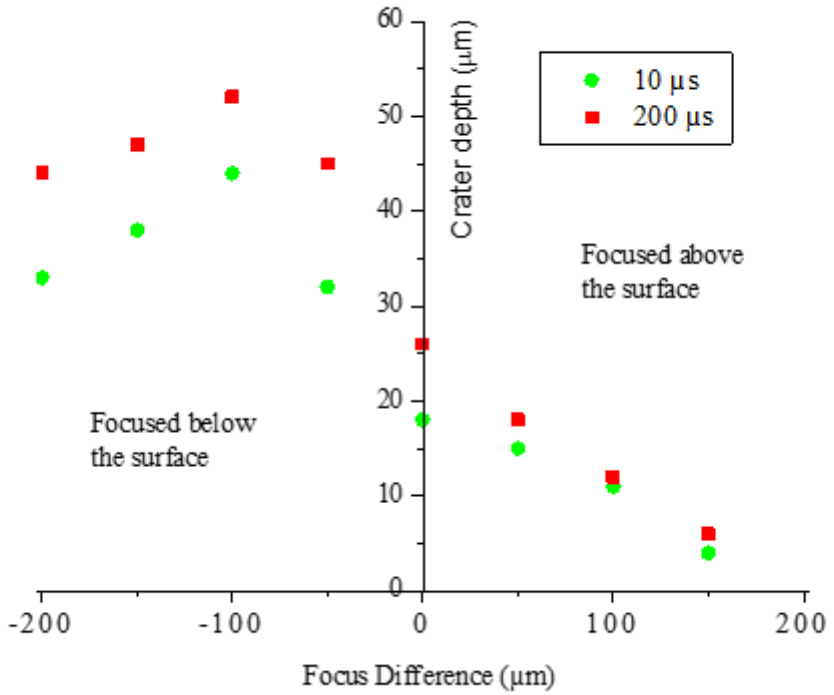

Figure 3.27 Cavity depth as a function of focus position for machining with converging and diverging beam for a pulse energy of 0.46 mJ (i.e. a focussed spot fluence of 40 J/cm^2).

Pulse duration	Focus position	Pulse duration
10 µs		200 µs
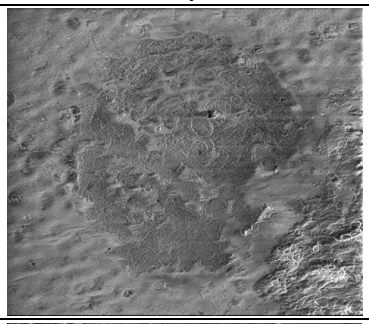	Focused 150 µm above the surface 50 µm	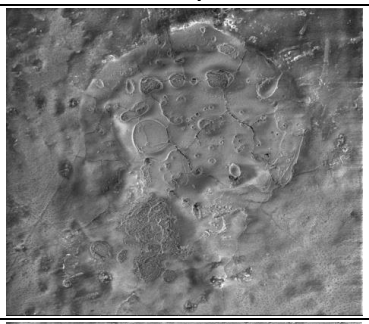
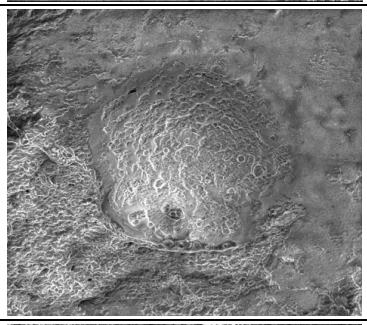	Focused 100 µm above the surface 50 µm	
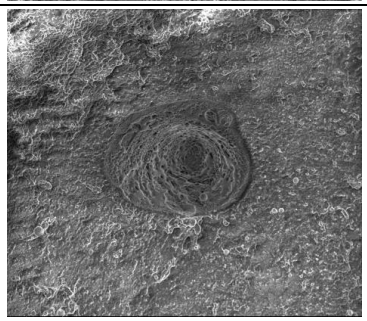	Focused on the surface 50 µm	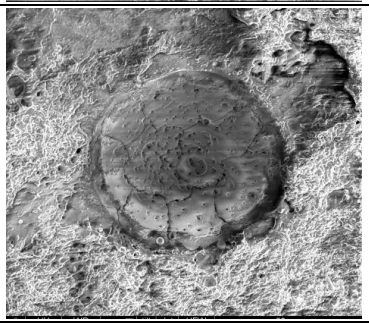
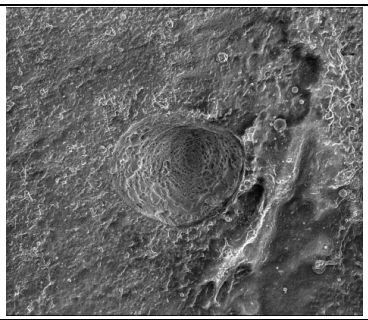	Focused 100 µm below the surface 50 µm	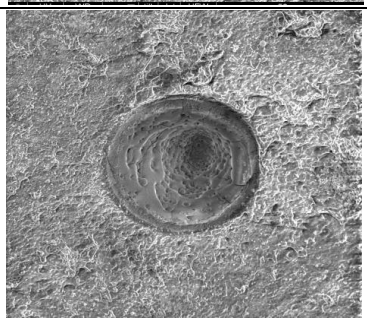
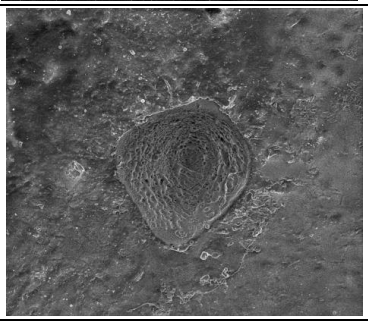	Focused 200 µm below the surface 50 µm	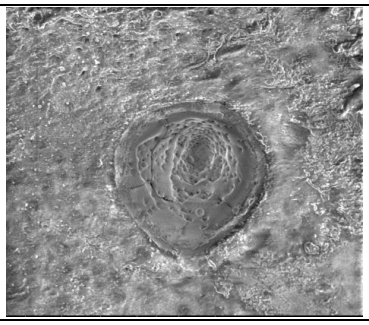

Figure 3.28 Craters created with single pulse ablation for 10 µs and 200 µs, with pulse energy of 0.46 mJ (i.e. fluence of 40 J/cm^2 at beam focus) with the beam focus 50, 100, 150 and 200 µm below the surface and 50,100 and 150 µm above the surface.

When focusing slightly below the surface the craters are deeper which is a result of the fluence on the surface being above laser removal threshold for enamel even for higher spot size. Maximum depth is reached when laser beam is focused ~100 μm below the surface. On the other hand whenever a beam is focused above the surface the created cavities are much wider but also much shallower due to the decreased fluence whenever laser beam is focused above the surface. When considering real life applications it is always beneficial to have increased ablation efficiency and focusing below the surface does provided that, but only when the fluence is significantly higher than the threshold value for ablation of the tissue. However, as discussed above this would be hard to ensure in a practical surgical application. The shape of the single cavity is not too important, because when considering multiple pulse ablation the final shape of the bigger cavity relies much more on parameters like repetition rate, or spot/line separation rather than the shape of a single cavity.

Again, this evidence supports the fact that for a practical device either some robust feedback system would need to be implemented that varied the laser energy, on-the-fly, according to a measurement of the stand-off from the tooth. Alternatively a device that would be mounted directly onto the tooth with a fixed focal plane, or one that could be controlled via software, would be needed.

3.6. Multiple pulse ablation

Single pulse laser ablation experiments provide a starting point when investigating the feasibility of a new laser machining process. It is possible to accurately evaluate the influence of the pulse on the ablation site and the adjacent tissue. However, for the application of drilling dental enamel, where it is required to create deeper craters than a single shot can produce and to remove higher volumes of tissue, there is a need to investigate multi pulse laser ablation.

3.6.1. Percussion laser drilling

The first type of multi pulse laser machining investigated was percussion drilling. This is a simpler approach, compared to trepanned laser drilling discussed later, as the position in X-Y planes stays constant and only the position of the focus may be changed throughout the process. Two different approaches have been investigated. Firstly, percussion drilling without adjusting focus, which results in each pulse after the first one being defocused from the surface and, secondly adjusting the focus after each pulse. For the second process the plane was lowered 20 μm after each pulse, which is the average depth of a single pulse ablation for a fluence of 40 J/cm^2 (see section 3.4.1). Figure 3.29 shows the crater depth as a function of number of pulses for ablation with fluence of 40J /cm^2 for the percussion drilling processes with and without focus adjustment.

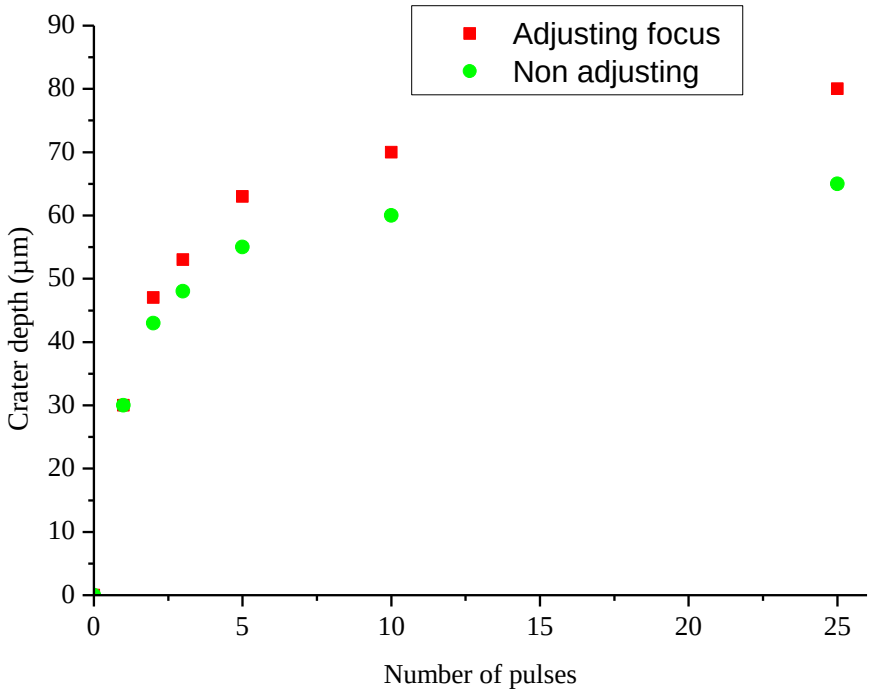

Figure 3.29 Crater depth as a function of the pulse number for percussion drilling with and without adjusting focus. For the process with focus adjustment the focus position was translated vertically down by 20 μm after each pulse.

Focus adjusted by 20 µm after each pulse *Focus plane approximately on the bottom surface of the crater*	Number of pulses	Focused unchanged *Focus plane always on the surface of enamel*
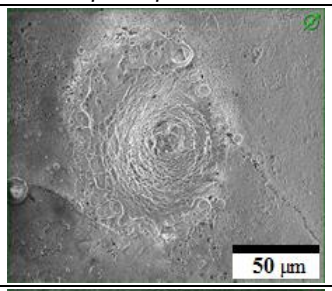	1	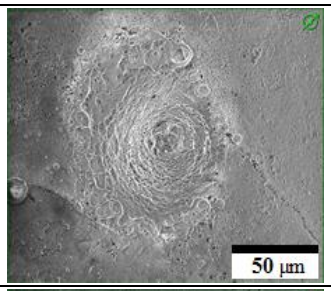
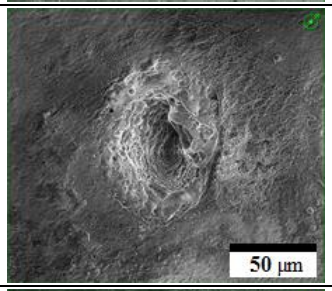	2	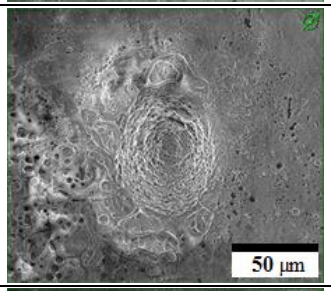
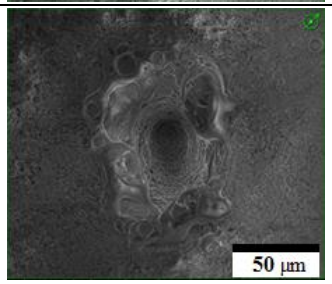	3	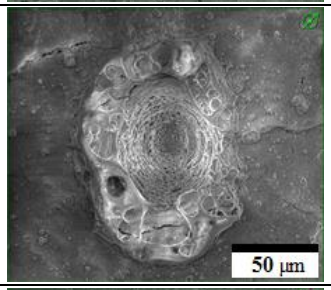
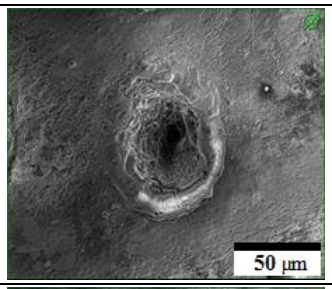	5	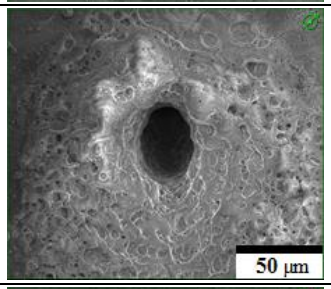
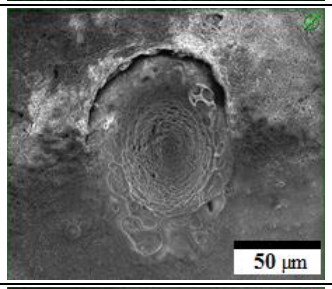	10	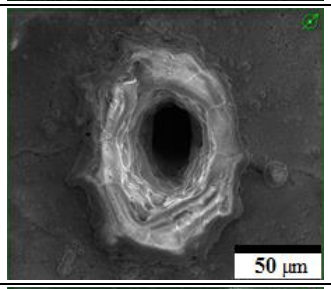
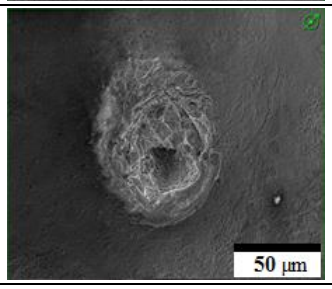	25	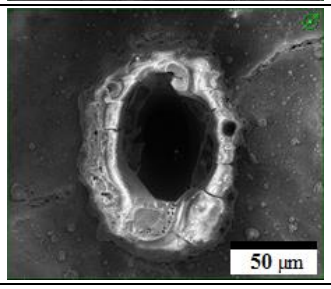

Figure 3.30 Figure shows SEM micrographs of craters created with either 1, 2, 3, 5, 10 or 25 laser pulses with (left) translation of the focus by 20 µm after each pulse and (right) without adjusting focus and the laser beam focused on the surface.

From Figure 3.27 it can be seen that for percussion drilling without adjusting focus the depth does not exceed ~65 μm irrespective of the number of pulses. Also, from Figure 3.27, when adjusting focus between pulses the depth limit is ~ 85 μm. which is is around 10-20% higher than the un-adjusted case. The taper angle of the cavity arises due to the Gaussian nature of the beam. The tapering of the crater during percussion drilling results in part of the subsequent pulses being incident on a sloped wall (as opposed to a flat surface) and hence the efficiency of the process is reduced. The maximum crater depth can be increased by implementing a flat top beam. The efficiency of each pulse is lower for each consecutive pulse, an effect that is significant after the fifth pulse (Figure 3.27). That is why experiment was limited only to 25 single pulses as the beam was defocused, which led to a value of fluence below the threshold value necessary for the ablation to occur.

From these initial experiments it was clear that fixed (in x and y) percussion drilling is not recommended because using this approach it is not possible to achieve the necessary depth of the crater (1-2 mm) needed to reach lower parts of the hard dental tissue. To try and solve those issues a different approach for drilling is necessary: trepanned laser drilling. Trepanned laser drilling will allow wider cavities which in turn allows drilling deeper into the tissue as the influence of a tapering would be minimized.

3.6.2. Trepanned laser drilling

To remove larger volumes of enamel a trepanned laser drilling process was investigated. Only initial, relatively simple tests were carried out due to the limitation of the system which did not have a galvanometer scan head. In this set-up the sample was moved after each pulse in the X-Y plane by motorized translation stages. The maximum time between pulses was up to 1 second, but it was different for each step and depended on the distance between consecutive spots. Such a large delay between pulses results in the energy deposited by one pulse was diffused before the subsequent pulse arrives and there was no thermal energy left after the first pulse. Initial tests of trepanned laser drilling of circular and square cavity were made using LabView code to control and synchronise the laser and the stages.

Figure 3.32 shows horizontal cross-sections and SEM micrographs of trepanned, square laser drilling patterns. All of the experiments were carried out with a pulse duration of 10 μs, fluence of 30 J/cm^2 with a focused spot size of 35 μm by 42 μm (same as in previous experiments, see Figure 3.6) and using different spot separations of 5, 10 and 20

µm. The scanning pattern is constructed of 4 rows and each one consists of 4 spots (Figure 3.31). When using a spot separation of 5 µm the created cavity is very narrow (< 50 µm) and, as seen for the percussion drilling, the maximum depth reached is limited by the taper of the walls. Consequently a larger spot separation of 10 µm was tested and the created cavity was shallower, but was flatter, than the cavity created with a 5 µm separation. Furthermore a larger spot separation of 20 µm was tested and produced a cavity that had the most uniform bottom surface out of all the tested cases.

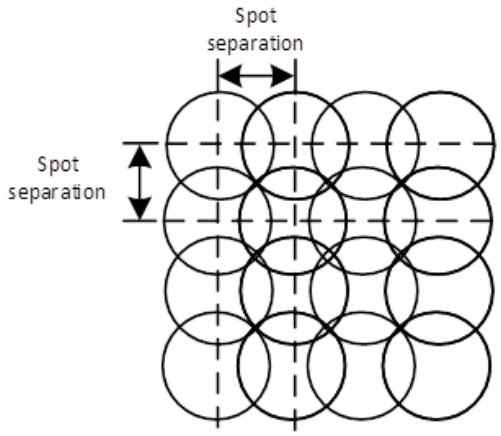

Figure 3.31 Scanning pattern used for square shaped trepanned laser drilling. One pulse per spot.

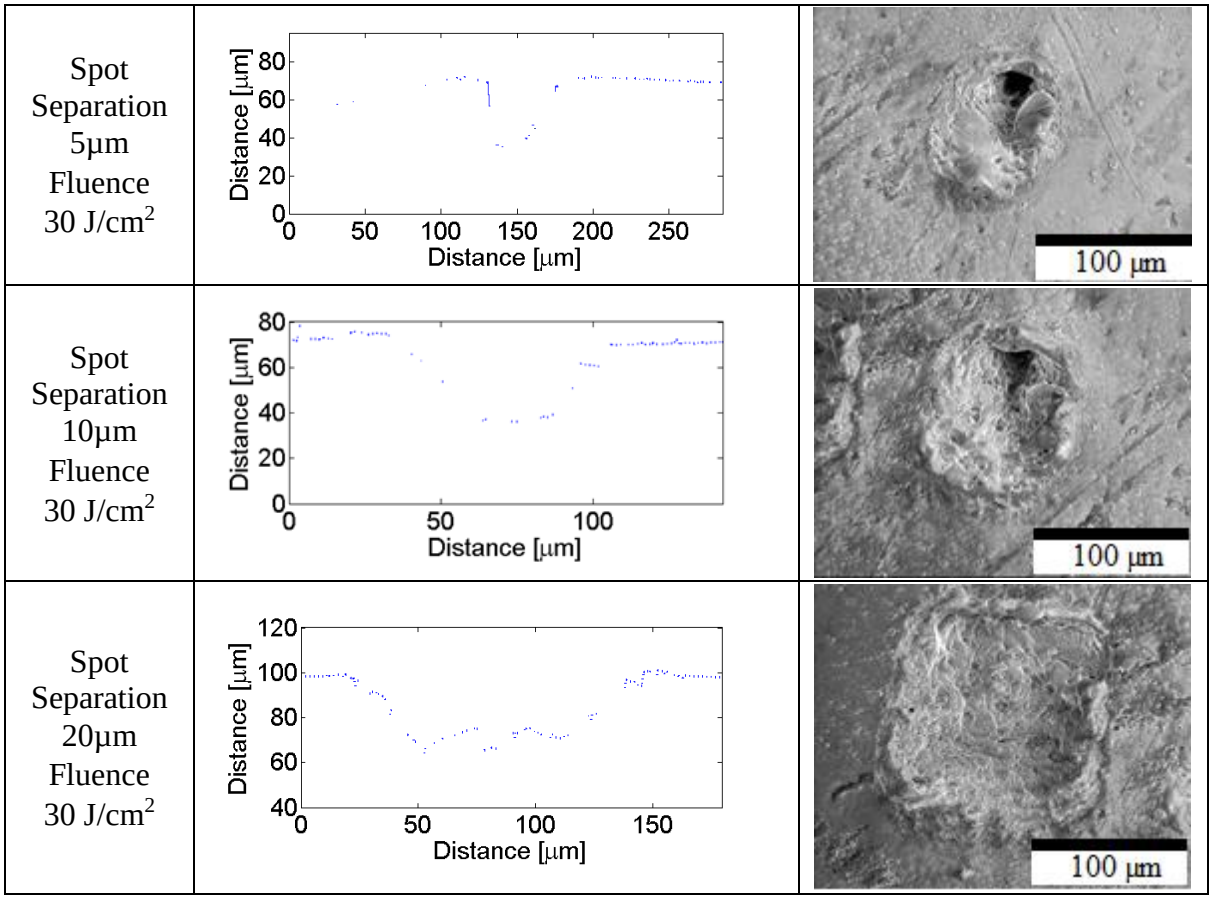

Figure 3.32 SEM micrographs and cross-sections through the centre of square cavities created using trepanned laser drilling with a fluence of 30 J/cm^2.

As an alternative scanning strategy, to a squared trepanned scanning pattern, a circular drilling pattern consisting of a centrally placed spot and a ring constructed of six evenly spread spots around it was implemented. Figure 3.33 shows the pattern with spot separation described on it.

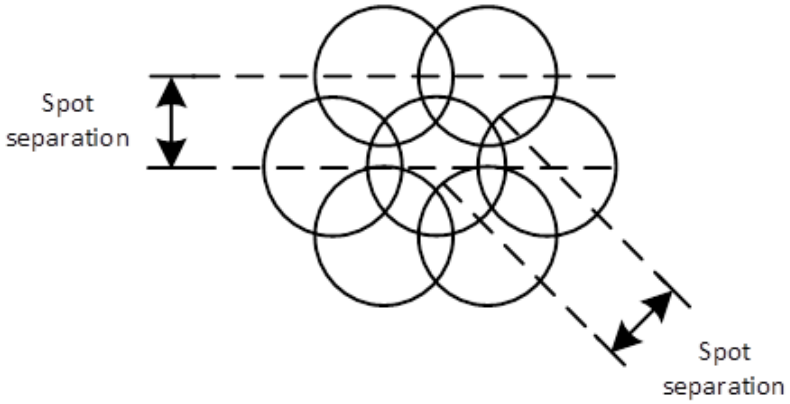

Figure 3.33 Scanning pattern used for circular shaped trepanned laser drilling.

Figure 3.34 shows the initial results for circular trepanned laser drilling. The circular pattern was repeated 2, 3 and 4 times. Each additional scanning pattern has led to increased depth of the crater. Unfortunately surface profilometers were not able to measure the depth as the created cavities were too deep and the amount of light reflected off the bottom was not sufficient for accurate measurement

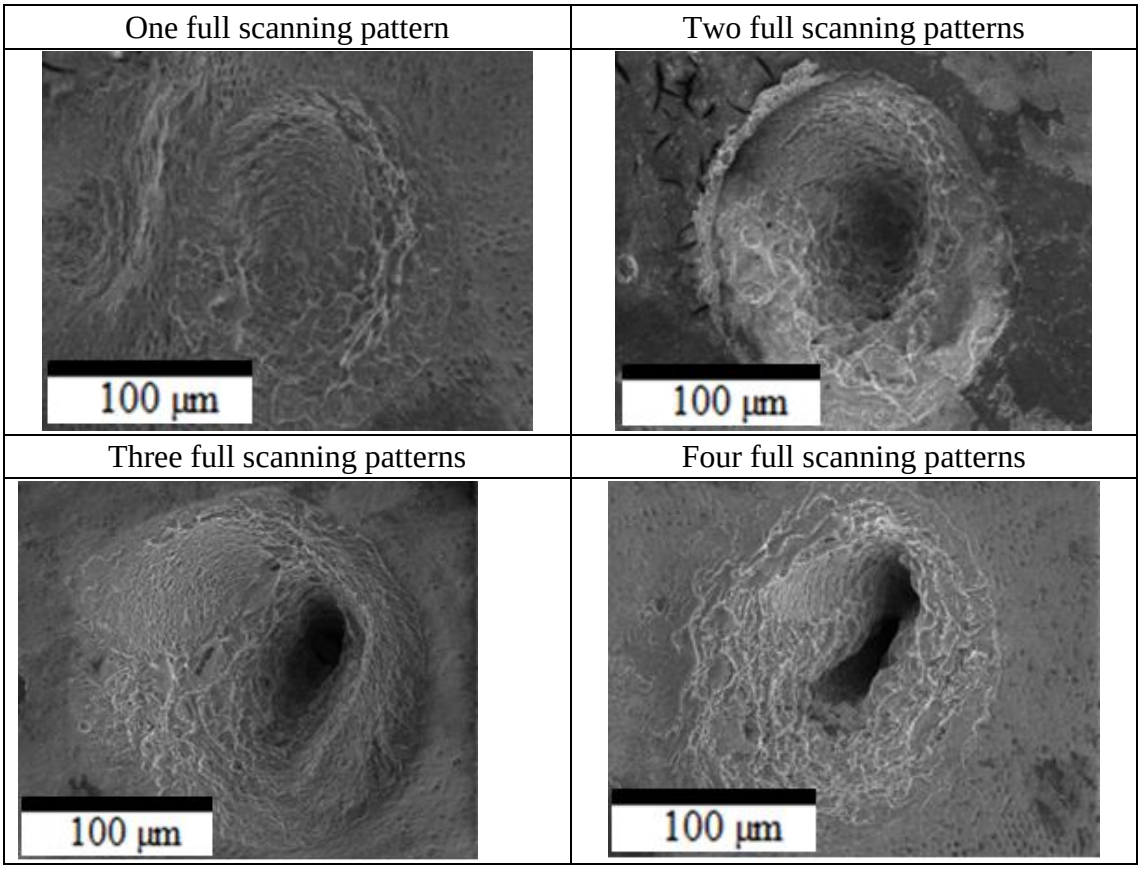

Figure 3.34 SEM micrographs of trepanned laser drilling using the circular scanning strategy. The focused spot diameter is 35 µm by 42 µm and the fluence is 30 J/cm^2.

It is hard to investigate and fully determine parameters that are best suited for trepanned laser drilling without the use of galvanometer scanner, which would allow to easily change settings and would allow for much shorter times between consecutive pulses. The combination of 9.3 µm CO_2 laser and galvanometer scanning head to remove dental tissue has been successfully presented by Fried et al. [17, 18]. Nevertheless initial results showed that 10.6 µm CO_2 laser based trepanned laser drilling could be used to create portal of entry through which a photo-activated antibacterial drug [125] targeting carious underlying tissue could be administrated. Moreover, laser radiation is capable of creating craters that are relatively narrow (~300 µm) minimizing loses of healthy dental tissue compared to using traditional dental burs which are restricted to larger diameters (~1 mm) [29].

3.7. Influence of using a water spray

In this section a basic understanding of the influence of the use of water spray on the depth of the crater created with a single pulse laser ablation is presented. A series of different pulse energies (10 – 60 J/cm^2 fluences, 10 µs pulse duration) are irradiated on a clean tooth surface as well as a surface that has a layer of water sprayed on just before the pulse. Figure 3.35 shows the maximum crater depth as a function of fluence with and without a water spray.

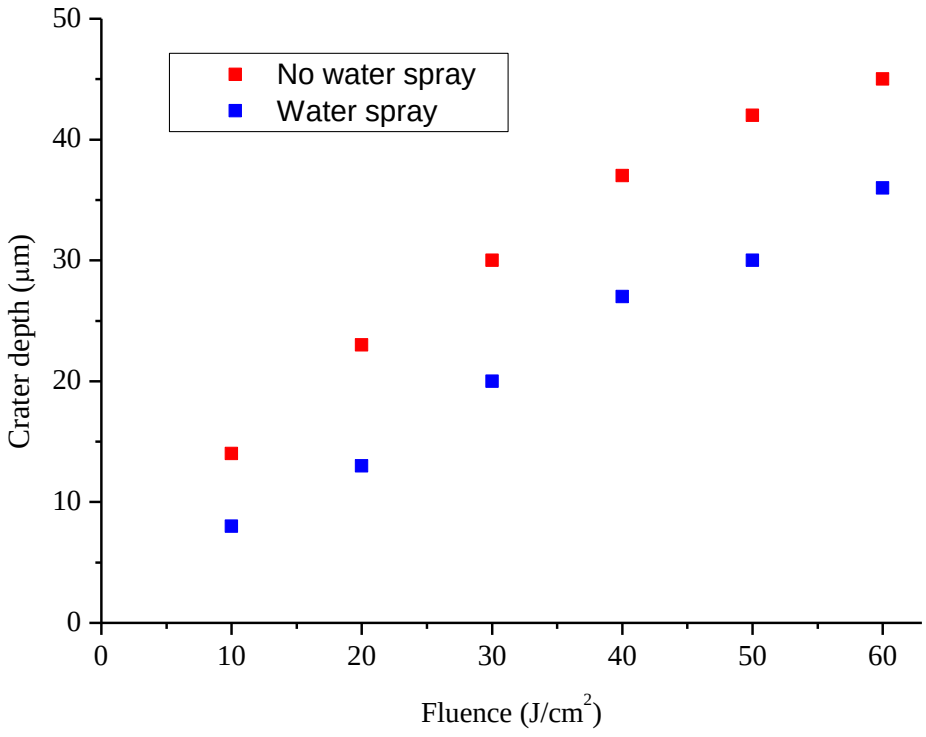

Figure 3.35 Cavity depth as a function of fluence with and without water spray present. Pulse duration of 10 µs.

The use of a water spray appears to shield the enamel as, whenever a water spray is used, the created cavity is shallower by 10 µm on average. This is likely due to the high absorption of water to 10.6 µm CO_2 laser radiation [131]. The use of water spray decreases the efficiency of the whole process however it may help to reduce the overall temperature rise from the process. This would reduce the risk of necrosis of pulpal tissue and may help to reduce thermomechanical damage in the tissue adjacent of the ablation site.

No water spray present	Fluence [J/cm^2]	Water spray present
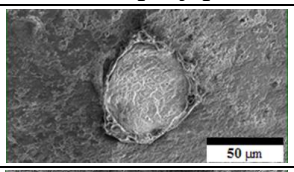	10	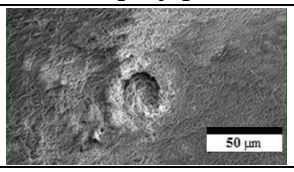
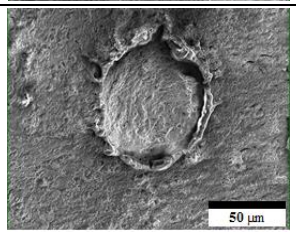	20	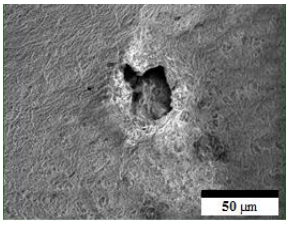
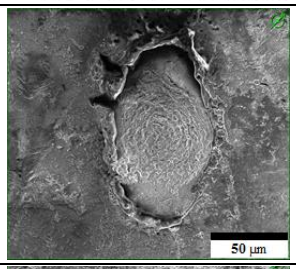	30	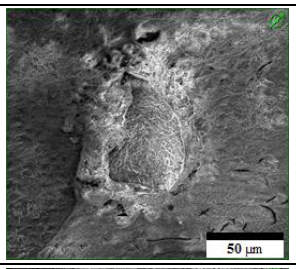
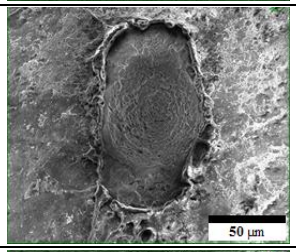	40	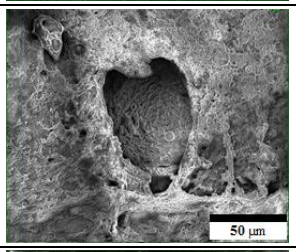
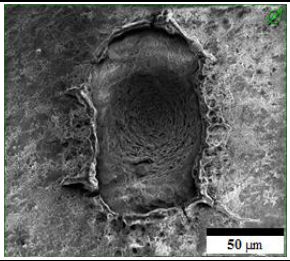	50	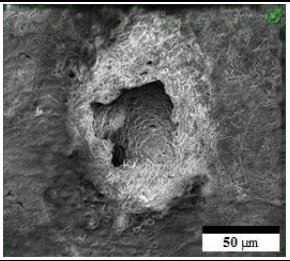
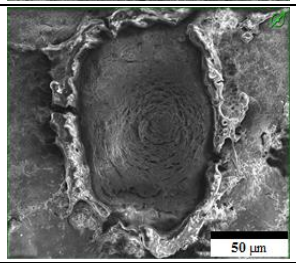	60	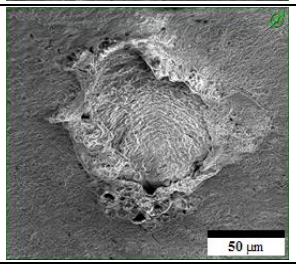

Figure 3.36 SEM micrographs of cavities created with single pulse ablation with 10 µs pulses with different laser fluences with and without the application of the water spray.

3.8. Temperature rise during laser ablation of dental enamel

When investing the feasibility of using laser pulses to remove both soft and hard biological tissue it is important to investigate how the temperature rises during laser machining. In dental application a temperature rise of 5.5 ^{o}C in the pulpal chamber could cause a necrosis of soft tissue [29]. The use of water spray might be essential to prevent peripheral thermomechanical damage and prevent tissue from severe dehydration.

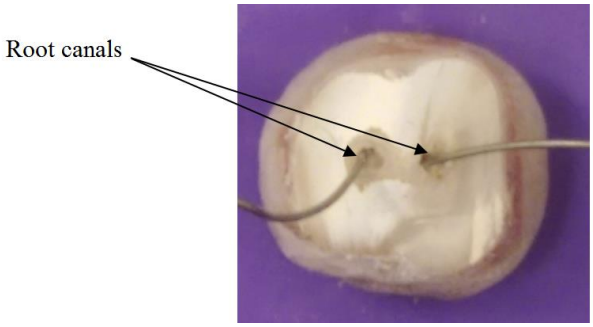

Figure 3.37 Picture of the molar tooth with the roots cut off and thermocouples placed in the pulpal chamber. Due to cut off roots access to root canals was available.

To investigate the temperature rise in the pulpal chamber during laser machining thermocouples were placed into the pulpal chamber. To allow direct access to the pulpal chamber roots were cut off (Figure 3.33). To increase thermal contact the pulpal chamber was filled with a thermal compound (HTS Silicone Heat Transfer Compound, 0.9 W/m·K) before thermocouples were placed. A third thermocouple was placed on the side of the tooth close to the ablation site. Figure 3.38 shows the experimental setup and placement of thermocouples. The thermocouples used in this experiment were type J and all of the data was acquired through a National Instruments Data Acquisition (DAQ) and recorded on a computer.

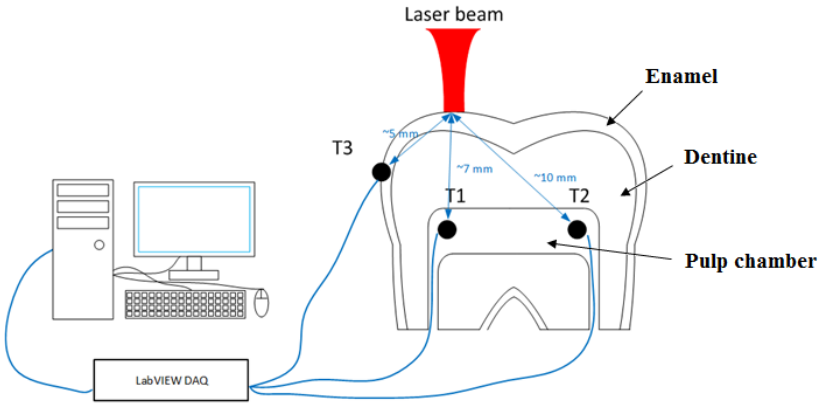

Figure 3.38 Experimental setup used to measure temperature rises in the pulpal chamber during laser processing highlighting placement of the three thermocouples (T1, T2, T3) used. Average thicknesses taken from [132, 133]

3.8.1. Extreme case scenario

The first experiment was created to investigate the thermal response of the enamel and dentine in an extreme situation. The laser beam was focused on the surface of the sample and it was continuously irradiated over the span of 5 minutes. Three laser repetition rates were tested - 20, 100 and 250 Hz. The fluence used in this experiment was 40 J/cm^2 and focused spot sized used was 91 μm by 74 μm (see Figure 3.7) and results are shown in figure 3.39.

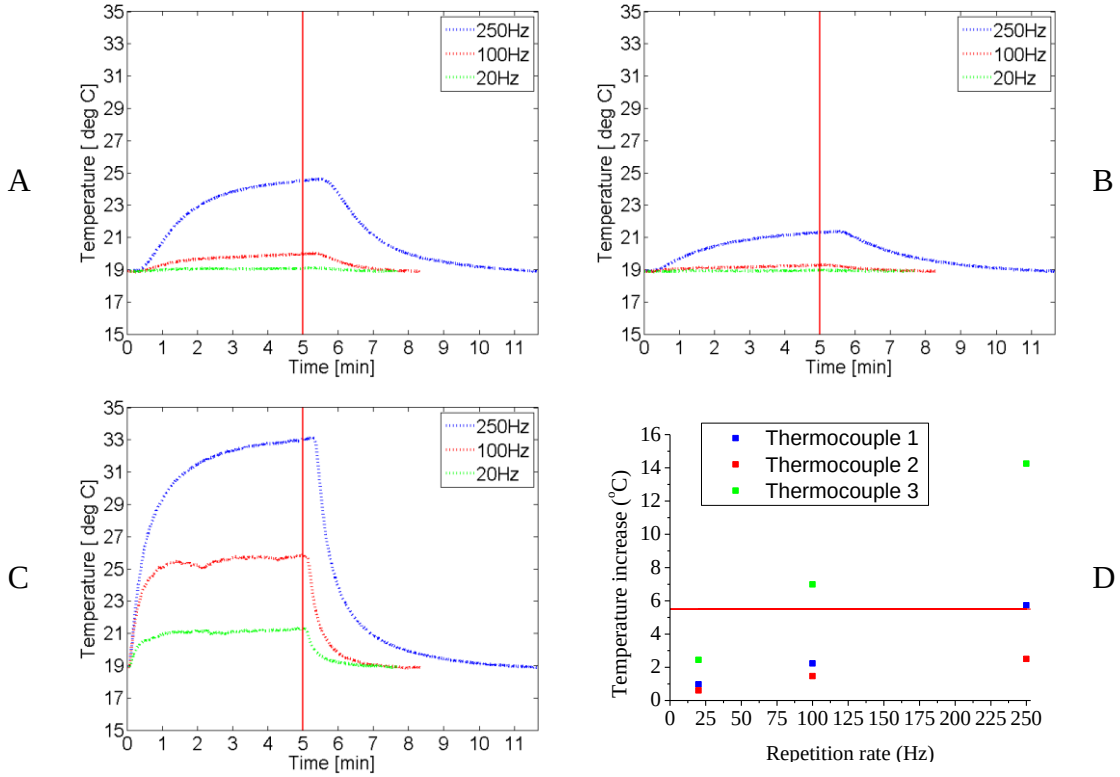

Figure 3.39 Temperature at three different positions (A – thermocouple 1, B- thermocouple 2, C – thermocouple 3) as a function of time for three different repetition rates 20, 100 and 250 Hz. Figure D shows the maximum temperature rise in all of the measurements. The vertical red lines represent when the laser has finished emitting and the horizontal red line in D represents the temperature rise above which necrosis of tissue can occur. No water spray was present.

The maximum temperature rise for the thermocouple T1, placed in the pulpal chamber directly below the laser beam, is 5.73°C for 250 Hz, 1.65°C for 100 Hz and 0.97°C for 20 Hz. Machining with the repetition rate of 250Hz raises the temperature in the pulpal chamber by a critical 5.73 °C. A rise of temperature in that regime is very likely to start to induce necrosis in the tissue in the pulpal chamber thus this repetition rate is too high to be used in clinical treatment without using a water spray. The maximum temperature recorded by T1 is higher than one reached by T2 due to a shorter distance to

the ablation site. As the distance between T2 and ablation site is higher, the increased thermal energy is more diffused before it reaches the thermocouple.

The temperature rise for the thermocouple placed through the second root, T2, is 2.5^{o}C for 250 Hz, 1.47 ^{o}C for 100 Hz and 0.61^{o}C for 20 Hz. All of the temperature rises are below the necrosis threshold for the tissue in the pulpal chamber. The temperature rise recorded by the thermocouple placed on the side of the samples, T3, is 14.25 ^{o}C for 250 Hz, 6.99 ^{o}C for 100Hz and 2.45 ^{o}C for 20 Hz. Figure 3.39 D shows the maximum temperature rise as a function of repetition rate used. The maximum temperature rise has a linear trend when increasing repetition rate which therefore allows scaling back of the temperature by adjusting the laser repetition rate. The maximum safe temperature on the surface can increase by more than 5.5 ^{o}C as is a threshold is for a living tissue inside the pulpal chamber and melting temperature for enamel is ~1200 ^{o}C [29]. As a result an increase in the range of 20-30 ^{o}C is safe for the enamel itself.

After the laser has stopped irradiating on the surface of the sample a temperature increase is observed for some time. This is the result of thermocouples being placed a certain distance from the centre of the ablation site. Accordingly the longest time (up to 40 seconds) where an increase in temperature is recorded is for T2 placed furthest away from the ablation site. This is the direct result of low thermal conductivity ~0.92 [W/(m·K)] [36] of the enamel. The shortest distance to the ablation site is for T3 which has the highest recorded temperature increase. Moreover T3 will cool down the quickest as it is placed on the side of the tooth exposed to ambient conditions.

Similar experiments were carried out with the use of water spray. Figure 3.40 shows the placement of all thermocouples and the direction of the water spray. The results of the experiment are shown in Figure 3.41.

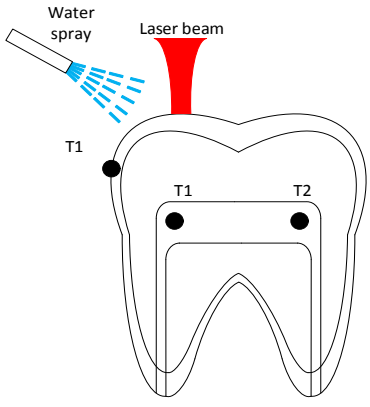

Figure 3.40 Experimental setup with water spray present highlighting placement of thermocouples used and the direction of the water spray.

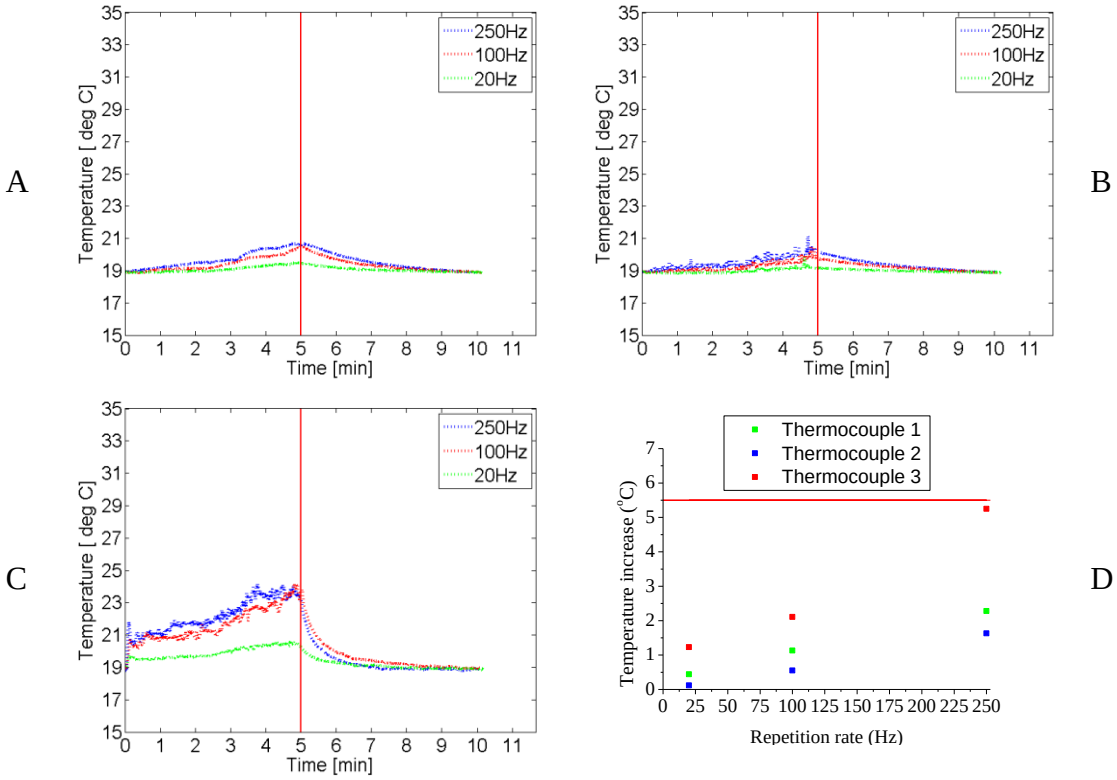

Figure 3.41 Temperature at three different positions (A – thermocouple 1, B- thermocouple 2, C – thermocouple 3 – position can be seen on Figure 3.40) as a function of time for three different repetition rates 20, 100 and 250 Hz. Figure D shows the maximum temperature raise in all of the measurements. The vertical red lines represent when the laser has finished emitting and the horizontal red line in D represents the temperature rise above which necrosis of tissue can occur. Water spray is present.

The temperature rise registered by the T1 is 2.28°C for 250 Hz, 1.13 °C for 100 Hz and 0.61°C for 20Hz. All of these temperature increases are well below the critical threshold of 5.5 °C [29]. The temperature increases for T2 at frequencies of 250 Hz, 100 Hz and 20 Hz are 1.63 °C, 0.55 °C and 0.12 °C respectively. Again, as expected the temperature registered by the T2 is lower. Temperature rises recorded by the T3 are 5.25 °C, 2.11 °C and 1.23 °C for 250 Hz, 100 Hz and 20 Hz.

For the previous measurement, without water spray, the temperature continues to increase for up to 40 seconds after the laser has been turned off due to the distance between the ablation site and thermocouples. This is not the case when there is a water spray present as it continuously cools the surface which decreases the amount of heat that diffuses deeper into the sample. The surface temperature falls faster, when compared to the experiment without water spray, and the temperature gradient in the area close to the surface is much smaller which prevents energy from transferring rapidly into the sample.

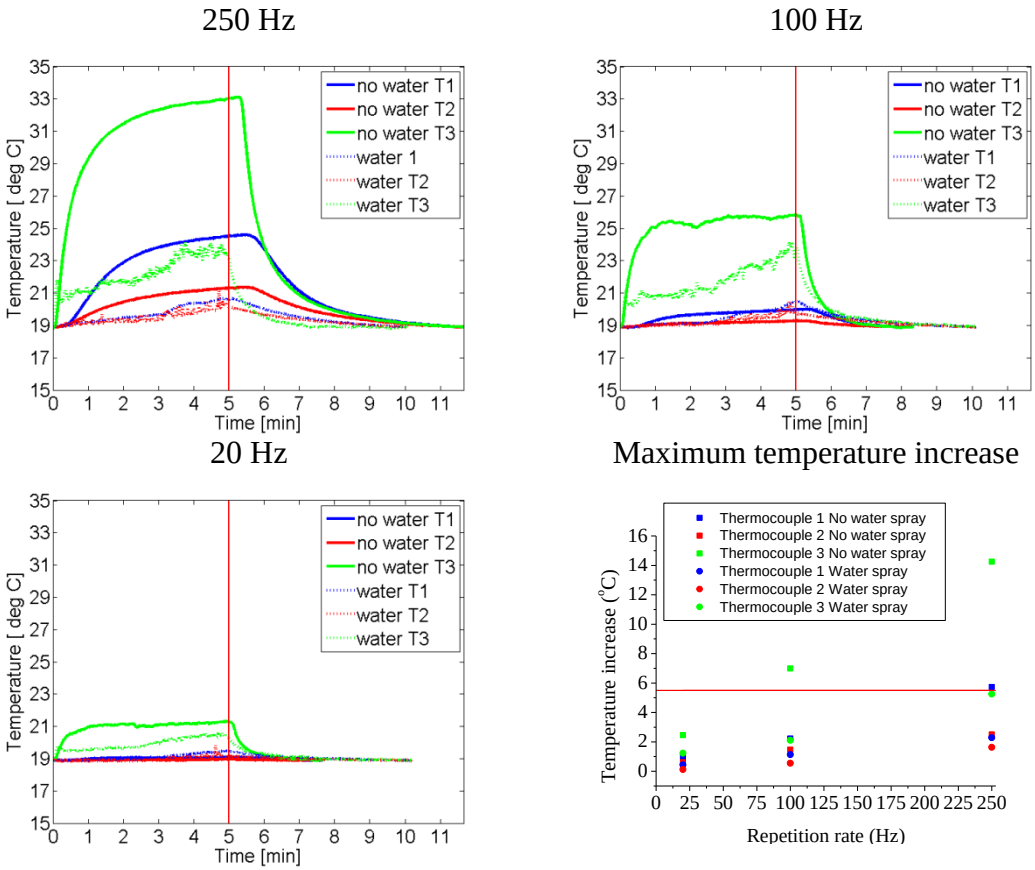

Figure 3.42 Comparison of measured temperatures with and without water spray present for three different repetition rates. The temperature was recorded by three thermocouples placement is visible on Figure 3.40.

Figure 3.42 is included to directly compare the temperatures rises and falls for machining with and without water spray present. To summarise the information presented in Figure 3.38 for 250 Hz repetition rate the water spray decreases the maximum temperature rise by 60% for T1, 35% for T2 and 63% for T3. For 100 Hz repetition rate the water spray decreases maximum temperature rise by 49% for T1, 63% for T2 and 70% for T3. For 20 Hz repetition rate the water spray decreases maximum temperature rise by 55% for T1, 80% for T2 and 50% for T3. Even at the higher repetition rates the maximum temperature raise is well below the maximum allowed threshold when the water spray is used. It should be pointed out that in this extreme case study, with the beam continuously radiated onto the sample surface, tissue carbonization occurs when a water spray is absent. The use of the water spray does generally decrease the amount of material removed, for a given laser fluence, but has a significant advantage in that it protects the surface, cools down the overall process keeping temperature rises below the critical threshold for necrosis and, it prevents tissue carbonization and dehydration.

3.8.2. Real case scenario for CO_2 laser machining of dental tissue

In the previous section an extreme case of laser irradiation has been tested, but it is highly unlikely that the laser would be required to machine tooth continuously for 5 minutes. In this experiment the aim was to try and simulate a more realistic approach that would be implemented in a dental practice. For two different pulse repetition rates of 250 Hz and 100 Hz, two different irradiation approaches are tested. Both of them consist of an irradiation time that is followed by a rest time. The first method is a 15 second long irradiation time followed by 45 second rest time and the second method is a 30 second irradiation time followed by 30 rest time. The temperature increase has been recorded again by three thermocouples T1, T2 and T3 placed as sown in Figure 3.38. The thermocouples were again embedded in a thermal compound. Figure 3.43 shows the temperature rise during laser processing with the red rectangles highlighting the time when the laser was irradiating the surface.

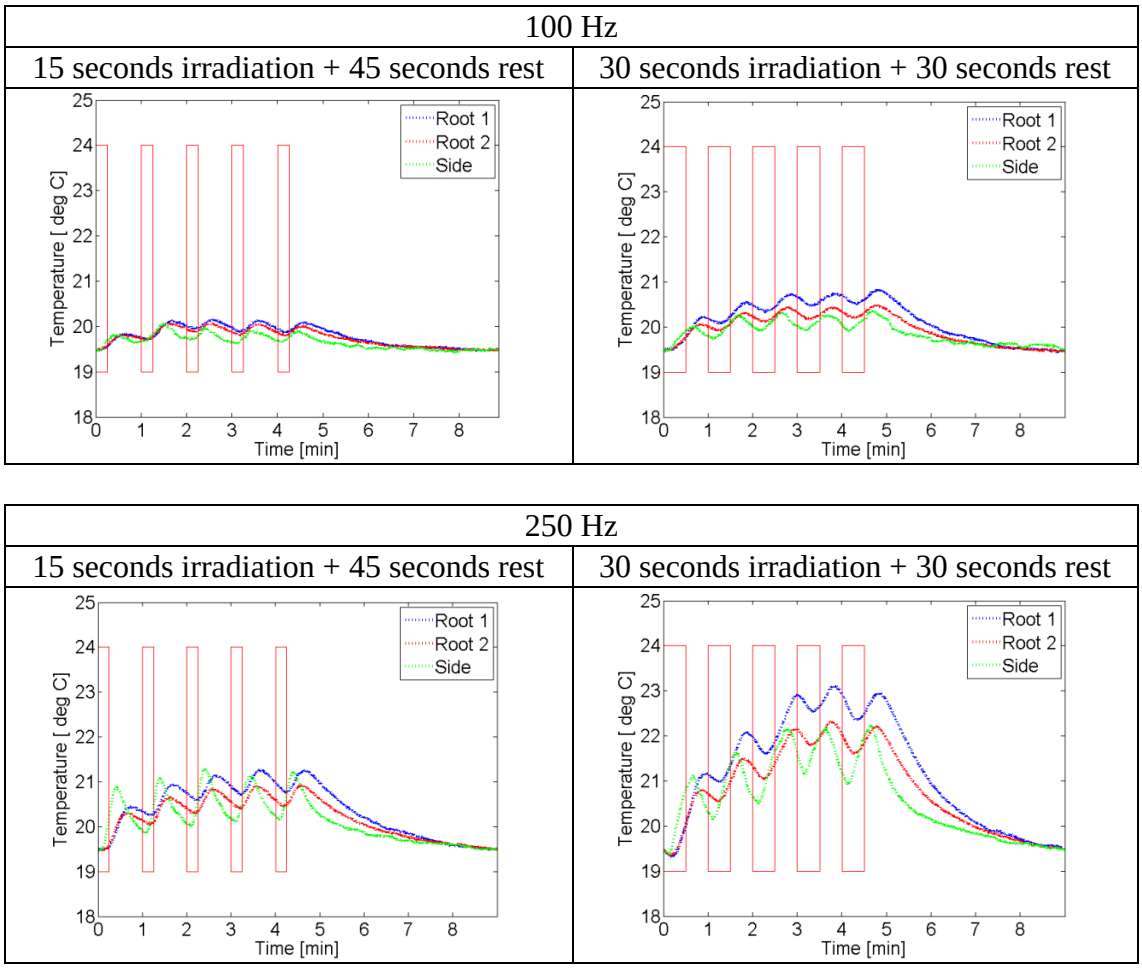

Figure 3.43 Temperature rise at three different positions (A – thermocouple 1, B- thermocouple 2, C – thermocouple 3) as a function of time for two different repetition rates 100 and 250 Hz and two different irradiation patterns (left) 15 seconds ON and 45 seconds OFF and (right) 30 seconds ON and 30 seconds OFF. Position of the thermocouples can be seen on Figure 3.40. The red rectangles highlight when the laser was irradiating the sample.

Table 3.3 shows the maximum recorded temperature rise during the interval of laser irradiation. The maximum temperature rise in the pulpal chamber was 3.8 ^{o}C recorded during the 30s-30s ON-OFF laser irradiation. This value does not exceed the value of the critical limit of 5.5 ^{o}C [29] . This interval irradiation pattern has a decreased temperature rise, by approximately 1.9 ^{o}C, compared to the continuous irradiation that has been described in the previous section (Section 3.8.1). In this experiment the delay for the heat to reach thermocouples placed in pulpal chambers is observed and, similarly to the continuous irradiation, the temperature keeps increasing after the laser has finished irradiating. Similar results were obtained by Fried [17] where the maximum recorded temperature inside the pulpal chamber during the creation of a circular cavity was 3.5 ^{o}C when using a 9.3 μm CO_2 laser (75 μs pulse duration, 400 Hz repetition rate, 2 W average power and 10 mJ pulse energy).

Table 3.3 Maximum temperature rise with intermittent irradiation. Thermocouple 1 and 2 are placed inside the pulpal chamber and thermocouple 3 was placed on the side. The position of the thermocouples can be seen in Figure 3.40

Repetition rate	Intervals		T1	T2	T3
	ON	OFF			
100 Hz	15 seconds	45 seconds	0.73 ^{o}C	0.62 ^{o}C	0.69 ^{o}C
	30 seconds	30 seconds	1.4 ^{o}C	1.05 ^{o}C	0.92 ^{o}C
250 Hz	15 seconds	45 seconds	1.8 ^{o}C	1.48 ^{o}C	1.83 ^{o}C
	30 seconds	30 seconds	3.8 ^{o}C	2.98 ^{o}C	2.86 ^{o}C

3.9. Conclusions

Successful ablation of human enamel has been demonstrated and described in this chapter. Different parameters have been tested and suitable machining parameters have been found for realistic drilling in a dental surgery for 10.6 μm CO_2 laser. To minimize the amount of cracking in the ablation site, it was shown that the pulse duration should not be longer than 10 μs. This results agree with predictions from simulation by Verde [14-16] that a 10 μs would be optimal when using a wavelength of 10.6 μm. In this regime the process is more influenced by plasma, compared to longer pulse durations, and only a thin layer on the surface is melted and solidified. For longer pulse durations 100 - 200 μs there significant amout of melting and cracking of the remelted layer. In this longer pulse regime the machining is a longer, more thermal process as the irradiance is 10 – 20 times lower. This in turn leads to a reduced amount of plasma creation.

Machining with diverging and converging beam was tested, by focussing the laser above and below the surface, with and without compensation of the fluence for a change in spot size on the surface. It was found that there is no benefit of using a defocused beam as it does not increase ablation efficiency or decrease the amount of cracking. However when a converging beam is focused below the surface it creates a deeper cavity, provided that the fluence used is higher than ablation threshold. Nevertheless it was shown that when the beam is defocussed by a small distance (~100 μm) and the fluence exceeds the ablation threshold (more than 40 J/cm^2) tissue will be removed at a fairly similar rate to an in focus beam.

Initial tests for multiple pulse ablations have been performed by testing percussion and trepanned laser drilling. Percussion drilling is limited by the taper angle in the cavity and holes no deeper than ~85 μm were produced even when translating the beam into the sample after each pulse. Testing of trepanned laser drilling was constrained by the absence of a galvanometer scanning system and was limited to simple square and circular patterns. Initial tests showed that for the larger cavities created via trepanning there was no more cracking present than for single pulse ablation. With this system the delay between successive pulses was up to 1 s due to the limited speed of the translation stages moving the sample.

Another crucial step that had to be considered when investigating the possibility of using laser radiation for modification and removal of biological tissue was to test whether it increased the temperature in the pulpal chamber above a critical value (5.5 ^{o}C rise) that would lead to necrosis of the living tissue. Tests showed that it is possible to control temperature and keep it below the critical limit by limiting repetition rate of the laser, using the laser in an ON-OFF interval mode and by employing a water spray. Without the water spray dehydration of the tissue occurs which is an unwanted change. When using water spray the ablation efficiency is decreased, but temperature rise is minimal and the tooth does not undergo dehydration. Consequently the results demonstrate the viability of employing a microsecond pulsed CO_2 laser at 10.6 μm wavelength for the practical drilling of dental enamel.

Chapter 4. Picosecond laser modification of porcine sclera

This chapter describes a comprehensive investigation into the possibility of using ultrashort picosecond laser pulses to modify ophthalmic tissue. It describes the development of a laser based thinning procedure of the sclera, which compared to the traditional surgical thinning is much less invasive. This results in a decreased possibility of infection and localised fibrosis [69]. The successful application of a picosecond laser to create portals; lesions of specifically tailored shape profiles, could offer a potential way of increasing the dosage of the drug delivered to the posterior part of the eye [59, 60]. Moreover such a process would allow for a much less invasive method for drug delivery. Current delivery methods for drugs targeting age related macular degeneration require drug delivery to a vitreous body using needles which penetrate through the outer layers of the eye. Additionally the capability to precisely remove sclera could also be used in glaucoma surgery. The goal of a procedure targeting glaucoma is to decrease the intraocular pressure within the eye [91, 102]. Thinning of the sclera can allow for localised increased flexibility of the tissue, allowing an increase in the volume of the vitreous body hence decreasing the intraocular pressure.

4.1. Introduction

The removal of soft biological tissue using ultrashort pulsed lasers is based on laser induced breakdown, which occurs due to the creation of a plasma caused by exceeding a certain irradiance threshold (specific for each target tissue) [70, 83]. Such a removal mechanism allows the use of ultrashort, picosecond pulse laser radiation in novel minimally invasive procedures. Laser induced breakdown has been investigated by Vogel [70, 82, 134] where he investigated different pulse regimes and characterized the properties of induced the plasma.

In this chapter many different parameters of picosecond laser ablation are tested and assessed:

- Single line scanning ablation,
- Square area removal,
- Circular area removal,
- Influence of different spot separation,
- Influence of various repetition rates of the laser,
- Influence of different scanning speeds.

The ideal final cavity shape would be to have a flat bottom surface, which would display precise control over the final depth of the cavity. The desired depth of the cavity would be in the range of 200 micrometres, as the average thickness of the sclera is 670 μm [57] and deeper incisions could weaken integrity of the whole eyeball.

In order to investigate the safety of using a 1030 nm picosecond laser when machining the eye, the transmission of potentially harmful (blinding) light through the sclera during the process was monitored. In addition, the temperature increase during the machining process was measured. Finally, to prove the viability of the thinning concept as a means to improve drug delivery, permeation tests were carried out using fluorescein dextran to assess change in the permeability of the sclera when a square cavity is created.

4.2. Experimental setup

The experimental setup is built around an industrial picosecond laser; TRUMPF TruMicro 5x50 which produces 6 ps long pulses at the wavelength of 1030 nm. The laser can operate at frequencies ranging from 40 Hz to 400 kHz with pulse energies up to 125 μJ, which allows flexibility when choosing the parameters of the laser processing. After the beam exits the laser it propagates through a magnifying telescope and is consequently raised to reach a galvanometer scan head (SCANLAB hurrySCAN II) with a 160 mm

focal length f-theta lens. The laser beam is focused down to a spot with a diameter of 35 µm. As a result this laser setup is capable of reaching fluences (*pulse energy / focused spot size*) up to 13 J/cm^2, irradiance (*maximum power / focused spot size*) of 2.17·10^{12} W/cm^2 and peak power of 15 MW. Considering that the galvanometer scan head is capable of reaching scanning speeds up to 300 mm/s, it is possible to precisely control the parameters of the process and to test many complicated scanning patterns. Figure 4.1 shows the schematic and a photograph of the experimental setup as well as the laser beam profile (measured at near field near focus using Spiricon software and a PULNIX TM6-CN camera.)

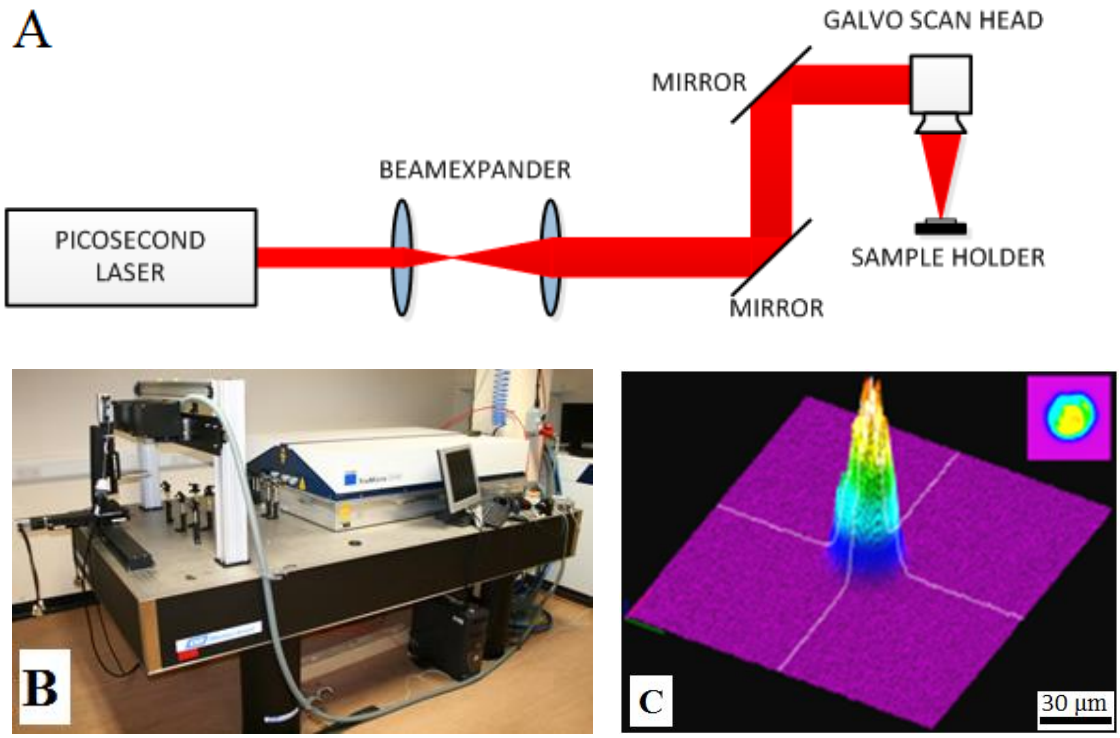

Figure 4.1 (A) Experimental setup beam path schematic. (B) Image of the Trumpf TruMicro 5x50 picosecond laser with Aerospace precision stages and galvanometer scan heads for various wavelengths. (C) A Near field profile of the laser beam measured and near focus of the 16 mm f-theta lens.

4.3. Tissue Samples

At this early stage of the research, porcine sclera has been selected as a suitable replacement for human tissue. Porcine sclera (sourced from an abattoir) was chosen due to the high structural similarity to human tissue; it has a similar histology, collagen fibre structure and water content (~70%) to human sclera [77]. Moreover it is much easier to handle and store animal tissue samples for the experiments, and there are no regulations concerning handling and disposal of the samples from an abattoir. Nevertheless care was

taken to ensure that health and safety issues were fully considered. Samples were prepared with a 5 mm and 8 mm diameter trephine (dissection instrument with circular blade) and were stored in phosphate buffered saline solution before they underwent laser machining. The average thickness of the samples used in our experiments was 1.2 mm. The average thickness of human sclera is 670 ± 80 μm [57]. Figure 4.2 shows an optical image of the sample. Figure 4.3 shows SEM micrographs of a fixed scleral sample with characteristic fibrous structure clearly visible.

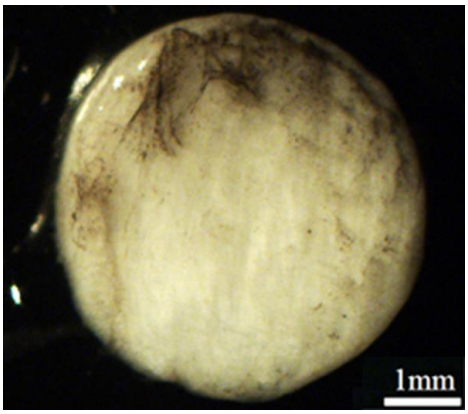

Figure 4.2 Typical example of a porcine scleral sample used in the experiments prepared with a 5 mm diameter trephine.

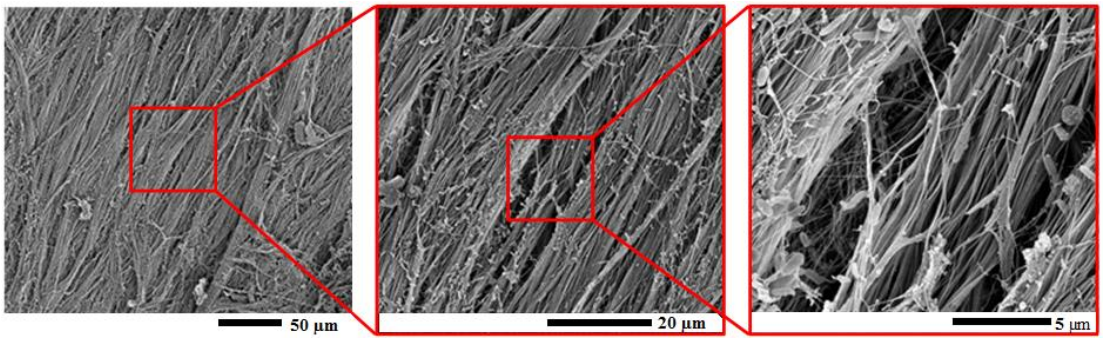

Figure 4.3 SEM micrographs of a fixed unmachined scleral sample that was sputter coated with 20 nm layer of gold. A fibrous structure of the tissue is clearly visible on the images.

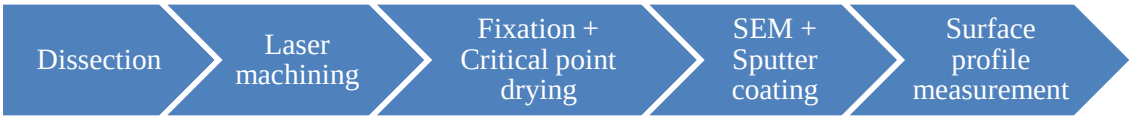

Figure 4.4 Diagram describing order of procedures regarding sample preparation and investigation.

After a sample has been dissected it undergoes laser machining, after which it is put into a 3% Glutaraldehyde solution to start the fixing process. This is necessary to prepare samples for vacuum, as a hydrated tissue will be distorted in vacuum conditions during SEM investigation [135]. Moreover, dehydrated samples become much more transparent, and investigation with optical instruments, like surface profilometers, becomes much

more challenging. Consequently samples are washed in a solution of 0.1 M sodium cacodylate buffer (3 x 10 minutes using fresh solution each time). The samples are then post-fixed in 1% osmium tetroxide in 0.1 M sodium cacodylate buffer for 45 minutes in order to provide staining and to prepare them for investigation using scanning electron microscopy [136]. A further 3 x 10 minute washes are performed in 0.1 M sodium cacodylate buffer. Consequently samples undergo dehydration in graded concentrations of acetone (50%, 70%, 90%, and 3 x 100%) for 10 minutes each, followed by critical point drying using liquid carbon dioxide. The final step before tissue characterization is sputter coating to increase surface conductivity for scanning electron microscopy, hence samples are sputter coated with a 20 nm thick layer of gold. SEM micrographs are taken with a Quanta 650 FEG microscope. Depth and surface profiles of the tissue and created lesions are measured with two different white light interferometers; Zygo NewView 5000 and Alicona 4G [137]. Surface profiles and cross section output from these systems are imported into MATLAB to produce plots. Figure 4.5 shows the equipment used in tissue characterization as well as SEM micrographs of fixed, un-machined porcine scleral tissue.

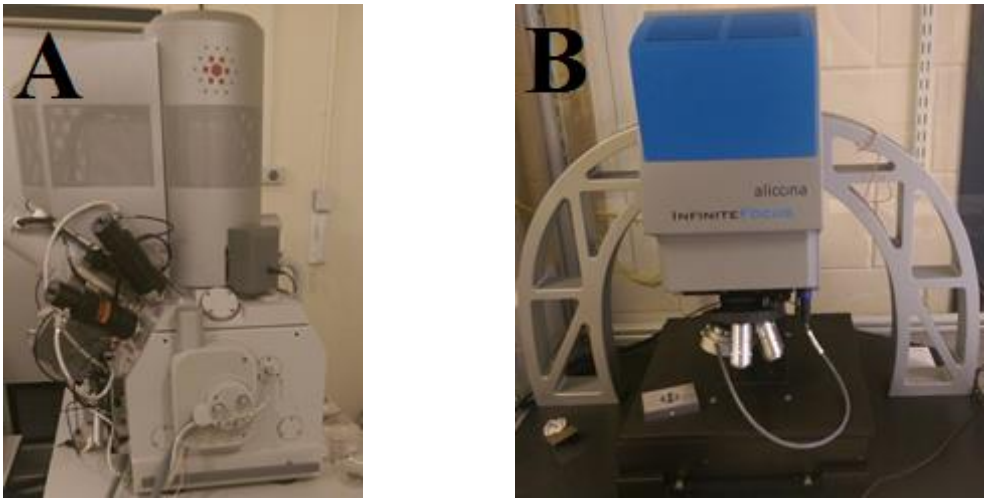

Figure 4.5 (A) Quanta 650 FEG scanning electron microscope and (B) Alicona 4G surface profilometers that were used to investigate features created in the sclera across all of the experiments within the thesis.

4.4. Single line scanning ablation

Initially the possibility of measuring the effect of single pulse plasma mediated ablation was investigated but the results were not observable on the sample due to the very small dimensions of created plasma. For these measurements the Gaussian laser beam is focused down to a spot of 35 μm, hence the value of irradiance reached in the centre is much higher than in the periphery of the beam. As a result, the created plasma is going to

be smaller than the diameter of the beam, and plasma mostly grows towards the laser radiation not the sides [70, 81-83, 138]. The initial feasibility tests were therefore designed to focus on single line scanning ablation. In this case the laser beam is focused on the sample surface and scanned to create a linear lesion. The length of each lesion differed for different experiments and was either 500 µm or 1 mm long. A number of different repetition rates were tested, starting from 100 Hz to 10 kHz. Initially a repetition rate of 100 kHz was tested as well, but it was discarded due to high thermal damage observed due to thermal accumulation. The issue of heat accumulation is going to be explained in more detail later in this section. Consequently when the repetition rate was increased, beam scanning speeds (0.1 mm/s – 70 mm/s) were also increased to maintain constant spot and line separations (1, 3, 5 and 7 µm). Figure 4.6 describes the difference between spot and line separation.

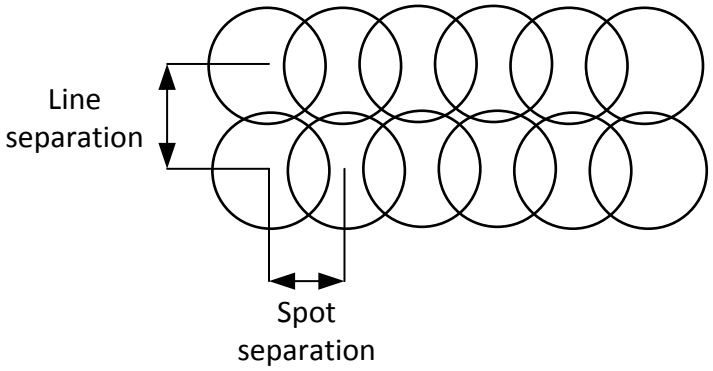

Figure 4.6 Schematic illustrating the difference between spot and line separation.

The maximum depth of the lesions is reached at the end of the scanning process. It was observed that with each pulse an increasing amount of material was removed up until the point when the depth saturates. For higher repetition rates and smaller spot separations the maximum depth reached was higher due to the larger pulse overlap and heat accumulation. Due to low thermal conductivity (k = 0.58 W/(m·K) [82]) and shorter periods of time between pulses, the accumulated energy doesn't have enough time to diffuse. As a result, due to thermionic emission, seed electrons for multiphoton avalanche are provided much more easily [70, 83]. This process is described in much more detail in section 2.4.5. Moreover, maximum depth is limited by the incoming pulses being incident on the sloping edge of the cavity. This process is described in more detail in section 5.3. Figure 4.7 shows a schematic of the single line scanning ablation removal process. The scanning process starts from the left and ends on the right.

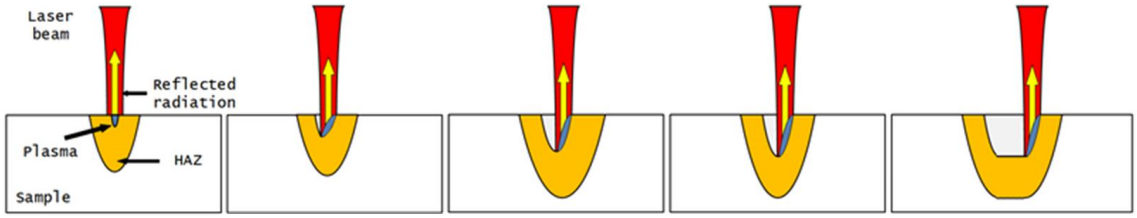

Figure 4.7 Schematic of single line scanning plasma mediated ablation removal of tissue. Due to residual heat leftover from previous pulses seed electrons are provided by thermionic emission which leads to an increased removal rate by incoming pulses. The heat affected zone (HAZ) is highlighted in yellow.

The first and lowest repetition rate that was investigated was 100 Hz. Figure 4.8 shows lesions created with single line scanning ablation for pulse energies ranging up to 125 µJ, and different pulse spot and line separations 1, 3, 5 and 7 µm (which equates to scanning speeds of 0.1, 0.3, 0.5 and 0.7 mm/s respectively) and figure 4.9 shows maximum depth as a function of pulse energy. Moreover this figure contains a plot of maximum depth reached in the experiment. Lesions created with 1 µm and 3 µm spot separations were clearly visible, but they were not clearly defined. On the other hand line incisions created with higher spot separation; 5 µm and 7 µm, are barely visible. The ablation sites are easily distinguished from the tissue untouched by the laser radiation, but in this instance the laser machined lesions are almost closed over and it was impossible to take any accurate measurements or profiles of the lesions.

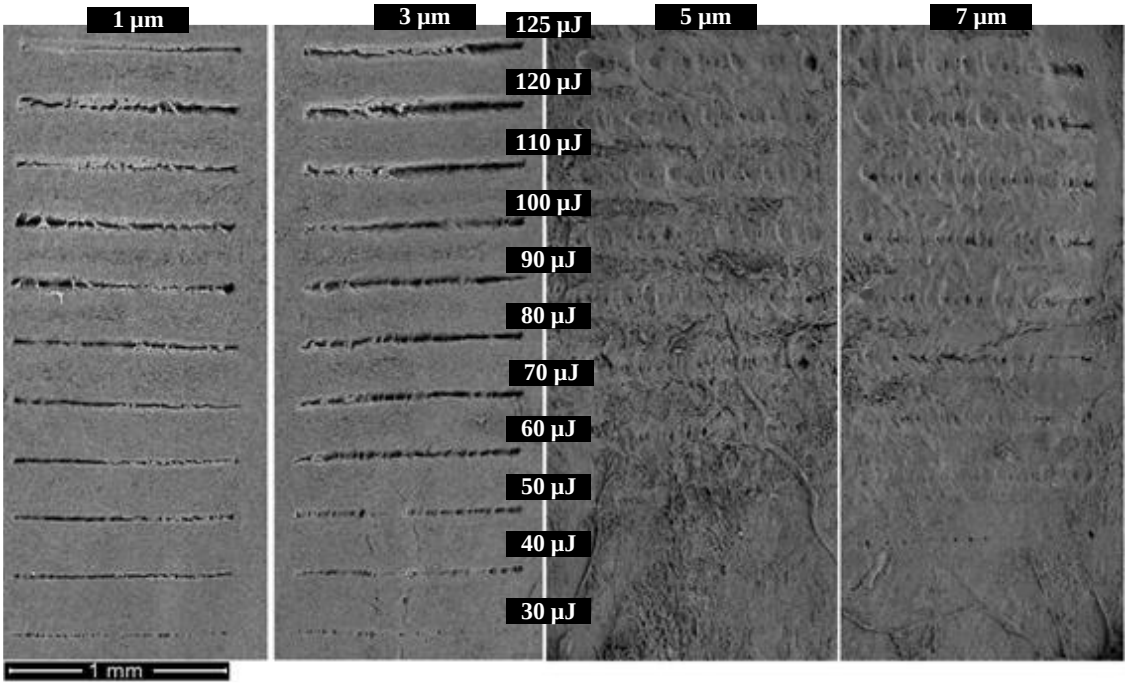

Figure 4.8 SEM micrograph of lesions created with single line linear ablation scanning pattern. Repetition rate - 100 Hz; spot separation 1, 3, 5, 7 µm (equivalent to scan speeds of 0.1, 0.3, 0.5, 0.7 mm/s respectively); pulse energies 10 – 125 µJ; wavelength – 1030 nm.

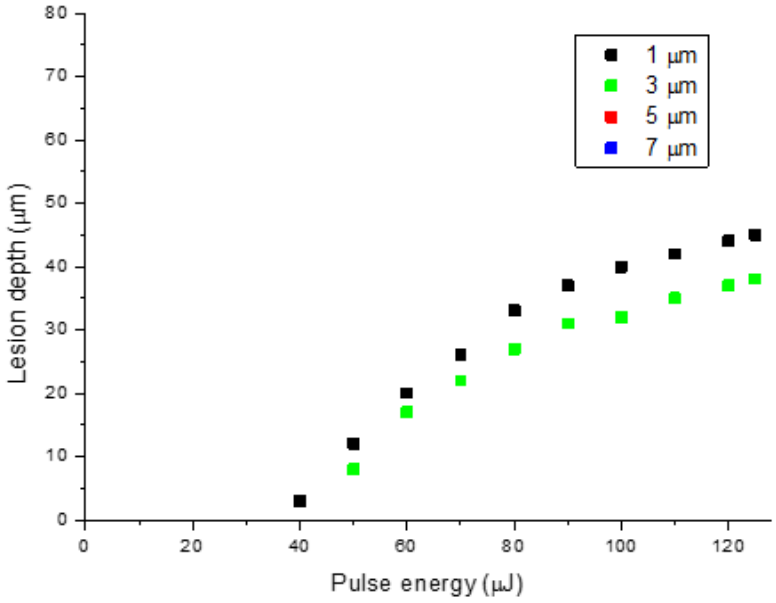

Figure 4.9 Maximum depth as a function of pulse energy for different spot separations for single line scanning ablation. Repetition rate - 100 Hz; spot separation 1, 3, 5, 7 µm (equivalent to scan speeds of 0.1, 0.3, 0.5, 0.7 mm/s respectively); pulse energies 10 – 125 µJ; wavelength – 1030 nm.

Consequently, a similar experiment was done with a higher repetition rate of 1 kHz. Figure 4.10 shows SEM micrographs of lesions created with single line scanning ablation (1 kHz, 1-7 µm spot separation, up to 125 µJ pulse energies) and figure 4.11 shows the maximum depth reached as a function of pulse energy. To maintain a similar spot separation distance, the scanning speed was increased proportionally to the increase in the repetition rate, and was consequently set at 1, 3, 5 and 7 mm/s. Compared to the results with a repetition rate of 100 Hz the lesions created at 1 kHz are much more visible and it was possible to get a depth measurement for of them. Some of the lesions, especially for the larger spot separations, seem to have small tissue connections over them which result from chemical manipulations when fixing and drying the tissue. To see if this issue could be resolved the protocol was adjusted by putting samples into a fixative straight after laser processing but unfortunately this did not solve the problem. This effect was not present when investigating area removal in successive sections. Lower spot separation between consecutive pulses leads to higher heat accumulation and higher thermal energy remains in the tissue. This allows for plasma to be created more rapidly due to the thermionic emission providing seed electrons for the plasma, and hence it requires lower irradiance than for the previous spot [70, 83]. As a result, a smaller spot separation leads to a decreased threshold in single line scanning ablation. For smaller spot separations (1 µm and 3 µm) lesions are much better defined. Maximal depths reached are approximately

20 µm deeper than the depth reached with the lower repetition rate of 100 Hz. There is no thermal damage visible to the ablation site or the adjacent tissue, as the lesions are characterized by a constant width, which won't be the case for higher repetition rate – 10 kHz, which can be seen in Figure 4.12.

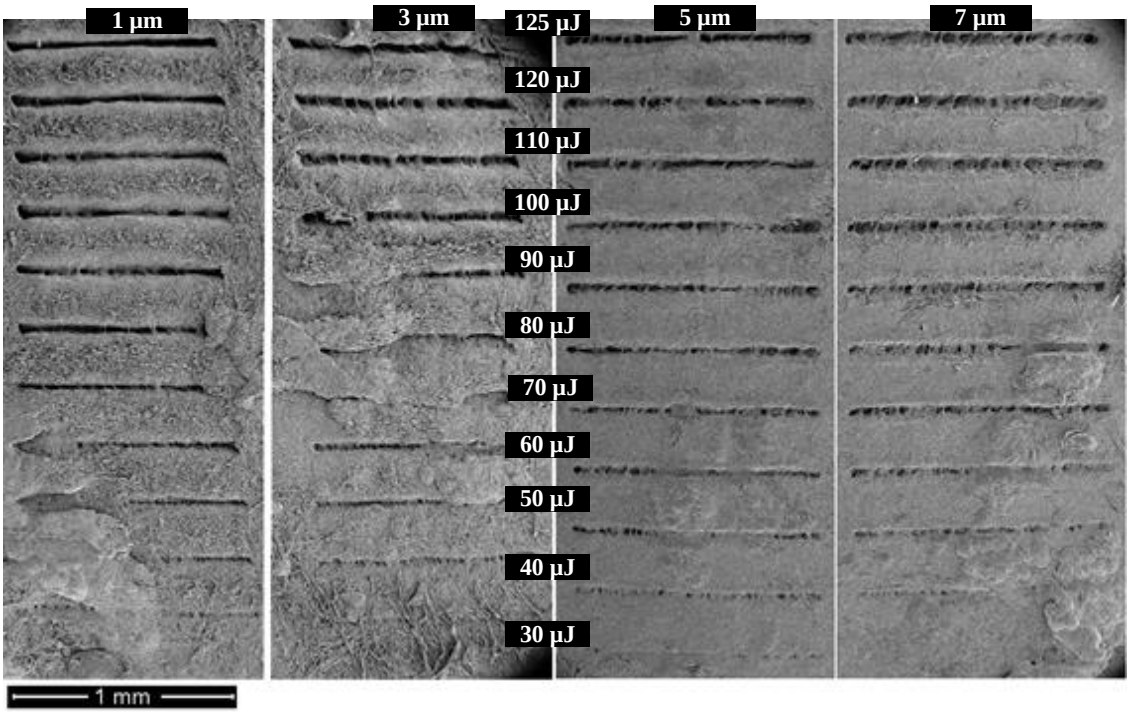

Figure 4.10 SEM micrograph of lesions created with single line linear ablation scanning pattern. Repetition rate of 1 kHz; spot separation 1, 3, 5, 7 µm (equivalent to scan speeds of 1, 3, 5, 7 mm/s respectively); pulse energies between 10 and 125 µJ; wavelength of 1030 nm.

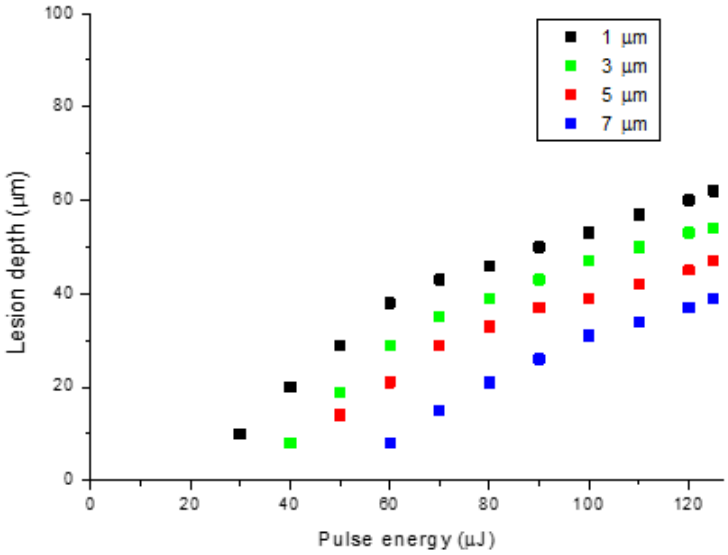

Figure 4.11 Maximum depth as a function of pulse energy for different spot separations for single line scanning ablation. Repetition rate of 1 kHz; spot separation 1, 3, 5, 7 µm (equivalent to scan speeds of 1, 3, 5, 7 mm/s respectively); pulse energies between 10 and 125 µJ; wavelength of 1030 nm.

Lastly, a higher repetition rate of 10 kHz was tested and as in previous experiments four different values of spot separation were tested: 1, 3, 5 and 7 µm with scanning speeds 10, 30, 50 and 70 mm/s respectively and pulse energies up to 125 µJ. Results are seen in Figure 4.12 which shows SEM micrographs of the lesions, and Figure 4.13 shows a graph that shows the relation between the maximum depth reached and pulse energy. For 1 µm spot separation and for higher pulse energies (above 90 µJ) lesions have a much more distorted shape compared to the previous results, resulting from increased thermal energy. This effect is much more visible when investigating square area removal in section 4.5.2. When the spot separation is increased to 3 µm, the lesions are much more even and less distorted. However, when investigating higher spot separation, there remains tissue connected from one side of the cavity to the other. Additionally, increasing the amount of heat deposited into the tissue (by increasing the pulse energy) did not resolve this issue and the results obtained were similar to those observed in experiments using lower repetition rates. The maximum depths reached for the highest repetition rate are approximately 25 to 30 µm deeper than for a 1 kHz repetition rate. Since thermal damage was clearly visible when using a repetition rate of 10 kHz, further detailed experiments on higher repetition rates have been discarded since there would be increasing thermal damage if the repetition rate were to be increase further.

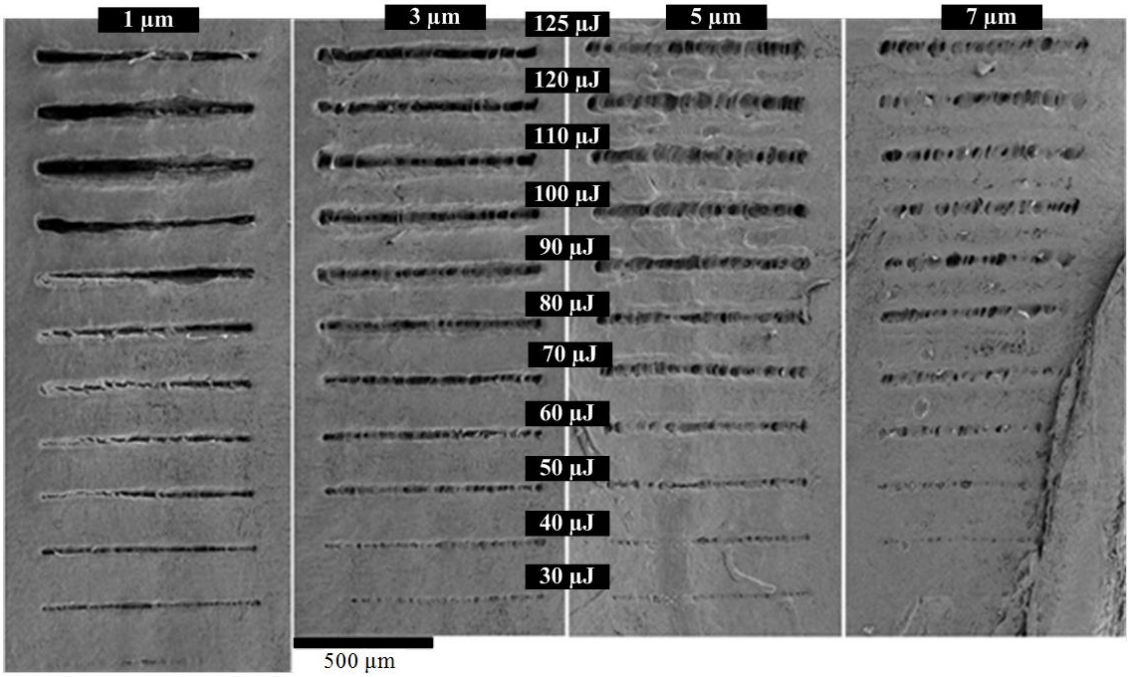

Figure 4.12 SEM micrograph of lesions created with single line linear ablation scanning pattern. Repetition rate of 10 kHz; spot separation 1, 3, 5, 7 µm (equivalent to scan speeds of 10, 30, 50, 70 mm/s respectively); pulse energies between 10 and 125 µJ; wavelength of 1030 nm.

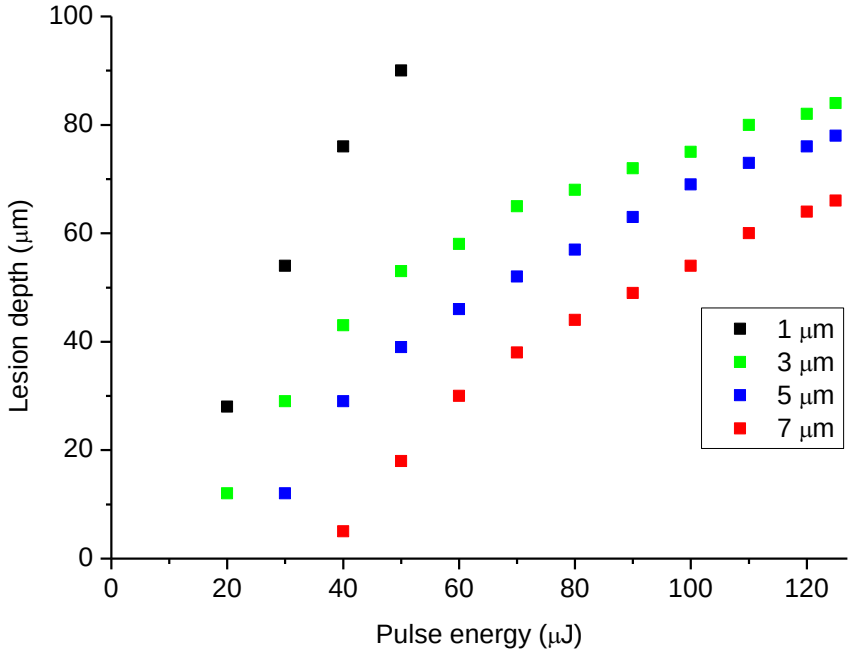

Figure 4.13 Maximum depth as a function of pulse energy for different spot separations for single line scanning ablation. Repetition rate of 10 kHz; spot separation 1, 3, 5, 7 μm (equivalent to scan speeds of 10, 30, 50, 70 mm/s respectively); pulse energies between 10 and 125 μJ; wavelength of 1030 nm.

From the results presented above it can be concluded that smaller spot separation, therefore more concentrated energy deposition, leads to a much deeper cavity. Aside from spot separation, the laser repetition rate has a significant influence on the process, as a higher frequency will lead to a higher amount of heat accumulated near the focussed spot. This is because an increased repetition rate means less time between consecutive pulses and therefore less time for the heat to diffuse into the tissue, which has a low thermal conductivity (k = 0.58 W/(m·K) [82]), before the next pulse arrives. Figure 4.14 shows maximum lesion depth as a function of pulse energy for three different repetition rates (0.1, 1, 10 kHz) while maintaining constant spot separation (3 μm). For a pulse energy of 60 μJ, the depth achieved for 100 Hz repetition rate is 15 μm, for 1 kHz is 29 μm and for 10 kHz is 58 μm. The only difference between these processes is the laser repetition rate and scanning speed to maintain a constant value of spot separation. Increasing the repetition rate by 10 and 100 times decreases the time between consecutive pulses proportionally, which minimizes heat dissipation in the tissue. As a result higher residual thermal energy assists the creation of plasma, which leads to a much higher amount of tissue being removed [70, 83].

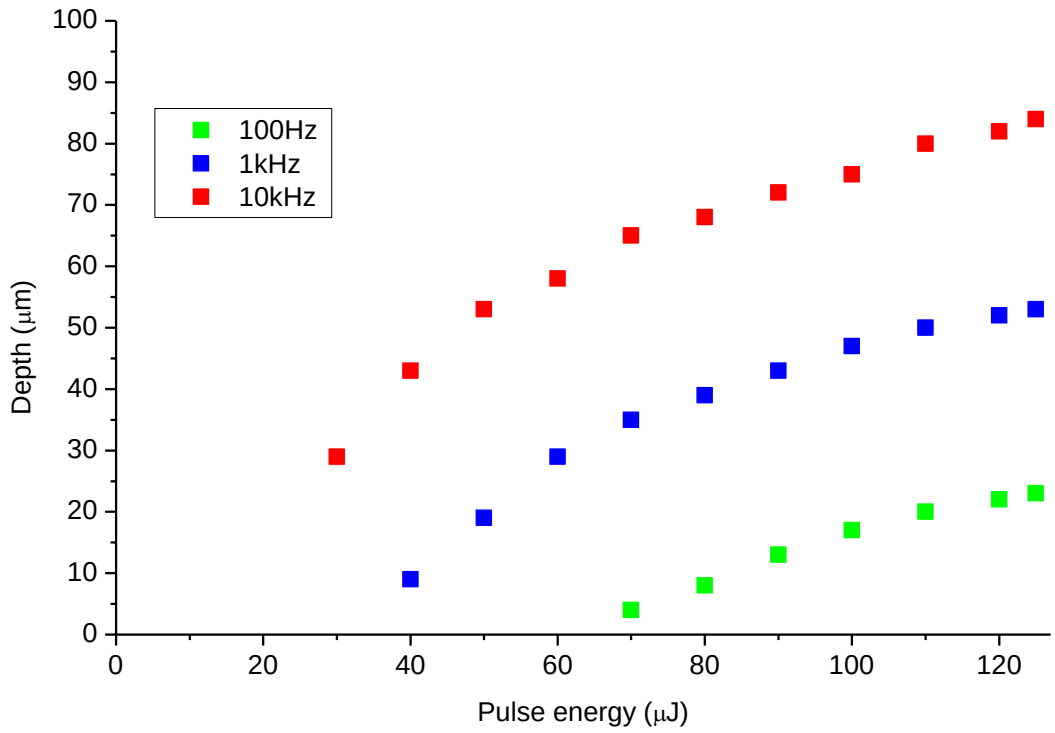

Figure 4.14 Graph shows maximum depth of a linear lesion as function of pulse energies for three different repetition rates and constant spot separation of 3 µm.

Previously, femtosecond laser ablation of linear lesions has been reported [89, 90] where a laser beam was focused 100 µm below the surface with a spot diameter of 14 µm, half the diameter of the spot size used in this thesis. Additionally in the research presented here, the laser beam was focused on the surface as opposed to 100 µm below. As a result, linear lesions created by the picosecond laser described above have much narrower width on the tissue surface – less than 30 µm compared to 80 µm (when using 112.5 µJ pulses) presented by Yang [90]. In both examples the created lesions do get wider as they become deeper. Similarly, both picosecond and femtosecond lasers were successful in creating linear lesions, but the picosecond laser is capable of higher removal rates. For picosecond machining the best results were obtained for a 3 mm/s scanning speed whereas Yang [90] had a much lower scanning speed of 0.1 mm/s.

4.5. Square area removal

In the previous section (Section 4.4), single line scanning ablation was investigated. This gives initial results about how to approach picosecond plasma mediated ablation of porcine sclera. However, in this section further parameter space is investigated and the influence of the following factors on the laser machining of larger areas of sclera are tested:

- scanning pattern
- repetition rate,
- spot separation,
- pulse energy.

4.5.1. The effect of scanning pattern

When laser machining over an area, the selection of the laser scanning pattern has a major influence on the results, as it defines the order in which pulses are applied, therefore directly influencing the amount of heat accumulation. Heat accumulation is a significant factor that has to be controlled to have a successful laser based process, and has been a major issue across different disciplines, e.g. dentistry [139], metals [140, 141] or waveguide writing [142]. Five different scanning patterns were tested: simple raster scan (Figure 4.15 a), raster scan with alternating directions (Figure 4.15 b), angular scan (Figure 4.15 c), angular scan with alternating directions (Figure 4.15 d) and square like with alternating direction left right and alternating side top-bottom (Figure 4.15 e). All of these patterns are shown on Figure 4.15. Most of the scanning patters selected are fairly simple designs as the final process is aimed to be used *in vivo*, where the amount of free space is minimal. Keeping scanning paths as simple as possible would allow a potential scanning device for the procedure to be minimized

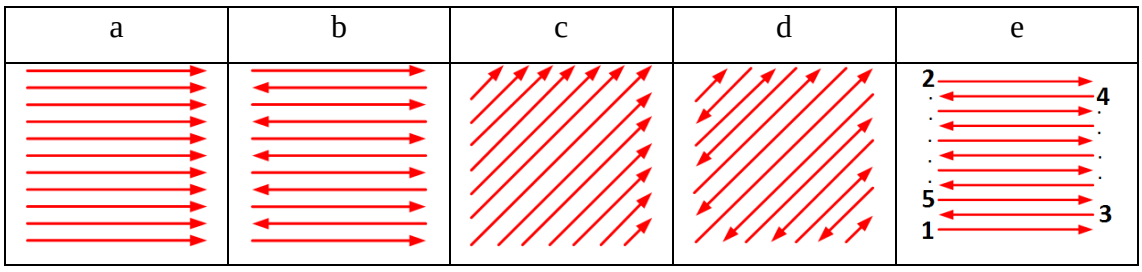

Figure 4.15 All of the scanning patterns investigated in current section. a- simple raster scan; b- raster scan with alternating directions; c - angular scan; d - angular scan with alternating directions; e- raster scanning pattern with alternating direction left right and alternating side top-bottom.

Figure 4.16 shows the SEM micrograph, surface profile and cross-sections of the cavity created with a simple raster scanning pattern. The repetition rate used in this experiment was 1 kHz, spot and line separation 3 µm, pulse energy 60 µJ and scanning speed 3 mm/s.

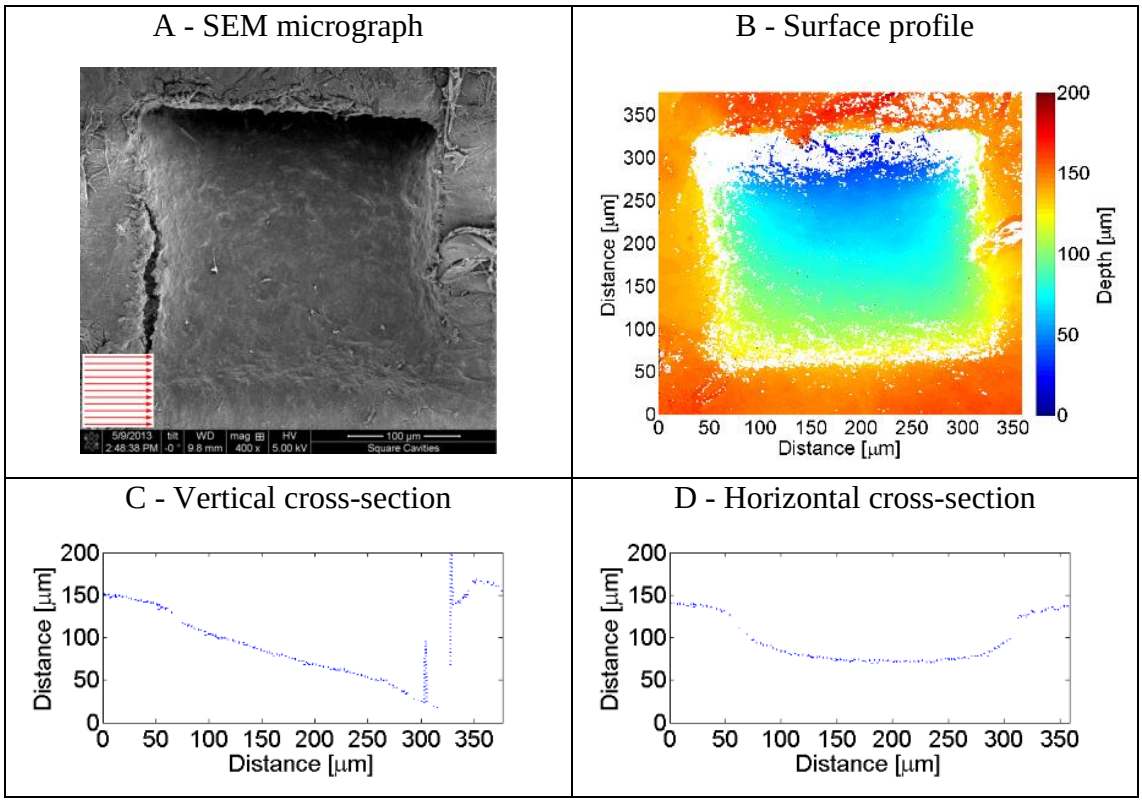

Figure 4.16 (A) SEM micrograph, (B) surface profile and (C) vertical and (D) horizontal cross-section plots for simple raster scanning pattern. Cross-sections were taken through the middle of the cavity Wavelength of 1030 nm, pulse energy of 60 µJ, repetition rate of 1 kHz, spot and line separation of 3 µm.

As in previous single line scanning ablation experiments (Section 4.4) heat accumulation has a significant influence on the results when raster scanning. Heat is deposited into the tissue with each scan and due to the low thermal conductivity, there is significant residual energy in the tissue, which does not dissipate before the next line of the raster scanning pattern passes. This can be easily seen looking at Figure 5.12 in Section 5.3.4 where simulation results are shown, indicating that after the whole scanning line is completed there is an increased amount of energy leftover where a consequent scan would begin. As a result, each consecutive scan over the tissue occurs in tissue with a higher residual amount of heat, and hence removes slightly more material which leads to the bottom surface of the cavity being sloped. This is a direct result of thermionic emission of seed electrons from the substrate when there is an increased thermal energy [70, 83].

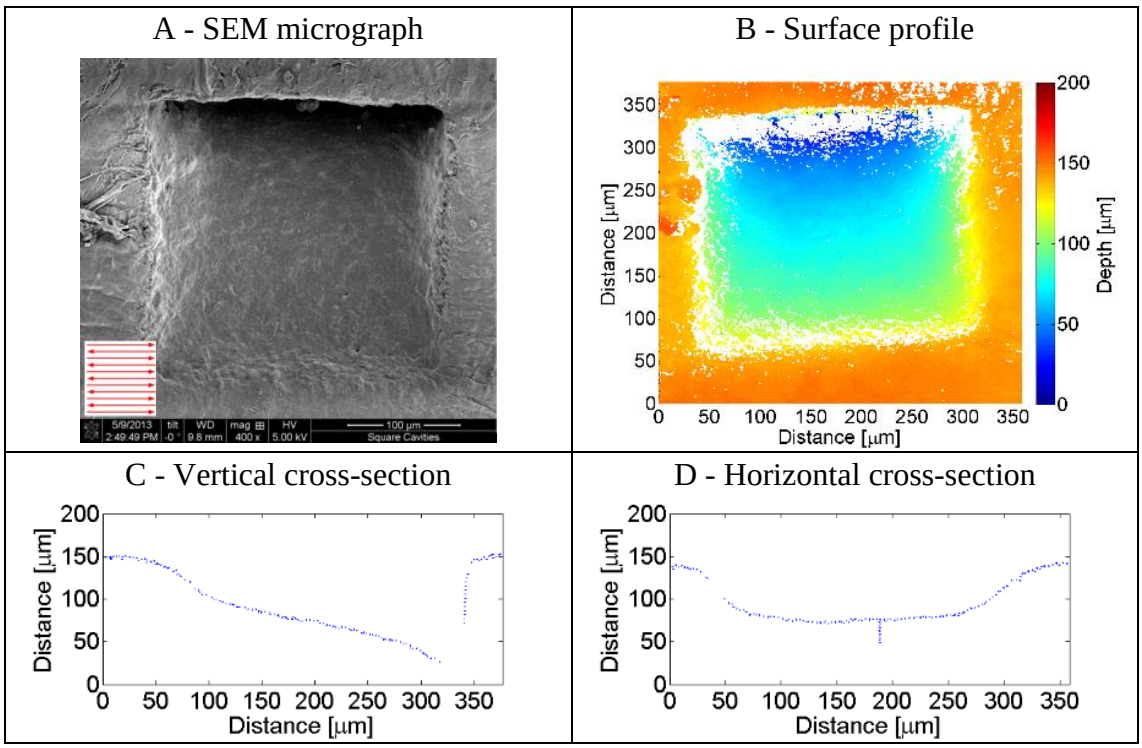

Figure 4.17 (A) SEM micrograph, (B) surface profile and (C) vertical and (D) horizontal cross-section plots for snake shape like scanning pattern. Wavelength of 1030 nm, pulse energy of 60 µJ, repetition rate of 1 kHz, spot and line separation of 3 µm.

The next scanning pattern investigated was a raster scan with alternating directions for each pass (a snake-like scanning pattern). Figure 4.17 shows the SEM micrograph, surface profile and cross-section of the created cavity. The application of this pattern was supposed to increase the continuity of the heat deposition into the tissue. This is in contrast to the previous scan where all of the scanned lines started on the left side and moved to the right. For the subsequent scan the laser would stop irradiating and start again form the left side. In the snake like pattern the direction of each scanned line is alternating, thus distributing the heat in a more continuous manner. As result the difference in the maximum depth reached is 127 µm (for raster scanning pattern) compared to 139 µm (for raster scanning pattern with alternating directions).

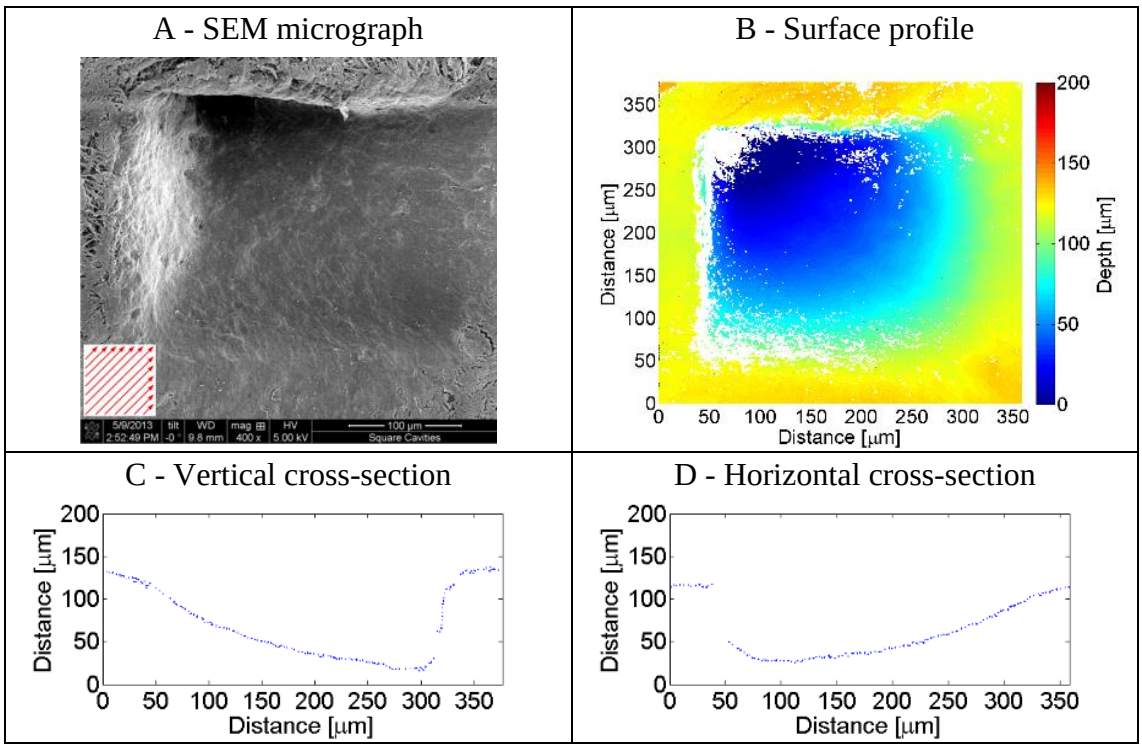

Figure 4.18 (A) SEM micrograph, (B) surface profile and (C) vertical and (D) horizontal cross-section plots for the raster scan at an angle without alternating direction if consecutive scanning lines. Wavelength - 1030 nm, pulse energy – 60 µJ, repetition rate 1 kHz, spot and line separation - 3 µm.

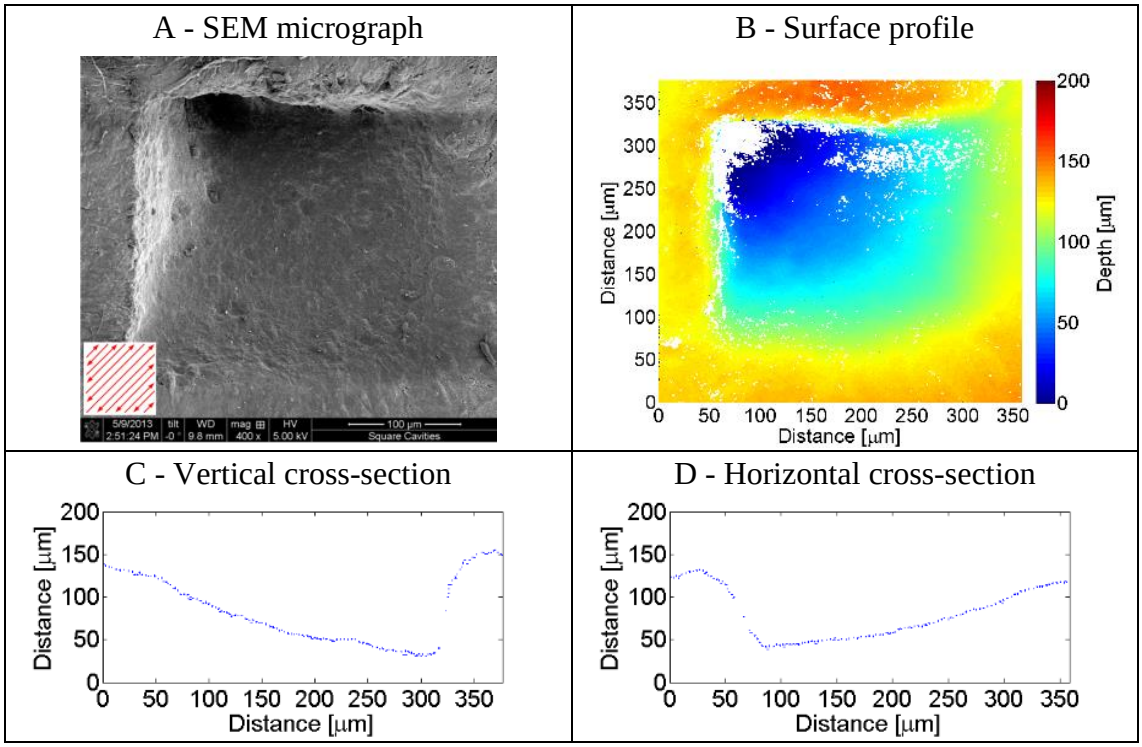

Figure 4.19 (A) SEM micrograph, (B) surface profile and (C) vertical and (D) horizontal cross-section plots for the raster scan at an angle without alternating direction if consecutive scanning lines. Wavelength - 1030 nm, pulse energy – 60 µJ, repetition rate 1 kHz, spot and line separation - 3 µm.

A similar experiment was carried out for a raster scan at a 45 degree angle, with and without alternating directions as seen in Figure 4.18 and Figure 4.19. Both experiments were using the same repetition rate of 1 kHz, spot and line separation of 3 µm and 60 µJ pulse energy.

Figure 4.18 and Figure 4.19 show SEM micrographs, surface profiles and cross sections of created cavities. The results produced from these scanning patterns are similar to those from previous experiments, and the depth of the cavity does increase from the starting point to the end of the scanning pattern. The maximum depth reached using the scanning pattern without alternating directions is 130 µm, and for the scanning pattern with alternating directions the maximum depth reached is 125 µm.

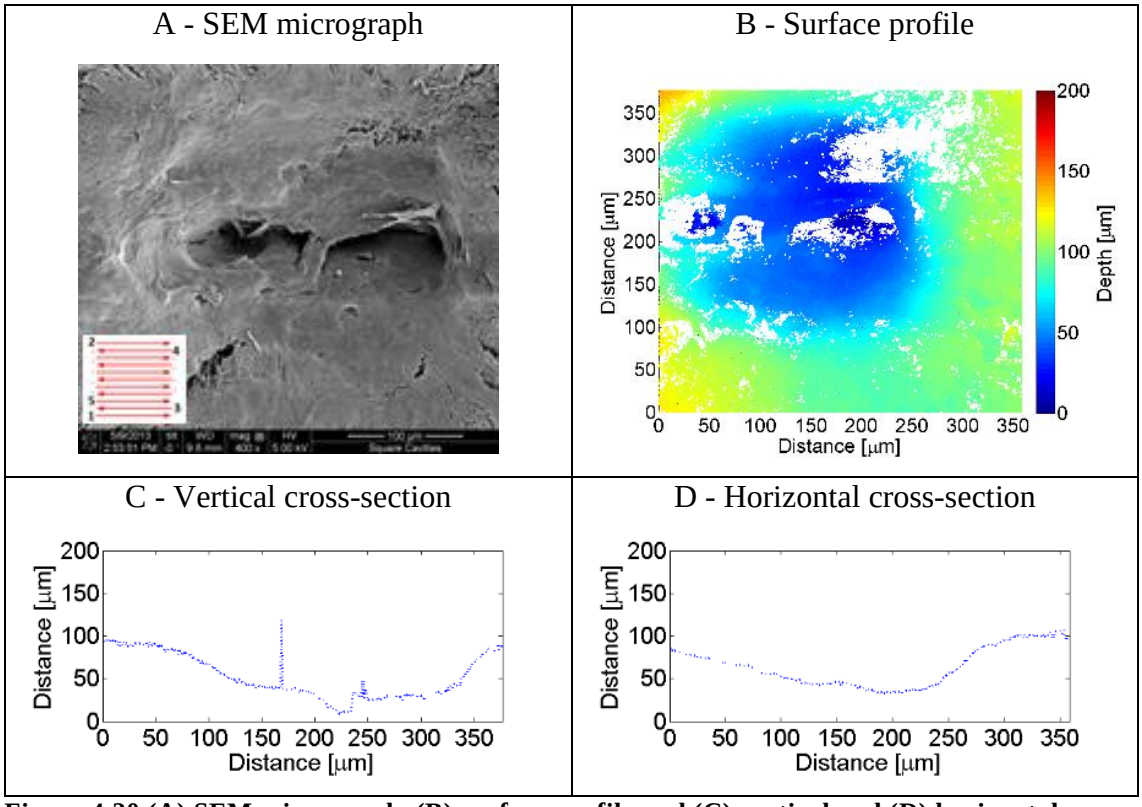

Figure 4.20 (A) SEM micrograph, (B) surface profile and (C) vertical and (D) horizontal cross-section plots for the raster scan with alternating directions and alternating lines between top and bottom. Wavelength of 1030 nm, pulse energy of 60 µJ, repetition rate 1 kHz, spot and line separation of 3 µm.

The final scanning pattern that was tested was alternating both the direction of the scan as well as position of the scan between top and bottom as shown in Figure 4.20. The idea was minimize heat accumulation by spreading consecutive scans as from each other as possible. Unfortunately this approach has not reduced the effect of the heat accumulation

and the cavity is again deeper towards the end of the scanning pattern. Additionally due to the complicated scanning pattern which has a constant change of direction, this results in much more irregular heat accumulation conditions. The cavity is noticeably more irregular compared to those produce with the other patterns as seen in Figure 4.20. As a result this approach was discarded for any future experiments as the created cavity is too irregular and does not provide consistent cavities. Moreover when considering potential future applications, a simpler scanning approach is desirable due to limited amount of space near the ablation site.

The next step when investigating different scanning patterns was focused on testing whether the introduction of additional scanning lines around the cavity would decrease the slope of the bottom surface. The addition of the extra laser passes around the main processing provides well defined borders to the cavity on all of the sides. In previous experiments, without that approach, the side at which the scanning pattern started was not always clearly defined which led to a sloped bottom surface. Hence this experiment tests whether this approach will make any significant improvement to the process.

To investigate whether this approach would have any benefit on the created cavities, three lines around the main scanning pattern were introduced (as shown in Figure 4.21). This extra scanning pattern was done for all of the previously investigated raster patterns. Figure 4.22 shows the SEM micrographs, surface profiles and vertical cross-section of the created cavities.

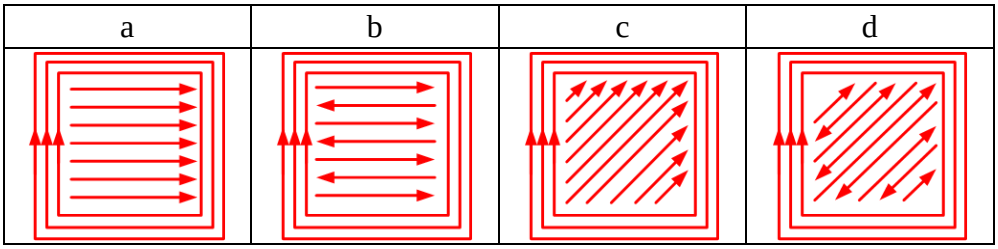

Figure 4.21 All of the scanning patterns investigated in current section with the three scanning passes around the main processing area: a- simple raster scan; b- raster scan with alternating directions; c - angular scan; d - angular scan with alternating direction.

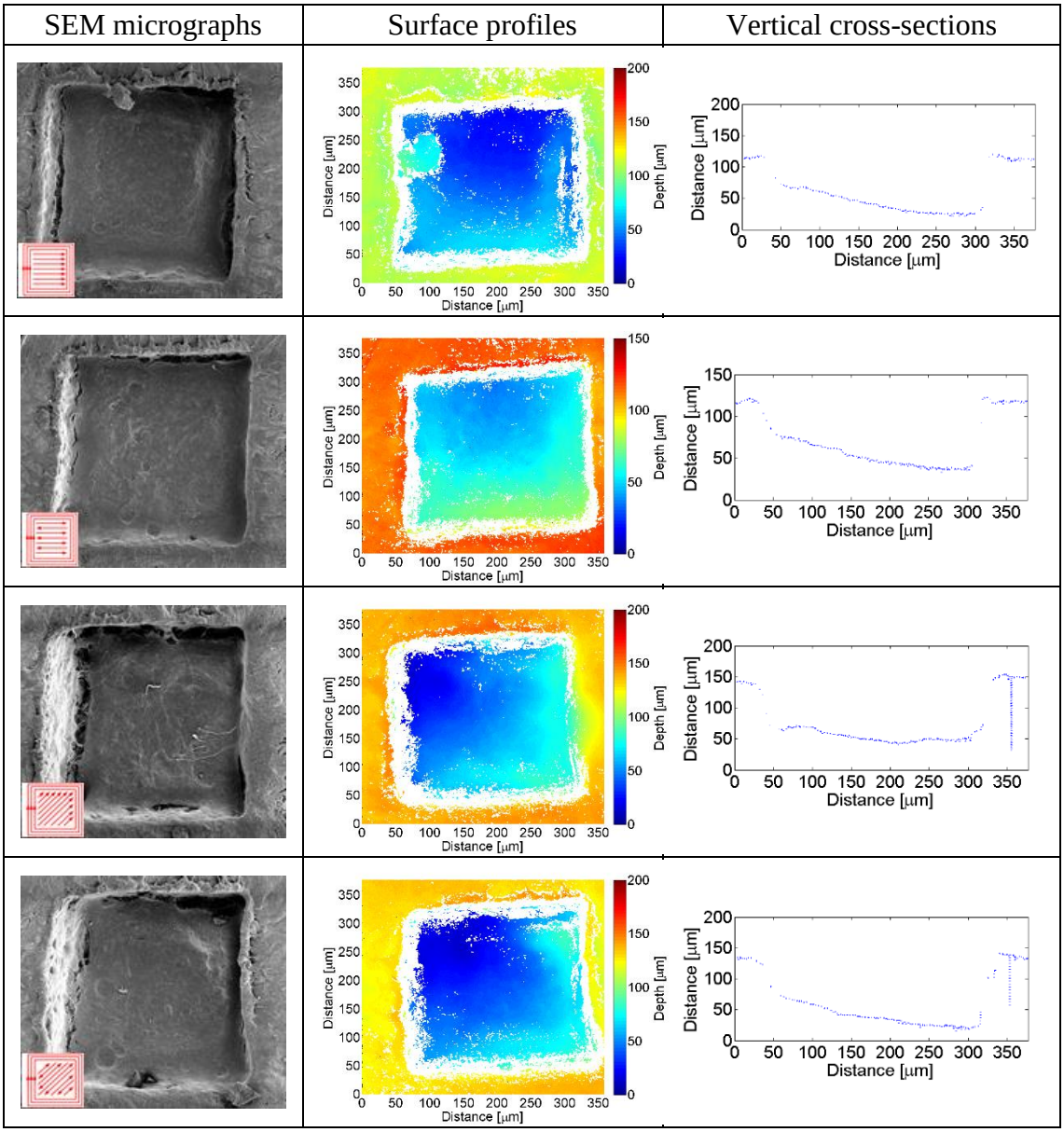

Figure 4.22 SEM micrograph, surface profile and vertical cross section through the middle of the cavity plots for a simple raster scan, snake like pattern, angle pattern, angle pattern with alternating directions. All of the scanning patterns have additional three scanning passes around the main part of the pattern added. Wavelength of 1030 nm, pulse energy of 60 µJ, repetition rate of 1 kHz, spot separation of 3 µm.

Most of the cavities produced with the additional scanning line around the main pattern have a bottom surface less sloped compared to those from previous experiments. The average angle of the slope is calculated from a right triangle constructed from the surface, point of maximum depth and point where cavity starts. Figure 4.23 shows the procedure of calculating the average slope angle of the cavity and the formula used is shown (Equation (3.1). For all four scanning patterns the introduction of the outer pre-scanning lines has led to decreased slope angle of the bottom surface. On average, using a pre-

scanning process before main removal process has led to a decrease of the average slope angle of the bottom surface by 22.5%.

$$\alpha = \tan^{-1} = \frac{length}{depth} \tag{4.1}$$

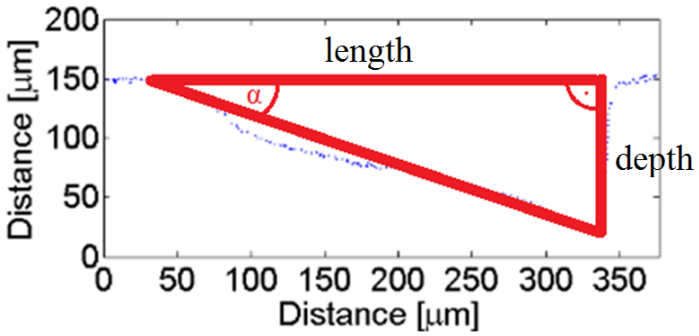

Figure 4.23 Procedure of calculating an average slope angle.

Table 4.1 Comparison of the bottom surface average slope angle for different scanning patterns. Wavelength of 1030 nm, pulse energy of 60 µJ, repetition rate 1 kHz, spot separation of 3 µm.

Average slope angle (deg) No additional scan around the main scanning pattern		Average slope angle (deg) Additional scanning lines around the main area present	
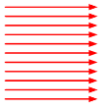	24.9	17.6	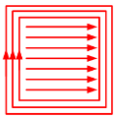
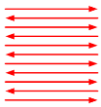	23.0	14.8	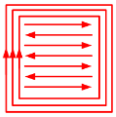
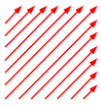	23.4	20.5	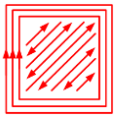
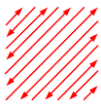	22.6	19.6	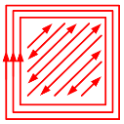

The final goal of the project is to create a lesion in scleral tissue towards the rear of the eye where there is limited space. This means that the beam delivery system needs to be relatively compact and hence relatively simple. Although some of the more complex patterns produced a more uniform cavity profile, the bottom surface was less sloped. Thus the simplest scanning pattern (without additional scanning lines around the main scanning area) was chosen as better suited for current research as it simplifies the potential design of the end probe delivery mechanism.

4.5.2. The effect of repetition rate

The previous section (4.5.1) was focused on investigating the influence of different scanning strategies on the shape and depth of created cavities. This section is focused on the influence that repetition rate has on the uniformity of obtained lesions. As mentioned in previous sections, heat accumulation is a major factor in the quality and shape of created cavities, and is influenced by the time delay between consecutive pulses. Higher repetition rates reduce the time between consecutive pulses and as a result energy deposited in the tissue by the previous pulse has less time to diffuse into the surrounding bulk tissue. Scleral tissue has a low value of thermal conductivity coefficient (k = 0.58 W/(m·K) [82]) therefore reducing the time between pulses has a large influence. It is clearly seen in the simulation chapter (Figure 5.12 in Section 5.3.4) that after one single line scan is completed there is residual energy leftover in the area where the beginning of the consequent scan would be. To investigate the influence of the repetition rate on raster scanning patterns, the same 4 patterns (without extra scanning lines around, see Figure 4.15) - simple raster scan (Figure 4.15 a), raster scan with alternating directions (Figure 4.15 b), 45^o angular scan (Figure 4.15 c), 45^o angular scan with alternating directions (Figure 4.15 d) - were again implemented. The speed of galvanometer scan head was adjusted accordingly to provide a constant value of spot separation between consecutive pulses of 3 µm. Firstly a test was carried out with a repetition rate much higher that any of the previously investigated, 100 kHz, to demonstrate the catastrophic damage caused for a highly non-optimised process.. Figure 4.24 shows an optical microscopy image of the cavity and severe damage can be seen as the whole are of the cavity is carbonized as a result of laser processing.

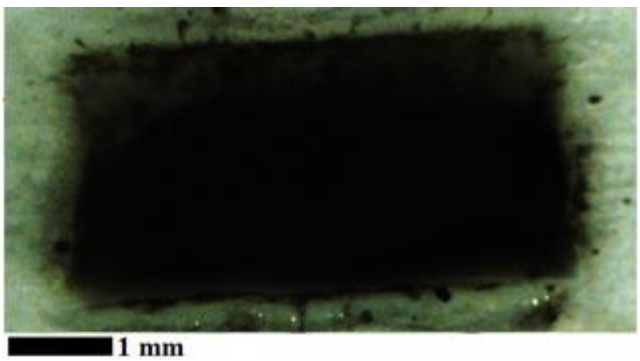

Figure 4.24 An optical microscopy image of the cavity obtained using simple raster scanning pattern with the repetition rate of 100 kHz. Wavelength of 1030 nm, pulse energy of 60 µJ, repetition rate 100 kHz, spot separation of 3 µm and stage speed of 300 mm/s.

Consequently, a lower laser repetition rate was tested - 10 kHz. Figure 4.25 shows SEM micrographs, surface profiles and cross sections of cavities created with the laser

repetition rate of 10 kHz, pulse energy 60 µJ, spot and line separation - 3 µm and scanning speed 30 mm/s.

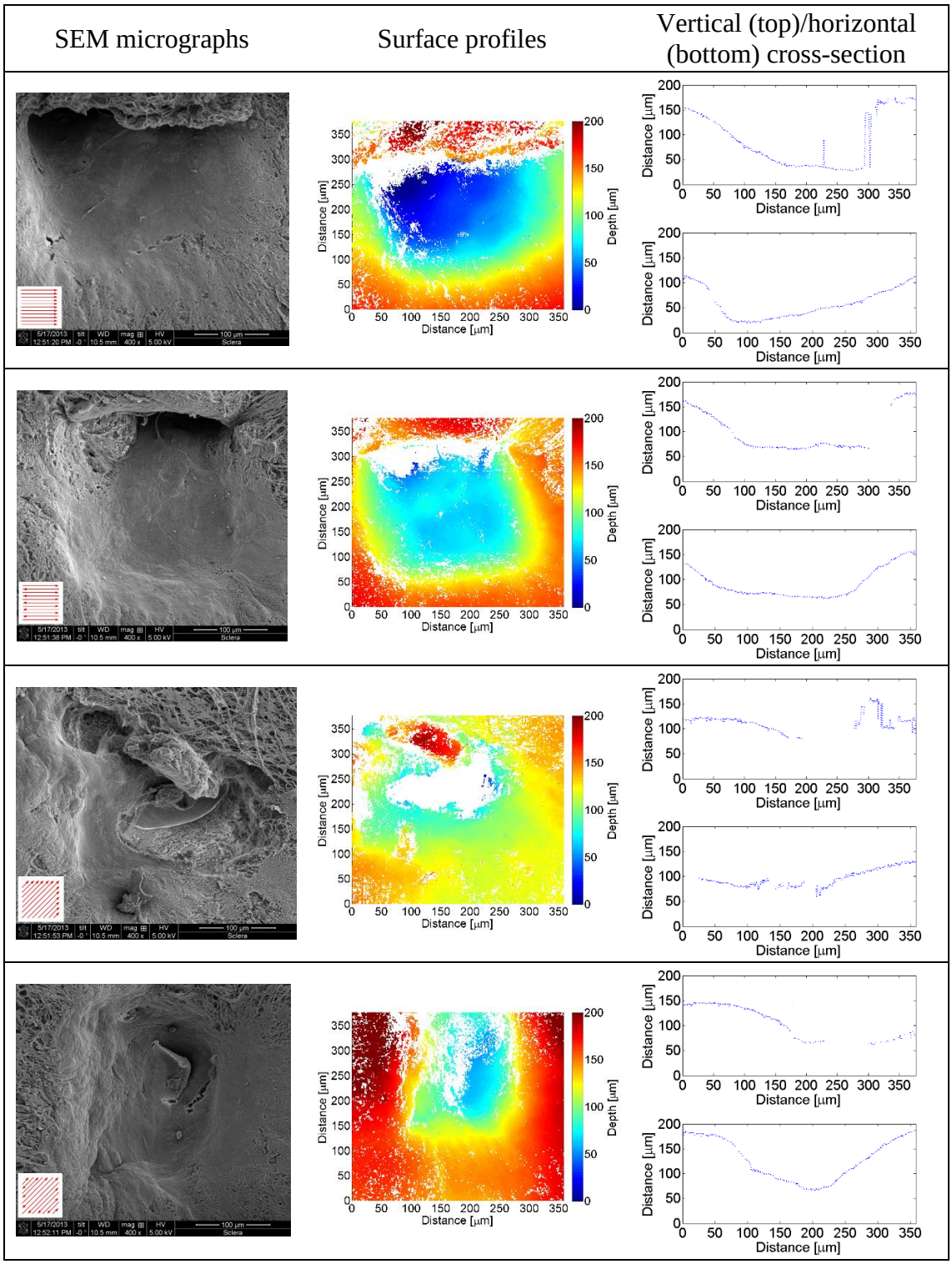

Figure 4.25 SEM micrograph, surface profile and vertical cross section plots for a simple raster scan, snake like pattern, angle pattern and angle pattern with alternating directions (without additional scanning lines around the main scanning pattern). Wavelength of 1030 nm, pulse energy of 60 µJ, repetition rate of 10 kHz, spot and line separation of 3 µm, scanning speed of 30 mm/s.

Cavities created with the repetition rate of 10 kHz show a high degree of heat accumulation. Compared to the cavities created with the lower repetition rate of 1 kHz described in section 4.5.1, cavities are distorted, uneven, have non-uniform shapes and exhibit localised deep regions. Consequently the laser repetition rate of 100 Hz was investigated to see if this produced more uniform cavities than those for 1 kHz. Figure 4.26 shows SEM micrographs, surface profiles and cross sections of cavities obtained with four different scanning patterns with the repetition rate of 100Hz.

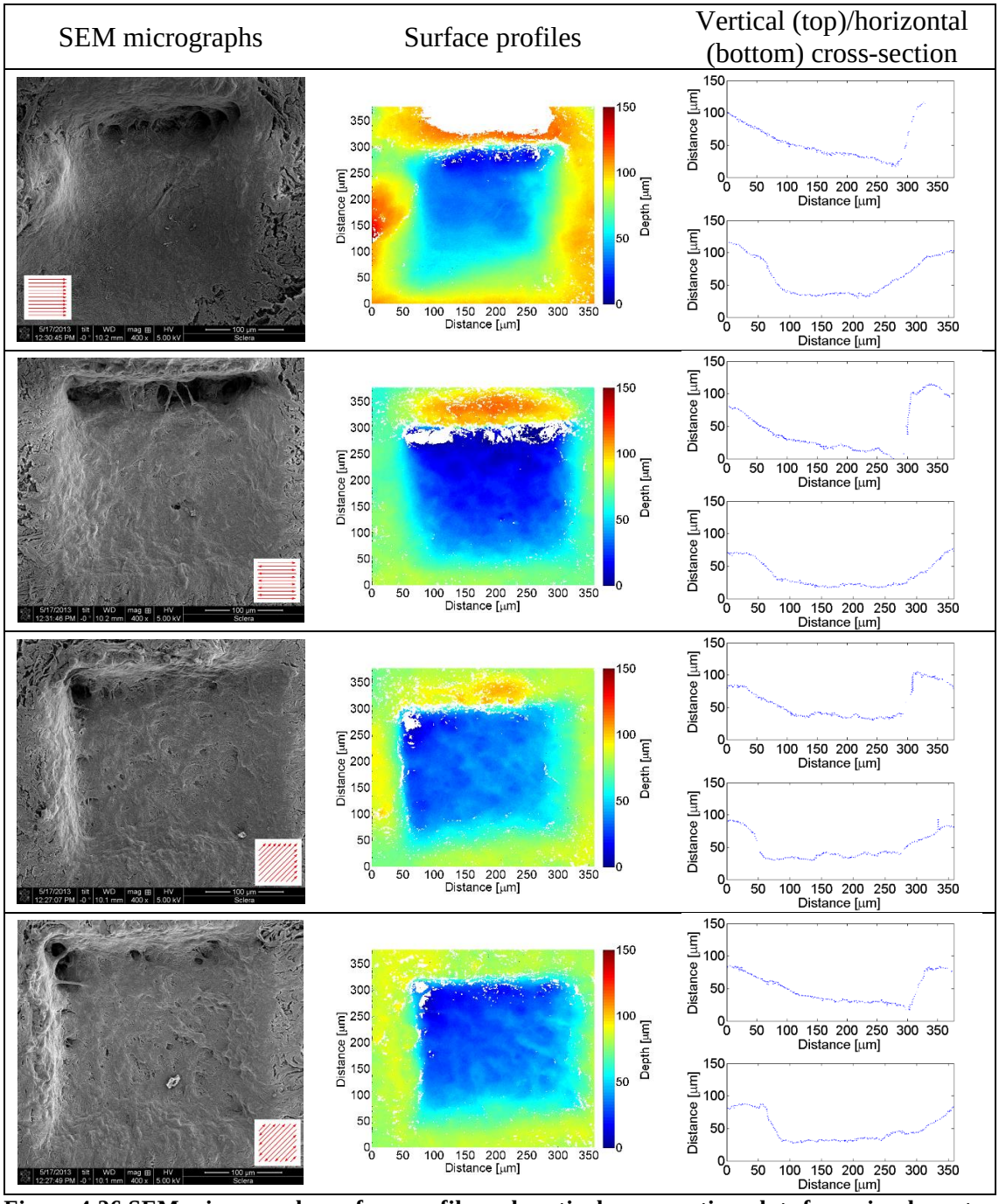

Figure 4.26 SEM micrograph, surface profile and vertical cross section plots for a simple raster scan, snake like pattern, angle pattern and angle pattern with alternating directions (without additional scanning lines around the main scanning pattern). Wavelength of 1030 nm, pulse energy of 60 µJ, repetition rate of 100 Hz, spot separation of 3 µm.

As expected ablation with the lower repetition rate has led to creation of cavities without introducing any unwanted damage, due to a much reduced thermal input into the sample. However, as would be expected with reduced energy input, the maximum depth of the created cavities was significantly lower than for cavities created with higher repetition rate of 1 kHz. The lower repetition rate increases the time between consecutive pulses, which allows for the thermal energy to diffuse before consecutive pulse arrive. As a result more energy is needed to create plasma and hence remove material.

To better compare three different repetition rates an average input of energy was calculated. To calculate the total amount of energy input into a sample, for a simple raster scanning pattern, equation 4.2 was used and the value was 576.24 mJ. For different repetition rates, the total value of energy is constant, but it does get delivered in longer (for lower repetition rate) or shorter (for higher repetition rate) span of time.

$$Totla\ energy = number\ of\ lines \cdot number\ of\ pulses \cdot pulse\ energy \tag{4.2}$$

Exemplary calculations for a raster scanning pattern – 300 μm by 300 μm, pulse energy of 60 μJ, spot separation of 3 μm and line separation of 3μm.

- Due to spot separation of 3 μm there are 98 pulses in one line. Both first and last pulse have a 3 μm separation between first scanning line and border line of the area that is scanned, hence:

$$\frac{300\ \mu m - 3\ \mu m - 3\ \mu m}{3\ \mu m} = 98\ \text{pulses}$$

- Due to line separation of 3 μm there are 98 lines in the scanning pattern. Both first and last line have a 3 μm separation between separation between first scanning line and border line of the area that is scanned, hence:

$$\frac{300\ \mu m - 3\ \mu m - 3\ \mu m}{3\ \mu m} = 98\ \text{lines}$$

$$\text{Total energy} = 98\ \text{lines} \cdot 98\ \text{pulses} \cdot 60\ \mu J = 576\ 240\ \mu J$$

Since a simple raster scanning pattern of 300 μm by 300 μm square cavity takes approximately 2 s for 10 kHz, 30 s for 1 kHz and 97 s for 100 Hz laser repetition rate, the average amount of energy delivered to the sample surface is 288120 μJ/s for 10 kHz, 19208 μJ/s for 1 kHz and 5940.8 μJ/s for 100 Hz. As a result the input of energy over time for 1 kHz is 15 times lower compared to the input of energy with 10 kHz repetition rate. Moreover the input of energy with the lowest 100 Hz repetition rate is 3.3 times

lower compared to a 1 kHz repetition rate and 48.5 times lower compared to 10 kHz. As a result, the energy deposition rate is significantly higher for higher repetition rates, which limits material capacity to dissipate heat, especially given that sclera has a low thermal conductivity (k = 0.58 W/(m·K) [82]).

A different factor that can be used to quantify the difference between scanning patterns is maximum cavity depth. To investigate two different repetition rates were used and the maximum depth and average slope angle of the cavities were measured. For an angular scanning pattern, slope angle is measured diagonally across the ablation site from the starting point to the end point of the scanning pattern.

Table 4.2 Maximum depth of cavities and the average angle of the bottom surface.

	Maximum Depth of the bottom surface slope [µm]		Average angle of the bottom surface slope [deg]	
	100 Hz	1 kHz	100 Hz	1 kHz
	80	139	14.9	24.9
	77	127	14.4	23.0
	72	130	13.5	23.4
	68	125	12.8	22.6

The cavities ablated by using lower repetition rate of 100 Hz are approximately half as deep as those created with higher repetition rate of 1 kHz. Laser machining at either 100 Hz or 1 kHz produced no unwanted thermal damage. Therefore it is more efficient to use the higher repetition rate of 1 kHz as heat accumulation works to assist material removal without causing unwanted effects

4.5.3. Different spot separation

A different approach to control the heat accumulation effect on the process is to increase pulse-to-pulse separation and line spacing. The increase of the distance leads to energy deposition being more separated in space. Moreover the total energy deposited into the tissue during one scanning process is smaller (for a given pulse energy) as it requires

fewer laser passes to cover the same area. For this experiment a simple raster scan was investigated and the spot separation was controlled by increasing the scanning speed. The smallest spot separation investigated was 1 µm and the biggest spot separation was 31 µm, which was similar to the diameter of the focused spot size – 35 µm. The line separation was equal to used spot separation. The repetition rate in this experiment was 1 kHz, pulse energy 60 µJ and the scanning speed varied from 1 mm/s to 31 mm/s to achieve the desired spot separations. Figure 4.27 shows the SEM micrograph of created lesions for different spot separation and pulse overlap values. The pulse overlap was calculated using Equation 4.3.

$$pulse\ overlap = \frac{spot\ diameter - spot\ separation}{spot\ diameter} \qquad \textbf{4.3}$$

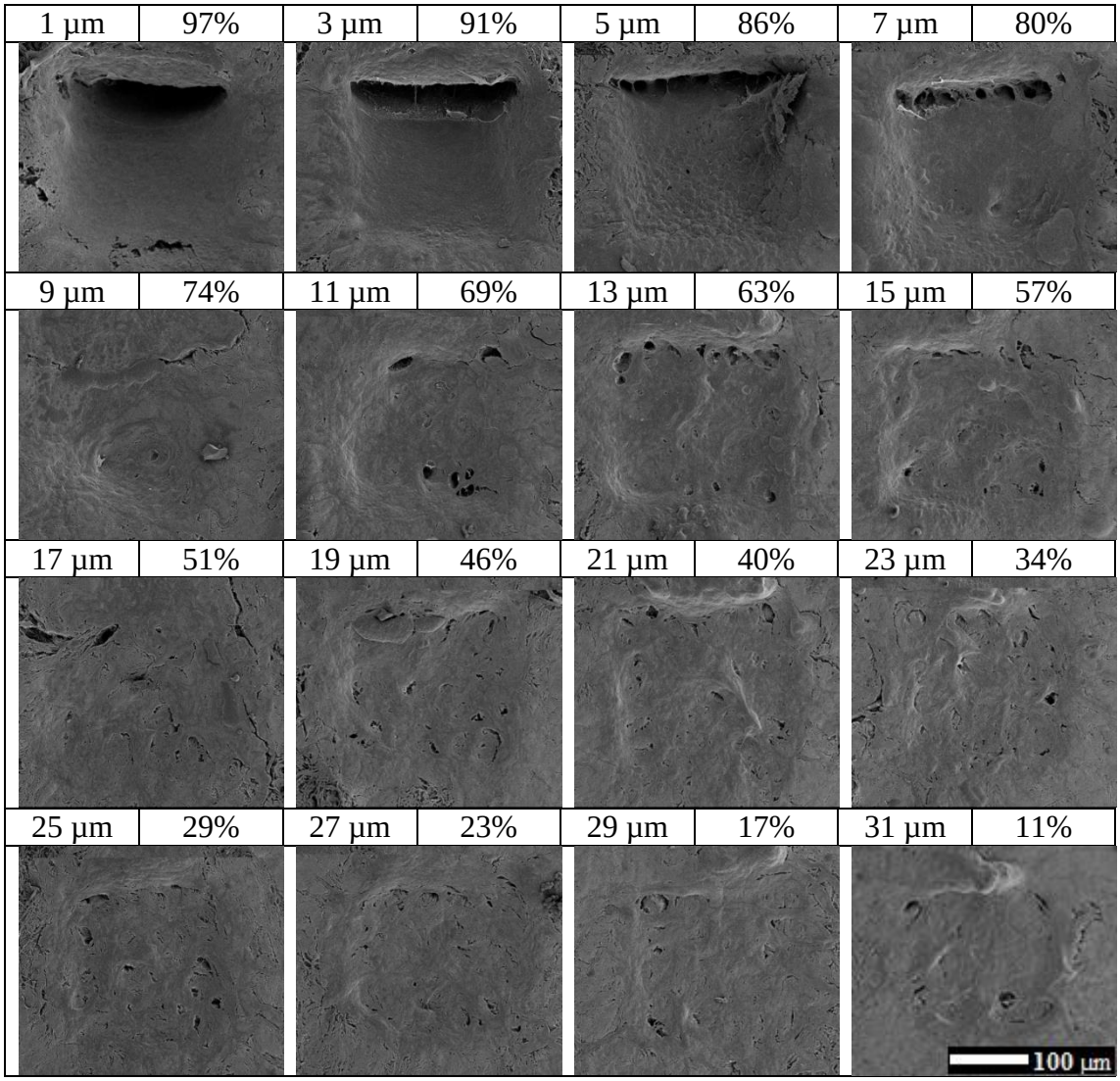

Figure 4.27 SEM micrographs of the cavities created with a simple raster scanning pattern with different spot separation. Above picture spot and line separation and pulse overlap is shown. Repetition rate used of 1 kHz.

The increased spot and line separation does have a major influence on the process since it decreases the total amount of energy deposited in the tissue, and the energy that is deposited on the surface is much more spread out. As a result, for higher spot separations there is almost no removal of tissue observed, and the area of ablation is hard to define, especially for spot overlaps lower than 50%. For pulse overlap between 50% and 85% the ablation area is visible but the cavity is not very well defined and the bottom surface is not uniform. Using the smallest spot separations (below 3 μm) which is equivalent to spot overlaps higher than 90%, created cavities were better defined with a bottom surface that is more uniform and consistent (although still shows the slope due to heat accumulation). Unfortunately cavities created with scanning patterns that have high spot and line separation are of a very bad uniformity and bottom surface quality. Hence using multiple passes with high spot separation will exaggerate the effect of having a non-uniform cavity. On the other hand patterns with low spot separation produce a smooth bottom surface.

4.5.4. Effect of pulse energy

These feasibility tests form part of the early stage research for a procedure that ultimately would be carried out *in vivo* using a novel customised surgical device. Therefore there is a desire to have as simple a scanning process as is possible in order to assist in device design, a requirement which is exacerbated due to space limitations behind the eye. Although more well defined and uniform cavities were obtained when extra scanning lines were introduced around the main area of removal, such a modification of the scanning pattern would increase the difficulty in performing the incision in a very limited space *in vivo*, and would add complication to the envisaged surgical device. As for the repetition rate, the optimal value that was selected was 1 kHz. Higher repetition rates (10 kHz or 100 kHz) were shown to introduce irreversible thermal changes to the ablation site as well as to adjacent tissue. Conversely, a lower repetition rate of 100 Hz leads to a lower amount of tissue removed and the process time is increased to around 10 times that for a process carried out at 1 kHz.

The final parameter space to investigate was the influence of pulse energy at the optimal repetition rate of 1 kHz. To investigate the influence of pulse energy on the depth and shape of the cavity, an experiment was carried out using 3 μm spot/line separation. Figure 4.28 shows the SEM micrograph of the created cavities. Figure 4.29 shows the maximum depth reached and Figure 4.30 shows the ablation efficiency (volume of the material removed per unit of energy).

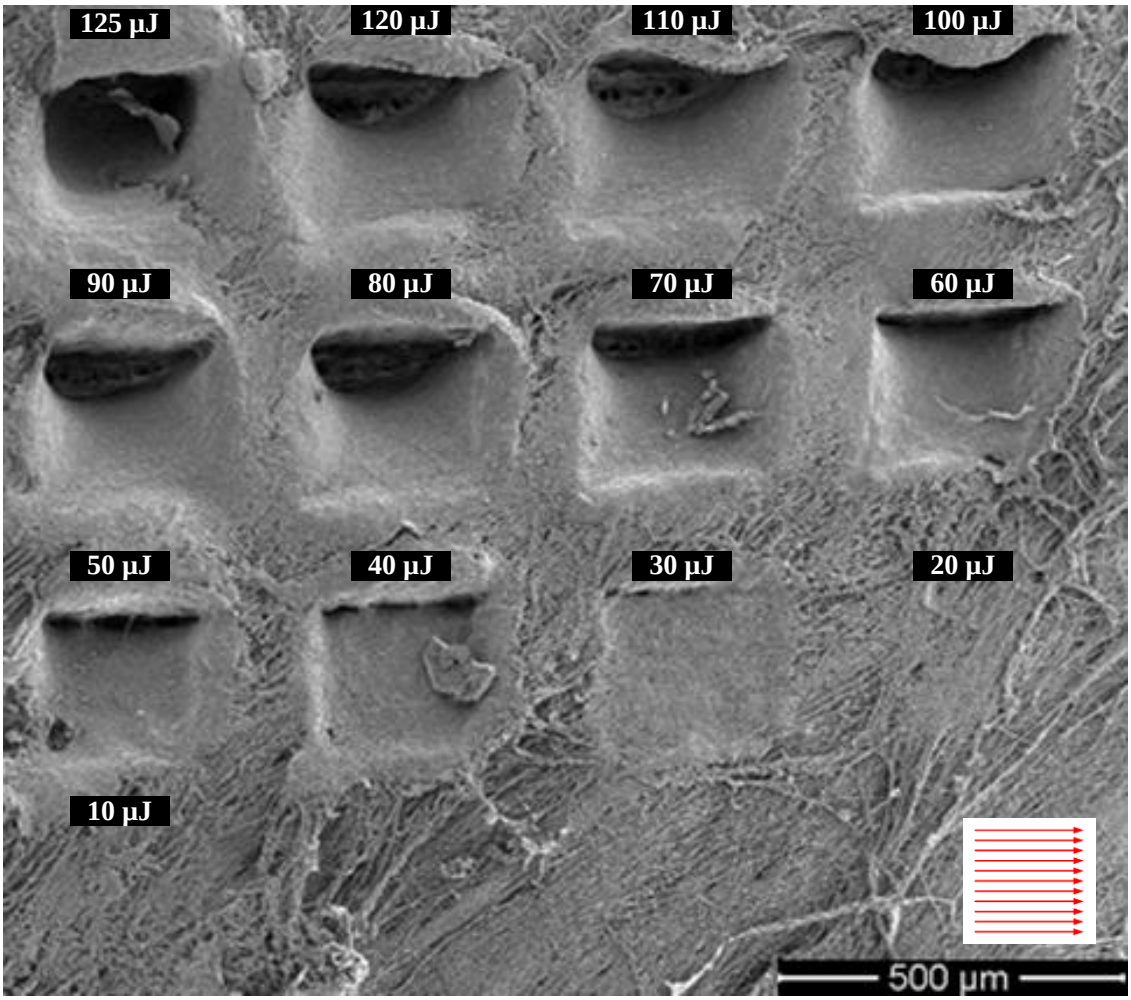

Figure 4.28 SEM micrograph of square cavities created with simple scanning pattern with different pulse energies. Wavelength of 1030 nm, repetition rate of 1 kHz, spot separation of 3 µm.

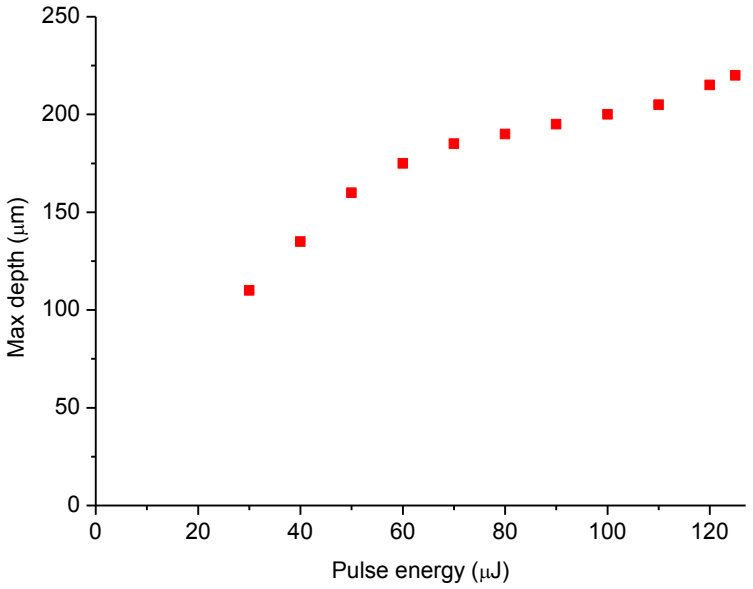

Figure 4.29 Maximum depth reached for a single square raster scanning pattern (1 kHz, 3 µm spot separation, 3 mm/s) as a function of pulse energy.

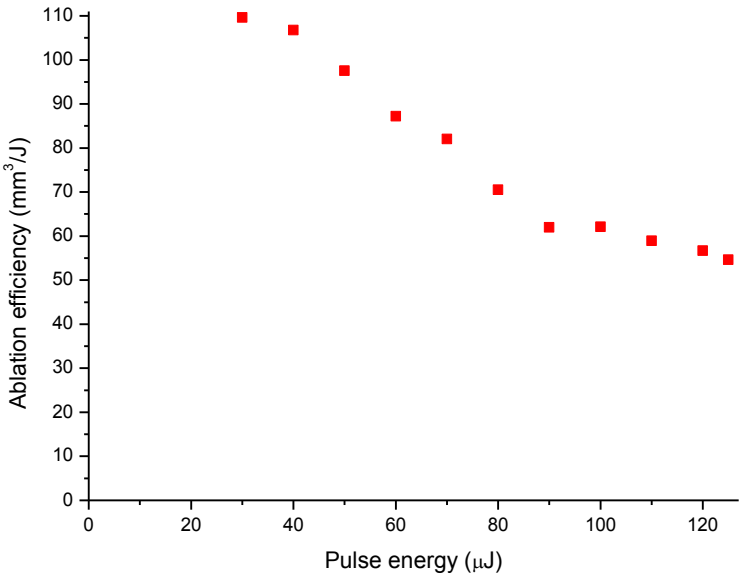

Figure 4.30 Ablation efficiency for a single square raster scanning pattern (1 kHz, 3 µm spot separation, 3 mm/s) as a function of pulse energy.

The first results were obtained when a pulse energy of 30 µJ was used, which agrees with the results achieved in the previous section focused on investigating single line ablation. When using 1 kHz repetition rate for pulse energies below 30 µJ the irradiance threshold is not high enough to reach a plasma creation threshold. The relationship between maximum achieved depth and pulse energy is not proportional, and if the energy is tripled (30 µJ → 90 µJ) the maximum depth is only increased by around 96% (105 µm → 201 µm). As a result of this effect, the value of ablation efficiency decreases when pulse energy increases. The volume of the removed tissue was calculated using the equation for the volume of a triangular prism created from the length, width and maximum depth of the cavity (Equation (4.4).

$$Volume = \frac{1}{2} \cdot width \cdot length \cdot maximum\ depth \qquad (4.4)$$

As a result, the calculated value for volume is directly influenced by changes in the maximum depth. Hence the pulse energy best suited for this process is in the range between 40 and 60 µJ as they enable creation of a well-defined cavity and they offer the most efficient ablation for these particular processing parameters.

Figure 4.31 shows the average angle of the bottom surface. The average angle of the slope was calculated using the maximum depth reached and by calculating right triangle assuming that surface was flat (Equation (3.1 and Figure 4.23). Naturally, the value of the average angle follows the same trend as the value of maximum depth reached as it is directly dependent on that value.

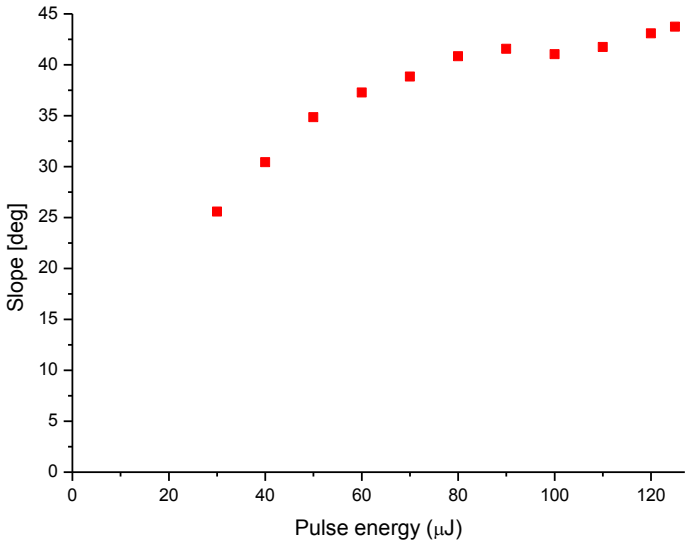

Figure 4.31 Average angle of the bottom surface for a single square raster scanning pattern (1 kHz repetition rate, 3 µm spot separation, 3 mm/s) as a function of pulse energy.

Using the simple raster scanning pattern it is possible to create a square cavity without introducing any unwanted thermal damage. One of the major benefits of the ultrafast lasers application is that it is possible to precisely define and control depth reached by the process. One major factor that has to be taken into consideration is heat energy accumulation, as this has a major influence on the final outcome of the process, especially on the slope of the bottom surface of the cavity.

Jiang and Yang [89, 90]have investigated a possibility of creating a square cavity with a femtosecond laser while using only snake shape like scanning pattern. They have only reported using one pulse energy and one scanning pattern as opposed to the investigation of different pulse energies, scanning patters and repetition rates. However, the square cavity published in that paper is not as sloped, but it is not flat either, exhibiting multiple drops in the bottom surface and a bigger drop at one end of the cavity. Moreover, they are using femtosecond instead of picosecond pulses, which decreases the amount of heat deposition (which increases process efficiency when controlled) but significantly increases processing times as the scanning speed is ~10 times lower and spot diameter is half the size. An image of the cavity can be found in literature review – Section 2.4.6 and Figure 2.27. Other reported results by Sacks [91-94] and Chai [95] investigate the possibility of creating subsurface cavities using a focused spot size which is almost 10 times smaller, resulting in a much smaller cavity. Using a picosecond laser results in a significantly more efficient process, as shown in this research, as the scanning speeds and

spot sizes are higher, which allows the removal of more material in a shorter period of time. Unfortunately it was not possible to create a subsurface cavity using picosecond pulses as longer pulse durations, compared to femtosecond lasers used in previously mentioned publications, led to thermal damage to the tissue due to increased energy absorption. Using shorter pulse durations it is possible to achieve plasma for lower irradiances which minimizes thermal damage.

4.6. The effect of scanning pattern

In previous sections single line ablation and square cavity ablation were investigated whereas this section is focused on finding the optimal parameters for creating flat bottomed circular cavities. A range of different concentric and spiral scanning patterns were tested. In particular, spiral scanning patterns offer the possible advantage over other patterns since the laser radiation can be continuously deposited onto the sample surface.

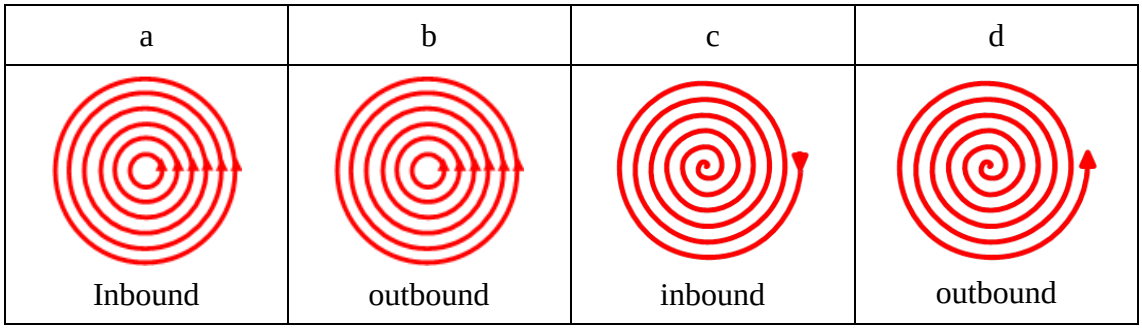

Figure 4.32 All of the scanning patterns investigated in current section. a - an inbound concentric circles scanning pattern; b - an outbound concentric circles scanning pattern; c – an inbound spiral scanning patter; d – an outbound spiral scanning pattern.

4.6.1. Concentric scanning patterns

Initial experiments regarding the possibility of creating a circular cavity were focused on a scanning pattern composed of concentric circles. The first investigated pattern was an inbound concentric pattern as shown Figure 4.32 which means that the outermost circle was scanned first and consecutively the laser beam was scanned in a smaller circular pattern. Similarly to the previous experiment, investigating square cavities, a range of different laser repetition rates were tested: 100 Hz, 1 kHz and 10 kHz for the same pulse energy of 60 µJ, and a spot separation of 3 µm. Figure 4.33 shows the SEM micrographs, surface profiles and horizontal cross-section of the cavities.

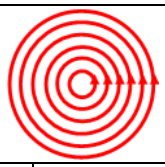	Inbound concentric circles scanning pattern		
	SEM Micrograph	Surface Profile	Horizontal cross-section
100 Hz	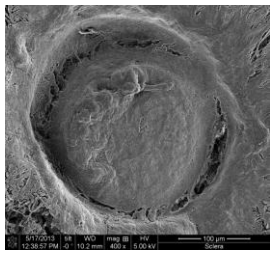	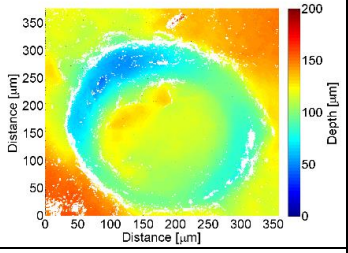	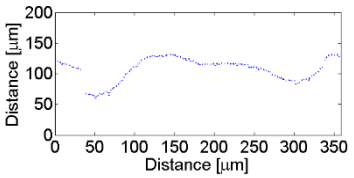
1 kHz	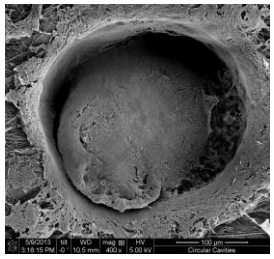	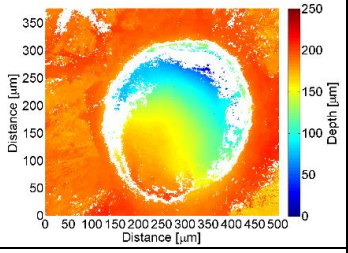	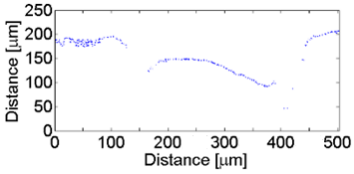
10 kHz	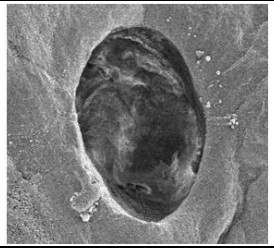	No data	No data

Figure 4.33 SEM micrographs, surface profiles and horizontal cross-section for an inbound scanning pattern for different repetition rates. (0.1, 1, 10 kHz repetition rates, spot separation of 3 µm, pulse energy of 60 µJ).

It is apparent that the results are very similar to those achieved for square cavities with characteristic sloped structures. With a repetition rate of 10 kHz there was a lot of thermal damage as the circular cavity was heavily distorted and irregular. Since the use of higher repetition rate (10 kHz) has led to thermal damage, the cavity profile was not measured as a 10 kHz repetition rate was found to be not suitable for picosecond laser machining of scleral tissue. For the lower repetition rate of 100 Hz, the bottom surface of the cavity is very uneven and the maximum depth that it reaches is around 45 µm. The best results were once again achieved when using a repetition rate of 1 kHz. There is some benefit from heat accumulation, as it is able to remove more material than lower repetition rates, but still doesn't show any sign of the unwanted thermal damage that is clearly visible for higher repetition rates. Unfortunately however, this scanning pattern was not capable of creating a flat bottomed cavity due to previously mentioned heat accumulation effect.

The next scanning pattern tested was an outbound concentric circle which is the reverse of the inbound pattern see Figure 4.32. Figure 4.34 shows SEM micrographs,

surface profiles and horizontal cross-sections of cavities created with an outbound scanning pattern constructed with concentric circles. The processing parameters were the same as those used in preceding experiment, that is: pulse energy 60 µJ, spot and line separation 3 µm. The change of the direction of the scanning did not have any major influence on the shape of the cavity, and the obtained results are very similar to those achieved with an inbound concentric circle scanning pattern. Even though scanning was designed with the aim of spreading out energy deposited from the inside of the ablation site to the outside for the repetition rate of 10 kHz there is a lot of thermal damage to the ablation site as well as to the adjacent tissue. There is still evidence of the heat accumulation effect causing the cavity to get deeper towards the edges (i.e. towards the end of the scanning pattern). This effect can be seen on a surface profiles on Figure 4.34 where the centre of the cavity is higher (where scanning pattern commences) than the outsides of the cavity (where scanning pattern finishes).

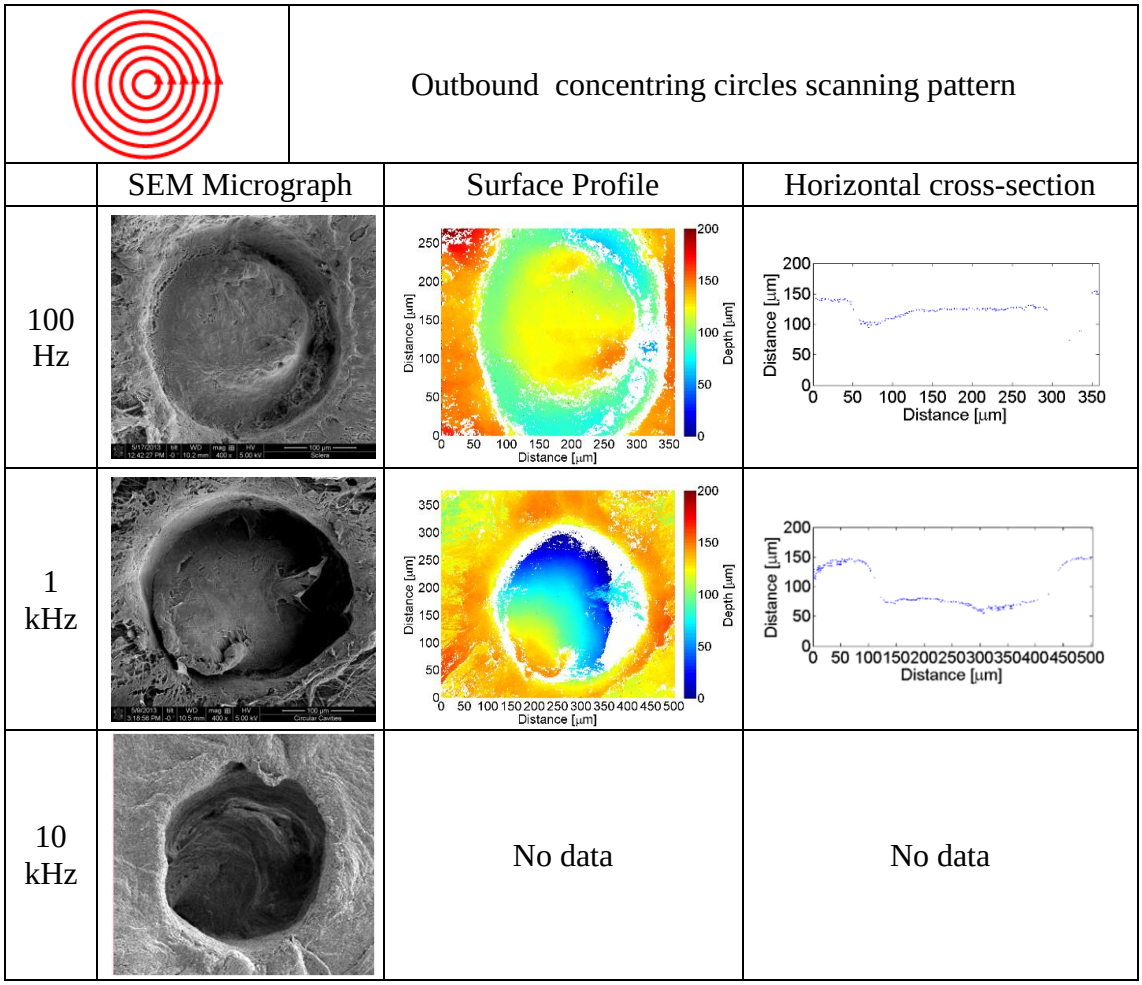

Figure 4.34 SEM micrographs, surface profiles and horizontal cross-section for an outbound scanning pattern for different repetition rates (0.1, 1, 10 kHz repetition rates, spot separation of 3 µm, pulse energy of 60 µJ).

4.6.2. Spiral scanning patterns

Another two patterns that were tested were an inbound and an outbound spiral scanning pattern. These patterns have one major difference when compared to all of the scanning patterns that were previously tested that is the laser beam is constantly depositing energy into the sample surface as the pattern is essentially one continuous line. As seen from simulations (Figure 5.12) presented later in Section 5.3.4 the peak of the accumulated energy "follows" the focused spot size. With the lower values of spot and line separation (usually 3 μm) a scanning pattern diameter of 300 μm and a scanning speed of 3 mm/s a symmetrical heat deposition is predicted in the tissue around the centre of the created cavity.

Firstly, an inbound scanning pattern was tested as shown in Figure 4.32. The parameters used in the experiment are the same as those used in all of the previous experiments: pulse energy 60 μJ, spot and line separation 3 μm and three different repetition rates 100 Hz, 1 kHz and 10 kHz. Figure 4.35 shows SEM micrograph, surface profile and a horizontal cross-section of the cavities. When machining with the highest repetition rate, the cavity and the adjacent tissue is heavily deformed due to thermal effects and accumulated heat, as was observed in all preceding experiments at 10 kHz. On the other hand, both of the cavities machined with a lower repetition rate do not display any unwanted thermal damage, even though this scanning pattern leads to much higher thermal deposition in one spot compared to the previous patterns. Cavities created with this pattern have a symmetrical shape and a characteristic cone like dip in the centre. As mentioned previously in this chapter and shown in the simulation chapter (Figure 5.12 in section 5.3.4) the heat accumulation "follows" the laser spot as it translates over the surface hence the use of an inbound spiral pattern led to the creation of dip in the centre. When using lowered repetition rate; 100 Hz compared to 1 kHz, the duration of the whole scanning pattern is 10 times longer and the heat has more time to dissipate. As a result a cavity created with 1 kHz repetition rate increases its depth in a rather uniform way, whereas for a 100 Hz repetition rate there is a dimple close to the centre of the cavity. Whenever the diameter of the scanning decreases, the time for the laser spot to make a whole revolution decreases and the heat accumulation in the area increases, leading to a higher removal rate.

Inbound spiral scanning patterns

	SEM Micrograph	Surface Profile	Horizontal cross-section
100 Hz	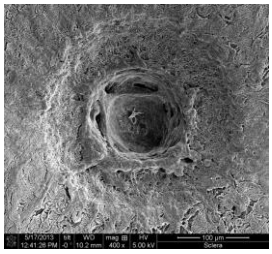	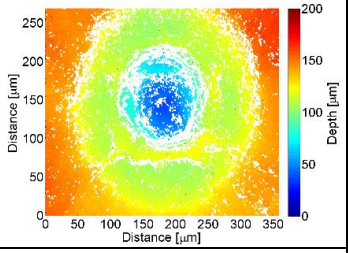	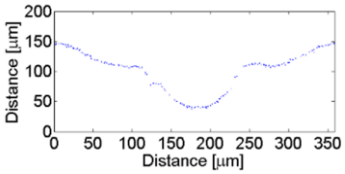
1 kHz	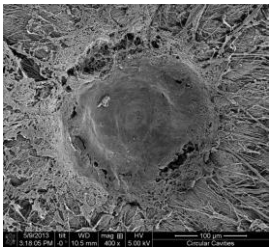	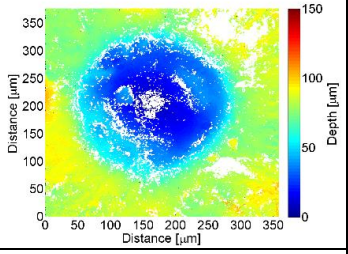	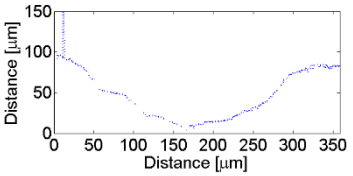
10 kHz	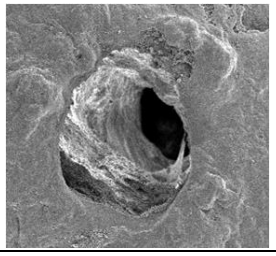	No data	No data

Figure 4.35 SEM micrographs, surface profiles and horizontal cross-section for an inbound spiral scanning pattern for different repetition rates (0.1, 1, 10 kHz repetition rates, spot separation of 3 µm, pulse energy of 60 µJ).

Consequently an outbound spiral scanning pattern (see Figure 4.32) was tested using the same laser processing parameters as previously: pulse energy 60 µJ, spot/line separation 3 µm and three different repetition rates 100 Hz, 1 kHz, 10 kHz. Figure 4.36 shows SEM micrographs, surface profiles and horizontal cross-section obtained in this experiment.

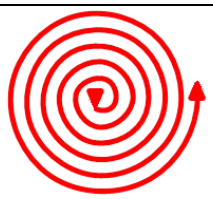	Outbound spiral scanning patterns		
100 Hz	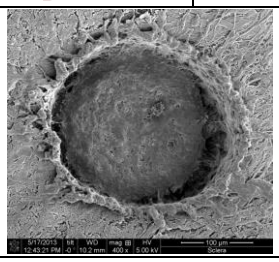	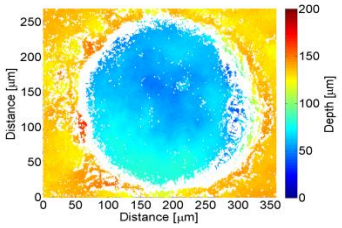	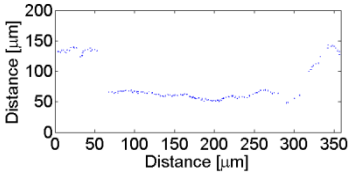
1 kHz	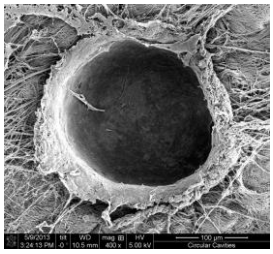	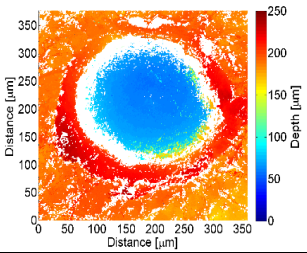	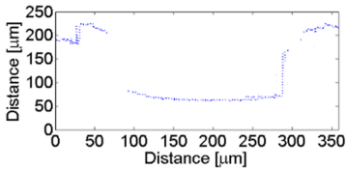
10 kHz	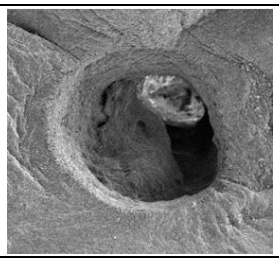	No data	No data

Figure 4.36 SEM micrographs, surface profiles and horizontal cross-section for an outbound spiral scanning patter for different repetition rates (0.1, 1, 10 kHz repetition rates, spot separation of 3 µm, pulse energy of 60 µJ).

Scanning of the laser beam with an outbound scanning pattern, starting from the centre of the ablation site, has been very successful in creating a well-defined cavity with a flat bottom surface. For both 100 Hz and 1 kHz repetition rates the cavities created have sharp edges and well defined side walls and most importantly flat bottom surfaces. Having a flat bottom surface shows much more precise control over the processing parameters. Moreover if the desired maximum depth of cavity is e.g. 200 µm, then using an outbound scanning pattern it is possible to have the whole bottom surface at that level, whereas when using square raster scanning, a sloped bottom surface is going lead to decreased volume of the cavity. As a result the volume into which drug could be potentially placed is being minimized, decreasing the efficiency of the drug delivery process.

In an outbound spiral scanning pattern, scanning starts from the inside to the outside. As a result the thermal accumulation conditions in the centre of the cavity are similar to those at the outside. Accumulated heat does "follow" laser spot size, and its value is going to be the highest at the end of the scanning pattern, but the time of the full revolution and return of the spot size to the same area (line separation was just 3 µm)

close to the centre of the cavity is much shorter than for the outer regions. When considering the last revolution of the pattern it takes ~0.3 s and when considering second revolution the time scale is ~0.06 s. As a result, even though heat accumulation is "following" the laser spot size, and is larger, it has more significantly more time to dissipate before the whole revolution of the scanning pattern. Unfortunately, even these improvements to the scanning technique have not minimized the scale of thermal damage caused to the ablation site and the adjacent tissue for the higher repetition rate of 10 kHz.

4.6.3. The effect of spot separation

The conclusions from the previous set of experiments are that an outbound spiral scanning pattern is best suited for removal of a circular shaped cavity, due to its capability of having a fairly uniform distribution of accumulated heat. Therefore a set of experiments was focused on the investigation of the influence of spot/line separation. To achieve the desired spot separation while maintaining same repetition rate, scanning speed was adjusted accordingly. The pulse energy used in this experiment was set at 60 µJ. Figure 4.37 shows SEM micrographs of all of the cavities obtained in this experiment.

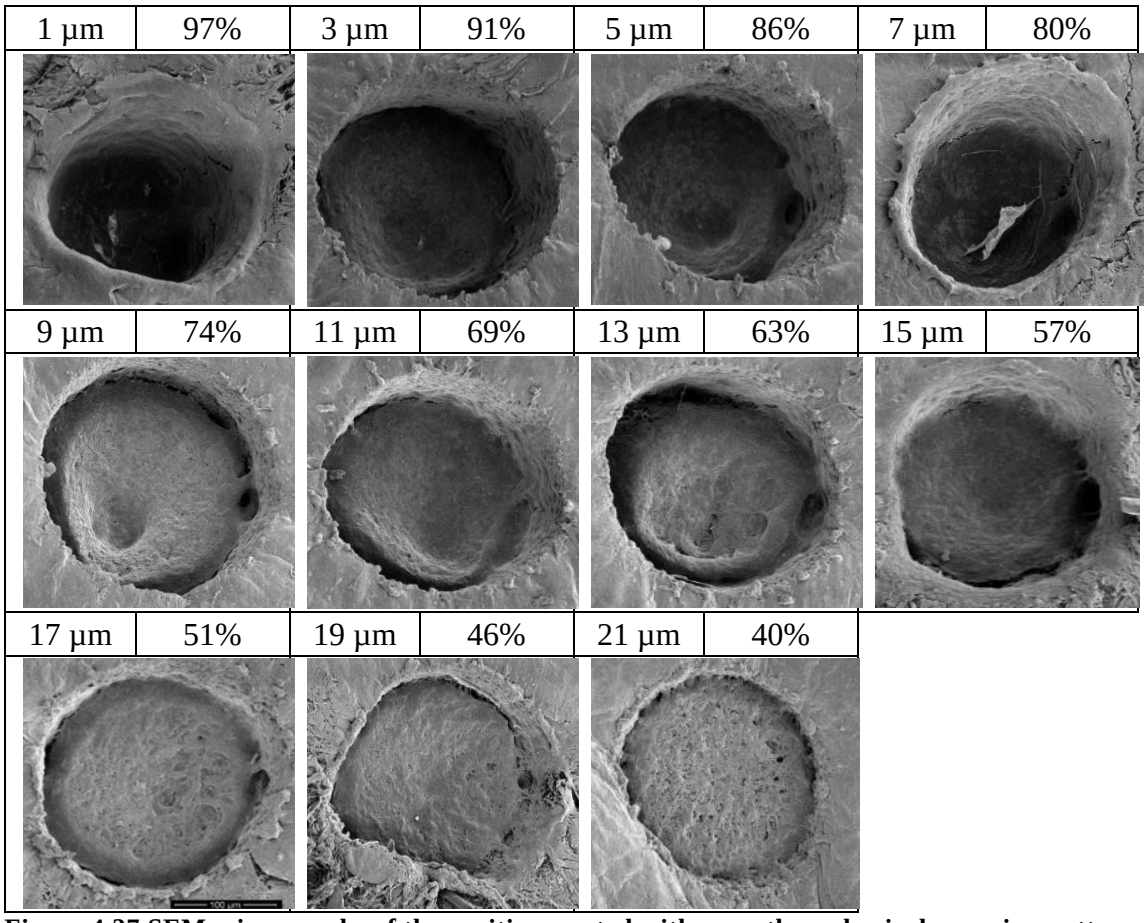

Figure 4.37 SEM micrographs of the cavities created with an outbound spiral scanning pattern with different spot separation. Above picture spot/line separation and pulse overlap is shown. Repetition rate used 1 kHz and pulse energy 60 µJ.

All of the tested spot/line separations were successful in creating circular cavities, but they have significantly different depths. Increasing the spot/line separation results in a decreased amount of pulses that interact with the tissue, as well as the total energy that is deposited into the tissue. Additionally it was observed that a larger spot/line separation does create a small slope closer to the side wall of the cavity in an otherwise flat bottomed profile. Figure 4.38 shows the maximum depth of the cavity created with an outbound scanning pattern for different spot and line separations.

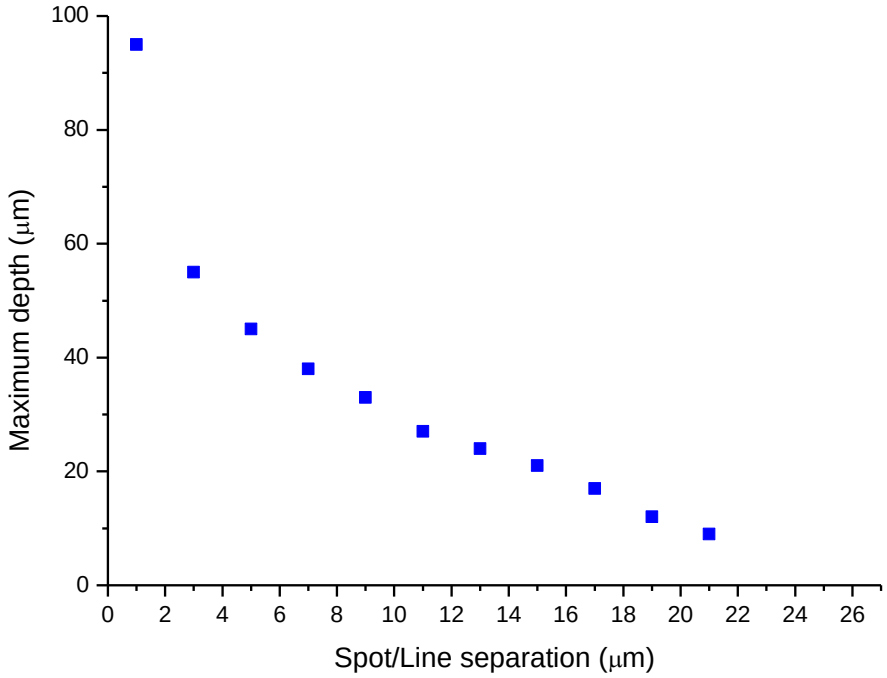

Figure 4.38 Maximum cavity depth as a function of different spot and line separations (1-21 μm) for an outbound spiral scanning pattern. Repetition rate used 1 kHz, pulse energy 60 μJ.

4.6.4. Effect of pulse energy

The last set of experiments were focused on investigating the influence that pulse energy has on cavity depth, while maintaining same lateral (spot and line separation) and temporal (laser repetition rate) parameters of the outbound spiral scanning pattern. In preceding experiments it was found that it is best to use repetition rate of 1 kHz, as processing does not cause any unwanted thermal damage to the ablation site or adjacent tissue. Moreover, heat accumulation allows more efficient (faster) material removal compared to processing with the lower repetition rate of 100 Hz. The spot separation that was chosen was 3 μm, as closely packed pulses provide a uniform flat bottom surface of the cavity. Figure 4.39 shows cavities created with different pulse energies with an outbound spiral pattern. Moreover the maximum depth of the cavities was measured using a white light interferometer and the ablation efficiency was calculated approximating the

volume of the removed tissue, using the equation for the volume of a cylinder. Figure 4.40 shows the maximum depth and ablation efficiency for different pulse energies.

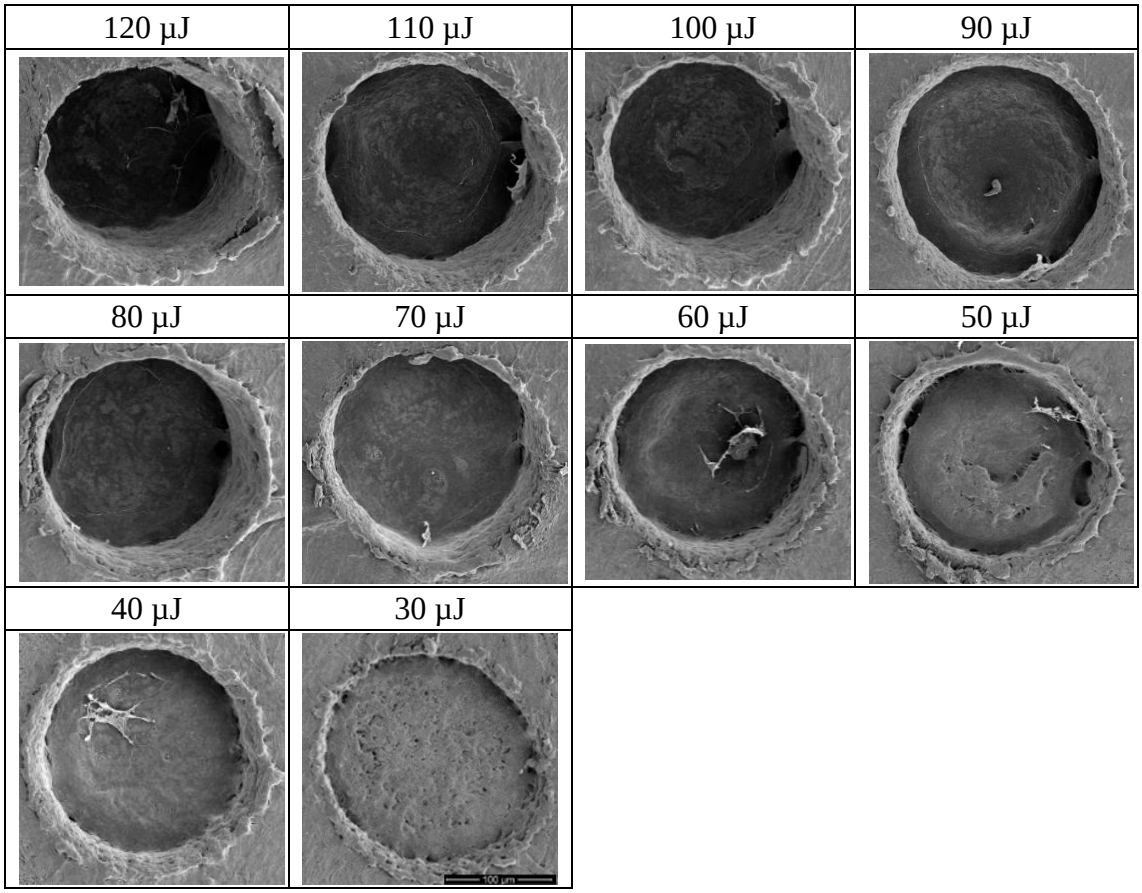

Figure 4.39 SEM micrograph of circular cavities created with an outbound spiral scanning pattern with different pulse energies. Repetition rate of 1 kHz, spot separation of 3 µm.

Using an outbound spiral scanning pattern, repetition rate of 1 kHz and spot/line separation of 3 µm it is possible to precisely control the depth of the cavity from 20 µm to 195 µm. These values fit the initial idea of having control over the cavity depth in the range of 200 µm, so that the structure of the whole eyeball was not disturbed by having deeper cavities. Consequently, this process allows precise control over the necessary depth of the cavity, because it is possible to achieve any depth of the cavity within range, simply by selecting the necessary pulse energy. The important feature of this is that the pulse energy limits the depth, so that in a real process it provides assurance that the cavities created will not go too deep i.e. a potentially fail safe process. The ablation efficiency of this process does increase when pulse energy increases due to the increased amount of heat accumulated. The increase in the maximum depth between 30 and 40 µJ is 6 µm whereas that increase between 100 µJ and 110 µJ is 28 µm. As a result the relation between depth and pulse energy is not linear, which leads to an increased value of ablation efficiency for higher pulse energies.

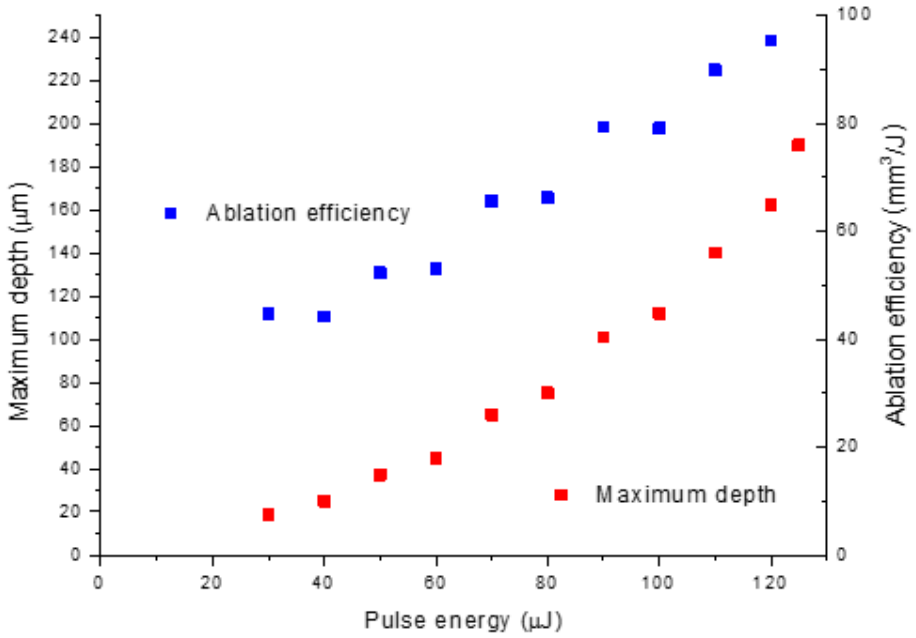

Figure 4.40 Maximum ablation depth and ablation efficiency as a function of pulse energy for an outbound spiral scanning pattern. Wavelength of 1030 nm, pulse energy of 60 µJ, repetition rate 100 Hz, spot separation of 3 µm.

When trying to create a circular cavity, there were the same issues with heat accumulation as when investigating ablation of the square cavity. The difference is that by selecting a much more appropriate scanning pattern, it is possible to use heat accumulation to the benefit of material removal without introducing any unwanted thermal damage. An outbound spiral scanning pattern was capable of creating a well-defined, flat bottomed cavity due to a uniform distribution of accumulated heat over the area of the ablation site. By changing the pulse energy it is possible to precisely control the depth of the cavity to fit necessary size requirements, depending on the size of the reservoir needed to deposit drugs or to potentially place a microelectromechanical system (MEMS) device that would release drugs over time.

There is little previous evidence of laser induced circular cavities in the literature. The experiment most similar to the work conducted here was done by Jian and Yang [89, 90] where they used a femtosecond laser to create a circular cavity. The cavity created by the femtosecond laser was small (~30 µm diameter), and the beam was stationary (not scanned) and focused below the surface. Although the femtosecond process allows the formation of sub surface voids of the order of 20 µm high and 200 µm long [93, 94] it does not seem a viable technique for removing the relatively larger areas (of the order of a few mm^2) that would be required to assist the drug delivery from a patch or other bespoke delivery device (which would have dimensions in the order of a few mm). The picosecond processing presented here takes advantage of a relatively non-thermal process

(if the parameters are optimised as discussed above) whilst still maintaining appreciable removal rates, enabling the expected surgical procedure time to be minimised.

4.7. Transmission measurement

When investigating the feasibility of a process that is envisaged to be used in medical practice, it is necessary to perform some basic experiments focusing on the safety of the process at this early stage of the research, in order to ensure that the process would be realistic from a patient safety aspect. Hence a set of experiments was carried out, focusing on investigating whether there is any residual radiation being transmitted through the tissue during the laser process that potentially could cause damage to the retina or blindness. The sclera is mostly composed of water (70%), which does not have a high value of absorption at a wavelength of around 1 µm, especially when compared to the Er:YAG wavelengths of 2.94 µm. However, the tissue is highly scattering (hence its white appearance) which would reduce the total amount of light transmitted. Moreover, most of the laser radiation is going to be absorbed or reflected by plasma, and only a fraction of it is going to be deposited into the tissue. Hence experiments testing a whole scanning pattern were performed to ensure the safety of the process. The damage threshold for retinal tissue for the picosecond pulse regime and 1030 nm wavelength is in the range $8 \cdot 10$ J/cm^2 [143], which is roughly similar to values achieved for 60 µJ pulse energies. Figure 4.41 shows the experimental setup. To ensure that any energy that could go through the sample was captured, both power meters used in the experiment were placed several millimetres below the bottom surface of the tissue. Moreover the smallest measuring surface of the power meters used was at least 9.7 mm in diameter and the biggest scanning pattern used was 2 mm by 2 mm, which ensures that any radiation transmitted through the sample will be picked up by the power meter.

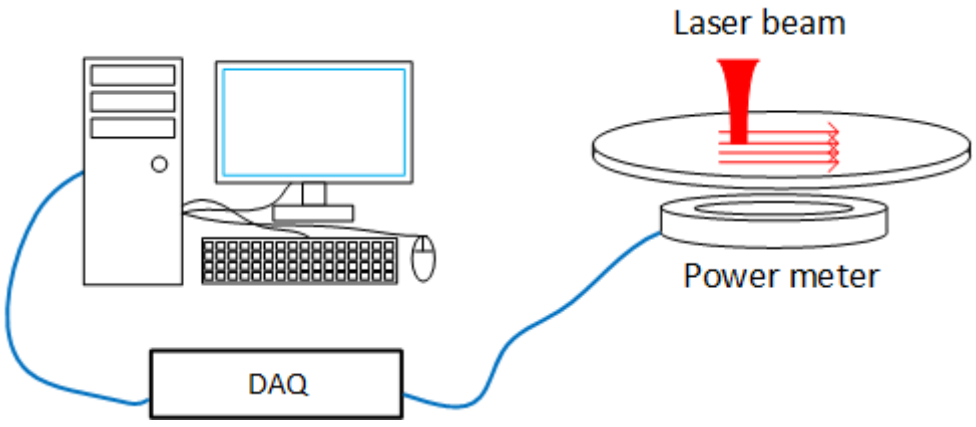

Figure 4.41 Experimental setup used in the transmission measurement.

Two repetition rates were tested: 10 kHz and 1 kHz. Even though it has been shown that processing with a repetition rate of 10 kHz is not suited for this application, as it introduces thermal damage into the tissue, it was tested to see the effect of repetition rate on transmission. A range of pulse energies was tested from 10 µJ to 125 µJ, to cover the range of parameters tested for machining of the cavities. The scanning pattern tested was a simple raster scan with a 3 µm spot and line separation and the area scanned was 1 mm by 1 mm. Even though the best results were obtained for an outbound scanning pattern, a simple raster scanning pattern was chosen for the optical transmission measurements as the spiral pattern was too quick and did not allow meaningful measurements to be taken. Firstly the average power of the whole scanning process was recorded with a thermal laser sensor – Ophir Optronics – FL250A-LP1-SH-V1. The power to noise level of this sensor is 10 mW and the response time is approximately 2.5 s [144]. Scans took around 10, 15 and 115 seconds depending on the repetition rate used, hence it was possible to have an initial measurement and record average power with this power meter and then use the more sensitive power meter - Thorlabs S120C, for selected measurements. Figure 4.42 shows the average power over the span of the process for three different repetition rates when using 60 µJ pulse energy. This is for the situation where the laser is directly incident on the power meter (i.e. no sclera). The value on the graph is lower than the average power of the laser, as this is the measurement of the average power over the whole processing time, but the laser is off while the scan head is changing lateral position to the next starting point in the scanning pattern. It should be noted that there are no major fluctuations of the measured power from the action of the laser switching on and off during the scan as the time that it takes for the scan head to travel is much lower that the response time of the power meter. The total time that the scan heads spend on ramping the speed up and down and traveling from the previous scanning line to the next one is in the range of ~5 second for the whole 1 mm by 1 mm square raster scanning pattern. Since in the whole pattern with 3 µm line separation there are 331 lines, the average time between consecutive scanning lines is ~3 milliseconds.

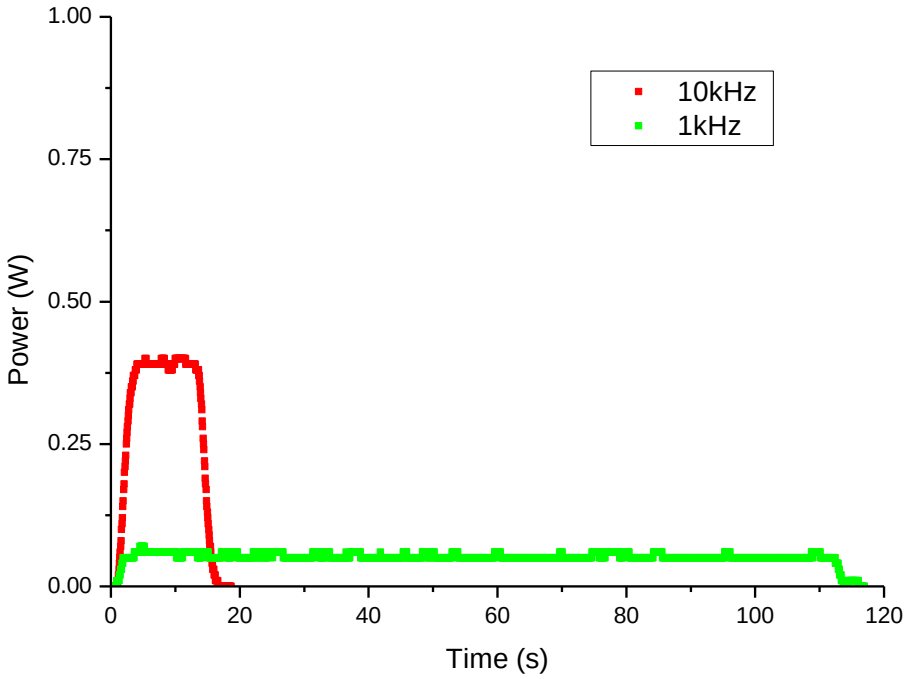

Figure 4.42 Average power of the scanning pattern over the span of the whole process for three different repetition rates: 10 kHz and 1 kHz Pulse energy used 60 µJ. Spot and line separation 3 µm.

After the average power of the whole process had been recorded, the same measurement was performed during actual laser processing of the tissue. Figure 4.43 shows the average power recorded during laser processing of the tissue for the different repetition rates: 10 kHz and 1 kHz. The power meter recorded minimal power fluctuations which were of the same order of resolution as the power meter [144]. Hence none of the tested scanning patterns and parameters were able to transmit any measurable amount of energy that was of any significance.

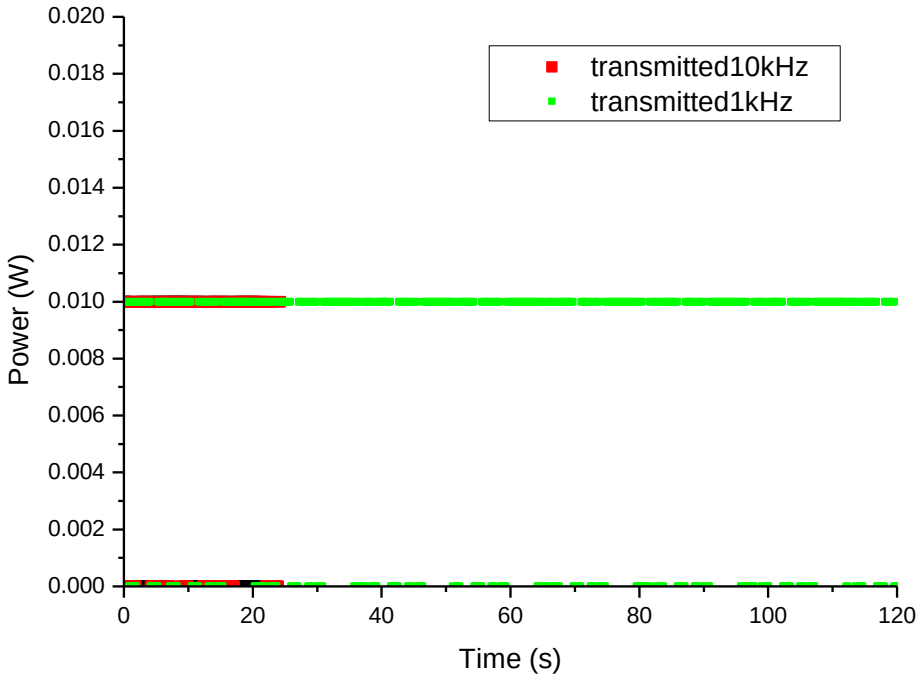

Figure 4.43 Average power transmitted through the scleral sample during the whole of the scanning process.

Since previously used power meter Ophir Optronics is a thermal meter with an uncertainty of 10 mW, there was a need to use a much more sensitive sensor to prove that there is no energy leakage through the sample during processing. In the next experiment a quick silicon photodiode power sensor was used – Thorlabs S120C. It has a response time below 1 µs and a measurement resolution of 10 nW [145]. To prevent any potential damage to this power meter, it was only used for a 1 kHz repetition rate and 60 µJ pulse energy scanning pattern. The measurement has not returned any meaningful data as only a background noise was recorded, hence it is possible to assume that no radiation was transmitted through the tissue.

This experiment has confirmed initial assumptions about the process and proved that there is essentially no laser energy being transmitted through the tissue. The majority of the laser energy is absorbed or reflected by the plasma. Any energy that is incident before the plasma is created is highly scattered and not transmitted through the tissue. Consequently it has been shown that the process it not likely to present any risk to the patient in terms of damage to the retina.

4.8. Temperature increase

In the previous section the safety of the process was investigated in relation to the transmission through the tissue. Another consideration regarding the safety of this process is the potential temperature rise during tissue processing which could cause damage to the eye. A critical temperature rise that will cause damage to the retina was investigated by Wang [146] and was found that for process of 10 s duration the damage threshold was the temperature increase of 23.8 ^{o}C and for longer process of 100 s the critical temperature increase was 11.7 ^{o}C [146]. As in the previous experiment, a simple raster scan was investigated as opposed to the outbound spiral scanning pattern as the spiral pattern was too quick to record reliably. The samples used in this experiment were again prepared with a 5 mm trephine. The temperature was measured using four thermocouples (type J) placed 1 mm from the centre on horizontal and vertical axes. To ensure best possible heat transfer between the sample and thermocouples the samples were put directly onto the tips of thermocouples and gently pushed down. Data was recorded on the PC using LabVIEW software and National Instruments Data Acquisition Module NI 9219 with Hi-Speed USB Carrier NI USB-9162. The scanning patterns used were designed to be scanned over the centre part of the sample. For 100 Hz and 1 kHz repetition rates, the created cavity had a 1 mm by 1 mm dimension, whereas for higher repetition rate of 10 kHz cavity was twice this size that is 2 mm by 2 mm, in order to have a process that was long enough to record the temperature rise. A range of pulse energies were tested from 20 µJ to 120 µJ in 20 µJ steps and the spot and line separation used was 3 µm. Figure 4.44 shows a schematic of the experimental setup that was used. Figure 4.45 shows the maximum temperature (maximum temperature recorded at any time by either of thermocouples) for each scanning pattern that was tested.

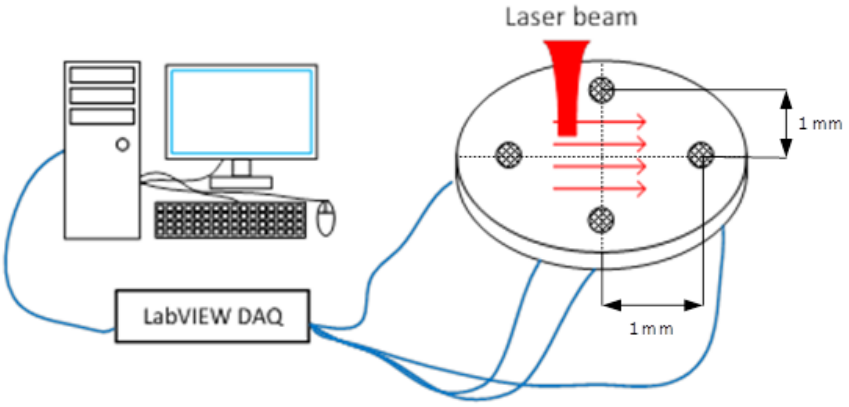

Figure 4.44 Experimental setup used to measure temperature raises during laser machining of the tissue.

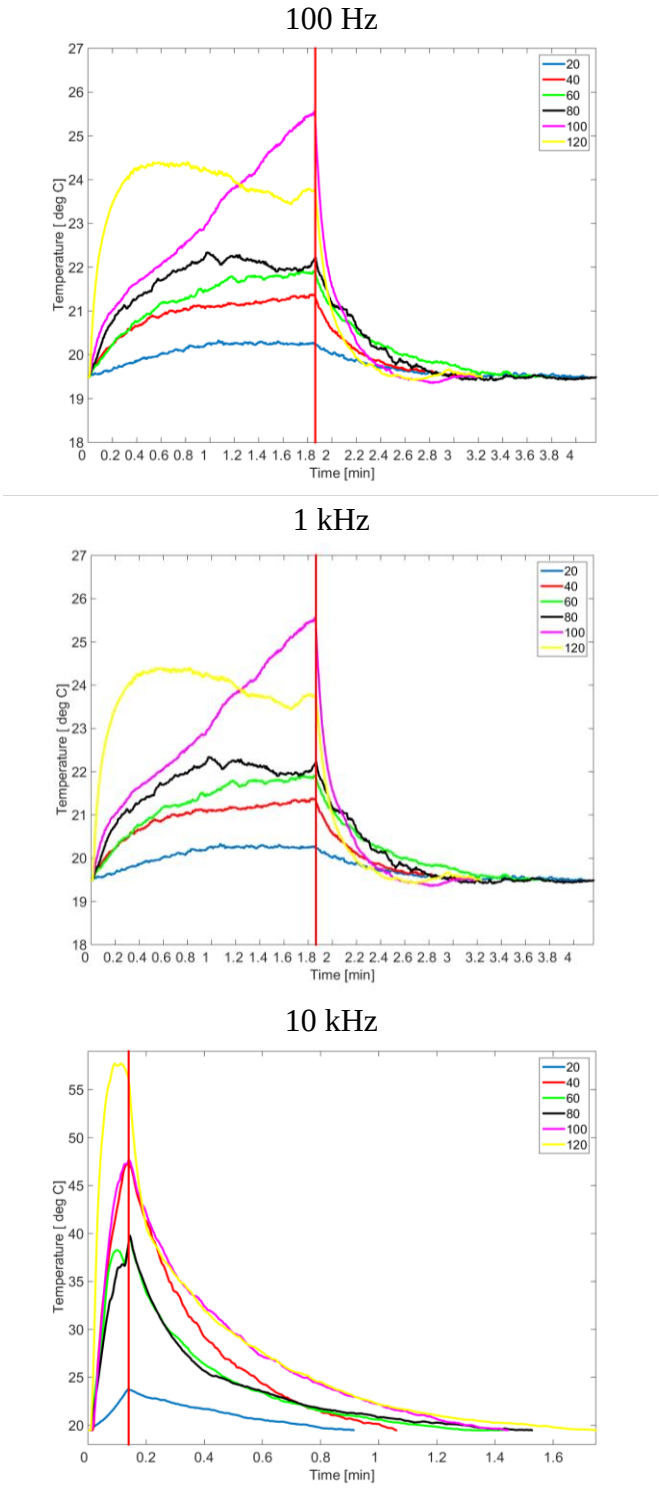

Figure 4.45 Maximum temperature (measured by either of thermocouples at any time) as a function of time for three different repetition rates (0.1, 1, 10 kHz) and a range of pulse energies (20-120 µJ). Wavelength - 1030 nm, repetition rate 100 Hz, spot separation - 3 µm. Red line represents end of laser processing.

The results measured when using the highest repetition rate, 10 kHz, show a significant temperature rise. Looking at specific pulse energies, the maximum average temperature increase for a 40 µJ pulse energy is 10.31 ºC whereas the temperature rise for the lowest

pulse energy used (20 µJ) is 2.38 °C. There is a significant jump in the results when comparing pulse energies 20 and 40 µJ, and this is a direct result of two different processing regimes. Application of 20 µJ and 6 ps pulses focused into the 35 µm diameter spot is not sufficient to create plasma, and hence the process is not in the plasma mediated ablation regime. On the other hand a 40 µJ pulse energy is more than sufficient to be above the threshold for plasma mediated ablation. The difference in the maximum average temperature between 20 and 40 µJ is 7.93 °C and between 40 and 60 µJ is 1.82 °C. From this we can deduce that when the plasma is created it deposits an increased amount of heat into the tissue compared to the processing below the specific plasma creation threshold.

A similar effect is visible for a lower repetition rate of 1 kHz. The maximum average temperature difference between 20 and 40 µJ is 1.88 °C and between 40 µJ and 60 µJ is 0.55 °C. On the other hand the maximum temperature increase of 3.9 °C reached for 120 µJ with 1 kHz repetition rate, is significantly lower than the maximum increase temperature reached with same pulse energy and higher repetition rate of 10 kHz – 21.52 °C. As for the lowest used repetition rate of 100 Hz, the maximum average temperature recorded was 2.23 °C, which is within less than one degree of temperature rise when compared to the 1 kHz repetition rate. However, as found previously, the processing at 1 kHz offers much quicker processing rate and is hence a favourable processing regime.

The presence of plasma increases the heat accumulation and therefore an increase in the maximum temperature reached is unavoidable as the process enters this regime. However, the plasma assisted removal has been shown to allow the creation of well-defined cavities in the sclera with minimal damage to surrounding tissue, and hence lends itself to minimally invasive tissue removal. There is a significant difference between the temperature reached when processing with 10 kHz repetition rate and when processing with both 100 Hz and 1 kHz. These findings do overlap with the conclusion drawn from previous experiments investigating single line scanning ablation, square and circular cavity creation, where use of 10 kHz repletion rate shows evidence of significant thermal damage introduced to the ablation site as well as to the adjacent tissue.

Finally it can be concluded that using a repetition rate of 1 kHz and pulse energy of 60 µJ, it is possible to create well defined cavities, with well controlled depth without introducing any unwanted damage, no residual harmful laser light being transmitted through the sclera and a maximum temperature rise of only by 3.25 °C. This value is three times lower than the critical temperature increase of 11.7 °C found by Wang [146] (for a process of duration around 100 s). It is therefore believed that this laser process could

realistically be used to create portals in eyes in order to assist drug delivery in the treatment of age related macular degeneration. The final issue to resolve is whether a measurable increase in the permeability of the sclera can be achieved by creating portals or cavities within the tissue.

4.9. Permeation

One of the main objectives of this project was an investigation in to the possibility of increasing permeability of the scleral tissue for drug delivery into the posterior eye, using a laser thinning approach. In previous sections, research was focused on finding the best parameters for creating a pocket in the scleral tissue. Such a pocket could act as a portal of entry to the tissue into which the drug would be inserted and a patch would be put on top to close up the pocket. Moreover it is proposed that the transscleral barrier would be reduced due to removal of the outer most layers of the sclera, and an increased treatment efficiency would be achieved. One of the potentially targeted diseases is age related macular degeneration, which requires the drug to be delivered to the posterior part of the eye. It is envisaged that drugs could be placed into such laser induced cavities from where they would be transported to the macula along channels through the fibres of the tissue [59, 60].

The main goal is to prove that by laser thinning it is possible to increase permeation through the tissue. Initially the goal was to set up a perfused eye model and use it as tissue model to prove increased permeability. However this involves significant experimental expertise to set up a reliable model [147] and limits the amount of available samples. Consequently the approach was changed to a simpler model that would allow for numerous samples to be tested, providing more statistically robust data. As a result the decision was made to prove increased permeation by using fluorescent dextran and flat sclera samples placed in Franz cells. Expertise and equipment for these experiments was provided by Prof. Clive Wilson and Dr Lisa MacIntosh (University of Strathclyde) and all tests were carried out in their labs.

Figure 4.46 shows a photo of the Franz cell setup and a schematic and close up image. The sample or “membrane” is placed between the donor and receptor chamber. The donor chamber is filled with a fluorescent dextran (Fluorescein isothiocyanate–dextran FD4 or FD10 from Sigma-Aldrich) and the heated receptor chamber with a HEPES buffer solution (1 M, pH 7.0-7.6). To investigate permeation change, fluorescein dextran was used, which is a common practice e.g. by Ambati [148] or Al-ebini [149] who investigated diffusion of high molecular weight compounds through sclera. Two

different type of fluorescein dextran were used: 4 kDa and 10 kDa, approximating molecular size of the potential drug.

Inside the receptor chamber there was a magnetic stir bar that rotated to mix the solution in the chamber to keep it as uniform as possible. At specific time intervals samples were taken from the receptor chamber through the sampling port. To keep a constant amount of the solution in the chamber a clean buffer solution was put back into the chamber to make up for the removed liquid. As a result the concentration of the solution within the chamber itself was lowered, which has to be taken into the consideration when calculating concentration of any further samples. After the sample was taken it was analysed using a fluorescence spectrometer. By using a specific wavelength light source (depending on the excitation wavelength of substance used – in this case 492 nm) to excite fluorescence of the dextran (emission at 518 nm) it is possible estimate the concentration of the sampled solution. This provides the ability to measure the time resolved penetration of the fluorescent dextran through the sample. By measuring the permeation through the non-machined, un-modified samples and comparing results to the permeation through modified samples, it is possible to calculate the ratio improvement of the tissue permeation.

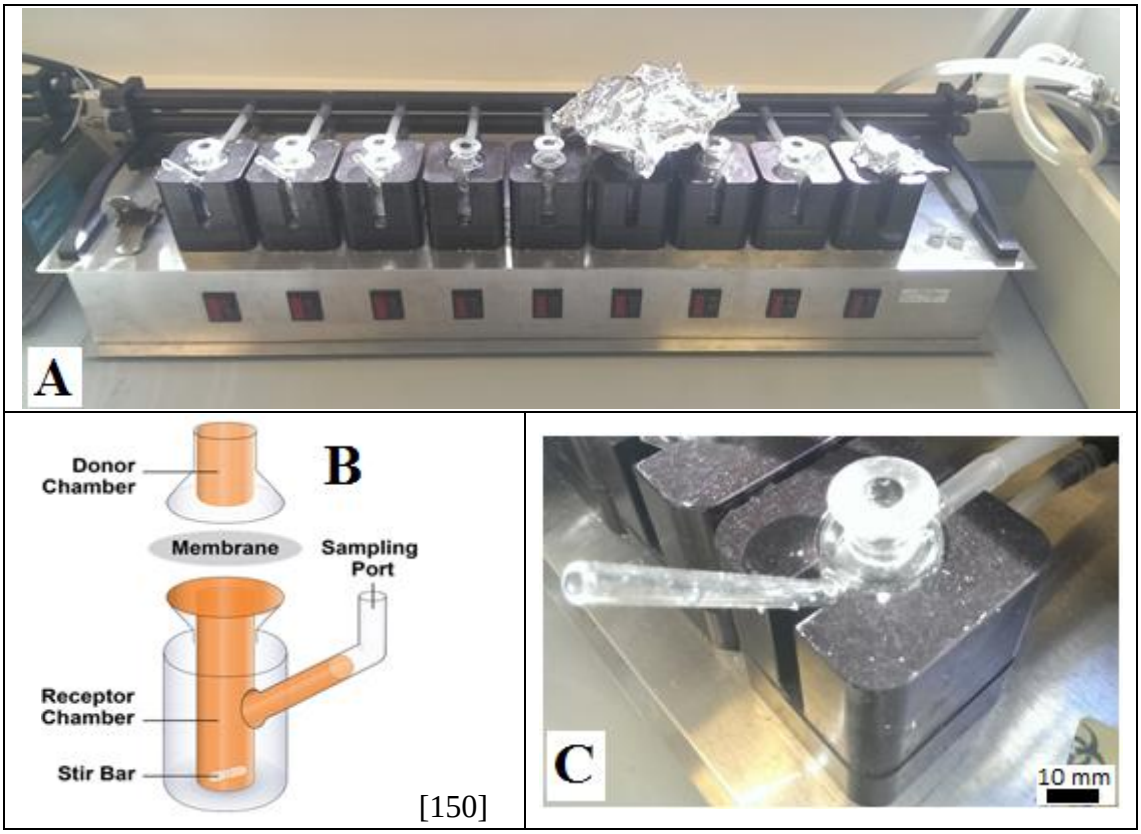

Figure 4.46 (A) Photo of the Franz cells, (B) a schematic of a Franz-cell and (C) a close-up photo of the one single Franz cell. The membrane is replaced by the sclera sample. Franz cells are not fully setup as they are missing a donor chamber/cap on the top.

Figure 4.47 Dissected eye sample shortly after samples for permeation have been cut out of it using circular trephine.

Samples used in the permeation experiment were prepared using an 8 mm circular trephine. From each eye there were only 4 samples taken and all of them were from the equator area so that they have similar thickness to each other. Moreover all of the samples were stored in the lactated ringer solutions to keep them as fresh as possible. Figure 4.47 shows a picture of the dissected eye after samples were cut out.

The thickness of the sclera samples was measured before the machining so that a penetration value per mm thickness can be calculated to normalise results. Samples from the buffer material were taken at 15, 30, 45, 60, 90, 120, 150, 180, 240, and 300 minutes after the donor chamber was filled with 150 µL of FD4 dextran. To measure how much of the fluorescein dextran have permeated through the sample each taken sample was put into fluorescence spectrometer to measure the amount of fluorescence.

The pattern of the machined sclera sample consisted of a square 5x5 mm with lines ~ 15 µm wide at a line separation of 17 µm and an average depth of ~100 µm. The laser repetition that was used was 1 kHz and the pulse energy was 80 µJ. Two samples from each eye were machined, and the other two samples were used as a control group. Figure 4.48 shows the SEM of the micrograph that was used for the experiments.

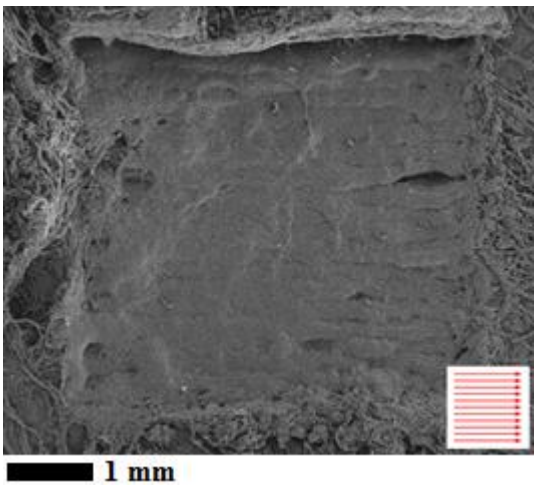

Figure 4.48 SEM micrograph of the cavity that was used when investigating the influence of the laser thinning on the permeability of the sclera. Measured average thickness of the porcine sclera was 1.2 mm.

The initial tests had leaks present, and as a result the Dextran was able to reach receptor chamber by going around the sample. Such a mistake would lead to much higher luminescence of the samples compared to all of the other results. This was subsequently improved by using silicone O-rings and a 3d printed inserts (Figure 4.49), to fit the sample tighter into the donor chamber.

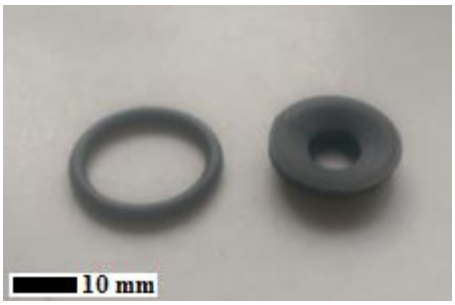

Figure 4.49 Silicone O-ring and 3D printed plastic adapter used to increase tightness of the Franz cell between donor and receptor chamber preventing from leaks.

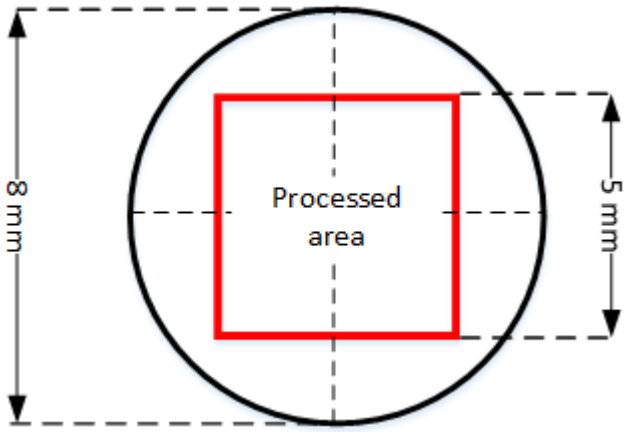

Figure 4.50 Presents the area difference between processed area (Red square) and the sample (Black circle) itself.

Since the whole sample surface was not machined there was a need to account for that difference when comparing results between unmachined and machined tissue. The size difference can be seen on Figure 4.50. The surface area of the samples was ~50 mm^2 and the area of the machined cavity was 25 mm^2, the results were normalized to account for different area sizes.

Firstly a lighter fluorescent dextran (4 kDa) was tested. Figure 4.51 shows the value of luminesce for machined and non-machined samples, as well as the ratio of these two trends. The values for intensity were normalized to account for the different thickness. Samples were taken over the span of 4 hours. Within the first 90 min there was no difference between samples that were machined or not machined. After that, values for the machined sample started rising, whereas the value of luminescence for a non-machined sample stayed at a steady level over the span of the experiment. At the last stage of the experiment, after 4 hours, the value of luminescence (measured using fluorescence spectrometer) for the machined sample was almost 12 times larger that the value for a non-machined sample clearly indicating that more Dextran was being transported through the laser machined samples.

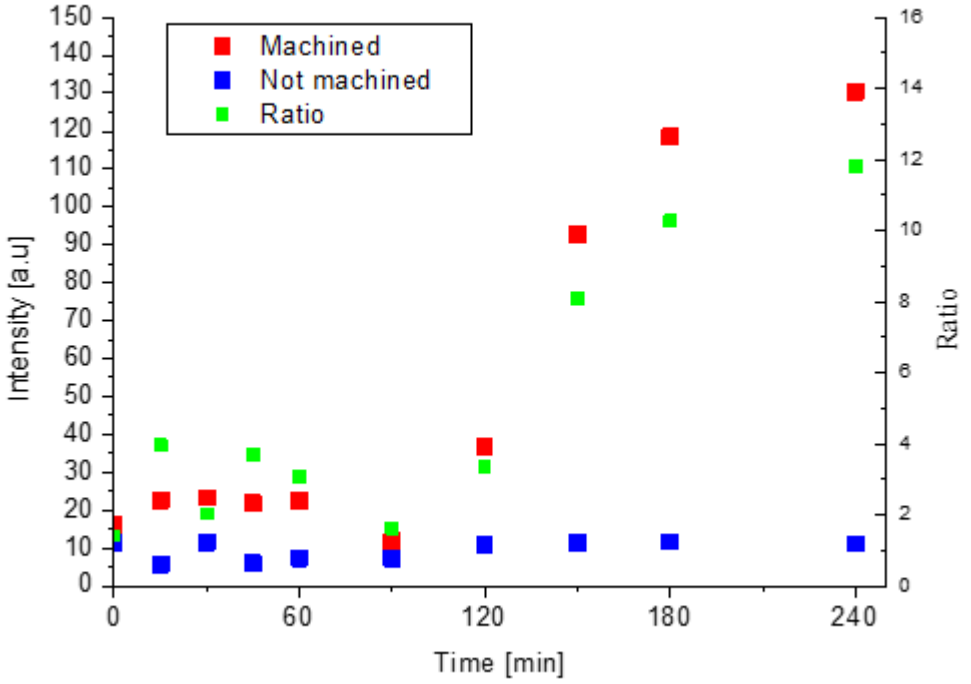

Figure 4.51 Plot of the luminescence for a machined and non-machined sample and their ratio over the span of 4 hours from starting the experiment. This graph presents results when using smaller 4 kDa fluorescent dextran.

Consequently, a heavier fluorescent dextran was tested – 10 kDa. Figure 4.52 shows the luminescence for a non-machined and machined sample that was normalized for an initial thickness of the sample, and a ratio of both of these trends. Similarly to the lighter 4 kDa dextran, there is almost no change for the first 90 to 120 minutes, as this is the time it takes for fluorescein dextran to permeate through the sample and into the receptor chamber. After the initial period both of the luminescence started to increase, but to a significantly different degree. As a result, after 4 hours the luminescence value for the samples obtained from a machined sample are around 10.5 times higher than those form the non-machined sample.

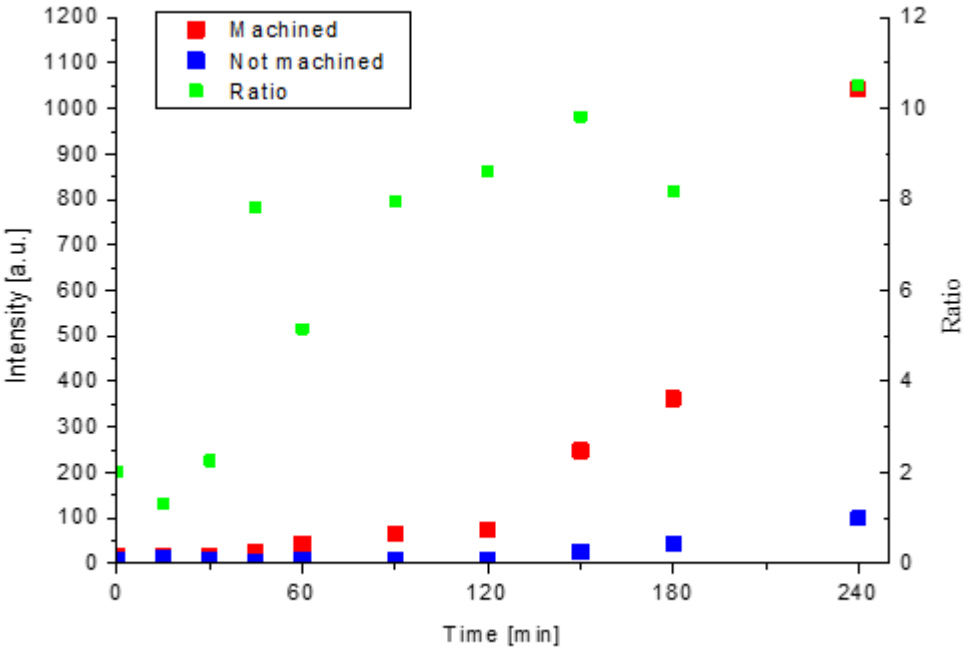

Figure 4.52 Plot of the luminescence for a machined and –non-machined sample and their ratio over the span of 4 hours form starting the experiment. This graph presents results when using bigger 10 kDa fluorescent dextran.

From these results it can readily be concluded that using the laser thinning approach to increase permeability of the tissue is a viable option. Using 10 kDa Dextran is a common practice when investigating permeation through tissue [59]. Currently drugs targeting age related macular degeneration have a slightly larger molecular mass, in the range 27.5 kDa (Ocriplasmin [151]) or 50 kDa (Lucentis[152]), but those drugs are delivered as an intravitreal injection, hence permeation through the sclera is not a crucial factor in their delivery. Moreover it is possible to tailor smaller molecular weight drugs and combine them with protein molecules that have weights of a few kDa [153]. However, it should be noted that in these experiments isolated sclera samples were used.

Nevertheless the advantage of laser thinning is clearly demonstrated by the above experiments, and it was shown that by creating a square cavity on the surface of the sample it is possible to increase the permeability by 10-12 times in 4 hours from the drug application. Such an improvement does offer a potential for innovative drug delivery. As a next step, the natural progression would be to investigate how the permeating compound (in this case fluorescein dextran molecules) spreads laterally and not only vertically. Sclera is a fibrous tissue that depending on the directionality of the tissue layer would direct molecules in a specific direction more than other. Moreover an investigation on

how does the shape of the cavity influence the lateral spread of dextran within the tissue is necessary. As a result a potential to create tailor-made cavities to try direct drug delivery in a particular direction could be investigated. Consequently a more realistic, perfused eye model could be tested. This would have fluid pumped through to represent a living eye and hence would provide an additional pressure barrier for the drug to overcome which would provide more realistic information compared to just using flat sectioned samples.

4.10.Future work

The final application of this early stage research would be to design a device consisting of an optical fibre for flexible delivery of the laser combined with a small (~ 2 mm) customised optical end probe to direct and/or focus the light on to the tissue surface. The whole device would need to be sufficiently compact and flexible to allow insertion into the space between the eye and the socket and allow delivery of laser radiation to the posterior eye where the macula is located. To demonstrate this possibility there have been feasibility tests carried out by Dr Rainer Beck within the Applied Optics and Photonics group at Heriot-Watt University.

Delivery of the pulses itself is possible using hollow core Negative Curvature Fibres (NCF) that have been produced at University of Bath and extensively investigated by Piotr Jaworski [154, 155] also a member of Applied Optics and Photonics group. Light is guided within the fibre on basis of the Anti-Resonant Reflecting Optical Waveguiding – ARROW. As a result the fibre behaves as a Fabry-Perot resonator, and the light that is in resonance with core walls is propagated within the core while other wavelengths are attenuated within the cladding. Figure 4.53 shows an SEM micrograph of an NCF fibre cross-section.

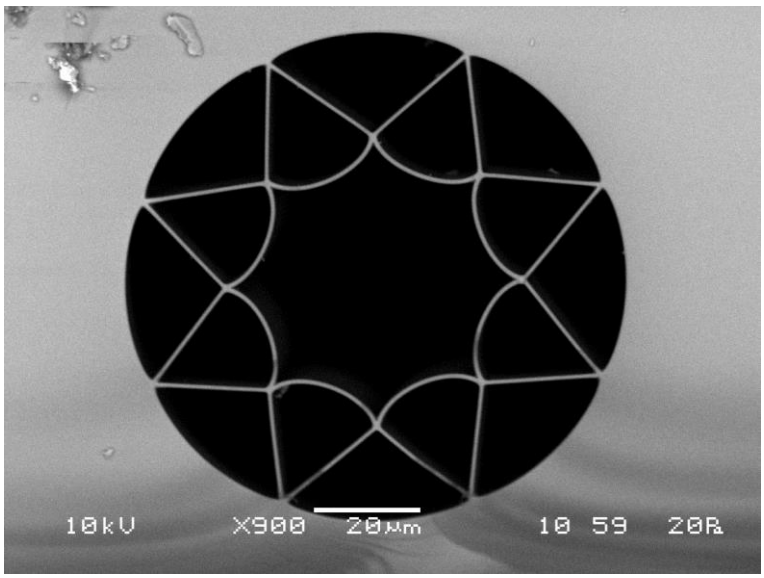

Figure 4.53 SEM micrographs of the NCF fibre cross-section with typical negatively curved fibre walls clearly visible [154].

NCF fibres are capable of delivering up to 92 µJ pulse energy with a 6 ps pulse at a wavelength of 1030 nm laser radiation [154]. Moreover NCF fibres do not show any bend loses down to a bend radius of 10 mm. For a bend radius of 5 cm loses are only around 1 dB. Figure 4.54 shows beam profiles and bend loses for 1030 nm picosecond pulses and 1064 nm nanosecond pulses for different bending radii. As a result, Negative Curvature Fibre can be used as a tool to deliver picosecond pulses into tight space where full flexibility of the delivery is necessary.

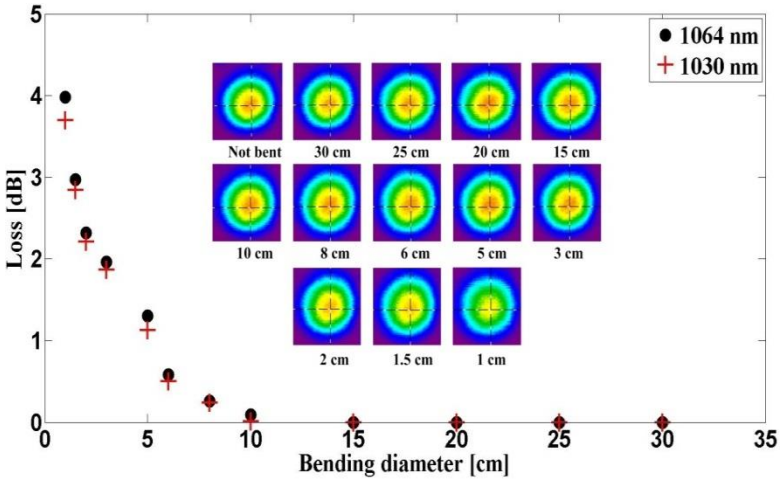

Figure 4.54 Beam profiles and bending losses for different bending diameters tested for 1030 nm picosecond and 1064 nm nanosecond laser radiation. [154]

Future work is being carried out by Dr Rainer Beck who is working on development of the end probe to direct laser radiation onto the surface of the sclera. The first feasibility tests were focused on producing an end tip out of a silica cube. To create a structure within the cube that could turn the beam through 90^{o} and focus it on to the surface of the tissue ultrafast laser inscription of three-dimensional integrated optics was used [156, 157]. The desired structure is inscribed within the fused silica cube and the irradiated region is then preferentially etched and removed using HF acid [156].The curved surface, required to provide a directional focussing mirror, is determined using Zemax ray tracing software in order to provide the correct spot size on the surface and hence the correct laser fluence (as discussed in section 4.4) in the focus position. Figure 4.55 shows a 3D representation of the designed end probe.

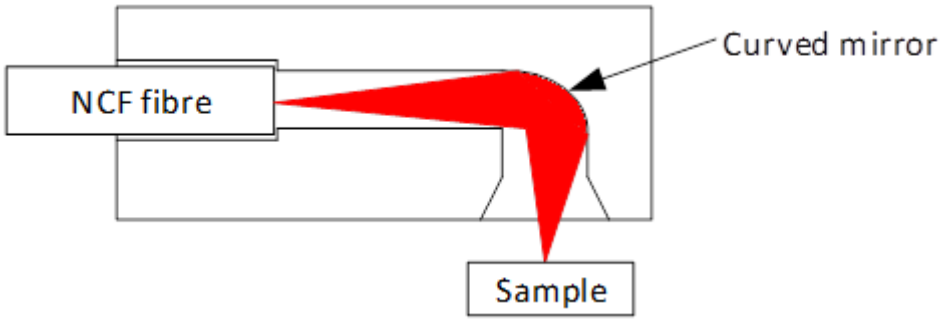

Figure 4.55 The basic schematic of the end probe design.

4.11. Conclusions

A successful plasma mediated ablation with 6 ps pulses has been demonstrated in this work. Several different removal approaches were tested, including single line scanning ablation, square area removal and circular cavity removal. Each approach has been investigated in depth to find the optimum processing parameters by varying repetition rate, pulse energy, spot separation and scanning pattern. One of the major factors in the quality of plasma mediated ablation has been the heat accumulation effect, which has a major influence on the shape and depth of the created cavity, and can even lead to catastrophic thermal damage. Nevertheless the research was successful in finding the parameters that are best suited for the removal of tissue when using ultrashort picosecond pulses. The optimal parameters identified were 1 kHz, 60 µJ and 3µm spot/line separation.

First, single line scanning ablation was investigated by creating a set of 1 mm long lesions in scleral tissue. The highest tested repetition rate of 10 kHz has led to thermal damage as the created lesions had irregular shapes. On the other hand the lowest tested repetition rate showed little material removal, which resulted in very shallow, irregular

lesions. The best results were obtained with a 1 kHz repetition rate, and the lesions created with that repetition rate were even along the whole length and clearly defined. Heat accumulation was noticeable when investigating different spot separation, as patterns that used smaller values of spot separation have had a lower threshold for creating the lesion.

Consequently different approaches for creating well defined square cavities were performed, and different scanning patterns, spot/line separations, repetition rate and pulse energies were tested. Five different scanning patterns were tested – simple raster scan, raster scan with alternating directions, angular scan, angular scan with alternating directions and square with alternating direction left right and alternating side top-bottom at the same time (see Figure 4.15). Additionally, tests including a pre-scanning process to create small linear lesions around the main scanning pattern were performed as well. Similarly to the single scanning line experiment, the highest tested repetition rate (10 kHz) introduced significant thermal damage to ablation site as well to the adjacent tissue. Both lower repetition rates – 100 Hz and 1 kHz – were capable of creating cavities without introducing unwanted thermal damage. The cavities created with the lowest repetition rate – 100 Hz – were shallow and had round edges. The best results were obtained by using a 1 kHz repetition rate, and it was possible to create well defined cavities. Heat accumulation is a major factor when investigating the raster scanning approach as well, with the cavity becoming deeper the longer the scanning progresses, and as a result it is deepest wherever the scan is finishing.

The same tests were carried out for creating a circular cavity. The tested scanning patters included inbound and outbound concentric circles scanning patterns, as well as inbound and outbound scanning patterns. In particular, a spiral scanning pattern offers the possibility of constant laser processing, which is not available when using the other tested scanning patterns. Similarly the highest tested repetition rate of 10 kHz introduced a lot of thermal damage to the ablation site and the adjacent tissue. The best results were obtained with 1 kHz repetition rate, which produced well-defined cavities without introducing any unwanted thermal damage. An outbound spiral scanning pattern was capable of creating a well-defined cavity with a flat bottom surface. Due to the possibility of having constant laser processing it does direct the heat away from the centre of the cavity. As a result heat is deposited into the tissue in a uniform manner.

To estimate how the permeation of the scleral tissue changed when a square cavity was introduced on its surface, an experiment using Franz cells was designed. Two different types of fluorescein dextran were used – 4 kDa and 10 kDa and a 5 mm by 5 mm square and 100 µm deep cavity was created on the surface of the tissue. The results

showed that creation of such cavity can increase permeation of the tissue in the first 5 hours by 5.5-6 times.

To ensure the safety behind the process, two experiments were performed. The first experiment was focused on the temperature increase whenever laser processing was in progress, and the other was focused whether there is any transmission through the tissue during processing. To investigate the temperature increase, a set of four thermocouples were placed underneath the sample and a square scanning pattern 1 mm by 1 mm was tested. When using the optimal scanning parameters (1 kHz, 60 µJ, and 3µm spot/line separation) the maximum temperature increase was 3.25 ^{o}C. To ensure that there is no energy transmitted through the tissue during laser processing two power meters were used; a thermal detector and a sensitive photodiode, to perform the measurement. Neither of the power meters was able to record any, potentially harmful or damaging, energy being transmitted through the sample.

The application of picosecond laser plasma mediated removal offers a potential minimally invasive route to increase drug delivery to the posterior eye as well as a potential way of decreasing intraocular pressure in treatment of glaucoma.

Chapter 5. Theoretical modelling of laser tissue interaction

Chapter 5 describes two different modelling approaches used to model laser tissue interaction. Firstly an ALE moving boundary approach is used to investigate single pulse CO_2 laser ablation of hard dental tissue using a COMSOL modelling software package. Secondly a finite element blow-off 2D model created using MathWorks MATLAB software is applied to simulate single line scanning picosecond laser plasma mediated ablation of porcine sclera.

5.1. Introduction

The development of robust theoretical models is a vital part of research into new laser processes. Modelling can help minimize the time spent searching for optimal parameters when considering an entirely new process or can be an essential part of developing a deeper understanding of the physical mechanisms when backed up by experimental results. In this research two different modelling approaches were investigated. For the removal of hard dental tissue a finite element model based on a moving boundary was developed using the COMSOL software package. A second finite element model was developed using MathWorks MATLAB software package focused on the removal of soft ophthalmic tissue.

5.2. Hard dental tissue removal simulation

5.2.1. Introduction

A significant mechanism for material removal for enamel with this pulse regime is mediated explosive ablation (see section 2.3.5). This is a highly dynamic event and detailed modelling of such a process would be complex. However, it was decided to see if a model based on a moving boundary linked to vaporisation temperature (representing the material removal process) would provide a simplistic approach to obtain information on heat transport through the enamel during the laser process.

This section describes a finite element blow-off model focused on single pulse laser removal of hard dental tissue. The model was created in two dimensions using the COMSOL 4.3b [116] software package. Firstly, a 3D approach was briefly investigated and tested but the processing time was prohibitively long. However a 3D model was deemed unnecessary (due to the symmetry of the problem) when considering only single pulse ablation as a 2D model was capable of representing all of the values. An ALE (Arbitrary Lagrangian–Eulerian) moving boundary method was developed, that describes material removal as a change in the position of a boundary [158]. It combines both the Lagrangian approach allowing for the movement of the mesh and a Eulerian approach that holds mesh fixed [158].

The velocity of this moving boundary is calculated proportionally to the vaporization heat flux and has the same direction, opposite to the laser radiation. The boundary velocity can be calculated using equation (5.1)

$$v = \frac{Q_{vap}}{Q_L \cdot \rho} \tag{5.1}$$

where v is velocity of the moving boundary, Q_{vap} is heat flux of vaporization, Q_L is latent heat and ρ is density.

<table>
<tr><td colspan="2">Applied laser energy</td></tr>
<tr><td colspan="2">$Q_{laser} = P_{peak}(1-R)\frac{3}{r\sqrt{2\pi}} e^{\frac{-3(x-x_0)^2}{2r^2}} e^{-4ln2\left(\frac{t}{\tau}\right)^2} e^{\frac{y}{\delta p}}$ [159, 160]</td></tr>
<tr><td rowspan="8"> 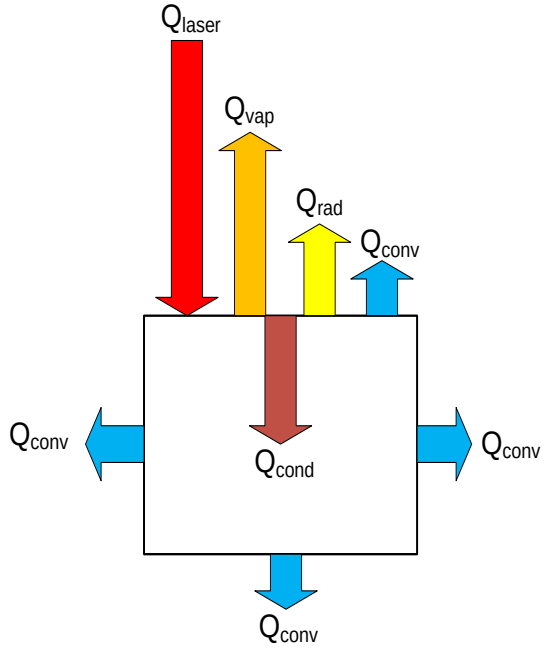
</td><td>Energy of vaporization</td></tr>
<tr><td>$Q_{vap} = Q_L\sqrt{\frac{M}{2\pi RT}} p_v e^{\frac{Q_L M}{RT_{vap}}\left(1-\frac{T_{vap}}{T}\right)}$ [161]</td></tr>
<tr><td>Convective heat losses</td></tr>
<tr><td>$Q_{conv} = h(T - T_{amb})$ [116]</td></tr>
<tr><td>Radiative heat losses</td></tr>
<tr><td>$Q_{rad} = \varepsilon\sigma_{Boltz}(T - T_{amb})$ [116]</td></tr>
<tr><td>Heat conduction</td></tr>
<tr><td>$Q_{cond} = -n(-k\nabla T)$ [116]</td></tr>
</table>

Figure 5.1 Schematic of the heat fluxes used in the simulation and the equations describing these heat fluxes.

Figure 5.1 describes all of the heat fluxes used in the simulation. The incident laser radiation is partially reflected from the sample surface and remaining energy is absorbed in the tissue according to the Beer-Lambert law (Equation 5.2) and transformed into thermal energy.

$$I(z) = (1-R)I_0 e^{(-\alpha z)} \tag{5.2}$$

where z describes plane, $I(z)$ is the intensity at a distance z, I_0 is the intensity at the surface of the sample, α is the absorption coefficient of the material and R is reflectivity of the sample surface.

To simplify the model for the side and bottom boundaries it is assumed that there is a steady heat flux proportional to the temperature difference between the boundary and ambient temperature. On the top surface heat can be removed by means of convection, heat radiation and the energy of vaporization. The thermal balance of the system can be described with Equation (**5.3**.

$$Q_{cond} = Q_{laser} - Q_{vap} - Q_{conv} - Q_{rad} \quad (5.3)$$

Table 5.1 Values of the parameters used in the simulation [21, 29, 30, 32, 33].

Parameter	Symbol	Value
Emissivity	ε	0.8
Penetration depth	δ_p	16 µm
Density	ρ	3000 kg/m^3
Heat transfer coefficient	*h_air*	10 W/(m^2·K)
Specific heat	C_p	880 J/(K·kg)
Ambient temperature	T_{amb}	293.15 K
Molar mass	*mmass*	18 g/mol
Reflectivity	*R*	0.15
Latent heat of vaporization	Q_{LV}	6000 kJ/kg
Latent heat of melting	Q_{LM}	16 kJ/kg
Vaporization temperature	T_v	1600 K
Melting temperature	T_m	1200 K
Pulse duration	τ	200 µs

To simulate phase transition latent heat of melting and vaporization was incorporated into the value of specific heat (Equation (**5.4**). This was done by increasing the specific heat capacity adding a smoothly increasing and decreasing peaks centred on temperatures were phase transition commences (Figure 5.2). The area under smaller peak is equal to latent heat of melting and the area under bigger peak is equal to latent heat of vaporization. As a result to cause a temperature rise across those areas an increased amount of energy is required compared to regions where value of specific heat is constant. The modified equation for specific heat can be seen below in Equation (**5.4**.

$$C_{pmodelled} = C_p + \frac{1}{dT\sqrt{\pi}} e^{\frac{-(T-T_V)^2}{dT^2}} * Q_{LV} + \frac{1}{dT\sqrt{\pi}} e^{\frac{-(T-T_M)^2}{dT^2}} * Q_{LM} \quad (5.4)$$

where the terms are defined in table 1.1.

The additional specific heat has been added with a Gaussian envelope instead of a step change, as a step increases the difficulty of the calculation close to the melting and

vaporization temperature. A similar approach has been used by Bruyere [120] where they used a moving boundary ALE method when investigating keyhole drilling during spot laser welding.

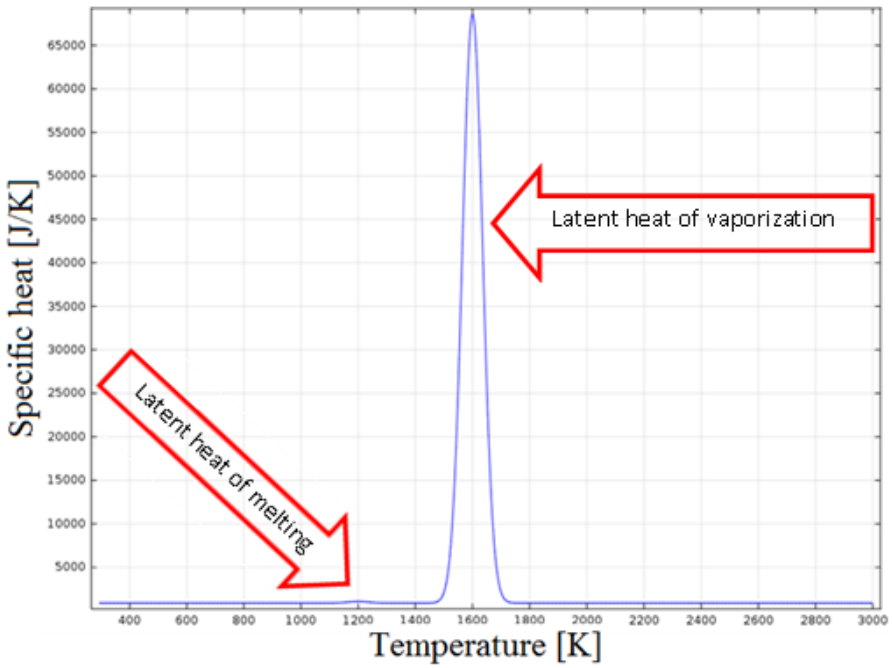

Figure 5.2 Specific heat as a function of temperature. The equation describing specific heat has increased values to incorporate the latent heat of melting (smaller peak) and vaporization (bigger peak). As a result an increase amount of energy is needed to raise the temperature across the areas of increased specific heat simulating latent heat energy.

The main mesh size incorporates elements of 2.5 by 2.5 µm. However a finer mesh is used in the regions near the surface where most of the interactions are applied.

5.2.2. Results

A simulation was carried out for a 200 µs pulse with a fluence of up to 100 J/cm^2. The main purpose was to illustrate how an ALE moving boundary model changes during the duration of the pulse and how energy is distributed over time after the pulse is finished. Additionally, this can be compared to the crater depths as measured from experiments described further in this section. Figure 5.3 shows the temperature distribution and arrows describing the heat flux both during and post pulse radiation as a function of time (with zero time defined as the commencement of the simulation). The incident Gaussian pulse starts from the beginning of the simulation and reaches peak irradiation at 0.35 ms into the simulation. The maximum temperature (~2950 ^{o}C) is reached around 0.40 ms µs after the commencement of the simulation. The boundary is still moving after the pulse is finished as the temperature is still above the temperature of vaporization which is a cut-off for the boundary velocity that is applied.

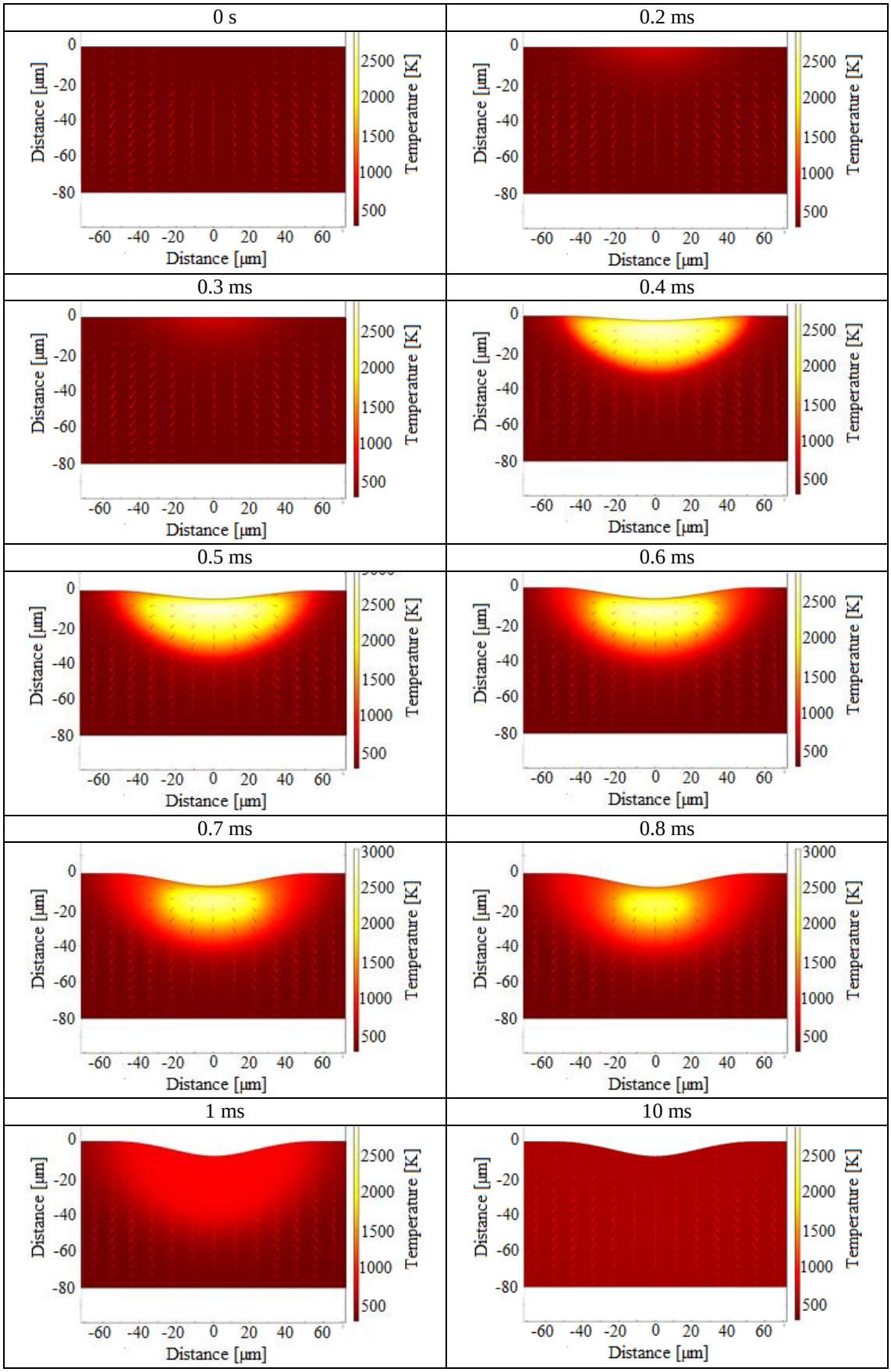

Figure 5.3 Temperature profile and arrows showing the direction of the heat flux at different moments during and after the surface has been irradiated by a laser pulse. The pulse duration is 200 µs with a fluence 30 J/cm^2. The maximum temperature reached ~2950 ºC at 350 µs after the start of the simulation.

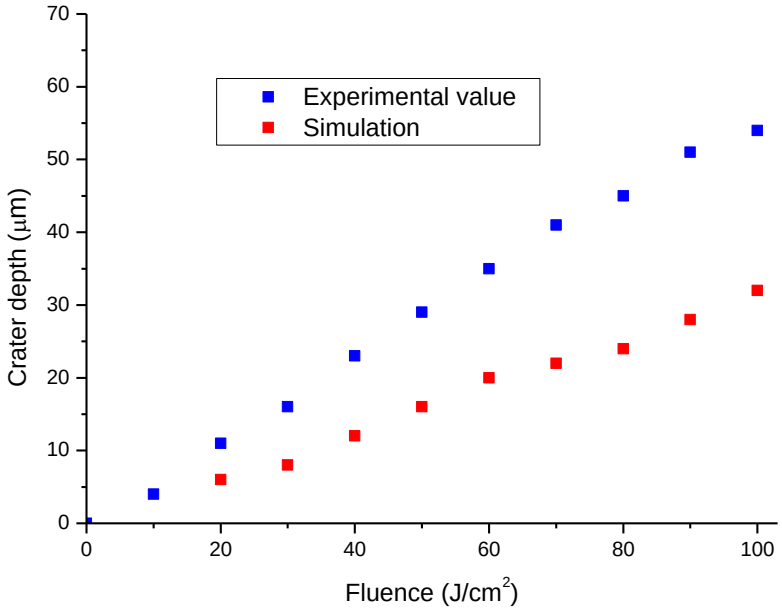

Figure 5.4 Experimental and theoretical values of crater depth for a 200 µs single pulse ablation for fluences up to 100 J/cm^2.

Figure 5.4 shows the experimental and theoretical values for crater depth obtained for single shot ablation with a 200 µs pulse duration. The values obtained through the theoretical simulations are ~40% lower that values obtained through experimental work. The main factor for this discrepancy is the timescale of the events. On one hand, the main tissue removal mechanism is water mediated explosive ablation, which is an abrupt removal mechanism driven by micro explosions of water within the tissue by abrupt vaporization and pressure increase [42] (For a more detailed explanation please look to Section 2.3.5). The simulation approach used – the ALE moving boundary – is not capable of simulating abrupt changes. Tissue removal from water mediated explosive ablation is immediate, within the pulse itself. In the simulation there is no change to the material surface with the pulse as it begins after the pulse was finished. As a result deposited thermal energy has time to diffuse within the material, instead of removing tissue, which leads to lower tissue removed.

As a consequence it is clear that an ALE moving boundary is not best suited to simulate water mediated explosive ablation [42]. The ALE moving boundary simulation has been shown to work well when considering different processing regimes or longer pulse durations, for example this approach has been successfully applied to the investigation of keyhole drilling during spot laser welding by Bruyere [120] with millisecond pulse durations. Therefore in order to model the dynamics of material removal in the case of millisecond processing of enamel a model that is capable of faster removal of material should be applied i.e. a blow-off model.

5.3. Ophthalmic tissue removal model

5.3.1. Introduction

A different type of simulation was used to improve the understanding of the interaction between picosecond laser irradiation and porcine sclera. A 2D finite element blow-off model has been developed using MathWorks – MATLAB software. The removal of biological tissue within the picosecond pulse regime is mainly due to plasma mediated ablation [70, 79, 83]. Porcine sclera is 70% water [77] and hence parameters such as latent heat, density and specific heat used in this model were taken from a table of properties for water [81, 82]. Optical parameters such as transmission, absorption or reflectivity were taken for values measured for sclera in other research [58].

This model assumes that laser radiation is transformed into plasma and thermal energy depending on the energy level in a given cell. Interactions between photons, electrons and phonons are neglected and the absorbed energy is directly transformed into thermal energy [162].

Applied laser energy	
$Q_{laser} = I_0(1-R)I_0 e^{\left(\frac{-2r^2}{{\omega_0}^2}\right)} e^{-4ln2\left(\frac{t}{\tau}\right)^2} e^{\frac{y}{\delta p}}$ [159, 160]	
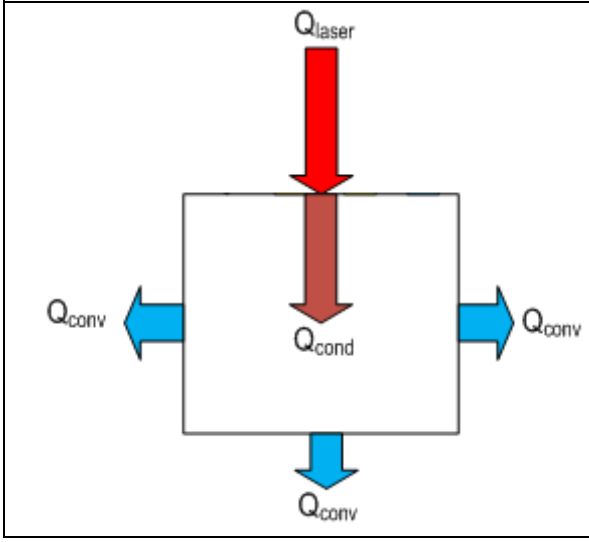	Convective heat losses
	$Q_{conv} = h(T - T_{amb})$ [116]
	Heat conduction
	$Q_{cond} = -n(-k\nabla T)$ [116]

Figure 5.5 Schematic of the heat fluxes used in the simulation and the equations describing these heat fluxes.

Figure 5.5 describes all of the heat fluxes used in the simulation. Laser beam profiles, both spatial (Equation (**5.5**) and temporal (Equation (**5.6**), used in this model have been approximated with a Gaussian function. The value of M^2 factor for the beam was measured to be ~1.3 for the 1030 nm picosecond radiation used for the experimental work.

$$I(r) = I_0 e^{\left(\frac{-2r^2}{{\omega_0}^2}\right)} \tag{5.5}$$

where z describes plane, $I(r)$ is the intensity at a distance r from the centre of the beam, I_0 is the maximum intensity in the centre of the pulse, ω_0 is the radius of the focused spot size [159].

$$I(t) = I_0 e^{-4ln2\left(\frac{t}{\tau_p}\right)} \tag{5.6}$$

where z describes plane, $I(t)$ is the intensity at a distance time t, I_0 is the maximum intensity in the centre of the pulse, τ_p is pulse duration [159].

Since it is a 2D model the assumed thickness of the subject is 1 μm. Part of the incident laser irradiation is reflected from the surface of the sample and rest is absorbed according to the Beer-Lambert law (Equation1.2).

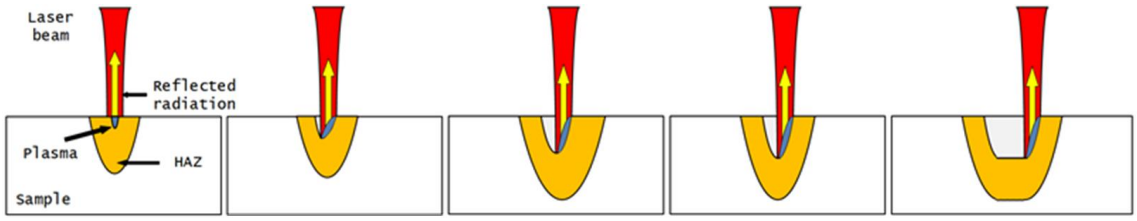

Figure 5.6 Schematic of the single line scanning ablation simulation showing laser beam as well as reflected radiation behaviour. Moreover heat affected zone and the way plasma is created are shown.

The heat transfer within the substrate is described by the heat conduction equation (Equation (5.7).

$$\rho C_p \frac{\partial T}{\partial t} = \nabla(k\nabla T) + Q_L \tag{5.7}$$

where ρ is density, $C_p$is specific heat, $Q_L$is energy deposited by laser radiation.

Table 5.2 Parameters used in the Matlab simulation for picosecond ablation of sclera [53, 58, 70, 80-82, 138, 163]

Parameter	Symbol	Value
Ambient temperature	T_0	293.15 K
Temperature of vaporization	T_V	373.15 K
Latent heat of evaporation	L_v	2270 J/kg
Thermal conductivity	k	0.58 W/(m·K)
Heat capacity	C_p	4200 J/(kg·K)
Density	ρ	1032 kg/m^3
Reflectivity	R	0.45
Absorption coefficient for sclera	α_s	222 cm^{-1}
Absorption coefficient for plasma	α_p	570 cm^{-1}

Typically, absorption in biological tissue at a wavelength of 1030 nm is comparatively low due to its high water content. However, scleral tissue is highly scattering resulting in a much higher effective value of the absorption coefficient α_s =222 cm^{-1}[53]. Moreover removal of biological tissue in the picosecond regime is based on plasma mediated ablation that is achievable when the laser beam is focused such that high irradiance regions exceed the threshold for laser induced breakdown. That mechanism is described in detail in Section 2.4.5. The amount of energy needed for laser induced breakdown in biological tissues has been extensively investigated by Vogel [58, 70, 79-82, 163, 164]. The plasma creation threshold for distilled water was found to be $4.5 \cdot 10^{11}$ W/m^2 [81, 82] for a 6 ps pulse length at a wavelength of 1030nm [11].

5.3.2. Absorption and plasma modelling

In our model plasma has been simulated as a localised change of the absorption coefficient for regions where the energy threshold for breakdown has been exceeded. The laser induced breakdown threshold used was $4.5 \cdot 10^{11}$ W/m^2[70] as measured for water. The absorption coefficient for plasma created in distilled water was measured by Vogel and found to be α_p=570 cm^{-1}[82]. Whenever the value of irradiance on the surface is below the laser induced breakdown threshold, the absorbed energy is deposited into the substrate and transformed into thermal energy. Figure 5.7Figure 5.12 - Figure 5.12 show the evolution of the plasma during the duration of the laser pulse as well how the transmission curve changes during that time.. Whenever plasma is created it absorbs the majority of the incoming laser energy hence the transmission curve changes. In this simulation, after the laser pulse has ended, the entire plasma region is removed instantaneously from the system and it does not interact with the rest of the sample. Figure 5.12 shows energy and plasma distribution as well as the transmission curve as a function of time during laser pulse. When a plasma is formed it absorbs most of the incoming energy hence the transmission curve drops significantly and there is much less energy deposited into the tissue directly below the plasma. This is a simplified approach to simulate plasma absorption and is similar to that used by Marla [122] to investigate plasma shielding in laser ablation of titanium carbide . A more accurate way of modelling that process would be to use a molecular dynamics simulation, increasing the complexity of this model, as used by Jiao [123] to simulate the behaviour of plasma in water.

A – Starting state

No energy introduced to the system. No plasma created. Transmission curve unchanged.

Time	Energy
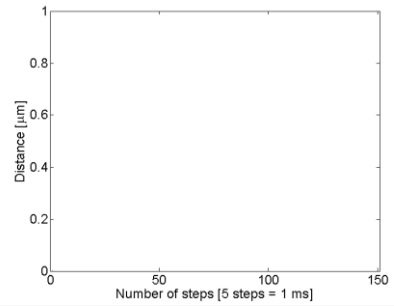	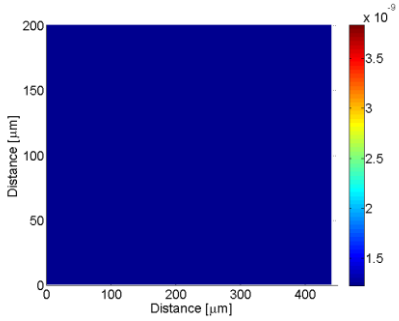
Plasma	**Transmission through plasma centre**
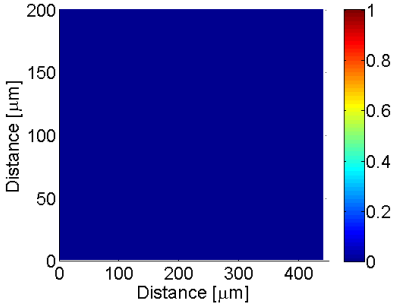	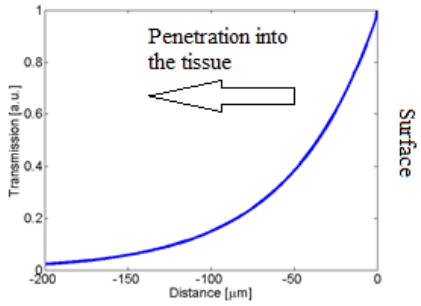

Figure 5.7 Energy deposition, plasma position, transmission curve at the beginning of the simulation.

B - After 10 ps from the simulation start

Plasma creation threshold not reached. Transmission curve unchanged.

Time	Energy
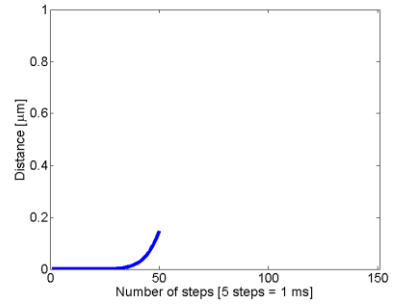	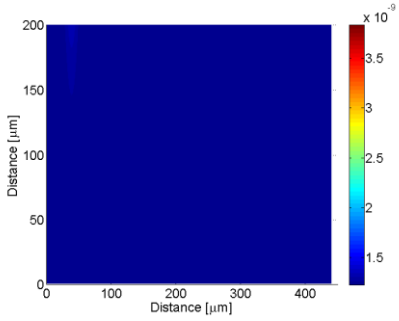
Plasma	**Transmission through plasma centre**
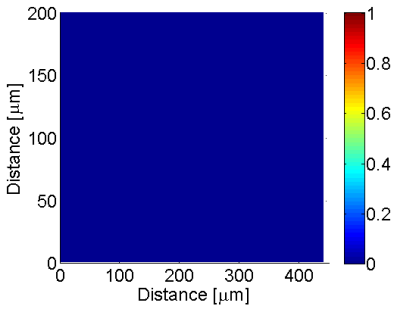	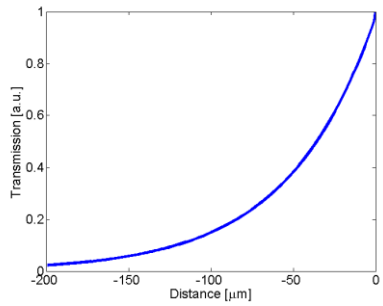

Figure 5.8 Energy deposition, plasma position, transmission curve after 10 ps from commencement of the simulation. Plasma creation threshold not reached. Transmission curve unchanged.

C - After 15 ps from the simulation start

Plasma creation threshold reached. Plasma is created. Transmission curve is changed as the absorption increases in the plasma region.

Time	Energy
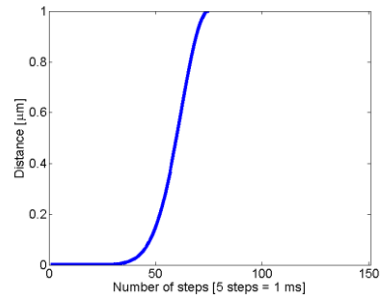	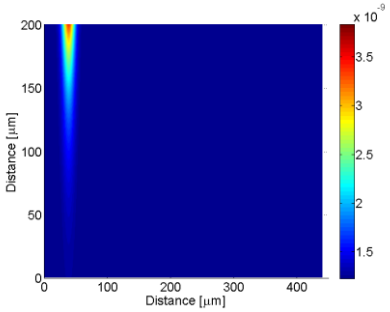
Plasma	**Transmission through plasma centre**
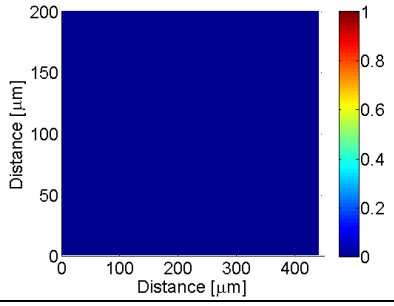	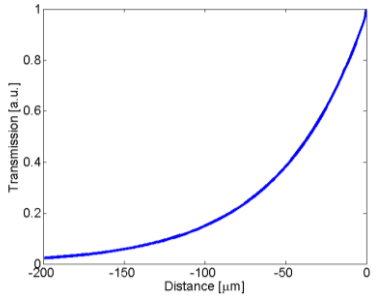

Figure 5.9 Energy deposition, plasma position, transmission curve after 15 ps from commencement of the simulation. Plasma creation threshold reached. Plasma is created. Transmission curve is changed as the absorption increases in the plasma region.

D - After 20 ps from the simulation start

Plasma increases in size. More and more energy is absorbed by plasma hence transmission curve decreases more.

Time	Energy
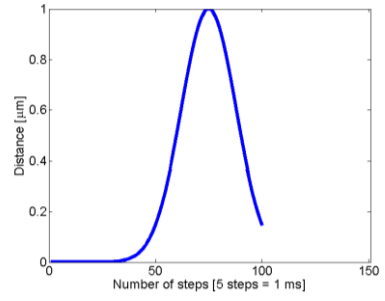	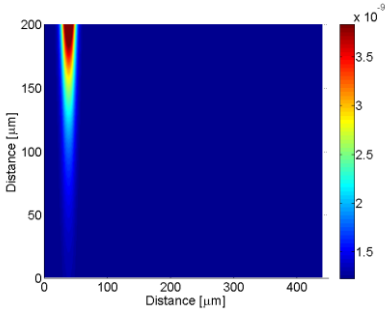
Plasma	**Transmission through plasma centre**
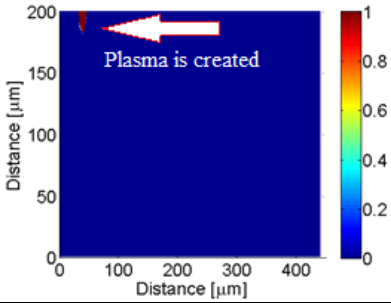	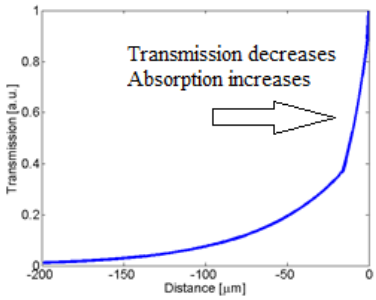

Figure 5.10 Energy deposition, plasma position, transmission curve after 20 ps from commencement of the simulation. Plasma increases in size. More and more energy is absorbed by plasma hence transmission curve decreases more.

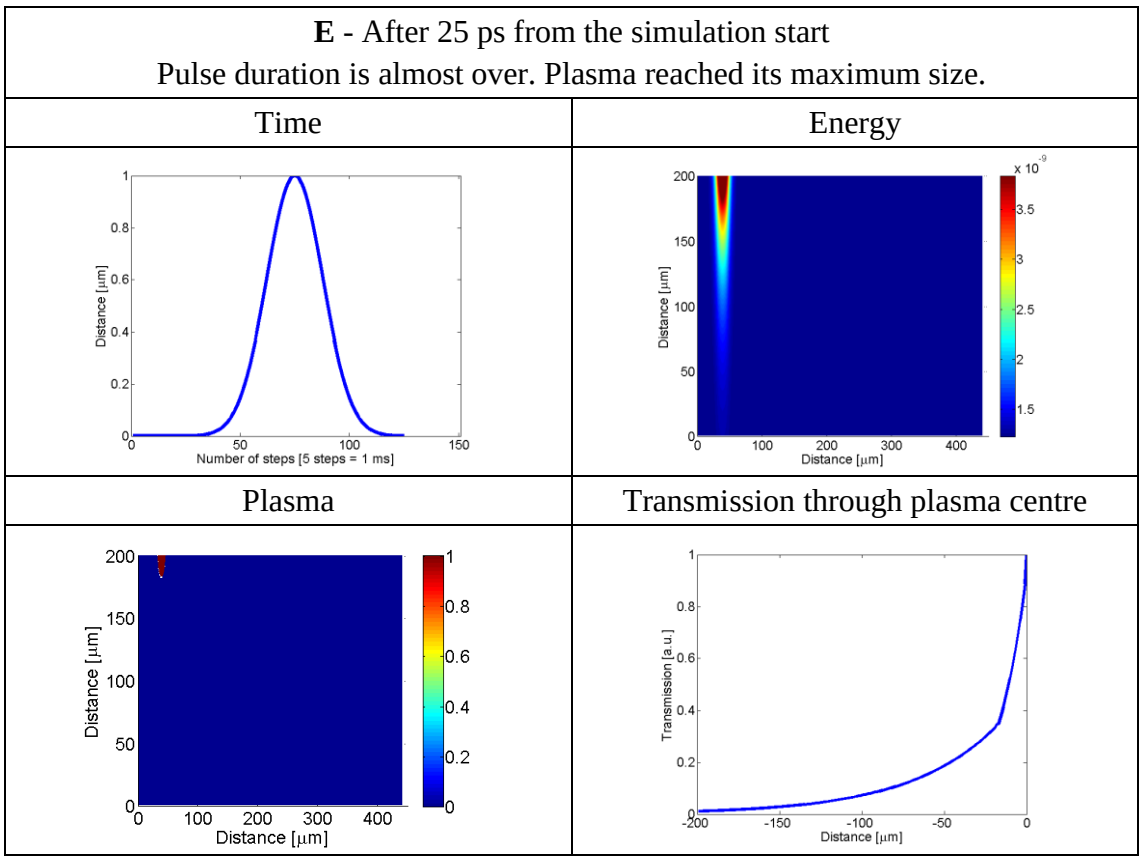

Figure 5.11 Energy deposition, plasma position, transmission curve after 20 ps from commencement of the simulation. Pulse duration is almost over. Plasma reached its maximum size.

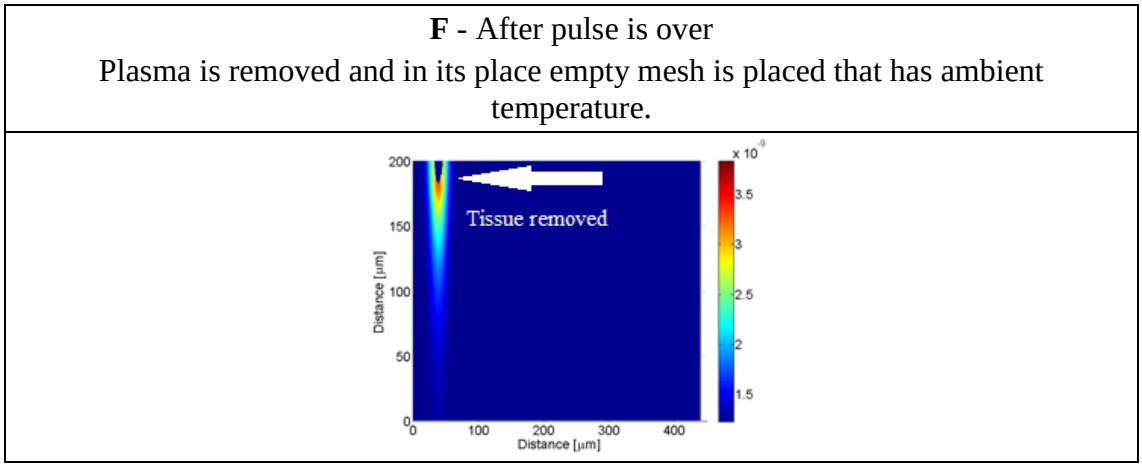

Figure 5.12 Tissue structure and energy deposition after plasma is removed from the sample.

5.3.3. Assumptions used in Matlab model for picosecond ablation of sclera

Theoretical modelling was used as an additional tool for increasing understanding of the heat accumulation effect during the processing of biological tissue. It was observed during experimental work (see section 3.3) that heat accumulation effect had an impact on the machined area of the sclera where the depth of square and circular cavities were non-uniform. Due to heat accumulation the cavities became deeper towards the end of the

process. To decrease the complexity of the model, hence decrease processing time, a number of assumptions and simplification were applied:

- Radiative and convective heat losses were neglected. During the simulation the magnitude of such losses were assumed to be less than 0.0001% of incoming laser radiation [76, 165].
- The size of the simulated tissue is 500 μm wide and 200 μm high. It is much smaller that the size of the actual samples, but decreasing the size of the simulated region decreases processing of the simulation significantly. To ensure that the system was not totally isolated a value of heat flux applied on the bottom and side boundaries proportional to the difference between the temperature on the boundary and the value of ambient temperature was introduced described by Equation (3.1.

$$h(T - T_{amb)} \qquad 5.8$$

  where T is temperature of the border layers and T_{amb} is ambient temperature.
- The value of each parameter is temperature dependent however to simplify the model these were kept constant. Additionally, there is a lack of data in the literature for the temperature dependence of these parameters.
- The plasma does not interact or deposit any heat into the tissue and is removed immediately after the laser pulse has ended. Research by Vogel [70, 81, 83] shows that the lifetime of picosecond induced plasmas is in the tens of nanoseconds regime. Moreover previous investigations into temperature increases (Section 3.7) shows that the presence of plasma has an influence on the overall temperature increase within the sample when compared to the regime below the plasma creation threshold. Nevertheless, again to simplify the model, this effect was neglected.

5.3.4. Results from the Matlab model for picosecond ablation of sclera

Theoretical modelling has been used to investigate single line scanning ablation to further investigate the influence of heat accumulation and to compare findings with those obtained experimentally (Section 3.3).

Figure 5.13 shows the evolution of the linear lesions created with single line scanning ablation for an increasing number of laser pulses. Figure 5.14 shows the evolution of the depth of the lesions as a function of the number of laser pulses. The pulse energy used in the simulation was 70 µJ, with a repetition rate of 10 kHz and a spot separation of 3 µm.

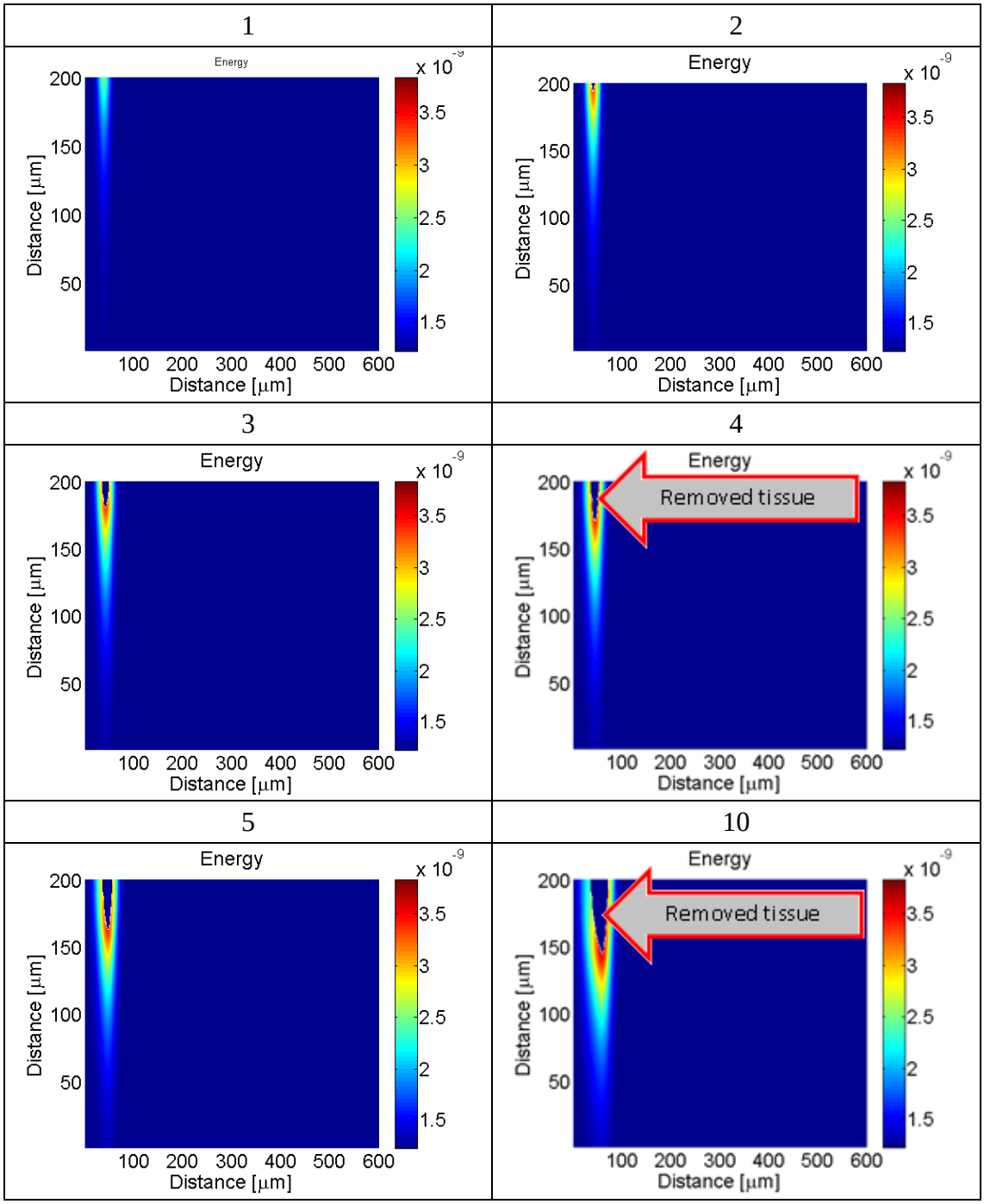

Figure 5.13 Matlab simulation for energy deposition in the tissue during single line scanning ablation for increasing pulses. The number of pulses is given at the top of each figure. The ablated region is highlighted. The pulse energy used in the simulations was 70 µJ, with a repetition rate of 10 kHz and a spot separation 3 µm. Figure continued on the next page.

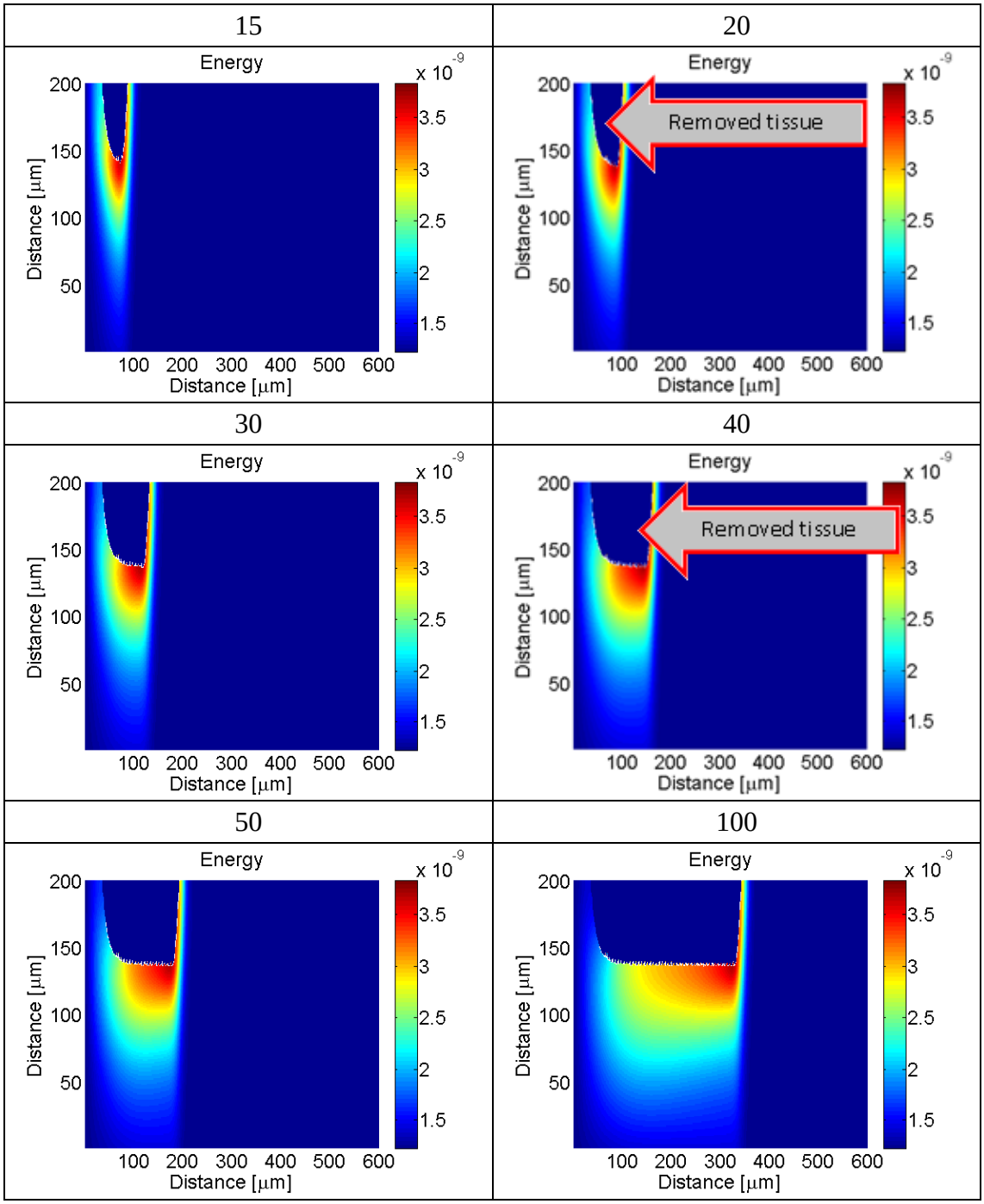

Figure 5.13 Matlab simulation for energy deposition in the tissue during single line scanning ablation for increasing pulses. The number of pulses is given at the top of each figure. The ablated region is highlighted. The pulse energy used in the simulations was 70 µJ, with a repetition rate of 10 kHz and a spot separation 3 µm.

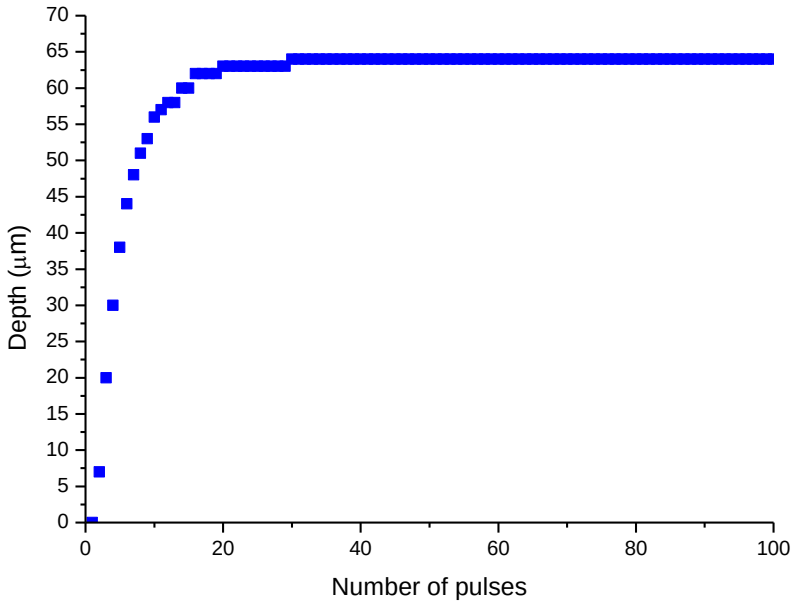

Figure 5.14 Maximum depth as a function of the number of the pulses during the single line scanning ablation simulation. The pulse energy used was 70 µJ, with a repetition rate of 10 kHz and a spot separation 3 µm.

The results of the simulation illustrate a mechanism for material removal in single line scanning ablation. Initially, each additional pulse ablates deeper into the sample until the maximum depth is reached at around 30 pulses. The maximum depth is reached because pulses are being irradiated onto the side of cavity created by previous pulses. Moreover the simulation illustrates that heat accumulation occurs during picosecond plasma mediated ablation of the tissue. The highest value of thermal energy "follows" the focused laser spot as it translates over the sample but there is residual heat in the tissue behind the laser spot. As a result, and as observed experimentally, when the next scanning line starts residual energy increases the process removal rate due to thermionic emission [70, 83]. Thus the next scanning line would go deeper and would starting creating a slope which has been discussed and shown in previous section 3.4.

To verify the output from the model was compared to data obtained experimentally for single line ablation as discussed in section 3.3. Figure 5.16 shows both the theoretical and experimental values for maximum depth of the lesion as a function of pulse energy for two different repetition rates: 1 kHz and 10 kHz. The spot and line separation used for this experiment was 3 µm.

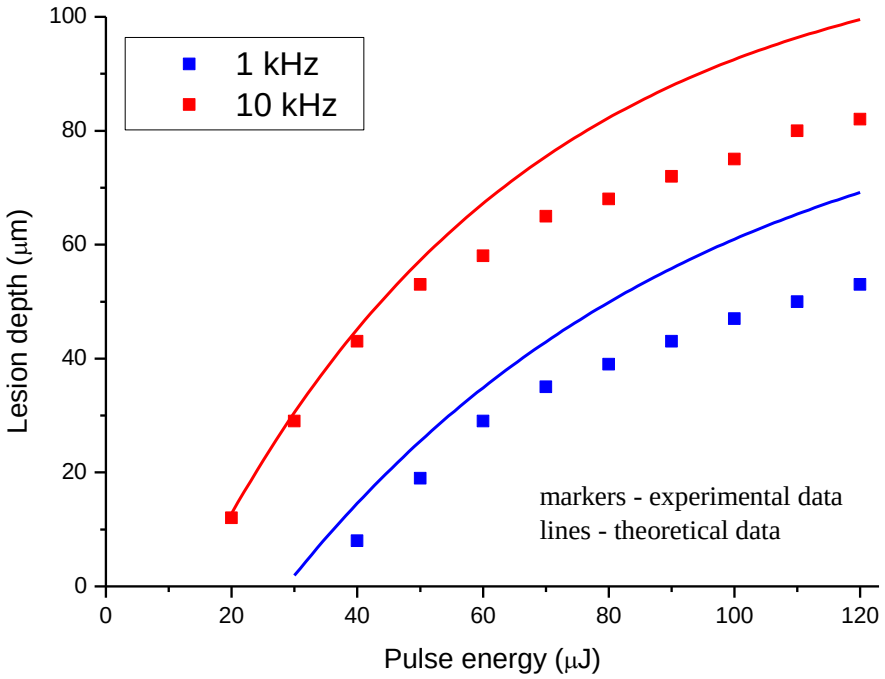

Figure 5.15 Experimental and simulation results for lesion depth as a function of pulse energy for two different repetition rates: 1 kHz and 10 kHz. The spot and line separation used for this experiment was 3 μm.

Theoretically obtained values for maximum depth of the lesion are slightly higher than values obtained experimentally. The main reasons for this discrepancy is that in this model plasma the created in and below the focus (as seen in figure 1.7) whereas it has been shown previously that plasma grows towards the source of laser radiation i.e. away from the surface [70, 83, 122], which leads to increased depth. Additionally, in the simulation the spot size is always in focus, whereas during the experiment laser beam will irradiate onto the sloped side of the crater leading to smaller value of irradiance due to a distorted and slightly larger, spot size. Moreover the approximated values for the tissue do not vary with temperature in the simulation which not the case in the reality. On the other hand the created plasma does not interact or deposit any energy into the tissue which would act to decrease the amount of tissue that is removed during the simulation.

The results obtained through the simulation do follow similar trends to the results obtained experimentally. They also identify a similar value of threshold for creation of the linear lesion as shown in figure 1.10. For further validation of the model a comparison was also made to investigate how the spot separation effects the results. Figure 5.16 shows the maximum depth of the lesions reached for a constant value of the repetition rate – 1 kHz, but for various spot separations: 1, 3, 5 and 7 μm.

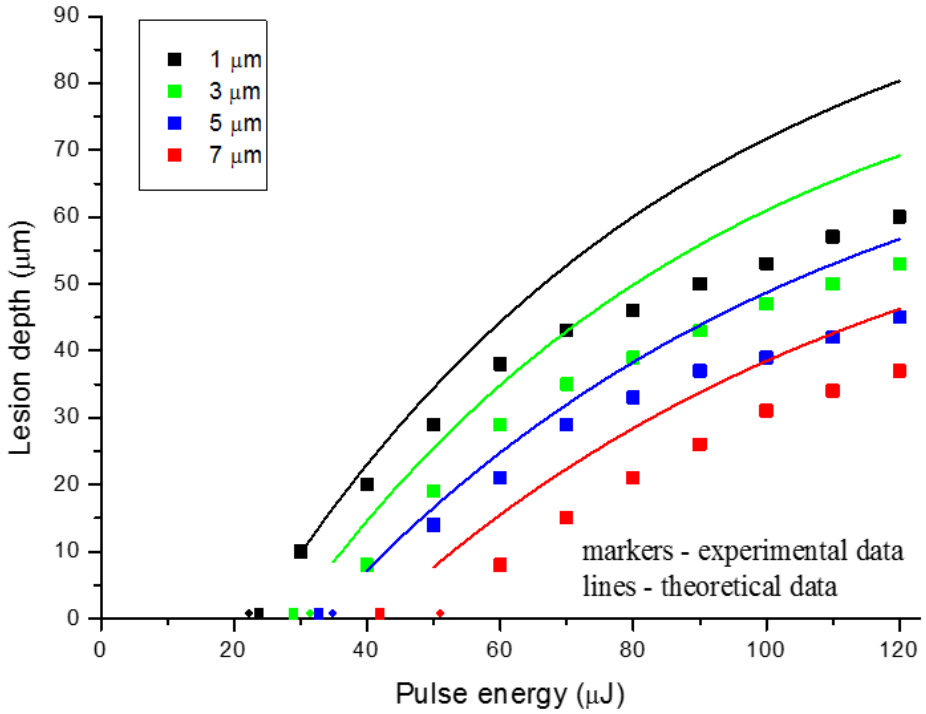

Figure 5.16 Maximum lesion depth as a function of pulse energy for various values of spot and line separation. The repetition rate is kept constant across the experiment and set at 1 kHz. Rectangles on the horizontal axis mark experimentally obtained threshold and sphere mark experimentally obtained value of threshold.

Both theoretical and experimental values follow a similar trend and generally point to similar values of the threshold. Again however, there is discrepancy between the model value and the experimentally determined values. Therefore it is safe to say that this simulation can be used to draw basic conclusions about the heat accumulation presence during picosecond plasma mediated ablation of biological tissue. Most useful is the demonstration of how a change of the repetition rate and spot separation influences final maximal depth reached by single line scanning ablation.

5.3.5. Sensitivity of the model

Using incorrect values of the parameters for the theoretical modelling can lead to incorrect results. Therefore an investigation as to how much of an influence a small variance of reflectivity and spot diameter can have on the calculated final depth of a linear lesion was carried out. The value of reflectivity used in the simulation was 0.4 and tests were carried for values ±5% from that value. A second test was carried out changing the value of the focused spot size where the accepted value of 35 µm was also varied by ±5 µm. Figure 5.17 shows how the maximum depth is influenced by the change in the reflectivity and

Figure 5.18 shows how the change in spot diameter influences the maximum depth of the simulated lesion.

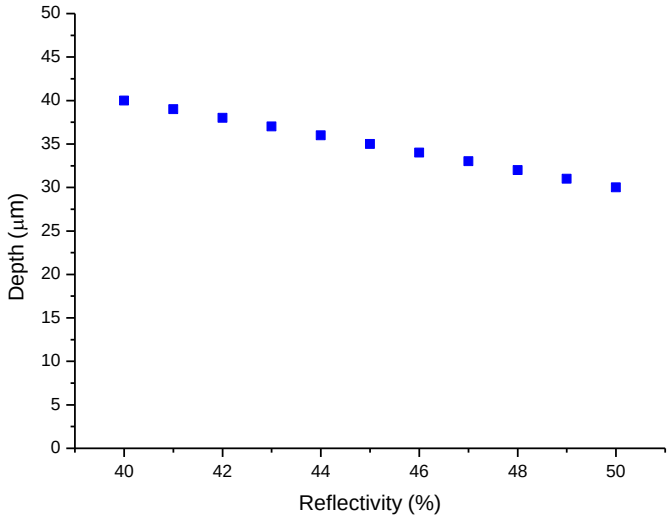

Figure 5.17 Maximum depth reached in a single line scanning ablation simulation for different values of reflectivity.

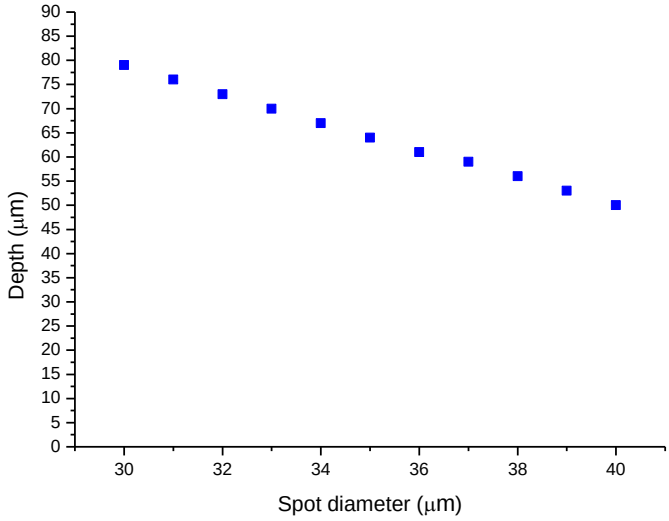

Figure 5.18 Maximum depth reached in a single line scanning ablation simulation for different values of spot diameter.

The 5 % change in the value of reflectivity results in a 14% change in the maximum depth of a simulated lesion. Moreover a 5 μm change (i.e. 14% change) in the spot diameter results in change to the final depth of up to 23%. Consequently, values obtained through this simulation have an inherent uncertainty but the simulation can be useful to representation the overall trend of the process and in particular demonstrates the presence of heat accumulation.

5.3.6. Conclusions

In the first part of this chapter an ALE moving boundary model was developed using COMSOL 4.3b to investigate single pulse ablation of CO_2 laser radiation on enamel. It was found that is approach does not effectively simulate a water mediated explosive ablation as the model was incapable of computing this highly dynamic process. The ALE moving boundary approach is much better suited for simulation of less explosive regimes preferably with longer pulse durations.

In the second part of this chapter a 2D finite element model developed using MATLAB software package was developed to simulate single line scanning plasma mediated ablation of porcine sclera. Although a number of assumptions were employed to simplify the model and there was some discrepancy between experimental and theoretical data, the model is useful tool to highlight the presence of the heat accumulation. When considering a square shape raster scanning pattern from the simulation we can conclude that after first scanned line there is residual energy leftover in the area where consecutive scanning line would commence. The next step in the evolution of this model would be an introduction of third dimension so that a full scanning pattern could be simulated. To further improve the quality of the modelling further work would be needed to incorporate parameters variance with temperature and the interaction between the plasma and the material. Moreover the evolution of plasma could be improved to more closely represent the direction of growth towards the incoming laser beam.

Chapter 6. Conclusions

Successful ablation of human enamel with 10.6 μm CO_2 laser radiation has been demonstrated and described in this thesis with the aim to enable more precise and less invasive dental procedures. An in-depth investigation of different parameters, with a particular focus on pulse duration and irradiating patterns, has been tested and suitable machining parameters have been found for realistic drilling in a dental surgery. To minimize the amount of cracking in the ablation site, it was shown that the pulse duration should be in the range of 10 μs (for fluences in the order of 40 J/cm^2), which agrees with predictions from previously published simulations [14-16]. Longer pulse durations in the range of 100 – 200 μs introduced significantly more cracking on the crater surface and larger heat affected zone. Moreover machining with an out of focus converging and diverging beam, with and without fluence compensation, was tested and it was found that defocusing by ~100 μm will result in an ablation efficiency decrease of up to 5%, assuming that the fluence used exceeds ablation threshold (more than 40 J/cm^2). Additionally, the safety of the procedure was tested by placing thermocouples into the pulpal chamber during laser processing. It is necessary to keep the maximum temperature increase below a critical value of 5.5^{o}C above which point would cause living tissue necrosis inside the pulpal chamber. It was found that when using a water spray the temperature is kept well below that threshold. For a 250 Hz processing rate the maximum temperature increase was 2.98 ^{o}C when considering 5 cycles of a 30 second laser irradiation (10 μs, 40 J/cm^2) separated by 30 second pause. Even though the addition of water spray decreases the ablation efficiency it helps keep the temperature below the critical level and prevents tissue dehydration.

In the second part of the thesis an in-depth investigation to find optimal processing parameters for picosecond plasma mediated ablation of scleral tissue in the eye was presented. The main goal was to assess whether cavities formed by laser ablation could enhance drug transport through the sclera to aid treatment of age related macular degeneration. Again a range of processing parameters were tested, pulse energy, repetition rate, spot and line separation and scanning strategies. During the experiments it was found that heat accumulation is a significant factor and has to be taken into consideration when finding optimal processing parameters. An outbound spiral scanning pattern was capable of creating the most uniform, well defined cavities with the flattest bottom surface. Such a scanning pattern ensures that the thermal accumulation condition

is relatively uniform across whole cavity. Optimal parameters identified were 1 kHz, 60 µJ and a 3µm spot/line separation for a 6 ps pulse. To ensure viability of this process from a safety aspect (i.e. to ensure no unwanted damage to the eye could occur) experiments focusing on the temperature increase in the tissue during laser processing as well as the transmission light through the tissue were tested. For creation of a 1 mm by 1 mm square cavity (1 kHz, 60 µJ and 3µm spot/line separation) the maximum temperature increase was ~2.7 ^{o}C, which is well below the critical increase of 11.7 ^{o}C [146]. The measurements to ensure that there is negligible radiation passing through the tissue during laser processing showed that no potentially damaging energy was transmitted through the tissue. To estimate a change in the permeation of the tissue resulting from creation of the pockets experiments were carried out using Franz cells and flat scleral sample. A 5 mm by 5 mm square and 100 µm deep cavity was created on the surface of the tissue. The results showed that creation of such cavity can increase permeation of the tissue in the first 5 hours by a factor of 11 to 12. It can be concluded that picosecond plasma mediated ablation offers a potential minimally invasive route to modify and remove tissue and increase its permeation as a means to enhance drug delivery for treatment of eye disease.

To further the understanding of the laser processes two different theoretical models were created. To simulate single pulse removal of dental hard tissue an ALE moving boundary model was developed using the COMSOL software package. It was found that this approach was not effective and was incapable of simulating highly dynamic removal of hard dental tissue. However it was a relatively simple model and did provide useful insight into the limiting thresholds of the process. A second model was created to simulate single line plasma mediated picosecond ablation of porcine sclera. Although a number of assumptions were employed to simplify the model, and there was some discrepancy between experimental and theoretical data, the model proved to be a useful tool to simulate the physical mechanisms and backed experimental observations of the presence of the heat accumulation.

Chapter 7. References

1. Maiman, T.H., *Stimulated Optical Radiation in Ruby.* Nature, 1960. **187**(4736): p. 493-494.
2. Chopra, S. and H.M. Chawla, *Lasers in Chemical and Biological Sciences* 1992: New Age International Publishers.
3. Welch, A.J., J.H. Torres, and W.F. Cheong, *Laser physics and laser-tissue interaction.* Tex Heart Inst J, 1989. **16**(3): p. 141-9.
4. Oh, H.-S. and J.-S. Kim, *Clinical Application of CO2 Laser* Wooridul Spine Hospital, Seoul
5. Jenoptik, *Lasers for Medical Applications*
6. O'Shea, P.G. and H.P. Freund, *Free-Electron Lasers: Status and Applications*. A. James Clark School of Engineering.
7. *Shore Laser*. 2008 accessed 2015; Available from: http://shorelaser.com/.
8. Jawad, M.M., S.T. Abdul Qader, A.A. Zaidan, B.B. Zaidan, A.W. Naji, and I.T. Abdul Qader, *An Overview of Laser Principle, Laser-Tissue Interaction Mechanisms and Laser Safety Precautions for Medical Laser Users.* International Journal of Pharmacology, 2011. **7**: p. 149-160.
9. journals, S. *Phlebology: The Journal of Venous Disease*. accessed 2015; Available from: http://phl.sagepub.com/content/25/1/11/F9.large.jpg.
10. California, U.o. *Introduction to Clinical Medicine*. 2010 accessed 2015; Available from: http://bme240.eng.uci.edu/.
11. Hibst, R. and U. Keller, *Experimental studies of the application of the Er:YAG laser on dental hard substances: I. Measurement of the ablation rate.* Lasers in Surgery and Medicine, 1989. **9**(4): p. 338-344.
12. Walsh, L.J., *The use of lasers in implantology: an overview.* J Oral Implantol, 1992. **18**(4): p. 335-40.
13. Lin, L.C., D.L. Pitts, and L.W. Burgess, Jr., *An investigation into the feasibility of photobleaching tetracycline-stained teeth.* J Endod, 1988. **14**(6): p. 293-9.
14. Verde, A.V., M. Ramos, and A. Stoneham, *The role of mesoscopic modelling in understanding the response of dental enamel to mid-infrared radiation.* Physics in medicine and biology, 2007. **52**(10): p. 2703.
15. Verde, A.V., M.M. Ramos, R.M. Ribeiro, and M. Stoneham, *Mesoscopic modelling of enamel interaction with mid-infrared sub-ablative laser pulses.* Thin solid films, 2004. **453**: p. 89-93.
16. Verde, A.C.V., M.M.D. Ramos, R.M. Ribeiro, and M. Stoneham. *Modeling of the human enamel laser ablation process at the mesoscopic scale*. in *Biomedical Optics 2003*. 2003. International Society for Optics and Photonics: p. 72-82.
17. Assa, S., S. Meyer, and D. Fried, *Ablation of Dental Hard Tissues with a Microsecond Pulsed Carbon Dioxide Laser Operating at 9.3-μm with an Integrated Scanner.* Proceedings of SPIE--the International Society for Optical Engineering, 2008. **6843**: p. 684308-684308.
18. Nguyen, D., K. Chang, S. Hedayatollahnajafi, M. Staninec, K. Chan, R. Lee, and D. Fried, *High-speed scanning ablation of dental hard tissues with a λ = 9.3 μm CO(2) laser: adhesion, mechanical strength, heat accumulation, and peripheral thermal damage.* Journal of Biomedical Optics, 2011. **16**(7): p. 071410.
19. Kirschner, R.A. and M. Unger, *Introduction to laser surgery.* Surg Clin North Am, 1984. **64**(5): p. 839-41.
20. Qian, P., J. Asta, C. Jiyao, O.S. Lars, W. Trond, G. Karl-Erik, and M. Johan, *Lasers in medicine.* Reports on Progress in Physics, 2008. **71**(5): p. 056701.
21. Featherstone, J.D. and D. Fried, *Fundamental Interactions of Lasers with Dental Hard Tissues.* Medical Laser Applications, 2001. **16**(3): p. 181-194.

22. Dental Health Foundation, I. *Structure & function of teeth*. accessed 2016; Available from: http://www.dentalhealth.ie/children/structure.html.
23. Wilson, R. *Rick Wilson DMD's dental blog*. 2010 accessed 2015; Available from: http://rickwilsondmd.typepad.com/rick_wilson_dmds_blog/2010/11/enamel-bonding-dentin-bonding.html.
24. Clarke, J. *Biology of the Human Dentition*. 1998 accessed 2015; Available from: http://www.uic.edu/classes/orla/orla312/BHDTwo.html.
25. Habelitz, S., S.J. Marshall, G.W. Marshall, Jr., and M. Balooch, *Mechanical properties of human dental enamel on the nanometre scale.* Arch Oral Biol, 2001. **46**(2): p. 173-83.
26. Ross, M.H. and W. Pawlina, *Histology: A Text and Atlas*. 2010.
27. *Information portal about teeth and dental disease*. accessed 2015; Available from: http://www.bleaching-dental.com.
28. Kentucky, U.o. *Oral Histology - Dental Pulp*. accessed 2015; Available from: http://www.uky.edu/~brmacp/oralhist/module4/lecture/oh4lect.htm.
29. Fried, D., R.E. Glena, J.D.B. Featherstone, and W. Seka, *Permanent and transient changes in the reflectance of CO2 laser-irradiated dental hard tissues at λ = 9.3, 9.6, 10.3, and 10.6 μm and at fluences of 1–20 J/cm2.* Lasers in Surgery and Medicine, 1997. **20**(1): p. 22-31.
30. Fried, D., J. Ragadio, M. Akrivou, J.D.B. Featherstone, M.W. Murray, and K.M. Dickenson, *Dental hard tissue modification and removal using sealed transverse excited atmospheric-pressure lasers operating at λ=9.6 and 10.6 μm.* Journal of Biomedical Optics, 2001. **6**(2): p. 231-238.
31. Fan, K., P. Bell, and D. Fried, *Rapid and conservative ablation and modification of enamel, dentin, and alveolar bone using a high repetition rate transverse excited atmospheric pressure CO2 laser operating at lambda=9.3 micro.* J Biomed Opt, 2006. **11**(6): p. 064008.
32. Rodrigues, L.K., M. Nobre dos Santos, D. Pereira, A.V. Assaf, and V. Pardi, *Carbon dioxide laser in dental caries prevention.* J Dent, 2004. **32**(7): p. 531-40.
33. Fried, D., S.R. Visuri, J.D.B. Featherstone, J.J.T. Walsh, W.D. Seka, R.E. Glena, S.M. McCormack, and H.A. Wigdor, *Infrared radiometry of dental enamel during Er:YAG and Er:YSGG laser irradiation.* Journal of Biomedical Optics, 1996. **1**(4): p. 455-465.
34. Pretty, I.A., *Caries detection and diagnosis: Novel technologies.* Journal of Dentistry, 2006. **34**(10): p. 727-739.
35. Magalhães, M.F., R.A.N. Ferreira, P.A. Grossi, and R.M. Andrade, *Measurement of thermophysical properties of human dentin: Effect of open porosity.* Journal of Dentistry, 2008. **36**(8): p. 588-594.
36. Lin, M., F. Xu, T.J. Lu, and B.F. Bai, *A review of heat transfer in human tooth--experimental characterization and mathematical modeling.* Dent Mater, 2010. **26**(6): p. 501-13.
37. Lin, M., Q.D. Liu, T. Kim, F. Xu, B.F. Bai, and T.J. Lu, *A new method for characterization of thermal properties of human enamel and dentine: Influence of microstructure.* Infrared Physics & Technology, 2010. **53**(6): p. 457-463.
38. Xu, H.H., D.T. Smith, S. Jahanmir, E. Romberg, J.R. Kelly, V.P. Thompson, and E.D. Rekow, *Indentation damage and mechanical properties of human enamel and dentin.* J Dent Res, 1998. **77**(3): p. 472-80.
39. Panas, A.J., M. Preiskorn, M. Dąbrowski, and S. Żmuda, *Validation of hard tooth tissue thermal diffusivity measurements applying an infrared camera.* Infrared Physics & Technology, 2007. **49**(3): p. 302-305.

40. Parker, W.J., R.J. Jenkins, C.P. Butler, and G.L. Abbott, *Flash Method of Determining Thermal Diffusivity, Heat Capacity, and Thermal Conductivity*. Journal of Applied Physics, 1961. **32**(9): p. 1679-1684.
41. Ana, P.A., W.F. Velloso, and D.M. Zezell, *Three-dimensional finite element thermal analysis of dental tissues irradiated with Er,Cr:YSGG laser*. Review of Scientific Instruments, 2008. **79**(9): p. 093910.
42. Seka, W.D., J.D.B. Featherstone, D. Fried, S.R. Visuri, and J.T. Walsh. *Laser ablation of dental hard tissue: from explosive ablation to plasma-mediated ablation*. in *SPIE Proceedings, Lasers in Dentistry II*. 1996. p. 144-158.
43. Itzkan, I., D. Albagli, M. Dark, L.T. Perelman, and M.S. Feld. *Short pulse laser ablation is photomechanical, not thermal or chemical*. in *Lasers and Electro-Optics Society Annual Meeting, 1994. LEOS '94 Conference Proceedings. IEEE*. 1994. Boston, USA: p. 71-72.
44. Rode, A.V., E.G. Gamaly, B. Luther-Davies, B.T. Taylor, M. Graessel, J.M. Dawes, A. Chan, R.M. Lowe, and P. Hannaford, *Precision ablation of dental enamel using a subpicosecond pulsed laser.* Aust Dent J, 2003. **48**(4): p. 233-9.
45. Rode, A.V., N.R. Madsen, V.Z. Kolev, E.G. Gamaly, B. Luther-Davies, J.M. Dawes, and A. Chan. *Subpicosecond and picosecond laser ablation of dental enamel: comparative analysis*. in *SPIE Proceedings, Commercial and Biomedical Applications of Ultrafast Lasers IV*. 2004. p. 76-86.
46. Fried, D., N. Ashouri, T. Breunig, and R. Shori, *Mechanism of water augmentation during IR laser ablation of dental enamel.* Lasers Surg Med, 2002. **31**(3): p. 186-93.
47. Souza-Gabriel, A.E., M.A. Chinelatti, M.C. Borsatto, J.D. Pecora, R.G. Palma-Dibb, and S.A. Corona, *SEM analysis of enamel surface treated by Er:YAG laser: influence of irradiation distance.* Microsc Res Tech, 2008. **71**(7): p. 536-41.
48. Rosa, A.D., A.V. Sarma, C.Q. Le, R.S. Jones, and D. Fried, *Peripheral thermal and mechanical damage to dentin with microsecond and sub-microsecond 9.6 μm, 2.79 μm, and 0.355 μm laser pulses.* Lasers in Surgery and Medicine, 2004. **35**(3): p. 214-228.
49. Stübinger, S., v.B. von Rechenberg, H.-F. Zeilhofer, R. Sader, and C. Landes, *Er:YAG laser osteotomy for removal of impacted teeth: Clinical comparison of two techniques.* Lasers in Surgery and Medicine, 2007. **39**(7): p. 583-588.
50. *Laterna - Dental Laser Systems*. accessed 2015; Available from: http://www.laterna-lasers.com/opus-duo-dental-laser.html.
51. *Fotona AT Fidelis*. accessed 2015; Available from: http://www.fotona.com/en/products/1093/at-fidelis/.
52. Zaret, M.M., H. Ripps, I.M. Siegel, and G.M. Breinin, *Laser photocoagulation of the eye.* Archives of Ophthalmology, 1963. **69**(1): p. 97-104.
53. Mardin, C.Y., R.P. Tornow, and E.K. Friedrich, *Laser in ophthalmology.* Physics Procedia, 2010. **5**: p. 631-636.
54. Moses, R.A., W.J. Grodzki, Jr., B.C. Starcher, and M.J. Galione, *Elastin content of the scleral spur, trabecular mesh, and sclera.* Invest Ophthalmol Vis Sci, 1978. **17**(8): p. 817-8.
55. Watson, P.G. and R.D. Young, *Scleral structure, organisation and disease. A review.* Exp Eye Res, 2004. **78**(3): p. 609-23.
56. Heinegård, D.O.Å., *Glycosylated matrix proteins.*, in *Connective Tissue and Its Heritable Disorders: Molecular, Genetic, and Medical Aspects, Second Edition*, B.S. Peter M. Royce, Editor. 2003, Wiley: New York. p. 189-209.
57. Norman, R.E., J.G. Flanagan, S.M. Rausch, I.A. Sigal, I. Tertinegg, A. Eilaghi, S. Portnoy, J.G. Sled, and C.R. Ethier, *Dimensions of the human sclera: Thickness*

measurement and regional changes with axial length. Exp Eye Res, 2010. **90**(2): p. 277-84.
58. Vogel, A., C. Dlugos, R. Nuffer, and R. Birngruber, *Optical properties of human sclera, and their consequences for transscleral laser applications.* Lasers in Surgery and Medicine, 1991. **11**(4): p. 331-340.
59. Janoria, K.G., S. Gunda, S.H. Boddu, and A.K. Mitra, *Novel approaches to retinal drug delivery.* Expert Opin Drug Deliv, 2007. **4**(4): p. 371-88.
60. Thrimawithana, T.R., S. Young, C.R. Bunt, C. Green, and R.G. Alany, *Drug delivery to the posterior segment of the eye.* Drug Discov Today, 2011. **16**(5-6): p. 270-7.
61. Peyman, G.A., E.M. Lad, and D.M. Moshfeghi, *Intravitreal injection of therapeutic agents.* Retina, 2009. **29**(7): p. 875-912.
62. Wu, H. and T.C. Chen, *The effects of intravitreal ophthalmic medications on intraocular pressure.* Semin Ophthalmol, 2009. **24**(2): p. 100-5.
63. Saishin, Y., R.L. Silva, Y. Saishin, K. Callahan, C. Schoch, M. Ahlheim, H. Lai, F. Kane, R.K. Brazzell, D. Bodmer, and P.A. Campochiaro, *Periocular injection of microspheres containing PKC412 inhibits choroidal neovascularization in a porcine model.* Invest Ophthalmol Vis Sci, 2003. **44**(11): p. 4989-93.
64. Bausch&Lomb. *Intravitreal Implant*. accessed 2016; Available from: http://www.bausch.com/portals/109/-/m/BL/United%20States/Files/MSDS/vitrasert.pdf.
65. Bausch&Lomb. *Retisert (fluocinolone acetonide intravitreal implant)*. accessed 2016; Available from: http://www.bausch.com/ecp/our-products/rx-pharmaceuticals/rx-pharmaceuticals/retisert-fluocinolone-acetonide-intravitreal-implant-059-mg.
66. Ghate, D. and H.F. Edelhauser, *Ocular drug delivery.* Expert Opin Drug Deliv, 2006. **3**(2): p. 275-87.
67. Gupta, S. and R. Gurjar, *OcuPhor™ – The Future of Ocular Drug Delivery*. 2011.
68. Jiang, J., J.S. Moore, H.F. Edelhauser, and M.R. Prausnitz, *Intrascleral drug delivery to the eye using hollow microneedles.* Pharm Res, 2009. **26**(2): p. 395-403.
69. Plamann, K., F. Aptel, C.L. Arnold, A. Courjaud, C. Crotti, F. Deloison, F. Druon, P. Georges, M. Hanna, J.-M. Legeais, F. Morin, É. Mottay, V. Nuzzo, D.A. Peyrot, and M. Savoldelli, *Ultrashort pulse laser surgery of the cornea and the sclera.* Journal of Optics, 2010. **12**(8): p. 084002.
70. Vogel, A. and V. Venugopalan, *Mechanisms of pulsed laser ablation of biological tissues.* Chem Rev, 2003. **103**(2): p. 577-644.
71. Krasnov, M.M., *Q-switched laser goniopuncture.* Archives of Ophthalmology, 1974. **92**(1): p. 37-41.
72. Aron-Rosa, D., J.J. Aron, M. Griesemann, and R. Thyzel, *Use of the neodymium-YAG laser to open the posterior capsule after lens implant surgery: a preliminary report.* J Am Intraocul Implant Soc, 1980. **6**(4): p. 352-4.
73. van der Zypen, E., F. Fankhauser, H. Bebie, and J. Marshall, *Changes in the ultrastructure of the iris after irradiation with intense light. A study of long-term effects after irradiation with argon ion, Nd:YAG and Q-switched ruby lasers.* Adv Ophthalmol, 1979. **39**: p. 59-180.
74. Krauss, J.M., C.A. Puliafito, and R.F. Steinert, *Laser interactions with the cornea.* Surv Ophthalmol, 1986. **31**(1): p. 37-53.
75. Trokel, S.L., R. Srinivasan, and B. Braren, *Excimer laser surgery of the cornea.* Am J Ophthalmol, 1983. **96**(6): p. 710-5.

76. Cox, B., *Introduction to Laser-Tissue Interactions*, in *Optics in Medicine courses MPHY3886, MPHYM886, MPHYG886 - University College London Lecture Notes*. 2013.
77. Nicoli, S., G. Ferrari, M. Quarta, C. Macaluso, P. Govoni, D. Dallatana, and P. Santi, *Porcine sclera as a model of human sclera for in vitro transport experiments: histology, SEM, and comparative permeability.* Mol Vis, 2009. **15**: p. 259-66.
78. Vogel, A., J. Noack, G. Huettmann, and G. Paltauf. *Femtosecond-laser-produced low-density plasmas in transparent biological media: a tool for the creation of chemical, thermal, and thermomechanical effects below the optical breakdown threshold*. in *High-Power Lasers and Applications*. 2002. International Society for Optics and Photonics: p. 23-37.
79. Vogel, A. and O. Heinrich, *Optical breakdown in water and ocular media, and its use for intraocular photodisruption*. 2001, Shaker: Medical University of Lübeck, Germany. p. 242.
80. Vogel, A., S. Busch, and U. Parlitz, *Shock wave emission and cavitation bubble generation by picosecond and nanosecond optical breakdown in water.* The Journal of the Acoustical Society of America, 1996. **100**(1): p. 148-165.
81. Vogel, A., K. Nahen, D. Theisen, and J. Noack, *Plasma formation in water by picosecond and nanosecond Nd: YAG laser pulses. I. Optical breakdown at threshold and superthreshold irradiance.* Selected Topics in Quantum Electronics, IEEE Journal of, 1996. **2**(4): p. 847-860.
82. Nahen, K. and A. Vogel, *Plasma formation in water by picosecond and nanosecond Nd:YAG laser pulses. II. Transmission, scattering, and reflection.* Selected Topics in Quantum Electronics, IEEE Journal of, 1996. **2**(4): p. 861-871.
83. Vogel, A., *Mechanisms of short-pulsed plasma-mediated laser ablation and disruption.* Lasers in Opthalmology-Basic, Diagnostic and Surgical Aspects. Kugler Publications, Den Haag, 2003. **1**: p. 99-113.
84. Nuzzo, V., K. Plamann, M. Savoldelli, M. Merano, D. Donate, O. Albert, P.F. Gardeazábal Rodríguez, G. Mourou, and J.-M. Legeais, *In situ monitoring of second-harmonic generation in human corneas to compensate for femtosecond laser pulse attenuation in keratoplasty*. Journal of Biomedical Optics, 2007. **12**(6): p. 064032-064032-11.
85. Nuzzo, V., F. Aptel, M. Savoldelli, K. Plamann, D. Peyrot, F. Deloison, D. Donate, and J.M. Legeais, *Histologic and ultrastructural characterization of corneal femtosecond laser trephination.* Cornea, 2009. **28**(8): p. 908-13.
86. Ripken, T., U. Oberheide, M. Fromm, S. Schumacher, G. Gerten, and H. Lubatschowski, *fs-Laser induced elasticity changes to improve presbyopic lens accommodation.* Graefes Arch Clin Exp Ophthalmol, 2008. **246**(6): p. 897-906.
87. Schumacher, S., M. Fromm, U. Oberheide, G. Gerten, A. Wegener, and H. Lubatschowski, *In vivo application and imaging of intralenticular femtosecond laser pulses for the restoration of accommodation.* J Refract Surg, 2008. **24**(9): p. 991-5.
88. Fisher, R.F., *The mechanics of accommodation in relation to presbyopia.* Eye (Lond), 1988. **2 (Pt 6)**: p. 646-9.
89. Jiang, F., X. Yang, N. Dai, P. Lu, H. Long, and L. Cui, *An in vitro study of femtosecond laser photodisruption in rabbit sclera.* Frontiers of Optoelectronics in China, 2008. **1**(1-2): p. 162-167.
90. Yang, X., N. Dai, H. Long, P. Lu, W. Li, and F. Jiang, *Experimental femtosecond laser photodisruption of rabbit sclera for minimally invasive laser sclerostomy: An in vitro study.* Optics and Lasers in Engineering, 2010. **48**(7–8): p. 806-810.

91. Sacks, Z.S., F.H. Loesel, C.G. Durfee Iii, R.M. Kurtz, T. Juhasz, and G.A. Mourou. *Transscleral photodisruption for the treatment of glaucoma*. in *SPIE Proceedings, Light Scattering Technologies for Mechanics, Biomedicine, and Material Science*. 1999. Saratov, Russia: p. 516-521.
92. Sacks, Z.S., R.M. Kurtz, T. Juhasz, and G.A. Mourou. *Femtosecond subsurface photodisruption in scattering human tissues using long infrared wavelengths*. 2001. p. 98-111.
93. Sacks, Z.S., R.M. Kurtz, T. Juhasz, and G.A. Mourau, *High precision subsurface photodisruption in human sclera.* Journal of Biomedical Optics, 2002. **7**(3): p. 442-450.
94. Sacks, Z.S., R.M. Kurtz, T. Juhasz, G. Spooner, and G.A. Mouroua, *Subsurface photodisruption in human sclera: wavelength dependence*, in *Ophthalmic Surg Lasers Imaging*. 2003. p. 104-13.
95. Chai, D., G. Chaudhary, E. Mikula, H. Sun, R. Kurtz, and T. Juhasz, *In vivo femtosecond laser subsurface scleral treatment in rabbit eyes.* Lasers Surg Med, 2010. **42**(7): p. 647-51.
96. Sun, H., R. Kurtz, and T. Juhasz, *Evaluation of human sclera after femtosecond laser ablation using two photon and confocal microscopy.* Journal of Biomedical Optics, 2012. **17**(8): p. 081411-081411.
97. Durrie, D.S. and G.M. Kezirian, *Femtosecond laser versus mechanical keratome flaps in wavefront-guided laser in situ keratomileusis: prospective contralateral eye study.* J Cataract Refract Surg, 2005. **31**(1): p. 120-6.
98. *IntraLase FS Laser*. accessed 2015; Available from: http://abbottmedicaloptics.com/products/refractive/ilasik/intralase-fs-laser.
99. Kurtz, R.M., C. Horvath, H.H. Liu, R.R. Krueger, and T. Juhasz, *Lamellar refractive surgery with scanned intrastromal picosecond and femtosecond laser pulses in animal eyes.* J Refract Surg, 1998. **14**(5): p. 541-8.
100. Jonas, J.B. and U. Vossmerbaeumer, *Femtosecond laser penetrating keratoplasty with conical incisions and positional spikes.* J Refract Surg, 2004. **20**(4): p. 397.
101. Buratto, L. and E. Bohm, *The use of the femtosecond laser in penetrating keratoplasty.* Am J Ophthalmol, 2007. **143**(5): p. 737-742.
102. *NHS - Glaucoma - Treatment* accessed 2015; Available from: http://www.nhs.uk/Conditions/Glaucoma/Pages/Treatment.aspx.
103. *Aura PT datasheet*. accessed 2015; Available from: http://www.ophthalmic.lumenis.com/pdf/AuraPT.pdf.
104. *Aura PT*. accessed 2015; Available from: http://www.ophthalmic.lumenis.com/Aura_PT.
105. *Optical-Thermal Response of Laser-Irradiated Tissue*, ed. A.J. Welch, van Gemert, Martin JC (Eds.). 2011.
106. Jansen, E.D., T.G. van Leeuwen, M. Motamedi, C. Borst, and A.J. Welch, *Temperature dependence of the absorption coefficient of water for midinfrared laser radiation.* Lasers Surg Med, 1994. **14**(3): p. 258-68.
107. J. E. Andrew, P.E.D., D. Forster and P. H. Key, *Direct etching of polymeric materials using a XeCl laser.* Appl. Phys. Lett., 1983. **43**: p. 717.
108. Ready, J.F., *Effects of High-Power Laser Radiation*. 1971, New York, USA: Academic Press.
109. Venugopalan, V., N.S. Nishioka, and B.B. Mikić, *The Effect of Laser Parameters on the Zone of Thermal Injury Produced by Laser Ablation of Biological Tissue.* Journal of Biomechanical Engineering, 1994. **116**(1): p. 62-70.
110. Olmes, A., H.G. Franke, E. Bänsch, H. Lubatschowski, M. Raible, G. Dziuk, and W. Ertmer, *Modeling of infrared soft-tissue photoablation process.* Applied Physics B, 1997. **65**(4-5): p. 659-666.

111. Batanov, V.A.F., V. B., *Flushing Out the Liquid Phase - A New Mechanism of Producing a Crater in Planar Fully Developed Evaporation of a Metallic Target by a Laser Beam.* Journal of Experimental and Theoretical Physics Letters, 1973. **17**: p. 247.
112. Reilly, J.P., A. Ballantyne, and J.A. Woodroffe, *Modeling of Momentum Transfer to a Surface by Laser-Supported Absorption Waves.* AIAA Journal, 1979. **17**(10): p. 1098-1105.
113. Frenz, M., A.D. Zweig, V. Romano, H.P. Weber, N.I. Chapliev, and A.S. Silenok. *Dynamics in laser cutting of soft media*. in *SPIE Proceedings, Laser-Tissue Interaction*. 1990. p. 22-33.
114. Lorazo, P., L.J. Lewis, and M. Meunier. *Molecular-dynamics simulations of picosecond pulsed laser ablation and desorption of silicon*. in *SPIE Proceedings, Laser Plasma Generation and Diagnostics*. 2000. p. 66-75.
115. Gacek, S.S., *Molecular dynamics simulation of shock waves in laser-material interaction*. 2009, Iowa State University: Iowa. p. 103.
116. *COMSOL Multiphysics® Modeling Software*. accessed 2015; Available from: http://www.comsol.com/.
117. *Abaqus - Dassault Systèmes*. accessed 2015; Available from: http://www.3ds.com/products-services/simulia/products/abaqus/.
118. MATLAB, M.-. accessed 2015; Available from: http://uk.mathworks.com/products/matlab/.
119. *Autodesk Simulation ALGOR*. accessed 2015; Available from: http://www.autodesk.com/.
120. V.Bruyere, C. Touvrey, and P.Namy. *Comparison between Phase Field and ALE Methods to model the Keyhole Digging during Spot Laser Welding* in *COMSOL Conference*. 2013. Rotterdam.
121. Cvetkovic, M., D. Poljak, and A. Peratta. *Thermal modelling of the human eye exposed to laser radiation*. in *Software, Telecommunications and Computer Networks, 2008. SoftCOM 2008. 16th International Conference on*. 2008. p. 16-20.
122. Marla, D., U.V. Bhandarkar, and S.S. Joshi, *Transient Analysis of Laser Ablation Process With Plasma Shielding: One-Dimensional Model Using Finite Volume Method.* Journal of Micro and Nano-Manufacturing, 2013. **1**(1): p. 011007-011007.
123. Jiao, J. and Z. Guo, *Modeling of ultrashort pulsed laser ablation in water and biological tissues in cylindrical coordinates.* Applied Physics B, 2011. **103**(1): p. 195-205.
124. Vila Verde, A., M.M. Ramos, and A.M. Stoneham, *Benefits in cost and reduced discomfort of new techniques of minimally invasive cavity treatment.* J Dent Res, 2009. **88**(4): p. 297-9.
125. Williams, J.A., G.J. Pearson, M.J. Colles, and M. Wilson, *The photo-activated antibacterial action of toluidine blue O in a collagen matrix and in carious dentine.* Caries Res, 2004. **38**(6): p. 530-6.
126. *Rofin UK SC x20 CO2 laser Datasheet*.
127. Wlodarczyk, K.L., *Surface deformation mechanisms in laser smoothing and micromachining of optical glasses*. 2011, Heriot-Watt University. p. 220.
128. technologies, N. *Operating manual. Germanium acousto-optic modulator model 37027-3*. accessed 2015.
129. Siegman, A.E., M.W. Sasnett, and T.F. Johnston, *Choice of clip levels for beam width measurements using knife-edge techniques.* Quantum Electronics, IEEE Journal of, 1991. **27**(4): p. 1098-1104.

130. Maung, L.H., C. Lee, and D. Fried, *Near-IR Imaging of Thermal Changes in Enamel during Laser Ablation.* Proc SPIE Int Soc Opt Eng, 2010. **7546**(1).
131. University, L.S.B. *Water Absorption Spectrum*. 2000 (Updated 2015); Available from: http://www1.lsbu.ac.uk/water/water_vibrational_spectrum.html.
132. Vellini-Ferreira, F., F.A. Cotrim-Ferreira, J.A. Ribeiro, and R.I. Ferreira-Santos, *Mapping of proximal enamel thickness in permanent teeth.* Brazilian Journal of Oral Sciences, 2012. **11**: p. 481-485.
133. Fahad Ata Siddiqui, A.S., Syed Ajlal Akhtar, Saqib Rashid, Zohaib Khurshid, Shariq Najeeb, *Radiographic evaluation of dentin thickness and pulp spacewidth for different age group.* Journal of the Pakistan Dental Association, 2012. **21**: p. 99-.
134. Vogel, A., K. Nahen, D. Theisen, and J. Noack, *Plasma formation in water by picosecond and nanosecond Nd:YAG laser pulses. I. Optical breakdown at threshold and superthreshold irradiance.* Selected Topics in Quantum Electronics, IEEE Journal of, 1996. **2**(4): p. 847-860.
135. *Biological Electron Microscopy*. accessed 2015; Available from: http://www.biologicalelectronmicroscopy.com/biological-sample-preparation-overview.html.
136. Navaratnam, V., *Biological Specimen Preparation for Transmission Electron Microscopy.* Journal of Anatomy, 1999. **195**(Pt 1): p. 155-157.
137. *Alicona Metrology*. accessed 2015; Available from: http://www.alicona.co.uk/home/.
138. Noack, J. and A. Vogel, *Laser-induced plasma formation in water at nanosecond to femtosecond time scales: calculation of thresholds, absorption coefficients, and energy density.* Quantum Electronics, IEEE Journal of, 1999. **35**(8): p. 1156-1167.
139. Fried, D., J. Ragadio, and A. Champion, *Residual heat deposition in dental enamel during IR laser ablation at 2.79, 2.94, 9.6, and 10.6 μm.* Lasers in Surgery and Medicine, 2001. **29**(3): p. 221-229.
140. Raciukaitis, G., M. Brikas, P. Gecys, and M. Gedvilas. *Accumulation effects in laser ablation of metals with high-repetition-rate lasers*. in *SPIE Proceedings, High-Power Laser Ablation VII*. 2008. p. 70052L-70052L-11.
141. Bauer, F., A. Michalowski, T. Kiedrowski, and S. Nolte, *Heat accumulation in ultra-short pulsed scanning laser ablation of metals.* Optics Express, 2015. **23**(2): p. 1035-1043.
142. Eaton, S., H. Zhang, P. Herman, F. Yoshino, L. Shah, J. Bovatsek, and A. Arai, *Heat accumulation effects in femtosecond laser-written waveguides with variable repetition rate.* Optics Express, 2005. **13**(12): p. 4708-4716.
143. Roy Henderson, K.S., *Laser Safety*. 2004, United Kingdom: Taylor Francis Ltd.
144. *Ophir FL250A / FL250A-LP1 / FL250A-EX* accessed 2015; Available from: http://www.ophiropt.com/laser/pdf/eol-FL250A-V1_FL250A-LP1-V1_FL250A-EX.pdf.
145. Thorlabs. *S120C - Standard Photodiode Power Sensor, Si, 400 - 1100 nm, 50 mW*. accessed 2015; Available from: https://www.thorlabs.com/thorproduct.cfm?partnumber=S120C.
146. Wang, J., C. Sramek, Y.M. Paulus, D. Lavinsky, G. Schuele, D. Anderson, D. Dewey, and D. Palanker, *Retinal safety of near-infrared lasers in cataract surgery.* Journal of Biomedical Optics, 2012. **17**(9): p. 0950011-09500112.
147. Mains, J., *The impact of physicochemical properties and physiological clearance mechanisms on ocular drug distribution*. 2011, University of Strathclyde.
148. Ambati, J., C.S. Canakis, J.W. Miller, E.S. Gragoudas, A. Edwards, D.J. Weissgold, I. Kim, F.C. Delori, and A.P. Adamis, *Diffusion of high molecular*

weight compounds through sclera. Invest Ophthalmol Vis Sci, 2000. **41**(5): p. 1181-5.
149. Al-ebini, Y., *Investigations into Drug Delivery to the Eye: Nanoparticle Comparisons*. 2014, University of Hertfordshire: University of Hertfordshire.
150. *Absorption Systems*. accessed 2015; Available from: http://www.absorption.com/.
151. *DrugBank: Ocriplasmin (DB08888)*. accessed 2015; Available from: http://www.drugbank.ca/drugs/DB08888.
152. *DrugBank: Ranibizumab(DB01270) - Lucentis*. accessed 2015.
153. Zaidi, M., A. Jilani, P. Bhattacharya, N. Islam, and S. Alam, *A study of aqueous humour proteins in patients of primary open angle glaucoma.* Advances in Bioscience and Biotechnology, 2010. **1**(2): p. 110-114.
154. Jaworski, P., F. Yu, R.R.J. Maier, W.J. Wadsworth, J.C. Knight, J.D. Shephard, and D.P. Hand, *Picosecond and nanosecond pulse delivery through a hollow-core Negative Curvature Fiber for micro-machining applications.* Optics Express, 2013. **21**(19): p. 22742-22753.
155. Jaworski, P., F. Yu, R.M. Carter, J.C. Knight, J.D. Shephard, and D.P. Hand, *High energy green nanosecond and picosecond pulse delivery through a negative curvature fiber for precision micro-machining.* Optics Express, 2015. **23**(7): p. 8498-8506.
156. Thomson, R.R., T.A. Birks, S.G. Leon-Saval, A.K. Kar, and J. Bland-Hawthorn, *Ultrafast laser inscription of an integrated photonic lantern.* Optics Express, 2011. **19**(6): p. 5698-5705.
157. Choudhury, D., A. Arriola, J.R. Allington-Smith, C. Cunningham, and R.R. Thomson. *Towards freeform microlens arrays for near infrared astronomical instruments*. in *SPIE Proceedings, Advances in Optical and Mechanical Technologies for Telescopes and Instrumentation*. 2014. p. 915146-915146-7.
158. Donea, J., Huerta, A., Ponthot, J.-P. and Rodríguez-Ferran, A, *Arbitrary Lagrangian–Eulerian Methods*, in *Encyclopedia of Computational Mechanics* 2004.
159. Griot, M. *http://nic.ucsf.edu/blog/wp-content/uploads/2014/06/Gaussian-Beam-Optics.pdf*. 2009 accessed 2015.
160. GmbH, R.P.C. *Gaussian Beams*. Available from: https://www.rp-photonics.com/gaussian_beams.html.
161. Wake Forest Student, F.a.S.W.P. *NAN 242 100 – Nanofabrication of Thin Films - Vacuum Evaporation*. Available from: http://users.wfu.edu/ucerkb/Nan242/L06-Vacuum_Evaporation.pdf.
162. Stoian, R., *Investigations of the dynamics of material removal in ultrashort pulsed laser ablation*. 2010, Freien Universität Berlin. p. Chapter 1. Laser induced optical breakdown.
163. Vogel, A., J. Noack, K. Nahen, D. Theisen, S. Busch, U. Parlitz, D. Hammer, G. Noojin, B. Rockwell, and R. Birngruber, *Energy balance of optical breakdown in water at nanosecond to femtosecond time scales.* Applied Physics B: Lasers and Optics, 1999. **68**(2): p. 271-280.
164. Vogel, A. and J. Noack. *Numerical simulations of optical breakdown for cellular surgery at nanosecond to femtosecond time scales*. in *SPIE Proccedings, Laser-Tissue Interactions, Therapeutic Applications, and Photodynamic Therapy*. 2001. International Society for Optics and Photonics: p. 83-93.
165. Y. Lawrence Yao, H.C., *Thermal Aspects in Laser Material Removal.* Proceedings of the NSF Workshop on Research Needs in Thermal Aspects of Material Removal Processes. www.columbia.edu/~yly1/PDFs3/nsf%201.pdf